EKSPLOATACJA I NIEZAWODNOŚĆ
MAINTENANCE AND RELIABILITY

60TH ANNIVERSARY OF THE FACULTY OF MECHANICAL ENGINEERING OF LUBLIN UNIVERSITY OF TECHNOLOGY

The Evening School of Engineering was founded by government order on May 13, 1953. Professor Stanisław Ziemecki, Ph.D., was appointed the first rector, while Stanisław Podkowa, M.Sc., Eng., took the position of dean of the Faculty of Mechanical Engineering (which was the only faculty the School had at that time). The Evening School of Engineering was transformed into the Undergraduate School of Engineering by government order on April 28, 1965. Apart from the Faculty of Mechanical Engineering, the Undergraduate School of Engineering also comprised of the Electrical Engineering Faculty (established in 1964) and the Faculty of Civil Engineering (established in 1965). Finally, on August, 1, 1977, the Undergraduate School of Engineering was transformed into Lublin University of Technology.

During the sixty years of its existence, the Faculty has been developing dynamically, adapting its structure to the economic situation of the times. At present, the Faculty has 3147 full-time and part-time students and it offers six major programs in the following disciplines: mechanics and machine design, transport, materials engineering, biomedical engineering, mechatronics (offered together with the Faculty of Electrical Engineering and Computer Science), as well as management and production engineering (offered together with the Faculty of Management). The Faculty of Mechanical Engineering also offers a wide variety of refresher and training courses. In addition to that, there are numerous courses in English, which results in a higher and higher number of international exchange students who choose to study at the Faculty. Our graduates are highly valuable to potential employers and many of them decide to found their own companies.

The Faculty of Mechanical Engineering employs 137 teaching and research staff (including 30 professors and doctors with habilitation, 88 assistant professors and lecturers, 19 teaching assistants) and 103 non-teaching staff (engineering and technical, administrative, and support staff). The Faculty is committed to professional development of its academic staff. It has the right to award both the Doctor of Science degree (habilitation) in the discipline of machine design and maintenance and the doctoral degree in the following disciplines: machine design and maintenance, mechanics, production engineering. The research conducted by the academic staff of the Mechanical Engineering Faculty is of high quality, which is reflected in the ever increasing number of published monographs and papers in prestigious scientific journals, active participation of the staff members in both national and international congresses and conferences, as well as their cooperation with international research bodies.

The Faculty of Mechanical Engineering has close relations with business entities, mainly from the Lublin region. Owing to this cooperation, the Faculty staff are constantly developing new innovative technological solutions that are later granted patents. The Faculty is a leader on the national scale in inventiveness, or the number of inventions applied for patent protection.

Some of the actions that will be taken in the foreseeable future to enhance the potential of the Faculty of Mechanical Engineering include:

- expanding the curriculum to include new fields of study as well as increasing the number of courses for overseas students;
- obtaining the right to award the Doctor of Science degree (habilitation) in another discipline;
- expanding the scientific and research base due to the creation of the Center for Innovation and Advanced Technologies of Lublin University of Technology;
- diversifying the sources of financing research and teaching activities;
- concentrating on the commercialization of its research and development work.

On the occasion of the 60th anniversary of our Faculty, I would like to wish all the staff members more success with their research and teaching work.

Because of this special occasion, the whole current issue of the *Eksploatacja i Niezawodnosc – Maintenance and Reliability* includes selected papers presenting the best scientific results of our Faculty research groups.

Professor Zbigniew Pater, Ph.D., D.Sc. (Eng.), Dean of the Faculty

Science and Technology

Spis treści – Contents

WEREMCZUK A, KĘCIK K, RUSINEK R, WARMIŃSKI J. **The dynamics of the cutting process with Duffing nonlinearity**. Eksploatacja i Niezawodnosc – Maintenance and Reliability 2013; 15 (3): 209–213.

The paper presents the nonlinear one degree of freedom model of cutting process. To describe the dynamics the Duffing model with time delay part is used. The model is solved analytically by using the multiple time scale method. The stability lobe diagrams are determined numerically and analytically. The obtained results show that stability region depends on initial conditions of the system.

PIERNIKARSKI D, HUNICZ J, KOMSTA H. **Detection of knocking combustion in a spark ignition engine using optical signal from the combustion chamber**. Eksploatacja i Niezawodnosc – Maintenance and Reliability 2013; 15 (3): 214–220.

The aim of the presented research was to investigate spectral properties of the combustion flame with special regard to the detection and estimation of intensity of knocking combustion. Research was made using modified single cylinder test engine with spark ignition (SI) equipped with an optical sensor having direct access to the combustion chamber. Measurements were based on wideband intensity of optical radiation and chemilumines¬cence phenomena occurring in the combustion flame under the influence of high temperature and pressure. Spectral recordings were done for wavelengths typical for emission of intermediate products, covering the range from 250 nm to 625 nm, including typically investigated radicals like C2, CH, CN, OH. Obtained results confirmed, that occurrence and intensity of knock can be determined on the basis of further signal analysis. Comparison with in parallel recorded indicated pressure have shown that characteristics of emitted spectra is more sensitive to the changing of engine operating conditions.

KĘCIK K, MITURA A, WARMIŃSKI J. **Efficiency analysis of an autoparametric pendulum vibration absorber**. Eksploatacja i Niezawodnosc – Maintenance and Reliability 2013; 15 (3): 221–224.

This paper presents results of a study of a dynamic response of an autoparametric system consisting of the oscillator with an attached pendulum vibration absorber. The harmonic balance method is applied to get the autoparametic resonance conditions. The analytical full vibration absorption condition has been determined and verified by numerical simulations. Additionally, the influence of oscillator and pendulum damping on dynamics and the vibration absorption effect is presented.

TOR-ŚWIĄTEK A. **Evaluation of the effectiveness of the microcellular extrusion process of low density polyethylene**. Eksploatacja i Niezawodnosc – Maintenance and Reliability 2013; 15 (3): 225–229.

From a processing point of view, evaluation of effectiveness is essential for the proper conduct of each polymer processing process. However, it is particularly important in the case of modified plastics processing aids, such as blowing agents, the addition of which causes changes in both the process course and the physical properties and structure of the resulting product. Carrying out a proper analysis of the efficiency of the process, taking into account the criteria and methods can efficiently and reliably carry out a extrusion process. This paper presents the results of assessing the effectiveness of the microcellular extrusion process of LDPE modified with selected microblowing agent in the form of microspheres.

BEER K, PAŁKA K, SUROWSKA B, WALCZAK M. **A Quality Assessment of Casting Dental Prosthesis**. Elements. Eksploatacja i Niezawodnosc – Maintenance and Reliability 2013; 15 (3): 230–236.

Properties of fixed and mobile dentures, as well as their design have a significant impact on their durability in a complex state of biomechanical loads that occur in the oral cavity during the chewing process. Elements that are usually mechanical damaged (cracking) in skeletal prostheses are metal clamps. Damage of fixation of dentures not only results in the inability to further operation, but also is causing discomfort in the patient and can lead to injury of the oral cavity, teeth and risk of complications in case of access into the digestive system.The aim of this study was to evaluate the quality of items of prostheses manufactured using available techniques and the analysis of the causes of premature loss of functional quality of these elements. Dental cobalt matrix alloy – Wironit Extra-hard was used for the study. Qualitative research consisted of the evaluation of the nature and intensity of internal casting defects and evaluation of macro-and microstructure of manufactured castings using microscopic techniques. Research of breakthroughs indicate the occurrence of casting shrinkages. Microstructural research revealed the presence of a typical dendritic structure of the matrix in form of solid a solution Co-Cr-Mo and eutectic. Strength test results achieved in the relation to the macro and microstructure were also carried out. A quantitative assessment of the intensity of casting defects using image analysis was realized. Potential risks of casting technology were identified and a methodology of monitoring the state of elements of dentures was proposed.

WEREMCZUK A, KĘCIK K, RUSINEK R, WARMIŃSKI J. **Dynamika procesu skrawania z nieliniowością Duffinga**. Eksploatacja i Niezawodnosc – Maintenance and Reliability 2013; 15 (3): 209–213.

W artykule przedstawiono jednowymiarowy nieliniowy model skrawania. Do opisu procesu przyjęto model Duffinga z opóźnieniem czasowym. Model rozwiązano analitycznie za pomocą metody wielu skal czasowych. Wykres stabilności otrzymano numerycznie i analitycznie. Wykazano, że obszary stabilności zależą od warunków początkowych układu.

PIERNIKARSKI D, HUNICZ J, KOMSTA H. **Detekcja spalania stukowego w silniku o zapłonie iskrowym za pomocą sygnału optycznego z komory spalania**. Eksploatacja i Niezawodnosc – Maintenance and Reliability 2013; 15 (3): 214–220.

Celem prezentowanych badań było zbadanie widmowych własności płomienia w komorze spalania ze specjalnym uwzględnieniem możliwości detekcji i oceny intensywnosci spalania stukowego. Badania zostały wykonane na zmodyfikowanym jednocylindrowym silniku o zapłonie iskrowym (ZI), wyposażonym w optyczny czujnik z bezpośrednim dostępem do komory spalania. W pomiarach wykorzystano zjawiska szerokopasmowej emisji optycznej oraz chemiluminescencji towarzyszące spalaniu mieszanki paliwowo-powietrznej. Sygnał optyczny poddawano filtracji, wyodrębniając długości fal typowe dla emsji produktów przejściowych, w zakresie od 250 do 625 nm, obejmującym typowe rodniki takie jak C2, CH, CN oraz OH. Uzyskane rezultaty potwierdziły, że pojawienie się i intensywność spalania stukowego mogą zostać ocenione na podstawie dalszej analizy sygnału zarejestrowanego zarówno w szerokim paśmie promieniowania jak i dla widma chemiluminescencji poszczególnych rodników. Porównanie z rejestrowanym równocześnie przebiegiem ciśnienia pokazało, że emitowane widmo jest bardziej wrażliwe na zmiany warunków pracy silnika.

KĘCIK K, MITURA A, WARMIŃSKI J. **Analiza efektywności autoparametrycznego wahadłowego tłumika drgań**. Eksploatacja i Niezawodnosc – Maintenance and Reliability 2013; 15 (3): 221–224.

W pracy przedstawiono analizę dynamiki autoparametrycznego układu składającego się z oscylatora wraz z dołączonym eliminatorem drgań w postaci wahadła. W celu uzyskania obszarów rezonansu autoparametrycznego zastosowano metodę bilansu harmonicznych. Wyznaczono analitycznie,a następnie zweryfikowano numerycznie warunek pełnej eliminacji drgań. Dodatkowo, przedstawiono wpływ tłumienia oscylatora i wahadła na zjawisko eliminacji drgań oraz dynamikę układu.

TOR-ŚWIĄTEK A. **Ocena efektywności procesu wytłaczania mikroporującego polietylenu małej gęstości**. Eksploatacja i Niezawodnosc – Maintenance and Reliability 2013; 15 (3): 225–229.

Z przetwórczego punktu widzenia ocena efektywności ma istotne znaczenie dla właściwego prowadzenia każdego procesu przetwórstwa tworzyw polimerowych. Jednak szczególnie ważna jest ona w przypadku przetwórstwa tworzyw modyfikowanych środkami porotwórczymi, których dodanie powoduje zmiany zarówno w przebiegu procesu, jak i we właściwościach fizycznych oraz strukturze otrzymanego wytworu. Przeprowadzenie właściwej analizy efektywności procesu, uwzględniającej odpowiednie kryteria i metody pozwala wydajnie i niezawodnie prowadzić proces wytłaczania. Artykuł prezentuje wyniki badań oceny efektywności procesu wytłaczania mikroporującego polietylenu małej gęstości modyfikowanego środkiem mikroporującym w postaci mikrosfer.

BEER K, PAŁKA K, SUROWSKA B, WALCZAK M. **Ocena jakościowa odlewanych elementów protetycznych**. Elements. Eksploatacja i Niezawodnosc – Maintenance and Reliability 2013; 15 (3): 230–236.

Właściwości stosowanych uzupełnień protetycznych stałych i ruchomych oraz ich konstrukcja mają istotny wpływ na ich trwałość w warunkach złożonego stanu obciążeń biomechanicznych, jakie występują w jamie ustnej w trakcie procesu żucia. Elementami, które najczęściej ulegają uszkodzeniom mechanicznym (pękaniu) w protezach szkieletowych są metalowe klamry. Uszkodzenie mocowania protezy skutkuje nie tylko brakiem możliwości jej dalszej eksploatacji, ale również jest przyczyną uczucia dyskomfortu dla pacjenta i może powodować skaleczenia jamy ustnej, uszkodzenia zębów oraz ryzyko powikłań w przypadku przedostania się do układu pokarmowego. Celem pracy była ocena jakościowa elementów protez wytwarzanych dostępnymi technikami oraz analiza przyczyn przedwczesnej utraty funkcjonalności tych elementów. Do badań zastosowano stop stomatologiczny na osnowie kobaltu Wironit Extra-hard. Badania jakościowe polegały na ocenie rodzaju i nasilenia wewnętrznych wad odlewniczych oraz ocenie makro- i mikrostruktury wytworzonych odlewów z wykorzystaniem technik mikroskopowych. Badania przełomów wskazują na występowanie rzadzizn spowodowanych skurczem odlewniczym. Badania mikrostrukturalne wykazały obecność typowej struktury dendrytycznej z osnową w postaci roztworu stałego Co-Cr-Mo i eutektyką. Wykonano również analizę wyników badań wytrzymałościowych w powiązaniu z uzyskiwaną makro i mikrostrukturą. Dokonano oceny ilościowej nasilenia wad odlewniczych wykorzystując analizę obrazu. Wskazano potencjalne zagrożenia technologii odlewania oraz zaproponowano metodykę monitorowania stanu elementów protez.

ŁUSIAK T. **The experimental and numerical analysis of helicopter performance in urban areas and in SAR operations**. Eksploatacja i Niezawodnosc – Maintenance and Reliability 2013; 15 (3): 237–240.

The paper discusses the methods of experimental and numerical analysis of helicopter performance in urban areas and search and rescue operations. The phenomenon of aerodynamic interference between the helicopter and the object located in its immediate vicinity was examined. The main focus was on the impact of interference on helicopter loading, airflow around the helicopter and helicopter properties in these specific cases. The paper provides a set of research results using the FLUENT software on the dynamic response to the disturbed simulation model of the helicopter rotor including the deformation of helicopter blades as well as the results of laboratory research on physical helicopter models.

KOWALIK K, SYKUT B, MARCZAK H, OPIELAK M. **A method of evaluating energy consumption of the cutting process based on the example of hard cheese**. Eksploatacja i Niezawodnosc – Maintenance and Reliability 2013; 15 (3): 241–244.

The article demonstrates a method of measuring energy requirements of a cutting process as researched at the Department of Process Engineering, Safety and Ecotechnology. The specially constructed workstation and examples of results obtained are presented. The cutting process has been conducted using stainless steel and low-friction coated blades with each blade's entry conditions variables, such as speed and the angle of entry, determined. In order to compare cutting resistance caused by friction between the blades' surface and the cut substance, wire cutting has also been performed.

JACNIACKA E, SEMOTIUK L. **Experimental methods for determining uncertainty of measurement using inspection probes**. Eksploatacja i Niezawodnosc – Maintenance and Reliability 2013; 15 (3): 246–252.

The paper presents the results of determining uncertainty of measurement using an inspection probe on numerically controlled vertical milling machines. To do the measurements, methods developed for coordinate measuring machines were employed. For the measurement system consisting of a vertical machining center FV-580A and OMP60 touch probe, the uncertainty of measurement was determined for the coordinates of the point, one-dimensional length measurement, two-dimensional length measurement, as well as for length measurement using multiple measurement strategies.

FERDYNUS M. **An energy absorber in the form of a thin-walled column with square cross-section and dimples**. Eksploatacja i Niezawodnosc – Maintenance and Reliability 2013; 15 (3): 253–258.

The object of the research was a thin-walled energy absorber made of aluminium in the form of a column having square cross-section and a series of dimples in the corners. As the possibilities of practical applications of the absorber appear to be considerable, the paper presents prospects of building a palletization head. An influence of the global initial deflections on sub-critical form of the equilibrium path was examined. This was an attempt to assess the structure's susceptibility to deviations of the column's axis from the ideal one. In the article a way of the column's model construction was described in detail. The model takes into account the corner dimples, the initial deflections and the perturbations caused by geometrical imperfections. Advantages of the new solution were presented in comparison with a column having smooth walls.

FILIPEK P. **Estimating air-fuel mixture composition in the fuel injection control process in an SI engine using ionization signal in the combustion chamber**. Eksploatacja i Niezawodnosc – Maintenance and Reliability 2013; 15 (3): 259–265.

The paper offers a comparison between signals produced by a lambda sensor and ionization sensor to estimate air-fuel mixture composition in the fuel injection control process in an SI engine. The method of measurement is described and characteristics of the ionization signal in the conducted experimental tests are given. The paper also presents a numerical model of the internal combustion engine that was designed and then used in the simulations to examine the usefulness of ionization signal for estimating air fuel mixture composition. The conducted tests demonstrated the advantage of the controller using the ionization measurement in the combustion chamber over the controller using signals produced by a classic lambda sensor.

JAKLIŃSKI P. **Analysis of the dual control system operation during failure conditions**. Eksploatacja i Niezawodnosc – Maintenance and Reliability 2013; 15 (3): 266–272.

The paper presents an analysis of the ASz-62IR-16E aircraft engine dual control system during failure conditions. The studies which are part of the certification tests in accordance with CS-E are described. The engine was equipped with a prototype electronic fuel injection control system. The experiments were conducted on the ASz-62IR-series piston aircraft engine test stand located in WSK "PZL-Kalisz" S.A. Robustness of the electronic control system has been studied for a single sensor failures and the effects of these failures have been evaluated. The tests included simulated

ŁUSIAK T. **Analiza eksperymentalna oraz numeryczna eksploatacji śmigłowców w aglomeracjach miejskich oraz w akcjach ratowniczych**. Eksploatacja i Niezawodnosc – Maintenance and Reliability 2013; 15 (3): 237–240.

Praca przedstawia sposoby analizy eksperymentalnej oraz numerycznej użytkowania śmigłowca w aglomeracjach miejskich oraz akcjach ratowniczych. Rozpatrzono zjawisko interferencji aerodynamicznej pomiędzy śmigłowcem a obiektem znajdującym się w jego bezpośredniej bliskości. Analizie poddano wpływ zjawiska interferencji na obciążenia, opływ i własności śmigłowca w szczególnych przypadkach jego użytkowania. Przedstawiono wyniki obliczeń wykorzystujących program FLUENT, odpowiedzi dynamicznych na zaburzenia symulacyjnego modelu wirnika śmigłowca uwzględniającego deformacje łopat oraz rezultaty laboratoryjnych badań eksperymentalnych na modelach fizycznych śmigłowca.

KOWALIK K, SYKUT B, MARCZAK H, OPIELAK M. **Metoda badania energochłonności procesu cięcia na przykładzie sera żółtego**. Eksploatacja i Niezawodnosc – Maintenance and Reliability 2013; 15 (3): 241–244.

W artykule przedstawiono metodę badania energochłonności procesu cięcia opracowaną w Zakładzie Inżynierii Procesowej, Bezpieczeństwa i Ekologii. Zaprezentowano skonstruowane stanowisko badawcze oraz przykładowe wyniki badań wykonane z wykorzystaniem tego stanowiska. Proces cięcia prowadzono nożami ze stali narzędziowej oraz pokrytymi powłokami charakteryzującymi się małym współczynnikiem tarcia, przyjmując w planie badań dla każdego noża zmienne wejściowe: kąt ostrza oraz prędkość cięcia. Aby porównać opory cięcia wynikające z tarcia materiału o powierzchnię noża przeprowadzono także cięcie materiału drutem.

JACNIACKA E, SEMOTIUK L. **Doświadczalne metody wyznaczania niepewności pomiaru sondami przedmiotowymi**. Eksploatacja i Niezawodnosc – Maintenance and Reliability 2013; 15 (3): 246–252.

W pracy przedstawiono wyniki wyznaczania niepewności pomiaru sondą przedmiotową na frezarkach pionowych sterowanych numerycznie. Do pomiarów zaadaptowano metody opracowane dla współrzędnościowych maszyn pomiarowych. Dla systemu pomiarowego składającego się z centrum obróbkowego FV580A i sondy OMP 60 wyznaczono niepewność pomiaru: współrzędnych punktu, jednowymiarowego pomiaru długości, dwuwymiarowego pomiaru długości oraz pomiaru długości z zastosowaniem przedmiotu niekalibrowanego.

FERDYNUS M. **Absorber energii w postaci cienkościennego słupa o przekroju kwadratowym z wgłębieniami**. Eksploatacja i Niezawodnosc – Maintenance and Reliability 2013; 15 (3): 253–258.

Obiektem badań jest cienkościenny absorber energii w postaci słupa o przekroju kwadratowym z szeregiem wgłębień w narożach wykonany z aluminium. Możliwości zastosowań praktycznych wydają się duże, przedstawiono perspektywę dotyczącą budowy głowicy do paletyzacji. Bada się wpływ globalnych ugięć wstępnych na podkrytyczną postać ścieżki równowagi, jako próbę oceny wrażliwości tej ko`nstrukcji na odchylenia od osi idealnej słupa. W pracy przedstawiono szczegółowo sposób budowy modelu słupa z wgłębieniami oraz ugięciem wstępnym i zaburzeniami imperfekcjami geometrycznymi. Zalety nowego rozwiązania przedstawiono w porównaniu ze słupem o gładkich ścianach.

FILIPEK P. **Szacowanie składu mieszanki w procesie sterowania wtryskiem benzyny w silniku ZI z wykorzystaniem sygnału jonizacji w komorze spalania**. Eksploatacja i Niezawodnosc – Maintenance and Reliability 2013; 15 (3): 259–265.

W artykule zawarto porównanie sygnałów z sondy lambda oraz czujnika jonizacji do szacowania składu mieszanki w procesie sterowania wtryskiem benzyny w silniku o zapłonie iskrowym. Opisano sposób pomiaru i charakterystykę sygnału jonizacji w przeprowadzonych badaniach doświadczalnych. Przedstawiono stworzony model matematyczny silnika spalinowego, którego użyto do przeprowadzenia badań symulacyjnych, testujących użyteczność sygnału jonizacji do szacowania składu mieszanki paliwowo-powietrznej. Wykazano przewagę regulatora wykorzystującego pomiar jonizacji w komorze spalania w porównaniu z regulatorem korzystającym z sygnału klasycznej sondy lambda.

JAKLIŃSKI P. **Analiza działania dublowanego systemu sterowania w stanach awaryjnych**. Eksploatacja i Niezawodnosc – Maintenance and Reliability 2013; 15 (3): 266–272.

W artykule przedstawiono analizę działania dublowanego systemu sterowania silnika lotniczego ASz-62IR-16E w stanach awaryjnych. Opisano badania stanowiące fragment próby dowodowej zgodnej z normą CS-E. Silnik wyposażony był w prototypowy, elektroniczny układ sterowania wtryskiem paliwa. Próby wykonano na stoisku hamownianym silników lotniczych tłokowych ASz-62IR w WSK „PZL-Kalisz" S.A. Badano odporność układu na pojedyncze awarie czujników oraz oceniano skutki tych awarii. Wykonano próby, w których symulowano awarie czujników prędkości obrotowej, ciśnienia powietrza w ko-

failures of engine speed, manifold air pressure and engine temperature sensors. The results of these tests were described and presented on the time-domain charts. The paper concludes with an analysis and a summary.

TARKOWSKI P, PYTKA J, BUDZYŃSKI P, KAZNOWSKI Ł. **A test method for evaluation and classification of unsurfaced airfields**. Eksploatacja i Niezawodnosc – Maintenance and Reliability 2013; 15 (3): 273–278.

The study presents a project of a method for testing, evaluation and classification of unsurfaced airfields, with respect to wheel-soil interactions analysis. Basic theoretical considerations have been included in this study, together with a review of existing methods as well as instrumentation, which will be applied in the presented method. It is supposed the method to be advantageous for a better utilization of grassy, unsurfaced airfields in Poland and other EU countries, mainly through improving the safety level of airfield operations.

TOMCZAK J, PATER Z, BULZAK T. **Effect of technological parameters on the rotary compression process**. Eksploatacja i Niezawodnosc – Maintenance and Reliability 2013; 15 (3): 279–283.

The paper presents results of a numerical analysis of the rotary compression process for producing extreme steps of a multi-step hollow shaft. The numerical simulations of the process were conducted by the finite element method (FEM), using Simufact Forming version 11.0. Applications of hollow parts in industry and benefits of their use are presented. With numerical modeling, the effect of basic rotary compression parameters (deformation ratio δ, wall thickness go, billet initial diameter D, advance speed v and rotary speed n of the tools) on shape of the produced parts are determined. Also, force parameters of the process, tool thrust force and torques are determined. The presented numerical analysis results confirm the possibility of producing multi-step hollow shafts using tube sections as billet material by metal machining methods.

BIENIAŚ J, JAKUBCZAK P, MAJERSKI K, OSTAPIUK M, SUROWSKA B. **Methods of ultrasonic testing, as an effective way of estimating durability and diagnosing operational capability of composite laminates used in aerospace industry**. Eksploatacja i Niezawodnosc – Maintenance and Reliability 2013; 15 (3): 284–289.

The paper presents selected issues in the field of exploitation research and the prediction capabilities of durability of composite laminates by ultrasonic methods used in the aerospace industry. Some research methods allow to set the quality parameters and operating in real aircraft structures. The study determined the relationship between the amplitude decrease of the ultrasonic wave and the level of porosity for hand lay-up manufactured glass / epoxy laminate using the method Through-Transmission of representative in C (TT C-Scan). In addition, showing the ability of amplitude attenuation imaging methods to detect and determine the extent of damage of high quality laminate and metal fiber composite after at low-dynamic velocity. It was specified real area an internal damage in FML laminates subjected to dynamic impact on low-energy, for which there was no visible damage in the outer layers. The study also determined the relationship between energy and the impact of dynamic surface area in testing laminates.

PYTKA J, TARKOWSKI P, KUPICZ W. **A research of vehicle stability on deformable surfaces**. Eksploatacja i Niezawodnosc – Maintenance and Reliability 2013; 15 (3): 290–295.

The paper includes results form a research of ride stability of a SUV (Sport Utility Vehicle), driven over deformable surfaces. An analytical method, in which stability of a mathematical model of vehicle's lateral dynamics is tested. The mathematical model has been reconstructed by means of a system identification method. We have used steering wheel angle as an input signal and lateral acceleration, side slip angle and yaw velocity as output signals to create the model. The data required to perform system identification have been gathered in a full size experiment, with the use of an instrumented vehicle. Final results in a form of poles and zeros diagrams have been included in the paper together with a discussion.

lektorze dolotowym i temperatury silnika. Wyniki tych prób opisano i przedstawiono na wykresach przebiegów czasowych oraz przeprowadzono ich analizę. Artykuł zakończono podsumowaniem.

TARKOWSKI P, PYTKA J, BUDZYŃSKI P, KAZNOWSKI Ł. **Metoda oceny i klasyfikacji gruntowych nawierzchni lotniskowych**. Eksploatacja i Niezawodnosc – Maintenance and Reliability 2013; 15 (3): 273–278.

W pracy przedstawiono projekt metody oceny gruntowych nawierzchni lotniskowych w aspekcie warunków współpracy kół podwozia samolotu z nawierzchnią. Zawarto podstawy teoretyczne, dostępne metody pomiarowe możliwe do zastosowania w projektowanej metodzie a także opisano projektowane rozwiązania. Przewiduje się, że przewidziana do wdrożenia metoda może przynieść znaczne korzyści w zakresie lepszego wykorzystania licznych lotnisk trawiastych w Polsce, także w aspekcie bezpieczeństwa operacji lotniczych.

TOMCZAK J, PATER Z, BULZAK T. **Wpływ parametrów technologicznych na przebieg procesu obciskania obrotowego**. Eksploatacja i Niezawodnosc – Maintenance and Reliability 2013; 15 (3): 279–283.

W artykule przedstawiono wyniki analizy numerycznej procesu obciskania obrotowego skrajnych stopni odkuwki wielostopniowego wałka drążonego. Symulacje numeryczne procesu przeprowadzono metodą elementów skończonych (MES), przy zastosowaniu komercyjnego pakietu oprogramowania Simufact Forming w wersji 11.0. Omówiono obszar wykorzystania elementów drążonych w przemyśle i przybliżono korzyści płynące z ich stosowania. Poprzez modelowanie numeryczne określono wpływ podstawowych parametrów obciskania obrotowego (stopnia gniotu δ, grubości ścianki go, początkowej średnicy wsadu D, prędkości postępowej v i obrotowej n narzędzi) na kształt otrzymanych wyrobów. Wyznaczono parametry siłowe procesu siły nacisku narzędzi i momenty obrotowe. Opisane rezultaty badań numerycznych potwierdzają możliwość wytwarzania odkuwek wielostopniowych wałków drążonych ze wsadu w postaci odcinków rury metodami obróbki plastycznej.

BIENIAŚ J, JAKUBCZAK P, MAJERSKI K, OSTAPIUK M, SUROWSKA B. **Metody badań ultradźwiękowych, jako efektywny sposób szacowania trwałości oraz diagnozowania zdolności eksploatacyjnych laminatów kompozytowych stosowanych w lotnictwie**. Eksploatacja i Niezawodnosc – Maintenance and Reliability 2013; 15 (3): 284–289.

W pracy przedstawiono wybrane zagadnienia z zakresu badań zdolności eksploatacyjnych oraz prognozowania trwałości metodami ultradźwiękowymi laminatów kompozytowych stosowanych w przemyśle lotniczym. Wybrane metody badawcze umożliwiają określenie parametrów jakościowych jak i eksploatacyjnych rzeczywistych struktur lotniczych. W pracy określono zależność pomiędzy wartością spadku amplitudy fali ultradźwiękowej a poziomem porowatościdla wytworzonego metodą laminowania ręcznegolaminatu szklano/epoksydowego przy użyciu metody Through-Transmissionw zobrazowaniu w trybie C (TT C-Scan). Dodatkowo pokazano zdolność metody obrazowania tłumienia amplitudowego do wykrywania i określania wielkości uszkodzeń wysokojakościowych laminatów kompozytowych i metalowo włóknistych po uderzeniach dynamicznych o niskich prędkościach. Określono rzeczywiste pola powierzchni uszkodzeń wewnętrznych laminatów FML poddanych uderzeniom dynamicznym o niskich energiach, dla których nie odnotowano widocznych uszkodzeń w warstwach zewnętrznych. W pracy wyznaczono również zależność pomiędzy energią uderzenia dynamicznego a polem powierzchni uszkodzenia badanych laminatów.

PYTKA J, TARKOWSKI P, KUPICZ W. **Badanie stabilności ruchu samochodu na podłożach odkształcalnych**. Eksploatacja i Niezawodnosc – Maintenance and Reliability 2013; 15 (3): 290–295.

W artykule zawarto wyniki badań stabilności ruchu samochodu osobowo-terenowego na podłożu odkształcalnym. Zastosowano analityczną metodę badania stabilności, w której badana jest stabilność matematycznego modelu danego obiektu. W rozpatrywanym przypadku, model matematyczny odtworzono na podstawie analizy sygnałów wejściowych (kąt obrotu kierownicy) oraz wyjściowych (przyspieszenie boczne i kąt bocznego znoszenia środka ciężkości, prędkość kątowa odchylania od kierunku ruchu, moment na kole kierownicy), z zastosowaniem metody identyfikacji systemów.

SCIENCE AND TECHNOLOGY

Andrzej WEREMCZUK
Krzysztof KĘCIK
Rafał RUSINEK
Jerzy WARMIŃSKI

THE DYNAMICS OF THE CUTTING PROCESS WITH DUFFING NONLINEARITY

DYNAMIKA PROCESU SKRAWANIA Z NIELINIOWOŚCIĄ DUFFINGA*

The paper presents the nonlinear one degree of freedom model of cutting process. To describe the dynamics the Duffing model with time delay part is used. The model is solved analytically by using the multiple time scale method. The stability lobe diagrams are determined numerically and analytically. The obtained results show that stability region depends on initial conditions of the system.

Keywords: *Duffing oscillator, nonlinear vibrations, time delay, stability.*

W artykule przedstawiono jednowymiarowy nieliniowy model skrawania. Do opisu procesu przyjęto model Duffinga z opóźnieniem czasowym. Model rozwiązano analitycznie za pomocą metody wielu skal czasowych. Wykres stabilności otrzymano numerycznie i analitycznie. Wykazano, że obszary stabilności zależą od warunków początkowych układu.

Słowa kluczowe: *oscylator Duffinga, drgania nieliniowe, opóźnienie czasowe, stabilność.*

1. Introduction

Systems with time delays are of interest when modelling processes in engineering, finance, and others [3]. They belong to a class of systems in which the current state of the process is an effect of the former state, delayed in time. Sometimes, the time delay is introduced into the system for control purposes. The mathematical description of delay dynamical systems naturally involve the delay parameter in some specified way. A differential equation with delay (DDE) describing a dynamical system belongs to the class of retarded functional differential equations (sometimes the equations are called *retarded differential-difference equations - RDDE*) [4]. The Duffing's oscillator is the simplest model of the dynamical behaviour of many complex systems. The equation with added delay part can be used of a model of cutting process [1]. In the turning process, a cylindrical workpiece rotates with a constant angular velocity, and the tool generates a surface as material is removed. The cutting force, which is a strong function of the chip thickness, becomes strongly dependent on the tool's delayed position $x(t-\tau)$ as well as its current position $x(t)$. Thus, to represent such a phenomenon, delay differential equations have been widely used as models for regenerative machine tool vibration (*regenerative chatter*).

Several phenomena occur during machining which adversely affect the course of the machining process, as well as tool life and surface quality. The main reason for these adverse events is self-excited vibration caused by the regenerative effect. This effect is caused by the overlap in the preceding trace tool to the passage trace from the current transition tools. The research has been conducted to increase productivity in machining processes, predict and avoid regenerative-type chatter.

In this paper we present the one degree of freedom model of a cutting process which is described by the Duffing's equation with time delay. The analytical study with numerical examples of chatter investigation is performed. Based on numerical simulation, the stability lobe diagram are constructed and compared with numerical results. The method of multiple scales (MMS) is used to solve the problem analytically. This method was also applied to do research on similar Duffing's system with time delay and external excitation [10].

2. Model of cutting

Here, the classical Duffing oscillator is connected with a time delay element to model regenerative effect in the cutting process [5]. Then, the model of regenerative cutting with nonlinear stiffness is presented in (Fig. 1). Vibrations that occur during machining can be described by delay differential equations (DDE) with shifted argument in the form:

$$x''(t) + \delta x'(t) + \omega_0^2 x(t) + \gamma x(t)^3 = \alpha \left[-\mu x(t) + x(t - \tau) \right], \quad (1)$$

where: δ is damping coefficient, γ is nonlinear stiffness, ω_o is natural frequency of the linear system. A cutting force is represented by the right side of the equation where, α is a specific cutting force factor, τ is time delay, μ is switching parameter which for the regenerative model of cutting is equal to one. The term with time delay represents a solution at previous state.
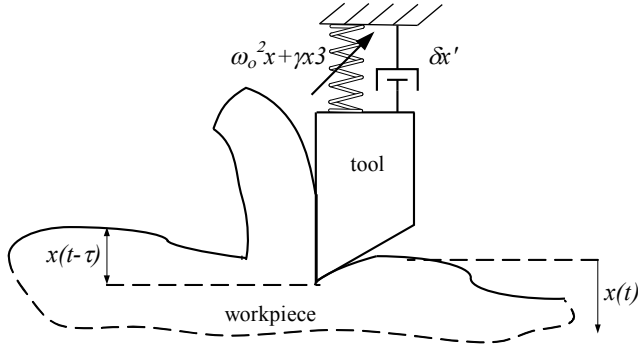

Fig. 1. Model of regenerative cutting with Duffing's stiffness

Chatter vibrations are the main problem occurring during cutting process [2, 6, 11], therefore this aspect is analysed here. In order to find stable cutting regions and the amplitude of chatter vibrations which exist in instability zones, an analytical and numerical solution of equation (1) and influence of the process parameters are determined in next sections.

3. Analytical solution

The system described by Eq. (1) is solved analytically with the help of the multiple time scale method [8, 9], we confine the study to the case of small damping and weak nonlinearity. We assume two scales (fast and slow) expansion of the solution. A fast scale T_0 and slow scale T_1 are described by eq. (2), then a solution in the first order approximation is sought in the form (3) and (4):

$$T_0 = t, T_1 = \varepsilon t , \tag{2}$$

$$x(t) = x_0(T_0, T_1) + \varepsilon x_1(T_0, T_1) , \tag{3}$$

$$x(t - \tau) = x_\tau = x_{0\tau}(T_0, T_1) + \varepsilon x_{1\tau}(T_0, T_1) . \tag{4}$$

It is assumed that:

$$\omega_0^2 = \omega^2 + \varepsilon\sigma, \gamma = \varepsilon\tilde{\gamma}, \alpha = \varepsilon\tilde{\alpha}, \delta = \varepsilon\tilde{\delta} , \tag{5}$$

where: ε is a formal small parameter [7]. Next, in order to facilitate notation, the tilde is omitted. By using the chain rule, the time derivative is transformed according to the expressions (6) and (7):

$$\frac{d}{dt} = \frac{\partial}{\partial T_0} + \varepsilon \frac{\partial}{\partial T_1} , \tag{6}$$

$$\frac{d^2}{dt^2} = \frac{\partial^2}{\partial T_0^2} + \varepsilon \frac{\partial^2}{\partial T_0 \partial T_1} + \varepsilon \frac{\partial^2}{\partial T_1 \partial T_0} + ... = \frac{\partial^2}{\partial T_0^2} + 2\varepsilon \frac{\partial^2}{\partial T_0 \partial T_1} + ... \tag{7}$$

Substituting eqs.(2) – (7) into (1) we let:

$$\frac{\partial^2 x(t)}{\partial T_0^2} + 2\varepsilon \frac{\partial^2 x(t)}{\partial T_0 \partial T_1} + \varepsilon\delta \frac{\partial x(t)}{\partial T_0} + \left[\omega^2 + \varepsilon\sigma\right]x(t) + \varepsilon\gamma x(t)^3 = \varepsilon\alpha[-\mu x(t) + x(t-\tau)] . \tag{8}$$

Expanding derivatives of the equation (8) we obtain (12):

$$\frac{\partial x(t)}{\partial T_0} = \frac{\partial x_0}{\partial T_0} + \varepsilon \frac{\partial x_1}{\partial T_0} , \tag{9}$$

$$\frac{\partial^2 x(t)}{\partial T_0^2} = \frac{\partial^2 x_0}{\partial T_0^2} + \varepsilon \frac{\partial^2 x_1}{\partial T_0^2} , \tag{10}$$

$$\frac{\partial^2 x(t)}{\partial T_0 \partial T_1} = \frac{\partial^2 x_0}{\partial T_0 \partial T_1} + \varepsilon \frac{\partial^2 x_1}{\partial T_0 \partial T_1} , \tag{11}$$

$$\frac{\partial^2 x_0}{\partial T_0^2} + \varepsilon \frac{\partial^2 x_1}{\partial T_0^2} + 2\varepsilon \frac{\partial^2 x_0}{\partial T_0 \partial T_1} + \varepsilon\delta \frac{\partial x_0}{\partial T_0} + \omega^2 x_0 + \varepsilon\omega^2 x_1 + \varepsilon\sigma x_0 + \varepsilon\gamma x_0^3 = \varepsilon\alpha(-\mu x_0 + x_{0\tau}) . \tag{12}$$

Equating coefficients of powers of ε^0 and ε^1, we obtain:

$$\varepsilon^0 \Rightarrow \frac{\partial^2 x_0}{\partial T_0^2} + \omega^2 x_0 = 0 , \tag{13}$$

$$\varepsilon^1 \Rightarrow \frac{\partial^2 x_1}{\partial T_0^2} + 2 \frac{\partial^2 x_0}{\partial T_0 \partial T_1} + \delta \frac{\partial x_0}{\partial T_0} + \sigma x_0 + \omega^2 x_1 + \gamma x_0^3 + \mu\alpha x_0 - \alpha x_{0\tau} = 0 . \tag{14}$$

It is convenient to express the solution of equation (13) in the complex form (15) and (16):

$$x_0(T_0, T_1) = A(T_1)e^{iT_0} + \bar{A}(T_1)e^{-iT_0} , \tag{15}$$

$$x_{0\tau}(T_0, T_1) = A(T_1)e^{i(T_0-\tau)} + \bar{A}(T_1)e^{-i(T_0-\tau)} , \tag{16}$$

where: $\bar{A}$ is the complex conjugate of A, which is an arbitrary complex function of T_1.

Substituting equations and into equation and expanding derivatives we get:

$$\frac{\partial x_0}{\partial T_0} = A(T_1)ie^{iT_0} - \bar{A}(T_1)ie^{-iT_0} , \tag{17}$$

$$\frac{\partial^2 x_0}{\partial T_0 \partial T_1} = A'(T_1)ie^{iT_0} - \bar{A}'(T_1)ie^{-iT_0} , \tag{18}$$

and then the following equation is obtained:

$$\frac{\partial^2 x_1}{\partial T_0^2} + \omega^2 x_1 + 2\left[A'(T_1)ie^{iT_0} - \bar{A}'(T_1)ie^{-iT_0}\right] + \delta\left[A(T_1)ie^{iT_0} - \bar{A}(T_1)ie^{-iT_0}\right] +$$

$$\sigma\left[A(T_1)e^{iT_0} + \bar{A}(T_1)e^{-iT_0}\right] + \gamma\left[A(T_1)e^{iT_0} + \bar{A}(T_1)e^{-iT_0}\right]^3 + \mu\alpha\left[A(T_1)e^{iT_0} + \bar{A}(T_1)e^{-iT_0}\right] -$$

$$\alpha\left[A(T_1)e^{i(T_0-\tau)} + \bar{A}(T_1)e^{-i(T_0-\tau)}\right] = 0.$$

(19)

Ordering equation (19) we get its final form:

$$\frac{\partial^2 x_1}{\partial T_0^2} + \omega^2 x_1 + \gamma A(T_1)^3 e^{3iT_0} + \gamma \bar{A}(T_1)^3 e^{-3iT_0} +$$

$$\left[-\alpha A(T_1)e^{-i\tau} + i\delta A(T_1) + \mu\alpha A(T_1) + \sigma A(T_1) + 3\gamma A(T_1)^2 \bar{A}(T_1) + 2iA'(T_1)\right]e^{iT_0} +$$

$$\left[-\alpha \bar{A}(T_1)e^{-i\tau} - i\delta \bar{A}(T_1) + \mu\alpha \bar{A}(T_1) + \sigma \bar{A}(T_1) + 3\gamma A(T_1)\bar{A}(T_1)^2 - 2i\bar{A}'(T_1)\right]e^{-iT_0} = 0.$$

(20)

The secular term of equation (20) vanishes if and only if equations (21) are complied. This leads to the equations (22) and (23):

$$ST_1 e^{iT_0} = 0, \quad ST_2 e^{-iT_0} = 0,$$

(21)

$$-\alpha A(T_1)e^{-i\tau} + i\delta A(T_1) + \mu\alpha A(T_1) + \sigma A(T_1) + 3\gamma A(T_1)^2 \bar{A}(T_1) + 2iA'(T_1) = \mathbf{0},$$

(22)

$$-\alpha \bar{A}(T_1)e^{-i\tau} - i\delta \bar{A}(T_1) + \mu\alpha \bar{A}(T_1) + \sigma \bar{A}(T_1) + 3\gamma A(T_1)\bar{A}(T_1)^2 - 2i\bar{A}'(T_1) = \mathbf{0}.$$

(23)

where: ST_1 and ST_2 are secular generating terms.

Eliminating from equation the secular generating terms we have equation (24):

$$\frac{\partial^2 x_1}{\partial T_0^2} + \omega^2 x_1 + \gamma A(T_1)^3 e^{3iT_0} + \gamma \bar{A}(T_1)^3 e^{-3iT_0} = 0.$$

(24)

Solving (24) for:

$$x_1(T_0, T_1) = B(T_1)e^{3iT_0} + \bar{B}(T_1)e^{-3iT_0},$$

(25)

$$x_{1\tau}(T_0, T_1) = B(T_1)e^{3i(T_0-\tau)} + \bar{B}(T_1)e^{-3i(T_0-\tau)},$$

(26)

where:

$$B(T_1) = -\frac{\gamma A(T_1)^3}{\omega^2 - 9},$$

(27)

$$\bar{B}(T_1) = -\frac{\gamma \bar{A}(T_1)^3}{\omega^2 - 9},$$

(28)

we obtain:

$$x_1(T_0, T_1) = -\frac{\gamma A(T_1)^3}{\omega^2 - 9}e^{3iT_0} - \frac{\gamma \bar{A}(T_1)^3}{\omega^2 - 9}e^{-3iT_0},$$

(29)

$$x_{1\tau}(T_0, T_1) = -\frac{\gamma A(T_1)^3}{\omega^2 - 9}e^{3i(T_0-\tau)} - \frac{\gamma \bar{A}(T_1)^3}{\omega^2 - 9}e^{-3i(T_0-\tau)}.$$

(30)

Substitution into equations and the polar form of the complex amplitude:

$$A(T_1) = \frac{1}{2}a(T_1)e^{i\beta(T_1)},$$

(31)

$$\bar{A}(T_1) = \frac{1}{2}a(T_1)e^{-i\beta(T_1)},$$

(32)

$$A'(T_1) = \frac{1}{2}a'(T_1)e^{i\beta(T_1)} + \frac{1}{2}ia(T_1)\beta'(T_1)e^{i\beta(T_1)},$$

(33)

$$\bar{A}'(T_1) = \frac{1}{2}a'(T_1)e^{-i\beta(T_1)} - \frac{1}{2}ia(T_1)\beta'(T_1)e^{-i\beta(T_1)}.$$

(34)

results in:

$$-\frac{1}{2}\alpha a(T_1)e^{-i\tau+i\beta(T_1)} + \frac{1}{2}i\delta a(T_1)e^{i\beta(T_1)} + \frac{1}{2}\mu\alpha a(T_1)e^{i\beta(T_1)} + \frac{1}{2}\sigma a(T_1)e^{i\beta(T_1)} +$$

$$\frac{3}{8}\gamma a(T_1)^3 e^{i\beta(T_1)} + 2i\left[\frac{1}{2}a'(T_1)e^{i\beta(T_1)} + \frac{1}{2}ia(T_1)\beta'(T_1)e^{i\beta(T_1)}\right] = 0,$$

(35)

$$-\frac{1}{2}\alpha a(T_1)e^{i\tau-i\beta(T_1)} - \frac{1}{2}i\delta a(T_1)e^{-i\beta(T_1)} + \frac{1}{2}\mu\alpha a(T_1)e^{-i\beta(T_1)} + \frac{1}{2}\sigma a(T_1)e^{-i\beta(T_1)} +$$

$$\frac{3}{8}\gamma a(T_1)^3 e^{-i\beta(T_1)} - 2i\left[\frac{1}{2}a'(T_1)e^{-i\beta(T_1)} - \frac{1}{2}ia(T_1)\beta'(T_1)e^{-i\beta(T_1)}\right] = 0.$$

(36)

After transformations (35) we obtain (37):

$$-\frac{1}{2}\alpha a(T_1)e^{-i\tau} + \frac{1}{2}i\delta a(T_1) + \frac{1}{2}\mu\alpha a(T_1) + \frac{1}{2}\sigma a(T_1) + \frac{3}{8}\gamma a(T_1)^3 +$$

$$ia'(T_1) - a(T_1)\beta'(T_1) = 0.$$

(37)

Then recalling:

$$e^{-i\tau} = \cos\tau - i\sin\tau.$$

(38)

The normal form is obtained:

$$-\frac{1}{2}\alpha a(T_1)\cos\tau + \frac{1}{2}i\alpha a(T_1)\sin\tau + \frac{1}{2}i\delta a(T_1) + \frac{1}{2}\mu\alpha a(T_1) + \frac{1}{2}\sigma a(T_1) +$$

$$\frac{3}{8}\gamma a(T_1)^3 + ia'(T_1) - a(T_1)\beta'(T_1) = 0.$$

(39)

Separating real and imaginary parts, the two, so called, modulation equations are found:

$$\frac{1}{2}\delta a(T_1) + \frac{1}{2}\alpha a(T_1)\sin\tau + a'(T_1) = 0$$

(40)

$$\frac{1}{2}\mu\alpha a(T_1) + \frac{1}{2}\sigma a(T_1) + \frac{3}{8}\gamma a(T_1)^3 - \frac{1}{2}\alpha a(T_1)\cos\tau - a(T_1)\beta'(T_1) = 0 \quad (41)$$

Transforming, we obtain the modulation equations in the form (42) and (43):

$$a'(T_1) = -\frac{1}{2}\delta a(T_1) - \frac{1}{2}\alpha a(T_1)\sin\tau,$$

(42)

$$\beta'(T_1) = \frac{3}{8}\gamma a(T_1)^2 + \frac{1}{2}\mu\alpha + \frac{1}{2}\sigma - \frac{1}{2}\alpha\cos\tau . \qquad (43)$$

In a case of a steady state solutions $a'=0$ and $\beta'=0$ then the chatter frequency (ω) and amplitude (a) is given as follows:

$$\omega = \sqrt{\omega_0 + \alpha\mu - \alpha\cos\tau} \qquad (44)$$

$$a_1 = \frac{2\sqrt{3}}{3}\sqrt{\frac{\sqrt{(\alpha^2 - \delta^2)} - \alpha\cos\tau}{\gamma}} \qquad (45)$$

$$a_2 = \frac{2\sqrt{3}}{3}\sqrt{\frac{-\sqrt{(\alpha^2 - \delta^2)} + \alpha\cos\tau}{\gamma}} \qquad (46)$$

Chatter frequency (ω) given by equation (44) depends only on delay parameters α, τ and natural frequency of linear system ω_o. Interestingly, the parameter of nonlinearity (γ) and vibrations amplitude do not influence the frequency. The amplitude of steady state chatter vibrations exist when:

$$\alpha^2 - \delta^2 > 0 \qquad (47)$$

Assuming, that system parameters are always positive, only for $\alpha > \delta$ the periodic solution appears. Then the critical value of α can be introduced $\alpha_{cr}=\delta$. On the other hand, the amplitude of vibrations is equals zero when the system parameters fulfil the condition:

$$\sqrt{(\alpha^2 - \delta^2)} - \alpha\cos\tau = 0 \qquad (48)$$

The amplitudes a_1 and a_2 represented by equation and are displayed in Figs. 2 and 3 as maps where colour means value of the vibrations amplitude.

The second solution exists only in narrow regions where the first solution does not exist. That means that when the condition (47) is fulfilled always periodic solution appears in the autonomous delayed Duffing's system regardless time delay. Whereas the condition (48)

Fig. 3. Analytical calculated amplitude a_2 of steady state solution represented by equation (46) versus Ω and α

is satisfied (amplitude equals zero) exactly on the border of the lobs shown in Fig. 2.

In the next section numerical simulations are done to show when the solution presented in this section can appear.
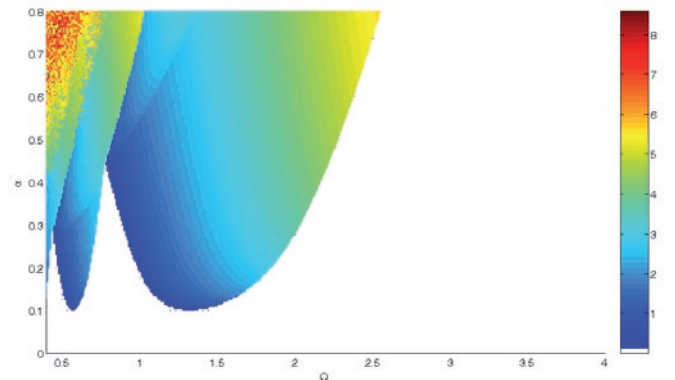
Fig. 4. Colour map of amplitude versus Ω and α for initial condition $x(0)=0.5$

Fig. 5. Colour map of amplitude versus Ω and α for initial condition $x(0)=3.5$

Fig. 2. Analytical calculated amplitude a_1 of steady state solution represented by equation of (45) versus Ω and α
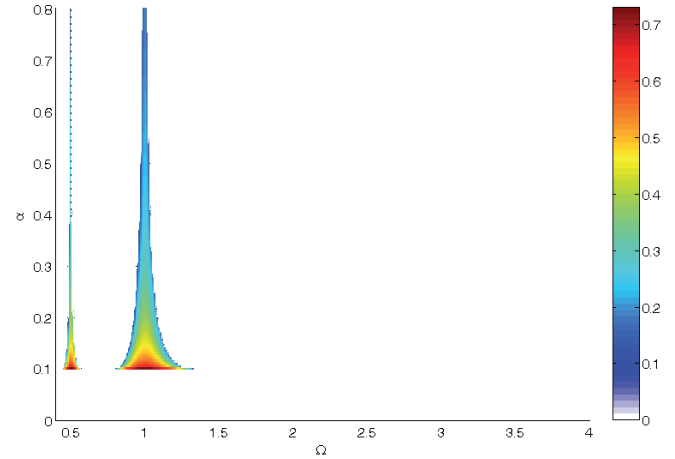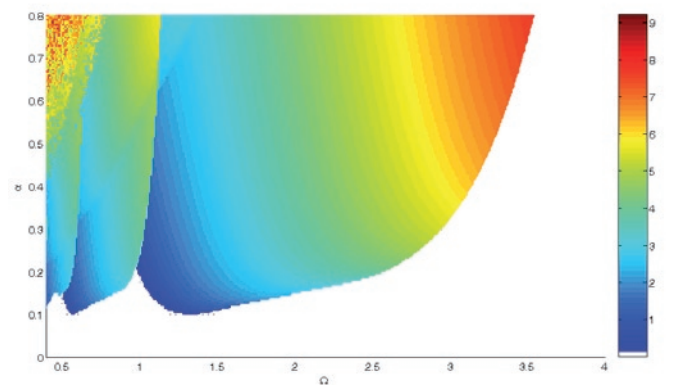
4. Numerical results

Since, as it has been shown in the previous section, chatter vibrations can exist always when α crosses $\alpha_{cr}=\delta$. The most interesting, from practical point of view, are the initial conditions which favours getting high amplitude vibrations. Therefore, the numerical simulations are performed on the basis of DDE in Matlab-Simulink with the help of 4th order Rungge-Kutta procedure with variable integration time. The system parameters are fixed as follows: $\gamma=0.25$, $\delta=0.1$, $\omega_o=1$, $\mu=1$. The value of vibrations amplitude is presented in Figs. 4 and 5 as colour map on the of two parameters plot $\Omega=2\pi/\tau$ and α.

The amplitudes of chatter vibrations are very sensitive on initial conditions because the region of unstable cutting is much wider for the initial condition $x(0)=3.5$ than $x(0)=0.5$. Moreover, vibrations amplitudes are bigger as well. Only $\alpha<\delta$ guarantees the cutting process without chatter vibrations regardless initial conditions.

5. Discussion and Final Conclusions

Since chatter vibrations are the main problem in cutting process therefore looking for regions of stable technological parameters is a primary goal. The linear model of regenerative cutting is well known and the derivation of its analytical solution does not introduce difficulties. But in the nonlinear case the system can have more than one periodic solution and also quasi-periodic, sub-harmonic or even chaotic ones. That depends, of course, on the system parameters and additionally on initial conditions. The analytical solutions shown graphically in Fig. 2 and 3 represent only steady state periodic solutions. Interestingly, for the analysed system there are no stable lobes, characteristic for the linear regenerative model. In the nonlinear model for any time delay chatter vibrations exist if delay amplitude $\alpha<\alpha_{cr}$. The numerical analysis is a complement of analytical research. Numerical investigations allow finding initial conditions regions which do not generate chatter vibrations. These regions are very important from practical point of view because the safe set of parameters (Ω, α) can be found providing the system stays in the proper initial conditions domains.

References

1. Bobrenkov AO, Khasawneh AF, Butcher AE, Mann PB. Analysis of Milling Dynamics for Simultaneously Engaged Cutting Teeth. Journal of Sound and Vibration 2010; 329: 585–606.
2. Butcher AE, Bobrenkov AO, Bueler E, Nindujarla P. Analysis of Milling Stability by the Chebyshev Collocation Method; Algorithm and Optimal Stable Immersion Levels. Journal of Computational and Nonlinear Dynamics 2009; 4: 31003-1.
3. Gorceki H, Fuksa S, Grabowski P, Korytowski A, Analysis and Synthesis of Time Delay Systems, John Wiley & Sons, 1989.
4. Hale JK, Theory of Functional Differential Equations, Springer, New York, 1977.
5. Hu H, Dowell EH, Virgin LN. Resonances of a Harmonically Forced Duffing.
6. Oscillator with Time Delays State Feedback. Nonlinear Dynamics 1998; 15(311): 327.
7. Hu HY, Wang ZH. Singular Perturbation Methods for Nonlinear Dynamic.
8. Systems with Time Delays. Chaos, Solitons and Fractals 2009; 40(1): 13–27.
9. Nayfeh AH, Chin CM, Pratt J. Perturbation Methods in Nonlinear Dynamics- Applications to Machining Dynamics. Journal of Manufacturing Science and Engineering 1997; 119: 485–493.
10. Nayfeh AH, Perturbation Methods. Wiley Interscience. New York 1973.
11. Nayfeh AH. Introduction to Perturbation Techniques. Wiley Interscience. New York 1981.
12. Rusinek R, Weremczuk A, Warmiński J. Regenerative Model of Cutting Process with Nonlinear Duffing Oscillator. Mechanics and Mechanical Engineering 2011; 15: 4.
13. Shaw MC. Metal Cutting Principles. Oxford University Press. New York 1984.

Andrzej WEREMCZUK, M.Sc. (Eng.)
Krzysztof KĘCIK, Ph.D. (Eng.)
Rafał RUSINEK, Ph.D. (Eng.)
Prof. Jerzy WARMIŃSKI, Ph.D., D.Sc. (Eng.)

Department of Applied Mechanics
Mechanical Engineering Faculty
Lublin University of Technology
Nadbystrzycka 36, 20-816 Lublin, Poland
E-mails: j.warminski@pollub.pl, r.rusinek@pollub.pl,
k.kecik@pollub.pl, a.weremczuk@pollub.pl

Dariusz PIERNIKARSKI
Jacek HUNICZ
Henryk KOMSTA

DETECTION OF KNOCKING COMBUSTION IN A SPARK IGNITION ENGINE USING OPTICAL SIGNAL FROM THE COMBUSTION CHAMBER

DETEKCJA SPALANIA STUKOWEGO W SILNIKU O ZAPŁONIE ISKROWYM ZA POMOCĄ SYGNAŁU OPTYCZNEGO Z KOMORY SPALANIA

The aim of the presented research was to investigate spectral properties of the combustion flame with special regard to the detection and estimation of intensity of knocking combustion. Research was made using modified single cylinder test engine with spark ignition (SI) equipped with an optical sensor having direct access to the combustion chamber. Measurements were based on wideband intensity of optical radiation and chemiluminescence phenomena occurring in the combustion flame under the influence of high temperature and pressure. Spectral recordings were done for wavelengths typical for emission of intermediate products, covering the range from 250 nm to 625 nm, including typically investigated radicals like C_2, CH, CN, OH. Obtained results confirmed, that occurrence and intensity of knock can be determined on the basis of further signal analysis. Comparison with in parallel recorded indicated pressure have shown that characteristics of emitted spectra is more sensitive to the changing of engine operating conditions.

Keywords: *knocking combustion, optical measurements, spectral flame properties, chemiluminescence, fiber optics.*

Celem prezentowanych badań było zbadanie widmowych własności płomienia w komorze spalania ze specjalnym uwzględnieniem możliwości detekcji i oceny intensywnosci spalania stukowego. Badania zostały wykonane na zmodyfikowanym jednocylindrowym silniku o zapłonie iskrowym (ZI), wyposażonym w optyczny czujnik z bezpośrednim dostępem do komory spalania. W pomiarach wykorzystano zjawiska szerokopasmowej emisji optycznej oraz chemiluminescencji towarzyszące spalaniu mieszanki paliwowo-powietrznej. Sygnał optyczny poddawano filtracji, wyodrębniając długości fal typowe dla emsji produktów przejściowych, w zakresie od 250 do 625 nm, obejmującym typowe rodniki takie jak C_2, CH, CN oraz OH. Uzyskane rezultaty potwierdziły, że pojawienie się i intensywność spalania stukowego mogą zostać ocenione na podstawie dalszej analizy sygnału zarejestrowanego zarówno w szerokim paśmie promieniowania jak i dla widma chemiluminescencji poszczególnych rodników. Porównanie z rejestrowanym równocześnie przebiegiem ciśnienia pokazało, że emitowane widmo jest bardziej wrażliwe na zmiany warunków pracy silnika.

Słowa kluczowe: *spalanie stukowe, szerokopasmowy sygnał optyczny, rodniki, chemiluminescencja.*

1. Introduction

An abnormal combustion resulting with knock phenomenon can occur in cylinders of both, spark ignition and compression ignition engines. Resulting pressure oscillations lead to deterioration of engine cycle efficiency, dramatic increase of exhaust emissions, as well as provide engine noise. Severe knock results in substantial reduction of engine lifetime and, in extreme cases can lead to damage of the engine. Typical engine damages caused by knock are cracks and fractures of the piston crown and piston-rings grooves as a result of shock wave action. Intensive knock occurring for a long period can even lead to piston seizure and melting of its edges [13]. Considering the recent trends in spark ignition engines development, i.e. downsizing, turbo- or supercharging and increase of compression ratios, knocking combustion poses a challenge for numerous researchers. Without exception, all actually being developed solutions for spark ignition engines are in favor of increasing knock risk [1, 5, 31].

Although a huge effort was done to understand knocking combustion, what can be confirmed by many scientific publications [11, 23], knock is yet not completely understood phenomena accompanying combustion in spark-ignition gasoline engines.

In general, scientific sources distinguish two mechanisms leading to knock: self-ignition and detonation [13, 24, 28]. Theory of self-ignition assumes spontaneous initiation of combustion in the part of the combustion chamber which lies usually in the most distant location from the spark-plug. Self-ignition zone is defined as end-gas region containing unburned charge. When temperature and charge pressure reach boundary conditions, a spontaneous self-ignition takes place in one or more points simultaneously. A very violent explosion follows, resulting in pressure waves, which oscillating, create typical sound effects. Theory of detonation in turn assumes initiation of knocking as a result of flame front propagation, which accelerates with supersonic speed from the spark-plug towards surrounding end-gas and peripheries of the combustion chamber. This creates shock wave (detonation), which reflects from the combustion chamber walls with its resonant frequency. Resulting momentary pressure changes but have high amplitude and cause typical knocking sounds.

Describing different types of knocking combustion occurring during vehicle operation, one can also distinguish knock related to the acceleration and knock at constant rotational speed of the engine [19]. It is accepted, that knock taking place during acceleration is mainly a burdensome effect for the driver and his passengers. Knocking com-

bustion occurring at the constant rotational speed of the engine (high speed driving) is usually hard to recognize, but can lead to the heavy engine damage.

There are two main reasons why knock should be avoided. First is the sound emitted by the engine during knocking combustion. Sounds emitted from the engine compartment can be nuisance for the driver, but the can be efficiently limited by improvement of the acoustic insulation. More serious problem is the fact, that self-ignition in the combustion chamber can lead to the engine damage. It is the reason, why engine manufacturers have introduced many countermeasures aimed at elimination of the knocking phenomena, as soon as it appears.

Detection and control of knocking combustion have become essential components of control systems in modern engines. Nowadays all contemporary SI engines are controlled on the border of knock limit in case of full load or higher partial load operation, what allows for reaching maximum fuel efficiency. In this context, precise recognition of knock occurrence and definition of its intensity are of great importance. In the series engines the most commonly knock detection method is based on the application of vibration sensors (accelerometers, knock sensors), which transmit vibration of engine components (usually engine block) [4]. Typically in the 4 cylinder engines, a pair of knock sensors is used. Knock detection is based on the analysis of time or frequency representations of the gathered vibration signal, however available specifications of signal properties recorded during knocking combustion are of low coherence. The most significant weakness of this method is very low signal-to-noise ratio, especially at higher engine speeds, resulting from high background noise level. In consequence, close-loop engine control is either impossible or retarded ignition is used as countermeasure what decreases engine efficiency and power [4].

Knock identification using pressure transducers inherits most of weaknesses mentioned above. However, in extreme situations pressure sensor cannot record any oscillations, as it can be located directly in the vibration's node of the combustion chamber. Moreover, misinterpretations of the self-ignition phenomena on the basis of the pressure signal can arise from the fact, that self-ignition has cyclic variability, even with the same in-cylinder pressures [3], e.g. due to variability of fuel concentration in the combustion chamber [8].

2. Knock detection using optical methods

As it was stated above, the main problem of knock detection is related to the exact separation of knock signal, according to the engine operating conditions. Frequency analysis of the engine block vibrations permits only rough estimation of knock intensity. Objective evaluation of knock intensity is possible, but it requires precise separation of knock signal from the primary signal of engine operation using band-pass filtering.

Optical and optoelectronic methods have become commonly used tool in the combustion research, what is confirmed by many publications [7, 22, 27]. Application of optical combustion sensors has some significant advantages in comparison to vibration knock sensors or pressure measurements. Their operation is not influenced by any mechanical or electrical disturbances, and they offer high speed of data processing with relatively low invasiveness in the process course (comparable with pressure sensors).

Intensity of optical radiation varies with crankshaft position and engine load, there is also randomness of the signal resulting from variability of consecutive combustion cycles. In case of wide-band optical radiation intensity, identification of knocking combustion can be done using some numerical or functional features of the signal, like peak values of the radiation intensity, mean value of total optical radiation or changes in radiation intensity during combustion. Furthermore, application of optical-fiber methods can be used for identification of the self-ignition location in the combustion chamber [10, 29]. Occurrence

of knock creates also changes in the spectrally measured intensity of optical radiation – i.e. at wavelengths corresponding to the optical emission of certain radicals existing in the combustion flame [25].

3. Spectrophotometry in combustion research

One of the promising techniques used in combustion diagnostics is based on estimation of concentrations of radicals existing in the flame. Investigation of radicals emission has many applications in the combustion diagnostics, like estimation of air-fuel ratio or local flame temperature, detection of knock or/and misfire [12, 17, 24, 27, 32, 33].

Concentration of radicals can be estimated using gas chromatography, mass spectrometry, electron paramagnetic resonance, laser induced fluorescence, ion current measurement [18] as well as spectrophotometric methods [6, 30]. Measured must be made only in the flame zone directly in the combustion chamber – it is not possible to isolate gases to make chemical analysis. Most reliable and relatively inexpensive methods used to acquire information about concentration of radicals are luminescence methods [25, 26] based on the measurement of spontaneous optical emission accompanying combustion process, recorded in a narrow bandwidth enabling evaluation of radicals' concentration in the reaction zone of the combustion flame.

In the flames of internal combustion engine there is constant thermal emission and linear emission resulting from transitions of molecules from higher to lower electron states. Simplifying, total radiation L is a sum of thermal radiation of combustion products $L_{therm-prod}$, thermal radiation of intermediate products $L_{therm-int}$ and chemiluminescence L_{chlum} of radicals $L = L_{therm-prod} + L_{therm-int} + L_{chlum}$.

Depending on which component of the emission is dominant, the course of the optical emission curve will alter. If the source of the radiation were chemiluminescence only, values of the optical emission signal would be proportional to the speed of heat generation. Mechanisms governing the existence of molecules are not completely recognized, but main chemical reactions are identified [10, 12]. The strongest source of chemiluminescence of hydrocarbon flames are radicals OH, CH and C_2 formed in the electron-excited states [32]. CH and C_2 radicals are present mostly in the reaction zone. Other relatively strong emission sources are radicals of HCHO, HCO, CN and NH [2, 20]. Fig. 1. presents main emission lines of molecules existing in the hydrocarbon flames. Emission cannot be however unequivocally identified with concentration of radicals. Resultant luminescence is a product of radicals' concentration and transition probability between excited and basic state.
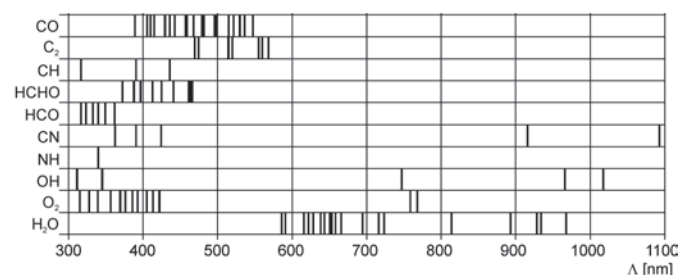
Fig. 1. Emission lines of some radicals existing in the hydrocarbon flames of IC engines [9]

Intensity of chemiluminescence is strongly correlated with combustion parameters, such as pressure, temperature and mixture composition [6]. It can be also modified by phenomena of abnormal combustion, for example engine knock. Development of optical combustion sensors, measurement methods and consecutive research of SI engines are in the scope of research activities of the authors [16], and considers detection of abnormal combustion [21, 22], measurements

of flame kernel development [14] as well as identification of diffusion flames in a partially stratified controlled auto-ignition engine [15].

4. Experimental research

Aim of the research. Presented experimental research was aimed at more comprehensive understanding of unwanted phenomena like knock occurrence. Research and further signal analysis were also supposed to settle the question, whether it is possible to use similar signal processing procedures which are used in knock detection algorithms based on the pressure analysis in relation to the signal of optical radiation. Results shown in this paper illustrate usage of autocorrelation function of the wide-band optical radiation intensity signal for the detection of knock and estimation of its intensity. The scope of described research is related to the characteristics of optical radiation recorded within several wavelengths, in conditions of normal and knocking combustion.

Research engine and measurement system. Research was done using modified Honda GX390 one-cylinder, air-cooled SI engine. Engine was retrofitted with specially designed electronic ignition and fuel injection systems controlled by the dedicated PC software. Table 1 shows main technical parameters of the modified Honda GX390 engine. The test stand and measurement system as well as complete description of the measurement system, its components and procedures regarding calibration techniques of the sensor can be found in previous publications of the authors [17, 21, 22, 23].

Table 1. *Modified Honda GX390 test engine – main technical characteristics*

Engine displacement	$V_s = 0.390$ dm^3
Cylinder diameter x piston stroke	D x S = 88 x 64 mm
Compression ratio	$\varepsilon = 8.0$
Maximum power	$N_e = 8.7$ kW (11.8 KM) at 3600 rpm
Maximum torque	$M_o = 26$ N·m at 2500 rpm

Measurement system was based on the optical combustion sensor recording intensity of optical radiation emitted from the combustion chamber. Sensor was mounted in the engine head and had direct access to the combustion chamber. System consisted of the optical combustion sensor with direct access to the combustion chamber coupled to the transmission fiber-optic bundle (lightguides), monochromator, photodetector and A-D acquisition card installed in a PC computer which recorded gathered data. Fig. 2 presents general set-up of the measurement system.
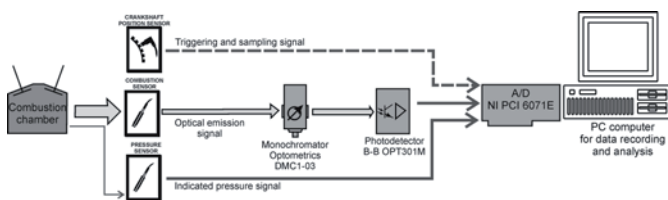

Fig. 2. General scheme of measurement system used for recording optical radiation from the combustion chamber

Panchromatic optical radiation was recorded using transducer with transmission band from 200 to 800 nm and peak sensitivity at 750 nm, then amplified. Emission spectrum from the combustion chamber war recorded using reticular monochromator with measurement range from 200 to 1100 nm. Operating frequency was set manually with accuracy 0.2 nm. Width of entry and exit slots is 600 μm, what gives in result band-pass of 4.4 nm.

During the whole cycle of experiments spectral measurements were done for 12 wavelengths, typical for emission of intermediate products (table 2). They are chemiluminescence traces of various radicals existing in the flame which are most commonly used in the spectrophotometric engine research. For every wavelength 100 consecutive engine cycles were recorded. Triggering and sampling signals were supplied by crankshaft position sensor, and instantaneous optical signal was recorded with resolution of 0.1°CA (crankshaft angle).

Table 2. *Wavelengths of intermediate radical emissions and their measurement codes*

Compound symbol	Characteristic wavelength [nm]	Measurement code
OH	282.9	**L01**
CH	314	**L02**
CH	431.4	**L03**
NH	336	**L04**
C_2	473	**L05**
HCO	318.6	**L06**
OH	306.4	**L07**
CH	387.1	**L08**
CN	388.3	**L09**
HCHO	395.2	**L10**
C_2	516.5	**L11**
HCO	329.8	**L12**

Research was done for different engine operating conditions: engine speed (n): 1600, 2500, 3500 rpm; throttle positions (a_p): 30, 60, 90%, ignition advance (i_a): 25–65°CA BTDC (crankshaft angle before top dead center). Mixture composition was always set manually by the operator to stoichiometric on the basis of readouts from wide-band lambda probe and exhaust gas analyzer. For comparative analysis a pressure signal was simultaneously recorded using miniature piezoelectric pressure transducer mounted in the spark-plug (AVL GU13Z-24).

5. Data processing and analysis

Onset of knock results in rapid increase in intensity of optical radiation I_{opt}, next it changes in accordance with indicated pressure p_i. Changes of intensity of optical radiation can be associated with high frequency pressure waves which reinitialize luminescence of burned gasses as a result of adiabatic heating. In case of boundary conditions – i.e. at knock limit – pressure traces would not indicate occurrence of knock, whereas optical signal shows rapid growth in value resulting from the presence of auto-ignition centers. This phenomena was confirmed by other researchers [25, 32]. Fig. 3 presents examples of traces of intensity of wide band optical radiation (I_{opt}) and indicated pressure (p_i) recorded for two different engine operation conditions. Knocking combustion was present at n = 3500 rpm, a_p = 90%, i_a = 55°CA BTDC, whereas at ignition advance of 40°CA BTDC normal combustion was identified. Magnitude of wide band optical radiation intensity in knock conditions has greater span of changes.

Autocorrelation analysis of the wide-band optical radiation intensity signal I_{opt} obtained from the combustion chamber in different engine operating conditions (rotational speed – load – ignition advance) has shown that it has much higher dynamics of changes resulting from different engine operating conditions. This confirms previous observations regarding higher influence of engine operating conditions on the changes of optical signal in comparison to the indicated pressure [22, 23].
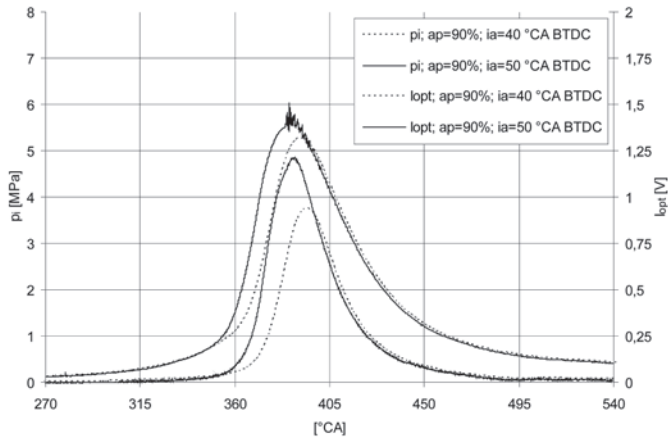
Fig. 3. Comparison of indicated pressure (pᵢ) and intensity of wide band optical radiation (I_{opt}) for normal and knocking combustion as a function of crankshaft position
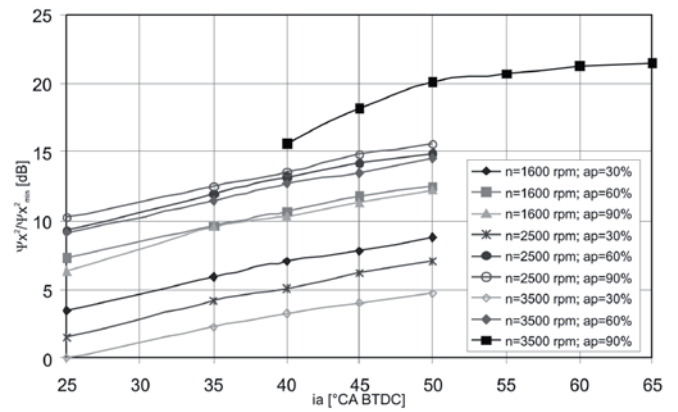

Fig. 5. Relative root mean square rms ($\Psi_x^2/\Psi_x^2{}_{min}$) of the I_{opt} signal for different engine operating conditions and different ignition advances (averaged from 100 consecutive cycles)[23]
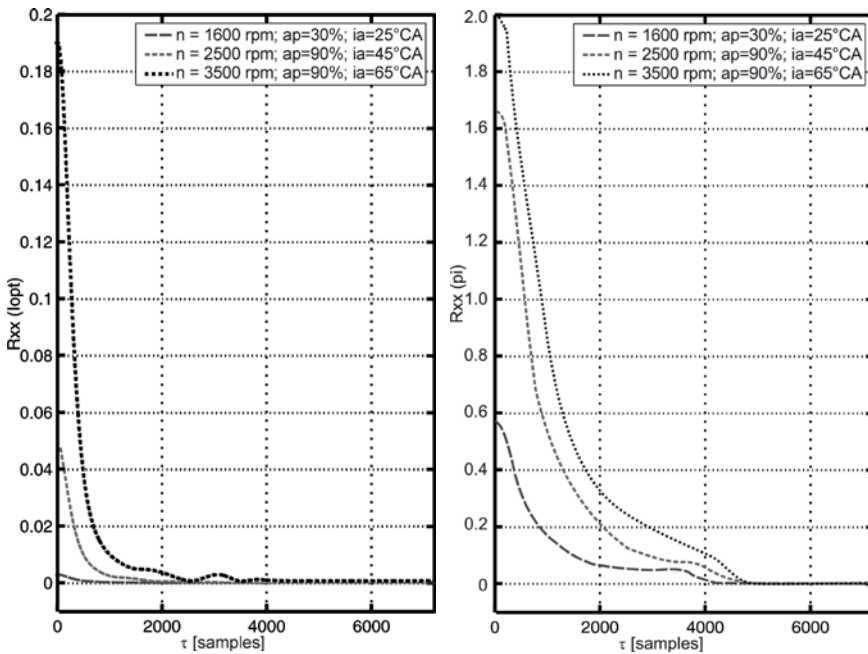

Fig. 4. Autocorrelation function of I_{opt} (left) and p_i (right) signals obtained for single engine cycle averaged from 100 consecutive runs, at different engine operating as a function of time shift

Such dependence can be observed on the charts shown on fig. 4. There is much higher dynamics of span changes of the autocorrelation function calculated for the intensity of optical radiation in relation to the indicated pressure: 11.3 and 18.0 dB for $R_{xx}(I_{opt})$ whereas for $R_{xx}(p_i)$ correspondingly it is only 4.6 and 5.5 dB. Autocorrelation function of indicated pressure p_i approaches zero significantly slower than it is in case of I_{opt}. It can point to the fact, that optical signal can be characterized by higher speed of changes and presence of quick-changing components in the analyzed courses, especially that graphs presented on fig. 4 were averaged from 100 consecutive runs.

For the time shift $\tau = 0$ autocorrelation function equals to root mean square (rms) Ψ_x^2 which is a common measure of signal energy. Fig. 5 shows rms values of I_{opt} signal for all investigated engine operating conditions. So as to make comparisons easier, individual values are represented in relative values, referred to minimum value of $\Psi_x^2{}_{min}$.

Onset of knocking combustion is accompanied by the increase of transmitted energy, which is visible as an increase of its root

mean square value. This phenomena can be clearly observed for the engine rotational speed $n = 3500$ rpm, throttle position $a_p = 90\%$ and ignition timings i_a equal to 50, 55, 60 and 65°CA BTDC. Relative changes of signal rms values ($\Psi_x^2/\Psi_x^2{}_{min}$) calculated for combustion without knock phenomena, independent from engine operating conditions were contained in the range <1÷20>. Increase of engine load and ignition advance leading to knock resulted in the increase of relative Ψ_x^2 values – maximum value calculated during the research was 141.77.

So as to more precisely describe characteristic features of autocorrelation function resulting from the presence of knocking combustion, it was necessary to analyze filtered combustion courses. Slow changing component related to cyclic combustion was removed.

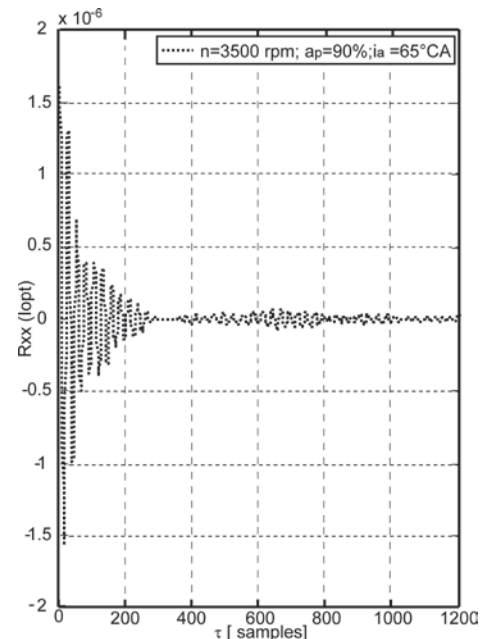Detailed data analysis has shown, that in all cases of researched engine operating conditions au-

Fig. 6. Autocorrelation function of filtered signal I_{opt} calculated for 100 consecutive cycles, window 120°CA: n = 3500 rpm, $a_p = 90\%$, $i_a = 65$°CA BTDC as a function of a time shift

tocorrelation function of filtered data decreases relatively quickly, and for higher values of shift τ, a Gaussian noise was observed. However, for operating conditions with presence of knocking combustion, periodic components were are clearly visible (fig. 6). Presence of these components should be therefore related to the knock phenomena.

Onset of knock results in much slower decrease of autocorrelation function, moreover its values in case of knock are higher even by one order of magnitude. Observed dependence can result from simultaneous existence of many, superimposing combustion spots, which increase intensity of recorded optical radiation signal. More detailed discussion of optical measurements within the visible light range (wideband) can be found in [21].

In the described experiments acquired optical radiation was spectrally filtered so as to obtain chemiluminescence traces of the commonly used radicals existing in the flame (see table 2). Further signal analysis was done in a function of angular crankshaft position. Fig. 7

presents emission traces of all measured radicals recorded in full load conditions of engine operation. Significant high frequency noise is visible in all bands, which results from electrical interference generated by the spark discharge. It can be assumed, that location of the optical probe in the combustion chamber allowed for recording of initial phase of combustion – clearly visible are local peaks of radiation in the range 310-320°CA following the ignition which took place at 310°CA. Relatively high level of radiation corresponds to the emission in bands L03 (CH, 431.4 nm), L11 (C_2, 515.5 nm), L10 (HCHO, 395.2 nm), L05 (C_2, 473 nm), L09 (CN, 388.3 nm) and L08 (CH, 387.1 nm), whereas bands L02 (CH, 314 nm), L06 (HCO, 318.6 nm) L12 (HCO, 329.8 nm) and L04 (NH, 336.4 nm) are up to 15 times smaller in magnitude. A good conformity between emission peaks and maximum of the indicated pressure can be also observed.

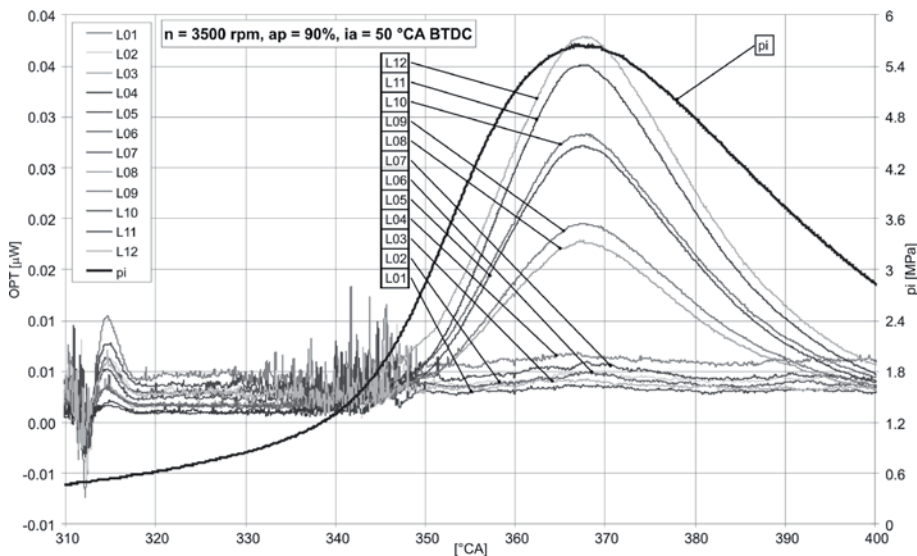Fig. 8 shows emission traces of some of the radicals recorded at engine operating conditions without knocking combustion. The highest level of radiation corresponds to the emission in bands L03 (CH, 431.4 nm), L11 (C_2, 515.5 nm), L09 (CN, 388.3 nm) and L08 (CH, 387.1 nm). In comparison with results shown on fig. 7, obtained for the full load operation conditions, traces of the bands L10 (HCHO, 395.2 nm) and L05 (C_2, 473 nm) remained at very low level. It is also noteworthy that at low engine load and low rotational speed (fig. 8), optical power of the emission corresponding to the L03 band (CH, 431.4 nm) was approx. 20% higher than power generated at full load and high engine speed (fig. 7). This probably can be associated with more stable course of combustion. Knocking combustion shown on fig. 8 resulted in significant increase of the measured optical power – for the "strongest" band L03 it was approx 2.7 times higher relative to non-knocking conditions presented on fig. 7. Is should be also noted that in case of regular (i.e. without knock) combustion emission peaks were retarded 3–5°CA relatively to the maximum of the indicated pressure (fig. 7), whereas in case of knock (fig. 8) no shift was observed.

Fig. 9 presents emission traces of the CH (L03 – 431.4 nm) recorded at different engine operating conditions at different engine speeds (1600, 2500 and 3500 rpm), loads (a_p = 30% and 90%) and ignition advances (i_a) of 30°CA BTDC (fig. 8, upper) and 50°CA BTDC (fig. 8, lower). It can be observed, that conditions which can lead to the knocking combustion – i.e. low rotational speed and high load – result in high levels of recorded emission power. Early ignition – i.e. ignition advance – significantly increases emission power. In case of CH emission (431.4 nm) at 1600 rpm and a_p = 90%, the difference in spectral power is up to 80% for two ignition advances.

6. Conclusions

Analysis of the results shows, that resultant wide-band optical radiation is more sensitive to the changing engine operating conditions in a wide-band region and less susceptible to the external interferences in comparison to the indicated pressure. A higher dynamics of span changes of the autocorrelation function calcu-

Fig. 7. Emission lines of all measured radicals and indicated pressure p_i for full load operating conditions as a function of crankshaft position
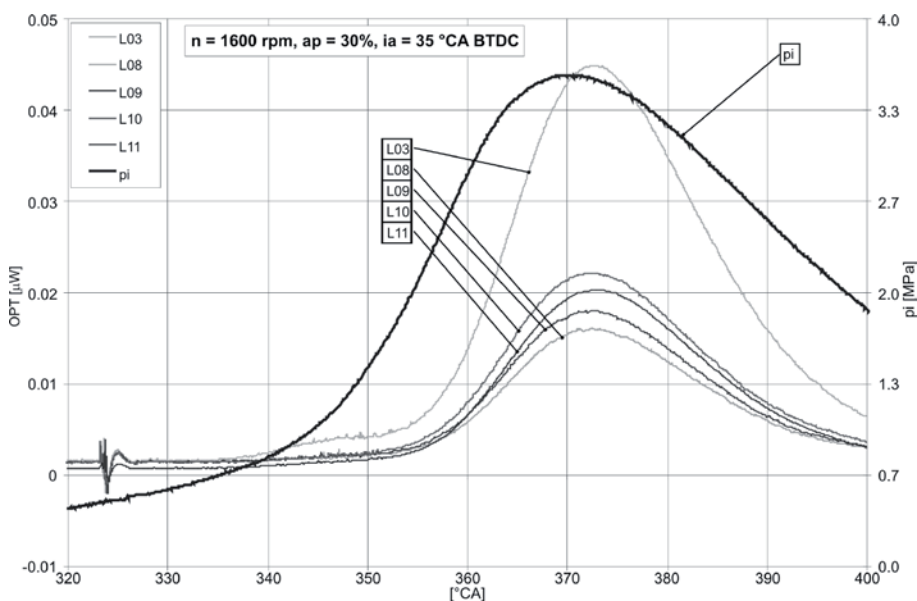

Fig. 8. Emission lines of radicals L03 – CH, L08 – CH, L09 – CN, L10 – HCHO, L11 – C_2 and indicated pressure p_i for engine operating conditions without knocking combustion as a function of crankshaft position

lated for the intensity of optical radiation can be also observed. Detailed analysis of results presented in this paper shows that autocorrelation function calculated for the intensity of optical radiation during knocking combustion shows periodic components.

Onset of knock results in much slower decrease of autocorrelation function, moreover its values in case of knock are higher even by one order of magnitude. Knock results also in a significant increase of the root mean square calculated for the signal. This can result from simultaneous existence of many, superimposing combustion spots. Violent increase of energy transmitted by the signal directly influences intensity of recorded optical radiation signal.

Recorded flame spectrum had very strong levels of emission lines of OH, CH and C_2 radicals typical of homogenous mixtures. In all recorded cases the strongest emission levels were obtained for CH at 431.4 nm (L03) and C_2 at 516.5 nm (L11), their magnitude varied depending on engine operating conditions. In knocking conditions relatively strong emission of HCHO (395.2 nm – L10) was observed – a radical typical of cold flames emerging in self-ignition centers.

Further and more detailed data analysis is required, including estimation of heat release and detailed quantitative and qualitative analysis of recorded emissions.
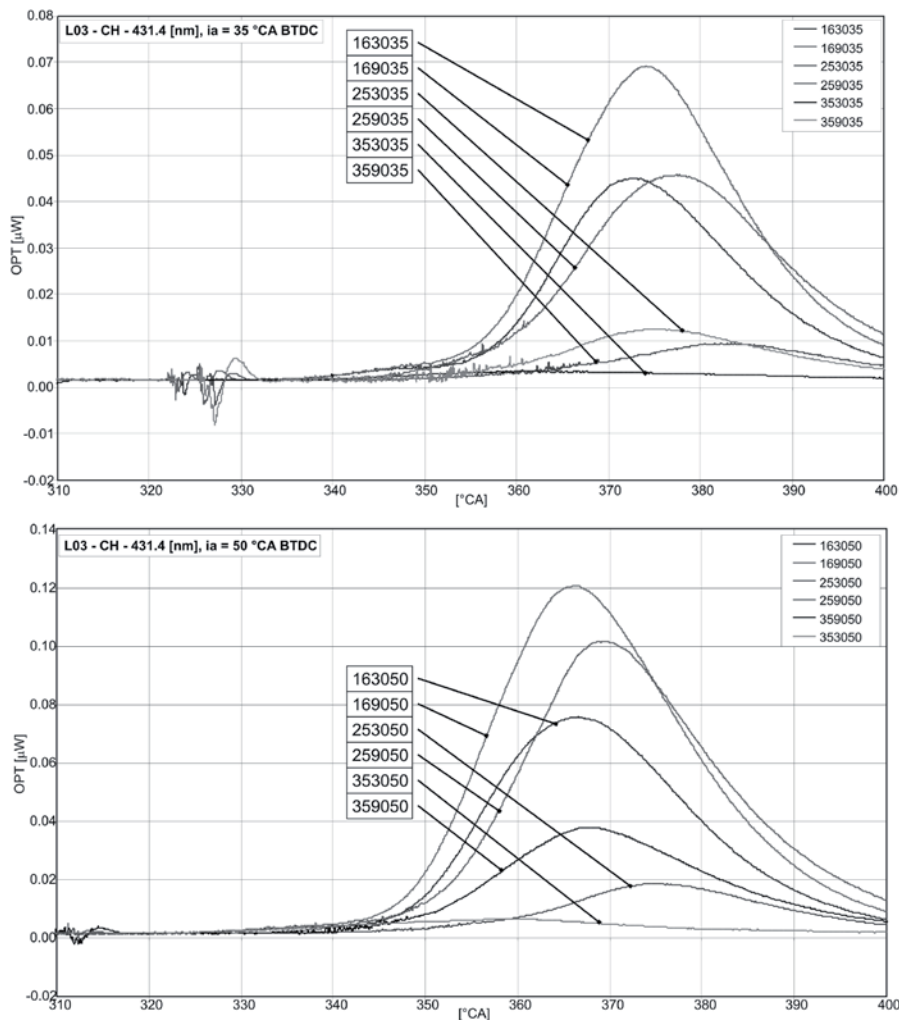
Fig. 9. Emission of CH radicals measured at 431.4 nm at different engine speeds (1600, 2500 and 3500 rpm), loads (a_p = 30% and 90%) and ignition advances (i_a) of 30°CA BTDC (upper) and 50°CA BTDC (lower) as a function of crankshaft position

References

1. Alkidas AC. Combustion advancements in gasoline engines. Energy Conversion and Management 2007; 48: 2751–2761.
2. Arias L, Torres S, Sbarbaro D, Ngendakumana P. On the spectral bands measurements for combustion monitoring. Combustion and Flame 2011; 158: 423–433.
3. Ballais R, Gallardo-Riuz JM, Merola SS. Optical diagnostics of the cycle-to-cycle variation in the kernel development and abnormal combustion SI. Journal of KONES Powertrain and Transport 2010; 17(2): 17–25.
4. Brecq G, Bellettre J, Tazerout M. A new indicator for knock detection in gas SI engines. International Journal of Thermal Sciences 2002; 42: 523–532.
5. Brewster S. Initial Development of a Turbo-charged Direct Injection E100 Combustion System. SAE Technical Paper 2007; 2007-01-3625.
6. Chang C, Clasen E, Song K, Campbell S, Rhee KT, Jiang H. Quantitative imaging of in-cylinder processes by multispectral methods. SAE Technical Paper 1997; 970872.
7. Docquier N, Candel S. Combustion Control and Sensors a Review. Progress in Energy and Combustion Science 2002; 28: 107–150.
8. Fansler TD, Drake MC, Stojkovic B, Rosalik ME. Local Fuel Concentration, Ignition and Combustion in a Stratified Charge Spark Ignited Direct-Injection Engine Spectroscopic, Imaging and Pressure-Based Measurements. International Journal of Engine Research 2003; 4(2): 61–87.
9. Fischer J, Kubach H, Tribulowski J, Spicher U. Analyse der Zylinderinnerströmung und des Verbrennungsverhaltes bei Ottomotoren mit Direktteinspritzung. 5. Internationales Symposium für Verbrennungsdiagnostik 2002: 177–192.
10. Gaydon AG, Wolfhard HG. Flames Their Structure, Radiation and Temperature. London: 1979.
11. Griffiths JF., Whitaker BJ. Thermokinetic interactions leading to knock during homogenous charge compression ignition. Combustion and Flame 2002; 131: 386–399.
12. Hardalupas Y, Orain M. Local measurements of the time-dependent heat release rate and equivalence ratio using chemiluminescent emission from a flame. Combustion and Flame 2004; 139: 188–207.
13. Heywood JB. Internal combustion engine fundamentals. McGraw–Hill, New York: 1988.

14. Hunicz J. Experimental research of flame kernel development and its relation to cycle-to-cycle variability of homogenous charge spark ignition engine. Archivum Combustionis 2009; 29 (1-2): 28–37.
15. Hunicz J, Kordos P. An experimental study of fuel injection strategies in CAI gasoline engine. Experimental Thermal and Fluid Science. 2011; 35(1): 243–252.
16. Hunicz J, Piernikarski D. Investigation of combustion in a gasoline engine using spectrophotometric methods. Proceedings of SPIE 2001; 4516: 307–314.
17. Hunicz J, Piernikarski D. Transient in-cylinder AFR management based on optical emission signals. SAE Technical Paper 2004; 2004-01-0516.
18. Kinoshita M, Saito A, Mogi K, Nakata K. Study on ion current and pressure behaviour with knocking in engine cylinder. JSAE Review 2000; 21: 483–488.
19. Leppard WR. Individual cylinder knock occurrence and intensity in multicylinder engine. SAE Technical Paper 1982: 820074.
20. Merola SS, Vaglieco BM. Knock investigation by flame and radical species detection in spark ignition engine for different fuels. Energy Conversion and Management 2007; 48: 2897–2910.
21. Piernikarski D. Statistic evaluation of usability of optical radiation intensity for the knock detection. Archivum Combustionis 2006; 26(3-4): 103–120.
22. Piernikarski D, Hunicz J. Diagnostics of abnormal combustion in a SI automotive engine using in-cylinder optical combustion sensor. Proceedings of SPIE 2004; 5566: 211–217.
23. Piernikarski D. Funkcja autokorelacji szerokopasmowej emisji optycznej w detekcji spalania stukowego. Silniki Spalinowe (Combustion Engines) 2009; 1(136): 44-51.
24. Saminy B, Rizzoni G. Engine knock analysis and detection using time-frequency analysis. SAE Technical Paper 1996; 960618.
25. Shoji H, Shimizu T, Nishizawa T, Yoshida K, Saima A. Spectroscopic Measurement of Radical Behavior Under Knocking Operation. SAE Technical Paper 1996; 962104.
26. Smith G, Luque G, Park C, Jeffries JB, Crosley DR. Low Pressure Determinations of Rate Constants for OH(A) and CH(A) Chemiluminescence. Combustion and Flame 2002; 131: 59–69.
27. Sohma K., Yukitake Y, Azuhata Y, Takaku Y. Application of Rapid Optical Measurement to Detect the Fluctuations of the Air-Fuel Ratio and Temperature of a Spark Ignition Engine. SAE Technical Paper 191; 910499.
28. Sun Z, Blackshear PL, Kittelson DB. Spark Ignition Engine Knock Detection Using In-Cylinder Optical Probes. SAE Technical Paper 1996; 962103.
29. Töpfer G, Reissing J,Weimar HJ, Spicher U. Optical Investigation of Knocking Location on S.I.-Engines with Direct-Injection. SAE Technical Paper 2000; 2000-01-0252.
30. Tosaka Y, Shoji H, Saima A. A study of the influence of intermediate combustion products on knocking. JSAE Review 1995; 16: 233–238.
31. Wildman C, Scaringe RJ, Cheng WK. On the maximum pressure rise rate in boosted HCCI operation. SAE Technical Paper 2009; 2009-01-2727.
32. Yang J, Plee S, Remboski D. Relationship Between Monochromatic Gas Radiation Characteristics and SI Engine Combustion Parameters. SAE Technical Paper 1993; 930216.

Dariusz PIERNIKARSKI, Ph.D. (Eng.)
Jacek HUNICZ, Ph.D., D.Sc. (Eng.)
Prof. Henryk KOMSTA, Ph.D., D.Sc. (Eng.)

Institute of Transport, Combustion Engines and Ecology
Mechanical Engineering Faculty
Lublin University of Technology
ul. Nadbystrzycka 36, 20-618 Lublin, Poland
e-mails: d.piernikarski@pollub.pl, j.hunicz@pollub.pl, h.komsta@pollub.pl

Krzysztof KĘCIK
Andrzej MITURA
Jerzy WARMIŃSKI

EFFICIENCY ANALYSIS OF AN AUTOPARAMETRIC PENDULUM VIBRATION ABSORBER

ANALIZA EFEKTYWNOŚCI AUTOPARAMETRYCZNEGO WAHADŁOWEGO TŁUMIKA DRGAŃ*

This paper presents results of a study of a dynamic response of an autoparametric system consisting of the oscillator with an attached pendulum vibration absorber. The harmonic balance method is applied to get the autoparametic resonance conditions. The analytical full vibration absorption condition has been determined and verified by numerical simulations. Additionally, the influence of oscillator and pendulum damping on dynamics and the vibration absorption effect is presented.

Keywords: *oscillations, pendulum, absorption, damping, resonance.*

W pracy przedstawiono analizę dynamiki autoparametrycznego układu składającego się z oscylatora wraz z dołączonym eliminatorem drgań w postaci wahadła. W celu uzyskania obszarów rezonansu autoparametrycznego zastosowano metodę bilansu harmonicznych. Wyznaczono analitycznie,a następnie zweryfikowano numerycznie warunek pełnej eliminacji drgań. Dodatkowo, przedstawiono wpływ tłumienia oscylatora i wahadła na zjawisko eliminacji drgań oraz dynamikę układu.

Słowa kluczowe: *drgania,wahadło,eliminacja, tłumienie, rezonans.*

1. Introduction

The problem of undesired vibration reduction has been known since many years ago and becomes more attractive nowadays. The dynamic vibration absorbers (DVA) are special devices, consisting of masses suspended on springs and dampers. In the classical theory of DVA, the primary structure is modelled as a spring mass system. However, other dynamic vibration absorption models also have high interest in research and engineering application. In particular, the pendulum type systems can play an important role in many fields such as machinery, transportation and civil engineering. But, dynamic behaviour of a pendulum absorber is significantly more complex than it is supposed by the widely used additional simple dynamical dampers.

The autoparametric vibration pendulum absorber (AVPA) is designed to absorb energy from the primary system (main mass). This absorption effect is efficient only in the limited band of vibration frequencies of the main system [1]. Unlike the classical absorber, the use of the pendulum absorber does not result in excitation of vibrations with considerable amplitudes at other frequencies. This is due to the rigid regime of excitation of vibrations of the pendulum only near its internal resonance frequency for a resonance excitation frequency ratio of 1/2, [2, 6, 8].

Many papers dealing with various types of dynamic dampers and related topics have been published during the last decades. Some pendulum type absorbers have been applied for vibration protection systems on tower-pipes, chimneys, civil structures (buildings and bridges) affected by wind or seismic vibration, etc. [5]. The collection of many vibration absorbers and their practical applications are presented by Sun [7].

This paper deals with a pendulum absorber connected to a damped oscillator system. In this type of structures different motions are pos-

sible: periodic, quasi-periodic, chaotic or the pendulum may rotate [9]. Especially transition to rotation and chaos can lead to unexpected increase of amplitude and eventually to destruction of the structure. If the pendulum plays a role of a dynamical absorber, this kind of motion is unwanted. The first possible intuitive solution is to increase the system damping. This study is to estimate how the system damping influences the absorption efficiency of AVPA. In addition, obtained results allow preparing the control algorithm based on change in the system damping.

2. Model of AVPA

Let us consider a pendulum vibration absorber attached to a damped oscillator. The oscillator is forced by harmonic force $F(t)$ with amplitude q and frequency ϑ near the principal parametric resonance. The suspension of the primary system consists of a linear spring with stiffness reduced in dimensionless form to one and a viscous damping function $\alpha_1 X'$. Damping of the pendulum is described by linear function $\alpha_2 \varphi'$.

The differential dimensional equations of motion of the two degrees-of-freedom autoparametric system (Fig. 1) are derived by the second kind of Lagrange equations and they are shown in papers [9]. The equations of motion are express in the dimensionless form:

$$X'' + \alpha_1 X' + X + \mu\lambda(\varphi''\sin\varphi + \varphi'^2\cos\varphi) = q\cos\vartheta\tau, \quad (1)$$

$$\varphi'' + \alpha_2\varphi' + \lambda(X'' + 1)\sin\varphi = 0. \quad (2)$$

The second equation represents the pendulum and the first one is the excited system (the oscillator). The μ and λ represent pendu-
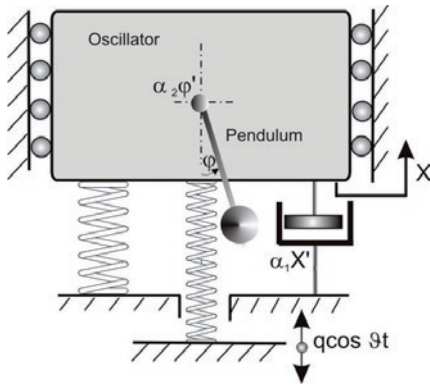
Fig. 1. Scheme of an autoparametric pendulum vibration absorber.

lum parameters. These parameters are responsible for the internal couplings of the pendulum absorber and the oscillator, also. Detailed information and definition of dimensionless parameters: α_1, α_2, μ, λ and q are presented in [10].

3. Parametric analysis of damping

3.1. Harmonic Balance Method

The harmonic balance method (HBM) is used to find an approximate solution for the system applied near the principal internal resonance condition. Thus, in the first approximation, the solutions are assumed as:

$$x(\tau) = A(\tau)\cos\left[\vartheta\tau + \phi_1\right], \varphi(\tau) = B(\tau)\cos\left[(\vartheta/2)\tau + \phi_2\right], \quad (3)$$

where $A(\tau)=A$, $B(\tau)=B$ and φ_1 and φ_2 are amplitudes and phase angles of the oscillator and the pendulum, respectively. Introducing eq. (3) and expand nonlinear terms ($sin\varphi$ and $cos\varphi$) in Taylor series (up to the third order), for steady states following algebraic equations are obtained:

$$\left(1-\vartheta^2\right)A - \mu\lambda\left(\vartheta/2\right)^2 B^2 \cos\left(2\phi_2 - \phi_1\right) = q\cos\phi_1, \quad (4)$$

$$-\vartheta\alpha_1 A + \mu\lambda\left(\vartheta/2\right)^2 B^2 \sin\left(2\phi_2 - \phi_1\right) = q\sin\phi_1, \quad (5)$$

$$\left(\vartheta/2\right)^2 - \lambda + \left(\lambda/8\right)B^2 + A\left(\lambda\vartheta^2/2\right)\cos\left(2\phi_2 - \phi_1\right) = 0, \quad (6)$$

$$\alpha_2\left(\vartheta/2\right) + A\left(\lambda\vartheta^2/2\right)\sin\left(2\phi_2 - \phi_1\right) = 0. \quad (7)$$

After some mathematical manipulations we get the phase angles:

$$\mathrm{tg}\phi_1 = \frac{4\vartheta\left(4A^2\alpha_1 + B^2\alpha_2\mu\right)}{16A^2\left(\vartheta^2-1\right) - B^2\mu\left(\left(B^2-8\right)\lambda + 2\vartheta^2\right)}, tg\left[2\phi_2 - \phi_1\right] = \frac{\alpha_2\left(\vartheta/2\right)}{\left(\vartheta/2\right)^2 - \lambda + \left(\lambda/8\right)B^2}, \quad (8)$$

and two equivalent equations for amplitudes of the oscillator:

$$A^2 = \frac{B^4}{16\vartheta^4} + \frac{B^2}{16\lambda^2\vartheta^4}\left(4\lambda\vartheta^2 - 16\lambda^2\right) + \frac{\left(64\lambda^2 - 32\vartheta^2\lambda + 4\vartheta^4 + 16\vartheta^2\alpha_2^2\right)}{16\lambda^2\vartheta^4}, \quad (9)$$

$$A^2 = B^4\frac{\left(2\lambda\mu\left(\vartheta^2-1\right) - \lambda^2\mu^2\vartheta^4\right)}{16\left(\vartheta^4 + \left(\alpha_1^2 - 2\right)\vartheta^2 + 1\right)} + B^2\frac{\left(16\lambda\mu\left(1-\vartheta^2\right) + 4\mu\vartheta^2\left(\vartheta^2 - 1 - 2\alpha_1\alpha_2\right)\right)}{16\left(\vartheta^4 + \left(\alpha_1^2 - 2\right)\vartheta^2 + 1\right)} + \frac{q}{\left(\vartheta^4 + \vartheta^2(\alpha_1^2 - 2) + 1\right)}. \quad (10)$$

Equating them, finally, we get the resonance curve which describes the pendulum oscillations in the steady state:

$$B^4\left[\frac{-\lambda^2\mu^2\vartheta^4 + 2\lambda\mu\left(-1+\vartheta^2\right)}{16\left(1+\left(-2+\alpha_1^2\right)\vartheta^2 + \vartheta^4\right)} - \frac{1}{16\vartheta^4}\right] + B^2\left[\frac{16\lambda\mu\left(1-\vartheta^2\right) + 4\mu\vartheta^2\left(\vartheta^2 - 1 - 2\alpha_1\alpha_2\right)}{16\left(1+\left(-2+\alpha_1^2\right)\vartheta^2 + \vartheta^4\right)} + \frac{16\lambda^2 - 4\lambda\vartheta^2}{16\lambda^2\vartheta^4}\right] + \left[\frac{q^2}{1+\vartheta^2\left(-2+\alpha_1^2\right)+\vartheta^4} - \frac{64\lambda^2 - 32\lambda\vartheta^2 + 4\left(4\alpha_2^2\vartheta^2 + \vartheta^4\right)}{16\lambda^2\vartheta^4}\right] = 0. \quad (11)$$

Detailed derivation of HBM and solution stability analysis is shown in the paper [10]. It should be noticed, that HBM gives reliable results near main parametric resonance and for weakly nonlinear system, only.

3.2. Full absorption condition

If, we assume that $A=0$ (oscillator doesn't vibrate) in equations, the algebraic equations yield:

$$-\mu\lambda\left(\vartheta/2\right)^2 B^2 \cos\left(2\phi_2 - \phi_1\right) = q\cos\phi_1, \quad (12)$$

$$\mu\lambda\left(\vartheta/2\right)^2 B^2 \sin\left(2\phi_2 - \phi_1\right) = q\sin\phi_1, \quad (13)$$

$$\left(\vartheta/2\right)^2 - \lambda + \left(\lambda/8\right)B^2 = 0, \quad (14)$$

$$\alpha_2\left(\vartheta/2\right) = 0. \quad (15)$$

Based on equation (15), we can conclude, that the full elimination of oscillator's motions condition is possible if damping of the pendulum equals $\alpha_2=0$, or if the system does not vibrate (i.e. trivial solutions $A=0$, $B=0$ and $\vartheta=0$). Then amplitude of pendulum motion can be calculated from eqs. (12)–(13) and eq. (14):

$$B_1^2 = \frac{q}{\mu\lambda\left(\vartheta/2\right)^2}, \quad B_2^2 = \frac{8\lambda - 8\left(\vartheta/2\right)^2}{\lambda}. \quad (16)$$

Comparing the amplitudes in equation (16), the two frequency excitation for full absorption effect are obtained:

$$\vartheta_1 = \sqrt{2\lambda + \frac{\sqrt{2}\sqrt{2\lambda^2\mu^2 - \mu q}}{\mu}}, \vartheta_2 = \sqrt{2\lambda - \frac{\sqrt{2}\sqrt{2\lambda^2\mu^2 - \mu q}}{\mu}}. \quad (17)$$

However, ϑ_2 is located beyond the main parametric resonance. Therefore, ϑ_1 denotes true amplitude for full absorption condition.

4. Absorption effect

4.1. Analysis of full vibration absorption effect (FVAE)

First, we analyse the FVAE of oscillator's motions. For data taken from [10]: $\alpha_1=0.1$, $\alpha_2=0$, $\mu=15.2$, $\lambda=0.25$, $q=0.05$, the analytical full absorption frequency, calculated from eqs. (17), is equal to $\vartheta_1=0.997$, and amplitudes of the pendulum $B_1=0.23$. The analytical resonance curves (eqs. (9)–(11)) for full absorption vibration effect are presented in Figs. 2. Close $\vartheta=1$, the dynamical elimination of oscillator's vibration caused by the pendulum swinging is clearly visible. The analytical resonance curves are in a very good accordance with numerical verification [10].
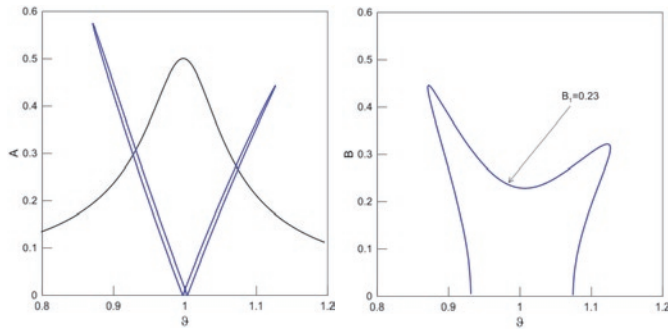

Fig. 2. Analytical resonance curves for full absorption effect.

Figure 3 shows numerical verification of FVAE. The amplitude of the oscillator tends to zero (Fig. 3a), while pendulum execute periodic swinging about amplitude equal $\varphi=0.23$, which agrees with analytical results. Additionally, we can conclude, that frequency ratio between oscillator and pendulum equals two. The initial conditions of system were set: $\varphi=0.1$, $\varphi'=0$, $x=0$ and $x'=0$.
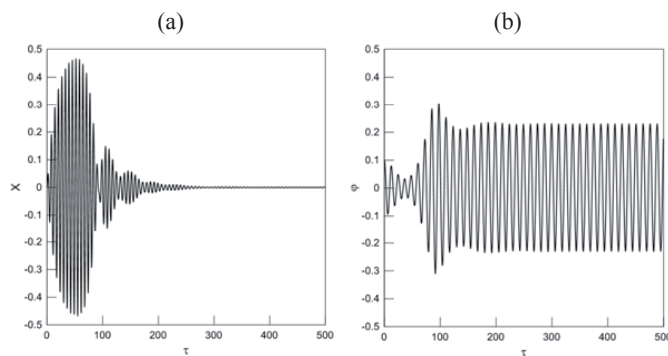

Fig. 3. Numerical verification of full absorption condition for $\vartheta=0.997$, time history of oscillator (a) and pendulum (b).

If the pendulum does not vibrate (i. e. $B=0$), then it plays just the role of an additional mass of the oscillator. The value of its amplitude can be estimated by the classical relationship for excited linear oscillator:

$$A = \frac{q}{\sqrt{1+\left(\alpha_1^2-2\right)\vartheta^2+\vartheta^4}}. \tag{18}$$

This formula is identical to that obtained from eqs. (4)–(7), if we put $B=0$. In our example this amplitude, for $\vartheta=0.997$ equals $A=0.5$ which is consistent with result in Fig. 2a.

4.2. Influence damping on absorption effect

In practice, FVAE is difficult to obtain because of existing friction related to damping in pivot of the pendulum. In this section we analyse the influence of system damping on the absorption effect. In Figs. 4, the influence of oscillator's damping on the oscillator (Fig. 4a) and the pendulum (Fig. 4b) behaviour is shown. Interesting, that increase of oscillator's damping does not eliminate dynamic absorption region, but only reduces it (Fig. 4a). This is very important from dynamic elimination vibrations point of view. This suggests to use this parameter to control the system behaviour.

However, the increase in pendulum's damping causes reduction of the pendulum amplitude (Fig. 5b), but absorption effect completely disappears (Fig. 5a). This denotes, pendulum's damping may impair the efficiently of AVPA.
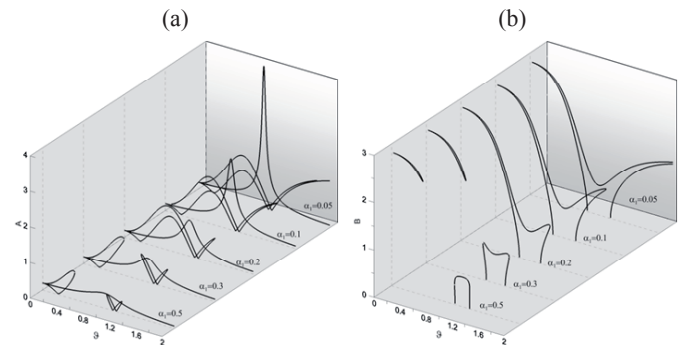

Fig. 4. Influence oscillator's damping on absorption effect (a) and pendulum swings (b) for $\alpha_2=0.002$, $\mu=6$, $\lambda=0.3$, $q=0.2$.
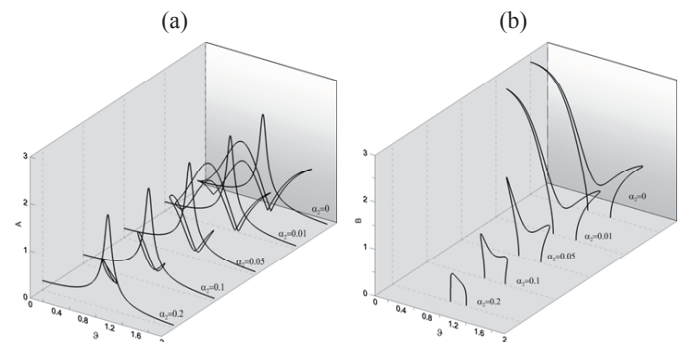

Fig. 5. Influence pendulum's damping on absorption effect (a) and pendulum swings (b) for $\alpha_1=0.1$, $\mu=6$, $\lambda=0.3$, $q=0.2$.

The obtained results show that the best absorption effect exists for small values of system's damping and absorption region is located near the main parametric resonance. Therefore, the dynamic pendulum damper should be properly designed to take system's damping parameters into consideration. The numerical and experimental verification of these results can be found in [3, 4].

5. Conclusions and final remarks

The vibration absorption effect by application of an autoparametric coupled pendulum is investigated in this paper. In the system, the motions of the pendulum and the oscillator are coupled therefore vibration absorption depends on dynamics of both subsystems. Near the autoparametric resonance region, the most effective absorption region is located. Analytical and numerical studies have shown that full absorption effect is possible if the damping of the pendulum is near to zero. The absorber can be highly efficient for correctly tuned subsystems.

The damping analysis shows, that the increase of pendulum's damping can reduce or eliminate the absorption region, while the increase of oscillator' damping only reduces the absorption. Therefore, the control method of AVPA by oscillator damping as a control parameter looks promising.

A smart suspension consisting of SMA spring together with MR damper leading to active dynamic vibration absorber will be prepared in the future.

References

1. Guskov AM, Panovko GY, Van Bin C. Analysis of the dynamics of a pendulum vibration absorber. Journal of Machinery Manufacture and Reliability 2008; 37 (4): 321–329.
2. Hatwall H, Mallik AK, Ghos A. Non-linear vibrations of a harmonically excitedautoparametric system. Journal of Sound and Vibration 1980; 81 (2): 153-164.
3. Kecik K, Warminski J. Dynamics of an autoparametric pendulum-like system with a nonlinear semiactive suspension. Mathematical Problems in Engineering 2011: Article ID 451047:1–18.
4. Kęcik K. Zastosowanie tłumika magnetoreologicznego do sterowania drganiami w układzie mechanicznym z wahadłem. Przegląd Elektrotechniczny (Electrical Review) 2012; 2, 2012: 223–226.
5. Korenev BG, Reznikov LM. Dynamic vibration absorbers, theory and technical applications, John Wiley & Sons, 1993.
6. Nabergoj R, Tondl A, Virag Z. Autoparametric resonance in an externally excited system. Chaos, Solitons, Fractals 1990; 4: 263–273.
7. Sun JQ, Jolly MR, Norris MA. Passive adaptive and active tuned vibration absorbers – a survey. Transaction of ASME 1995; 117: 234–242.
8. Warminski J, Kecik K. Autoparametric vibrations of a nonlinear system with pendulum. Mathematical Problems in Engineering 2006; Article ID 80705: 1–19.
9. Warminski J, Kecik K. Instabilities in the main parametric resonance area of a mechanical system with a pendulum. Journal of Sound Vibration 2009; 332: 612–628.
10. Warminski J, Lenci S, Cartmell MP, Rega R and Wiercigroch M. Nonlinear Dynamic Phenomena in Mechanics. Springer 2012, 181.

Krzysztof KECIK, Ph.D. (Eng.)
Andrzej MITURA, Ph.D. (Eng.)
Prof. Jerzy WARMINSKI, Ph.D., D.Sc. (Eng.)

Department of Applied Mechanics
Faculty of Mechanical Engineering
Lublin University of Technology
Nadbystrzycka 36, 20-816 Lublin, Poland
e-mails: k.kecik@pollub.pl, a.mitura@pollub.pl, j.warminski@pollub.pl

Aneta TOR-ŚWIĄTEK

EVALUATION OF THE EFFECTIVENESS OF THE MICROCELLULAR EXTRUSION PROCESS OF LOW DENSITY POLYETHYLENE

OCENA EFEKTYWNOŚCI PROCESU WYTŁACZANIA MIKROPORUJĄCEGO POLIETYLENU MAŁEJ GĘSTOŚCI*

From a processing point of view, evaluation of effectiveness is essential for the proper conduct of each polymer processing process. However, it is particularly important in the case of modified plastics processing aids, such as blowing agents, the addition of which causes changes in both the process course and the physical properties and structure of the resulting product. Carrying out a proper analysis of the efficiency of the process, taking into account the criteria and methods can efficiently and reliably carry out a extrusion process. This paper presents the results of assessing the effectiveness of the microcellular extrusion process of LDPE modified with selected microblowing agent in the form of microspheres.

Keywords: *microcellular extrusion process, effectiveness of process, low density polyethylene, blowing agent, microspheres.*

Z przetwórczego punktu widzenia ocena efektywności ma istotne znaczenie dla właściwego prowadzenia każdego procesu przetwórstwa tworzyw polimerowych. Jednak szczególnie ważna jest ona w przypadku przetwórstwa tworzyw modyfikowanych środkami porotwórczymi, których dodanie powoduje zmiany zarówno w przebiegu procesu, jak i we właściwościach fizycznych oraz strukturze otrzymanego wytworu. Przeprowadzenie właściwej analizy efektywności procesu, uwzględniającej odpowiednie kryteria i metody pozwala wydajnie i niezawodnie prowadzić proces wytłaczania. Artykuł prezentuje wyniki badań oceny efektywności procesu wytłaczania mikroporującego polietylenu małej gęstości modyfikowanego środkiem mikroporującym w postaci mikrosfer.

Słowa kluczowe: *wytłaczanie mikroporujące, efektywność procesu, polietylen małej gęstości, środek porujący, mikrosfery.*

1. Introduction

Microcellular extrusion process is now more frequently used method for processing of thermoplastics. The process according to the distribution characteristics of blowing agent can be carried out using standard production lines, but with regard to the proper selection of processing conditions. Consequence of the introduction of special blowing agents to plastic is [4] to obtain the products of a certain physical properties and structure.

Due to the presence of blowing agents with the characteristics of the distribution endo-or exothermic on the processed material, contained in the plasticizing system, affects variables conditions such as high temperature, high pressure, large shear stresses. This makes the microcellular extrusion process difficult to proceed [1, 2].

Considering the effectiveness of the extrusion process takes into account certain criteria and methods for assessing the effectiveness and impact of various features design particular processing machines and tools [6, 7]. Among the criteria to assess the effectiveness of the extrusion process should be distinguished quantitative, qualitative and operational criteria [13]. Quantitative criteria include, for example, the physical parameters characterizing the extrusion process, such as the degree of plasticity, volumetric flow rate of material, the mass flow rate of material (efficiency extrusion) and energy efficiency. Among the criteria of quality, replace the distribution and fluctuation of processing temperature, the longitudinal and cross degree of mixing, stability of the process efficiency (pulsation of the flow rate and pressure), structural changes and physical properties of the products.

Operational criteria include durability, the availability of production and process automation and robotics.

In the plastics processing with the addition of various auxiliary agents, including blowing agents, mixing efficiency is very important. It is primarily determined by the design of the plasticizing system, in particular a screw and cylinder design [5, 8, 12].

Quality evaluation of microcellular extrusion process is very complex. Requires consideration of a large number of direct and indirect indicators describing the quality and the proper conduct of the process [9]. Direct indicators include physical quantities characterizing the plasticization of the process and added blowing agents because of the stability of the process [15]. The measurement of these values is made directly during the process or after the relevant calculations. Direct indicators include mainly factors determining the extrusion process course, the stream of input and dissipation of heat, distribution of temperature and pressure, distribution of the residence time of material in the extruder, the degree of plastic homogenization, the energy consumption and rheological properties [14]. Indirect indicators are physical quantities that describe in detail the process of plasticization and instability. These include temperature fluctuation of plastic, pulse of the pressure, thermal and mechanical homogenization of the material. Specific criteria and methods of extrusion evaluation are used depending on variety of extrusion process [3].

Microcellular extrusion efficiency is the ability of the plasticizing system, which processor the plastic modified with blowing agent, to manufacture of high-quality components with the possible greatest effectiveness and energy efficiency of the process.

The purpose of this study is to evaluate the extrusion process on the basis of factors characterizing the effectiveness, such as pressure and temperature distribution of the plastic in the extruder plasticizing system and extrusion head, the mass flow rate of material from the extrusion head (process efficiency), the Barus effect, extruder energy efficiency and process energy efficiency of LDPE porous extruded. Great importance for the assessment of the process is extrudate quality, which is determined by the degree of mixing of polyethylene and blowing agent.

2. Working stand and characteristic of research

Microcellular extrusion process was carried out in technological line for shapes (fig. 1), equipped with single screw extruder W-25D, extrusion head with slot die for tape extrusion, calibration device, the cooling bath and collecting device. The extruder is made up of motor, reduction gear and plasticizing system. Extruder plasticizing system consist of segment cylinder assembled from three segments. The plasticizing system can be supplied with different segments, which together made up of three screw length: 18D, 23D and 28D. In the first set, used to test of the extrusion process efficiency of the porous LDPE, the cylinder has two heating zones and provided with a screw with a diameter of 25 mm and length of 450 mm. Screw drive is implemented using a DC motor with a capacity of 3.57 kW with infinitely variable number of rotations, belt transmission, gear and overload clutch. This ensures the operation of the extruder screw rotation speed varying in the range from 0 to $5.35s^{-1}$. Extrusion head for tape is equipped with a heating zone with an annular electric heater, sensor of pressure and temperature of the plastic and the second temperature sensor – a thermocouple. The head has a removable flat slot die, the width of the die used in the studies is 22.00 mm, and the height of 1.40 mm.

To the studies the low density polyethylene LDPE with the trade name Malen E FABS 23 D022 produced by Basel Polyolefins was used. The plastic contains an antioxidant, reducing the degradation of material in terms of processing and slip additives and anti blocking. This material is characterized (by the manufacturer) density of 922 kg/m³, a nominal melt flow rate MFR at 190°C and 2.16 kg equal to 2g/10 min, tensile strength of 18 MPa, hardness 48°Sh and softening point VST (50°C /10N) of 91°C.
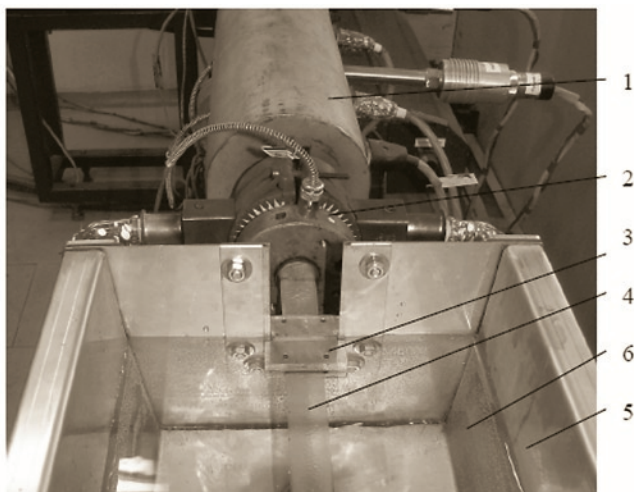

Fig. 1. Fragment of technological line of tape extrusion: 1 – plasticizing system of extruder , 2 – extrusion head, 3 – calibration device, 4 –extruded porous LDPE tape, 5 – cooling bath, 6 – cooling water

Low density polyethylene was modified with a special blowing agent in the form of polymer microspheres called Expancel 950 MB

120 manufactured by Akzo Nobel. Microspheres used are made of thermoplastic polymer capsules comprising a gas - a liquid hydrocarbon, which, under the influence of elevated temperature increases the volume of the microspheres. Polymer coat of microspheres is formed during their manufacture by polymerization of a mixture of acrylonitrile and methacrylonitrile. The most important characteristics of this agent are primarily density of 6.5 kg/m³, size before processing from 28 to 38 μm and a processing temperature of 180 to 200°C.

3. Programme of research

In order to know the impact of the microspheres on LDPE extrusion process the test program was developed, taking into account the content of dispensed microspheres, the temperature in the extruder plasticizing system and extrusion head, the screw rotation speed, the rotational speed of the collecting device.

The process was carried out under specified processing conditions, taking into account the type of the plastic and the characteristics of the distribution of selected blowing agent. Set temperature of the zones of the extruder plasticizing system and the extrusion head, with values 130, 150, 180°C, read after process stabilization for each screw rotational speed and the content of microspheres in the base material being processed.

It was found that the quantity of the dispensed microspheres will be 0%, 0.1%, 0.3% and 0.5% by mass relative to the mass of LDPE. These values are based on data from the manufacturer of the Expancel and own preliminary tests.

During microcellular extrusion of LDPE the extruder screw rotation speed was changed and it was 50, 100 and 150 rpm. Withdrawing shaft rotational speed of collecting device amounted respectively to a 4, 8 and 15 rpm.

As part of the established research program of microcellular extrusion process effectiveness was made the measurements of real plastic temperature and pressure in the plasticizing system and extrusion head, the mass and dimensions of the extruded measuring sections, extrusion time of measuring section and time of extruder power consumption during measuring section extrusion.

After a series of calculations was determined the mass flow rate of the extrudate, which is a measure of extrusion process efficiency, the plastic enthalpy growth, flow of energy supplied to the extruder and the extrusion head, the heat flux carried by the material, the energy efficiency of extruder and microcellular extrusion process. The designation of the above figures is important for the physical changes taking place and the obtained microporous structure of extrudate.

Barusa effect studies was made in order to determine the expansion of the extrudate stream flowing from the die of extrusion head due to different normal stresses resulting from plastic flow. Measurements were performed after the cooling of extrudate at the normal temperature. The value of this effect was determined from the dependence, which is the ratio of the cross-section of extrudate to the cross-sectional area of the die, expressed as a percentage.

To properly determine the quality of the microcellular extrusion process and the degree of mixing polyethylene and microspheres the resulting extrudate microporous structure was also evaluated by performing microscopic image.

4. Research results

Studies of plastic temperature distribution (Table 1) in the extruder plasticizing system and the extrusion head has shown that the addition of microspheres to the LDPE occurring temperature differences. The highest temperature increase of about 40% was observed at the dosage of 0.1% of the microspheres irrespective of the change of extruder screw rotational speed. On further increasing the content of the microspheres in the plastic in an amount of 0.3% and 0.5% the

Table 1. Research results of plastic temperature and pressure in extruder plasticizing system (I, II) and extrusion head (III)

No.	Dosage of micro-spheres, %	Screw rotational speed, rpm	Temperature in plasticizing system and extrusion head, °C			Pressure in plasticizing system and extrusion head, MPa	
			I	II	III	I	III
1.	0	50	128,8	154,4	175,1	17,1	2,0
		100	129,5	154,6	175,6	10,3	2,6
		150	131,6	159,6	179,6	9,9	3,4
2.	0,1	50	142,6	186,2	181,7	16,9	2,0
		100	143,6	186,8	178,0	12,9	2,4
		150	143,8	179,4	177,9	10,9	2,8
3.	0,3	50	140,5	175,5	200,0	18,8	1,2
		100	139,8	163,1	190,0	11,5	2,4
		150	142,4	165,3	198,6	9,9	2,3
4.	0,5	50	132,1	162,5	187,0	12,4	1,1
		100	140,0	169,4	197,9	10,9	1,7
		150	141,0	169,0	199,0	7,0	2,0

material temperature is changing in relation to the set temperature, but this increase is not as intense and is about 9%.

The sharp increase of material temperature in the first zone of the plasticizing system, occurring after the addition of the microspheres can result from the use of the innovative design of the extruder, which provides high-intensity mixing process of plastic. In the process, heating of the LDPE takes place by means of electric heaters arranged on the cylinder of the extruder. However, in the second zone of the plasticizing system and after the process stabilization, reach a certain temperature and screw rotational speed about 100 rpm the autothermal extrusion process be started [11]. Then heat generation that is necessary for the of plasticization occurred as a result of external friction plastic granules themselves and cylinder working surfaces and the screw and the internal friction of the plastic macromolecules and the added blowing agent. This results in a significant increase in plastic temperature with an increase in extruder screw rotational speed.

In the case of pressure measurements (Table 1) of the plastic in the extruder plasticizing system and extrusion head, the pressure is increasing and then rapidly falls in extrusion head, which is according to the data available in the literature [14]. As a result of increasing the extruder screw rotational speed, the pressure in the plasticizing system of plastic decreases on average by 30% with the increase in screw rotation speed of 50 to 100 rpmin and a 17% at the next increase screw rotational speed of 150 rpm. Pressure of the plastic in extrusion head increases with a light intensity with increasing screw rotational speed. The plastic pressure changes in the extruder plasticizing system and extrusion head does not affect the content of the microspheres or this influence is very small.

Research of the microcellular extrusion allowed to determine the efficiency of this process and to determine occurring the Barus effect. Based on the results of measurements the dependences of the tested factors described in the test program, as a function of the screw rotational speed were done, which are shown in Figures 2÷5.

On the basis of the measurements results it can be concluded that with increasing screw rotational speed the microcellular extrusion process efficiency increases by an average of about 30%. In addition, with increasing content of microspheres in LDPE takes place a gradual slight increase of efficiency of the ongoing process. For the screw rotational speed of 50 rpm the process efficiency is increased by 3.4% for a dosage of 0.1%, by 4.7% for a dosage of 0.3% and by 1.5% for a dosage of 0.5%. At higher screw rotational speeds the

process efficiency changes slightly with increasing dosage of microspheres in LDPE.

Barus effect tests have shown a slight expansion of extrudate stream flowing from the extrusion head only with the extruder screw rotational speed of 150 rpm. As a result of increasing the dosage of the microspheres in LDPE a gradual decrease in the effect is observed, which may be associated with decreased amounts of extruded plastic, which is accompanied by porous processes. When the screw rotational speed of 50 rpm the Barus effect changes by 5.3% for a dosage of 0.1% and 0.3% and by 8% for a dosage of 0.5%. When the screw rotation speed of 100 rpm the value of the effect is reduced: by 3.1% for a dosage of 0.1%, by 12.4% for a dosage of 0.3%, and by 5% for a dosage of 0.5%. The largest effect Barus changes occur when the screw rotational speed of 150 rpm and are: 13.4% for a dosage of 0.1%, 8.6% for a dosage of 0.3% and 2% for a dosage of 0.5%.

Measurements of heat flux carried by the LDPE containing microspheres and flow of energy supplied to the extruder made it possible to determine the energy efficiency of the extruder (Fig. 4) and extrusion process (Fig. 5).

Experimental studies have shown a gradual impact of both variables factors, such as dosage of microspheres and screw rotational speed on the value of energy efficiency of extruder and extrusion process. With the increase of screw rotational speed increases the energy efficiency of both the extruder and the extrusion process of porous LDPE, which is confirmed by the information from the literature [10]. The energy efficiency of the extrusion process increases by about 20% when increasing the screw rotational speed to 100 rpm, and about 15% at a speed of 150 rpm. For energy efficiency of extruder this increase is about 20% at a speed of 100 rpm and 11% at a speed of 150 rpm.

Simultaneously, the addition of microspheres to the polyethylene caused a gradual decrease of the energy efficiency of the extrusion process in the whole range of changed extruder screw rotational speed. This may be due to the characteristics of the microspheres, which in order to increase their dimensions take heat from the plasticized material.

Following the addition blowing agent in the form of microspheres to the polyethylene extrudate in the form of a strip with microporous structure was obtained. The appearance of samples in the cross-section are shown in Figure 6. On microscopic images are visible micropores with different diameter and distribution. The largest difference in the dimensions of the micropores take place at dosage of 0.1%, which
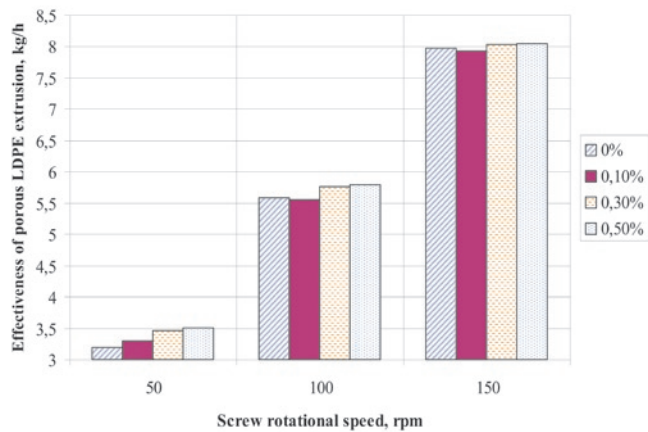
Fig. 2. *Dependence of efficiency of LDPE microcellular extrusion on screw rotational speed and dosage of microspheres*
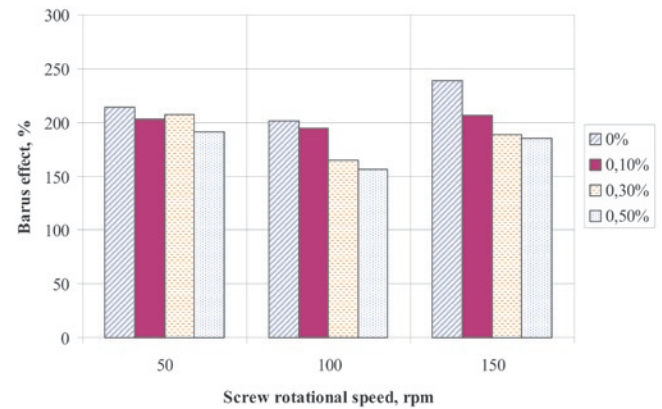

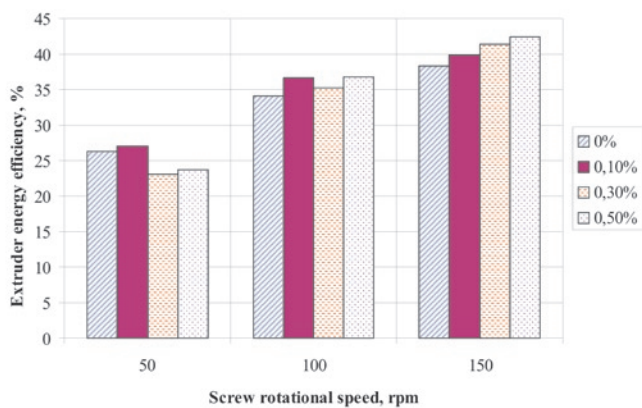Fig. 3. *Dependence of Barus effect on screw rotational speed and dosage of microspheres in LDPE*

Fig. 4. *Dependence of extruder energy efficiency on screw rotational speed and dosage of microspheres in LDPE*
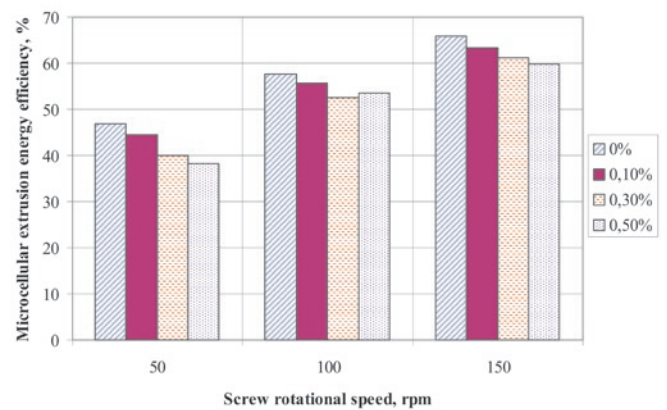

Fig. 5. *Dependence of microcellular extrusion process energy efficiency on screw rotational speed and dosage of microspheres*

may be due to a greater possibility of the growth of microspheres in the solid LDPE. Increasing the amount of the dispensed microspheres resulted in growth reduction due to its amount in extrudate.

Based on evaluation of the obtained microporous extrudate structure can be concluded that the degree of mixing of the LDPE and the microspheres is not sufficient. The newly created structure is not homogeneous across the cross-section of extrudate, which can affect the particular physical properties of the product. It is necessary to use additional devices such as dosing dispenser capable of blowing agent in very small quantities or changes in screw construction.

5. Summary

Analyzing the effectiveness of the microcellular extrusion process it has to be consider a number of factors affecting the course and the quality of the process. The most important include primarily changes of the temperature in the extruder plasticizing system and in the extrusion head and the associated pressure fluctuations, changes of the screw rotational speed and increased dosage of microspheres contained in the plastic being processed.

Based on the research it can be concluded that the low density polyethylene modified with blowing agent in the form of microspheres is efficiently extruded by the extruder screw rotational speed of 150 rpm and with a dosage of 0.5% of the microspheres. This is due to the low temperature and pressure changes of the plastic, which positively influences on the degree of mixing, the smallest Barus effect, highest effectiveness and energy efficiency of the extruder and the process.

Presented the results of the temperature and pressure changes of plasticized material, and also dependings of the effectiveness, energy
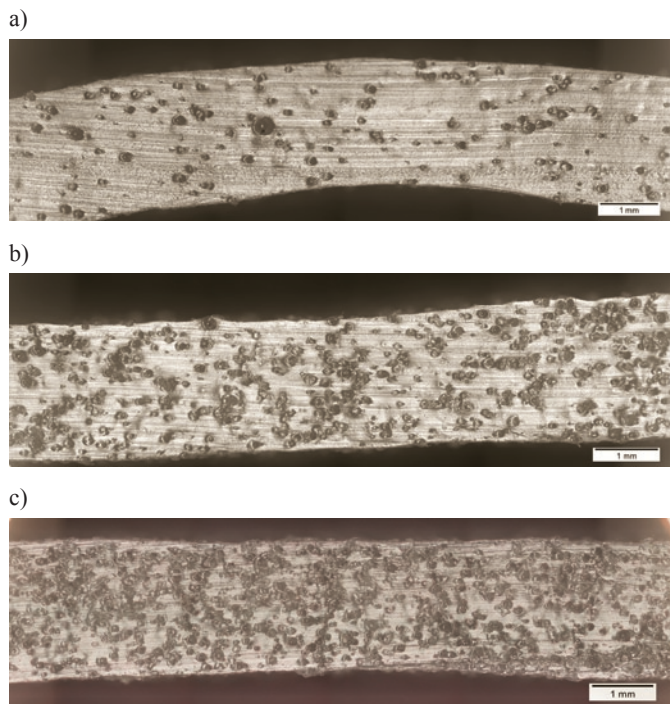

Fig. 6. *View of microporous extrudate physical structure (cross section) obtained with screw rotational speed of 50 rpm and with content of microspheres: a) 0,1%, b) 0,3%, c) 0,5%*

efficiency of the extruder and microcellular extrusion process as a function screw rotational speed is reflected in the literature. However, changes of the efficiency tested as a function of quantity dispensed microspheres show necessity of a broader analysis of the impact of blowing agents on particular process parameters, taking into account different method of agent dosage, the extruder screw design and the residence time of the material in the plasticizing system.

During the evaluation of the effectiveness of this process must take into account its efficiency, which has significant influence on weight reduction of extrudate, resulting from the addition of microspheres to a plastic. These changes result from the amount of energy flux fed to the extruder and the extrusion head, the heat flux (thermal power) carried by the material in the plasticizing system, plastic enthalpy, energy flux heaters of extruder cylinder and extrusion head and also mechanical power supplied to the screw shaft. The values of these factors significantly affect the energy efficiency of the extruder and the extrusion process, which in addition to changes of temperature and pressure as well as the mixing degree of plastic and microspheres are the basic criteria to assessing the effectiveness of the microcellular extrusion process.

References

1. Bieliński M. Techniki porowania tworzyw termoplastycznych. Wydawnictwo Uczelniane Akademii Techniczno-Rolniczej, Bydgoszcz 2004: 10–25.
2. Garbacz T, Tor A. Wpływ zawartości środka porującego na właściwości użytkowe zewnętrznych powłok kabli. Polimery 2007; 52; 4: 286–293.
3. Iwko J. Wybrane problemy procesu wytłaczania tworzyw polimerowych cz. 1. PlastNews 2008; 7/8: 52–55.
4. Jonsson L, Rosskothen KR. Mikrospharen – ein universelles treibmittel. Kunststoffe – Plast Europe 2003; 7: 86–87.
5. Kelly AL, Brown EC, Coates PD. The effect of screw geometry on melt temperature profile in single screw extrusion. Polymer Engineering and Science 2006; 46; 2: 1706–1714.
6. Klepka T. Efektywność wytłaczania polimerowych, specjalnych warstw ślizgowych. Polimery 2002; 47; 9: 649–653.
7. Klepka T. Charakterystyka stanu powierzchni specjalnych warstw ślizgowych utworzonych w procesie wytłaczania. Polimery 2004; 49; 2: 123–127.
8. Kracalik M, Laske S, Gschweitl M, Friesenbichler W, Langecker GR. Advances compounding: extrusion of polypropylene nanocomposites using the melt pump. Journal of Applied Polymer Science 2009; 113; 3: 1422–1428.
9. Schneider HP. Improved efficiency and quality trends in PVC profile and pipe extrusion. Kunststoffe – Plast Europe 2000; 90; 10: 42–45.
10. Sikora JW. Charakterystyka badań sprawności energetycznej procesu wytłaczania i wytłaczarki. Polimery 1999; 3: 190–197.
11. Sikora JW, Sasimowski E. Influence of the length of the plasticating section on the selected characteristics of an autothermal extrusion process. Advances in Polymer Technology 2005; 24; 1: 21–28.
12. Sikora JW. Increasing the efficiency of extrusion process. Polymer Engineering and Science 2008; 48; 9: 1678–1682.
13. Stasiek J. Eksperymentalne metody oceny jakości procesu wytłaczania. Polimery 1996; 1: 15–21.
14. Stasiek J. Wytłaczanie tworzyw polimerowych. Wydawnictwa Uczelniane Uniwersytetu Technologiczno – Przyrodniczego w Bydgoszczy, Bydgoszcz 2007: 93–108.
15. Tor-Świątek A, Samujło B. Use of thermo vision research to analyze the thermal stability of microcellular extrusion process of poly(vinyl chloride). Eksploatacja i Niezawodnosc – Maintenance and Reliability 2013; 15 (1): 58–61.

Aneta TOR-ŚWIĄTEK Ph.D. (Eng.)
Department of Polymer Processing
Mechanical Engineering Faculty
Lublin University of Technology
ul. Nadbystrzycka 36, 20-618 Lublin, Poland
e-mail: a.tor@pollub.pl

Karolina BEER
Krzysztof PAŁKA
Barbara SUROWSKA
Mariusz WALCZAK

A QUALITY ASSESSMENT OF CASTING DENTAL PROSTHESIS ELEMENTS

OCENA JAKOŚCIOWA ODLEWANYCH ELEMENTÓW PROTETYCZNYCH*

Properties of fixed and mobile dentures, as well as their design have a significant impact on their durability in a complex state of biomechanical loads that occur in the oral cavity during the chewing process. Elements that are usually mechanical damaged (cracking) in skeletal prostheses are metal clamps. Damage of fixation of dentures not only results in the inability to further operation, but also is causing discomfort in the patient and can lead to injury of the oral cavity, teeth and risk of complications in case of access into the digestive system.The aim of this study was to evaluate the quality of items of prostheses manufactured using available techniques and the analysis of the causes of premature loss of functional quality of these elements. Dental cobalt matrix alloy - Wironit Extra-hard was used for the study. Qualitative research consisted of the evaluation of the nature and intensity of internal casting defects and evaluation of macro-and microstructure of manufactured castings using microscopic techniques. Research of breakthroughs indicate the occurrence of casting shrinkages. Microstructural research revealed the presence of a typical dendritic structure of the matrix in form of solid solution Co-Cr-Mo and eutectic. Strength test results achieved in the relation to the macro and microstructure were also carried out. A quantitative assessment of the intensity of casting defects using image analysis was realized. Potential risks of casting technology were identified and a methodology of monitoring the state of elements of dentures was proposed.

Keywords: durability of prosthetic devices, casting defects, cobalt alloys.

Właściwości stosowanych uzupełnień protetycznych stałych i ruchomych oraz ich konstrukcja mają istotny wpływ na ich trwałość w warunkach złożonego stanu obciążeń biomechanicznych, jakie występują w jamie ustnej w trakcie procesu żucia. Elementami, które najczęściej ulegają uszkodzeniom mechanicznym (pękaniu) w protezach szkieletowych są metalowe klamry. Uszkodzenie mocowania protezy skutkuje nie tylko brakiem możliwości jej dalszej eksploatacji, ale również jest przyczyną uczucia dyskomfortu dla pacjenta i może powodować skaleczenia jamy ustnej, uszkodzenia zębów oraz ryzyko powikłań w przypadku przedostania się do układu pokarmowego. Celem pracy była ocena jakościowa elementów protez wytwarzanych dostępnymi technikami oraz analiza przyczyn przedwczesnej utraty funkcjonalności tych elementów. Do badań zastosowano stop stomatologiczny na osnowie kobaltu Wironit Extra-hard. Badania jakościowe polegały na ocenie rodzaju i nasilenia wewnętrznych wad odlewniczych oraz ocenie makro- i mikrostruktury wytworzonych odlewów z wykorzystaniem technik mikroskopowych. Badania przełomów wskazują na występowanie rzadzizn spowodowanych skurczem odlewniczym. Badania mikrostrukturalne wykazały obecność typowej struktury dendrytycznej z osnową w postaci roztworu stałego Co-Cr-Mo i eutektyką. Wykonano również analizę wyników badań wytrzymałościowych w powiązaniu z uzyskiwaną makro i mikrostrukturą. Dokonano oceny ilościowej nasilenia wad odlewniczych wykorzystując analizę obrazu. Wskazano potencjalne zagrożenia technologii odlewania oraz zaproponowano metodykę monitorowania stanu elementów protez.

Słowa kluczowe: trwałość aparatów protetycznych, wady odlewnicze, stopy kobaltu .

1. Introduction

Despite the growing popularity of implants, dental partial prosthetics are still eagerly used due to its functionality and low cost of production [1,10]. One of the types of partial dentures is skeletal denture. It is used in patients who have a too large loss of teeth and it is impossible to use a bridge reconstruction. Skeletal dentures cover the patient's toothless mouth appendages. In the case of the upperdenture also part of the palate, the lower denture – part of the sublingual area. These are periodontium supported, reduced plate prosthesis. They consist of a metal skeleton – including bonds and supporting components, metal fasteners (clamps, bolts) and the reconstructed teeth (Fig.1a). Their functionality is based on the ease of forming and individual adaptation to the anatomical characteristics of the patient while providing high mechanical strength and corrosion resistance.The metal substructure-

of partial dentures are made, inter alia, froma cobalt-chromium alloys, which have a high resistance to corrosion due to the formation of the protective oxide layer on the surface [5, 11, 15].

Metal implants based on Co-Cr-Mo alloys can be manufactured by various methods, [6] inter alia, by a hot forging or by powder metallurgy, but the formation of partial dentures, because of the need to obtain a high accuracy of the geometric in case of small cross-sections, is realized by a melted models method.

This method is provide to obtain complex shape castings, fitting to the individual patient's anatomical features, in a dental laboratory. For melting alloys induction heating is used, which allows for a short time of operation, eliminates a large part of casting defects and reduces costs. The liquid alloy is cast usinga centrifugal or vacuum-pressure method. Casting with the use of centrifugal force is recommended, especially for complex shapes castings and larger in sizes,
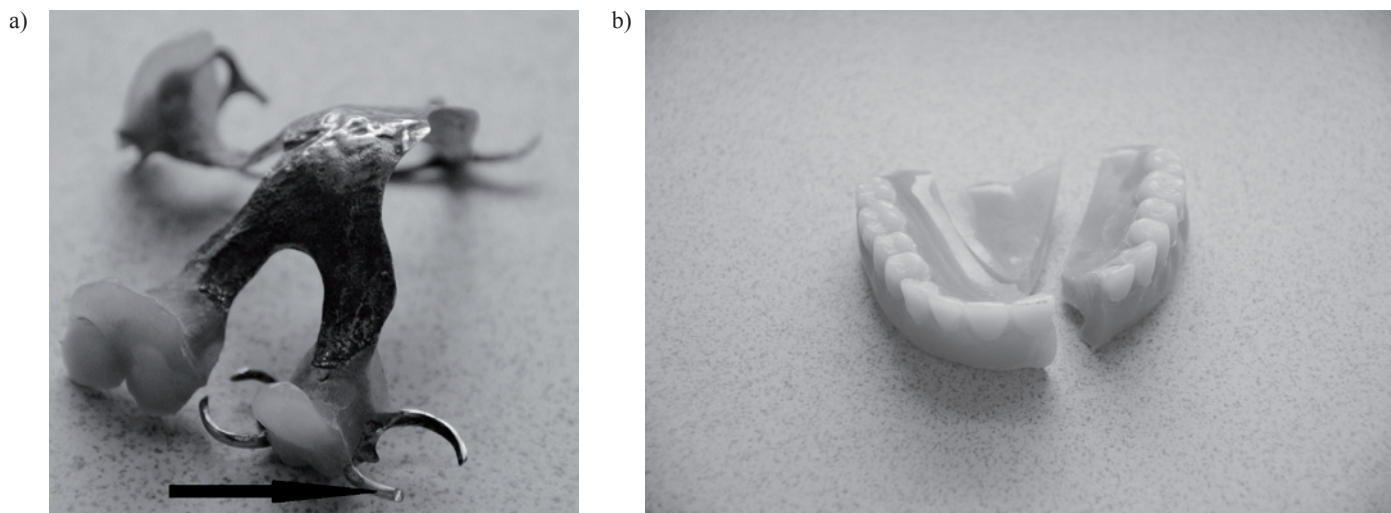
---

a)

b)

Fig. 1. a) Clamp damage of a skeletal denture, b) Failure of an acrylic denture

such as skeletons of dentures or multi-span bridges. Vacuum casting is mainly used for smaller items, such as crowns or short bridges.When the manufacturing process is properly conducted it should provide similar results of macro-and microstructure in the case of elements with small cross sections (e.g. clamps).

Properties of used fixed and mobile dentures, and their design have a significant impact on their durability in a complex state of biomechanical loads that occur in the mouth during the chewing process. The mechanical loads are responsible in the main part for the damages and failures of prosthetic supplies. Clamping forces depending on the size, intensity, duration and location cause varying degrees of stress concentration in the hard tissues of the tooth and dental restorations, which often results in damage to fasteners or damage to the entire denture prosthesis (Fig. 1a, b). There are two groups of denture failures:

– intraoral, they are mechanical, violence, diseases (eg. epilepsy);

– outside the oral cavity, can include chronic mechanical failures – wear of a prosthesis, conditions changes in prosthetic ground that cause an inaccurate adhesion of plates and uneven load, no offloads, ragged occlusion of teeth and habits – occlusion and no-occlusion parafunctions [2].

Elements that are usually mechanical damaged (cracks) are clamps. Damage to fixing dentures not only results in the inability to continue service (prosthesis no longer fulfills its function, does not carry the mechanical loads), but also cause discomfort in the patient. In addition, a damaged clamp, unnoticed by the patient, can cause a mouth injury, mechanical damages to the teeth or get into the digestive system, where a sharp foreign body is the biggest danger because of the possibility of complications.

Prostheses and their parts are a significant part of a set of sharp foreign bodies in case of adults. Weiland et al. [19] describe the 256 foreign bodies in the 10-clinical observation, and O'Sullivan et al. had conducted 308 foreign bodies observation over 4 years, of which 88.3% had accidentally ingested [14]. Velasco et al. report that in the years 1981–1989, 617 foreign bodies was endoscopically removed, 541of which from adults, the oldest adult was at the age of 98 years [16]. The Velitchkov et al. based on their own experience, from the 20-year follow-up, found 542 foreign bodies in patients aged from 15 to 82 years [17].

Favorable physico-mechanical properties of cobalt alloys and availability of the manufacture method (*Best Available Techniques*) affect the prevalence of the metal frame based prostheses and their affordable price. However, the analysis of potential dangers and their

number indicate a need to recognize the problem of premature failure of prostheses, mainly clamp failures, due to the many risks of injury. Understanding the causes of premature failures and consequently, loss of performance characteristics of metal partial dentures will later develop methods to extend their reliability. The aim of the study is to assess the quality of prostheses elements manufactured using available techniques and an analysis of the causes of premature loss of function of these elements.

2. Materials and methods

The process of manufacturing of examined elements was carried out in the conditions of the professional prosthetic workshop according to the procedures used for the manufacture of partial dentures. Casting was performed using an induction centrifugal casting machine ROTOCAST (Roko Dental Equipment, Poland) and the vacuum-pressure method in the Nautilius casting machine (Bego, Germany) using the ceramic crucibles.

For the test a dental cobalt matrix alloy Wironit Extra-hard (Bego, USA) was used, with a nominal composition (by mass) 63% Co, 30% Cr, 5% Mo, 1.1% Si and Mn<1% C <1 % [20]. This alloy is used for casting partial dentures, clamp dentures and dentures mounted on bolts and fasteners. The melting point for this alloy is 1533K – 1578K, and the casting temperature is 1693K.The single casts were applied. Models of clamp of partial dentures are ready to use, identical contour masters (Fig. 2). On their base a ceramic mold was made using melted models method and aceramic pulp by Wirovest (Bego, USA) and the mold firing temperature 1273K. After removing the ceramic shell and cutting off parts of the casting gate a surface of samples was blasted using a sand spreader – ECOBLAST ESTATE 1 (Prodento-Optimed, Poland). Applying the same principle the cylindrical samples were prepared for the strength tests according to DIN EN 10002-1, with a measuring diameter ϕ 3 mm and a measuring length of 15 mm. Research methodology of mechanical properties is shown in previous publications of the authors [3, 18].

As-cast samples as well as samples after tensile tests were subjected to observation. Qualitative research consisted of the evaluation of the nature and severity of internal casting defects and evaluation of macro-and microstructure of castings using microscopic techniques. Microscopic examination was performed using a scanning electron microscope (Zeiss Ultra Plus) and a light microscope (Nikon MA200). The severity of defects is defined as the percentage of defects in the cross-section of an element using an image analysis software Image-Pro Plus (Media Cybernetics, USA), and images with a resolution of 3530×4404 pixels.

3. Results and discussion

Visual assessment, including scanning electron microscopy in range of small magnification, showed that manufactured elements had a good surface quality and a lack of defects. There has not also been observed the shape and dimensional deviations. The results of observations are given in Figure 3.

Observations of the fractures of elements made by both methods: centrifugal and vacuum pressure, point to the distinctive structure of the cast with the main direction of crystallization from the external surface of the product with the completion of the crystallization in the center of the element (Figure 3 (a) and (c)). Dendritic structure is also clearly exposed. In the central part of the elements the shrinkage porosity is observed, the details of these areas are shown in Figure 4.

Microstructural studies showed the presence of a typical dendritic structure (fig. 5a, d) with a solid solution of Co-Cr-Mo with eutectic. Microsegregations have been observed within crystallites. Primary precipitates of continuous nature are located in the interdendritic spaces and along the borders of crystallites. Specimens made by a vacuum-pressure method are characterized by the presence of single cases of microporosity and shrinkage porosity (fig. 5b, c) whereas castings made by a centrifugal method are characterized by the presence of porosity that occurs along the axis of the dendrites (fig. 5e) and shrinkage porosity occurring in the arms and microcracks propagate between shrinkage porosity arms (fig. 5f). Similar structures are observed in the casting Co-Cr-Mo alloys with a lower carbon content [4, 7, 9, 12].

Tensile tests (Tab. 1) show that the properties of the castings made by a vacuum-pressure method are higher those made by centrifugal one. However, for both methods of casting mold filling (vacuum-pressure and centrifugal) the mechanical properties are lower than these declared by the manufacturer (R_m = 910 MPa, $R_{e0,2}$ = 625 MPa [20]). These figures and the fact that some of the fractures of the test samples have occurred outside of the measuring length (fig. 6) indicate the presence of structural defects in castings.

Fig. 2. Ready to use a waxen contour master of prosthetic clamps
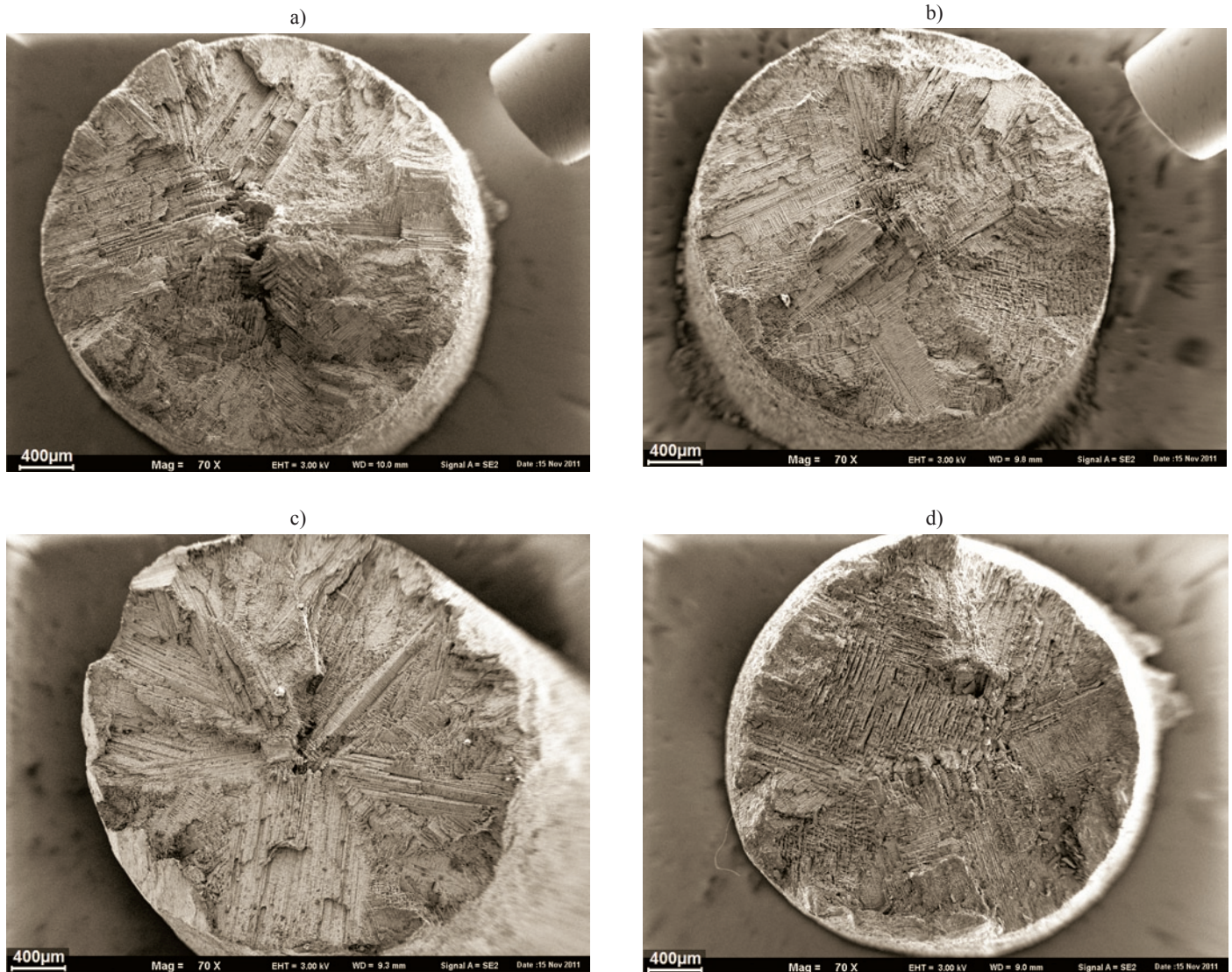
a)

b)

c)

d)

Fig. 3. Macrostructures of fractures of selected elements: a), b) - made by a vacuum pressure casting method; c), d) – made by a centrifugal casting method
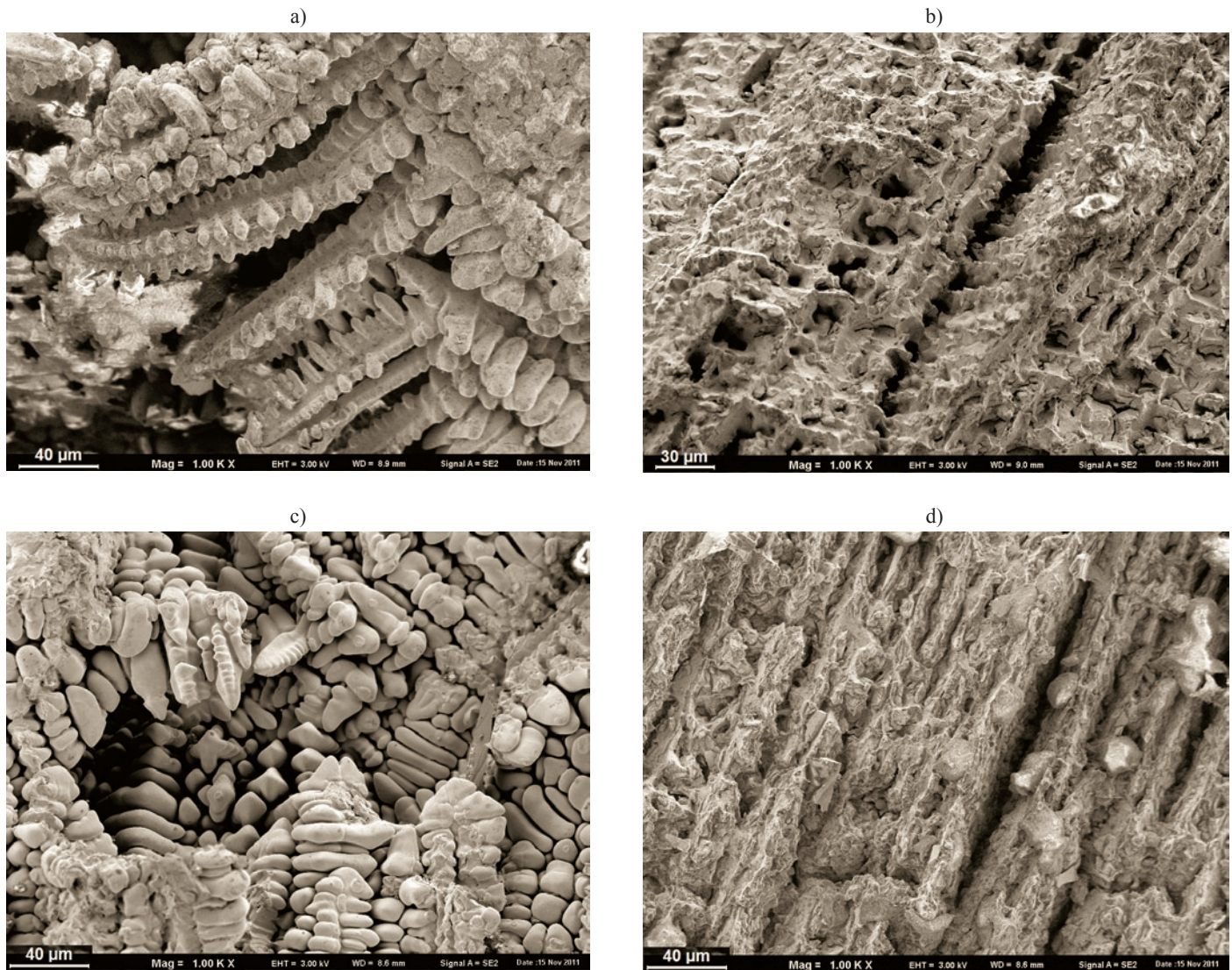
Fig. 4. Casting defects in the structure of tested elements: a),b) made by a vacuum pressure casting method: shrinkage –a) crack along the dendrite –b); c),d) made by a centrifugal casting method: shrinkage - c), shrinkage and porosity c) and d)

Strength reduction in relation to the manufacturer's data may be the result of the presence of shrinkage porosity in the structure of the cast. They reduce the cross section of the element and cause a notch effect. In addition, the arrangement of the shrinkage porosity and microcracks (in the dendritic arms, along the axis of the dendrites) prevents plastic deformation of these areas and compensation for the propagation of cracks. The relatively low plasticity of the alloy may be the source of the microcracks propagation arising between areas of shrinkage porosity, where the metal zone is not able to transmit the thermal stresses during cooling. These microcracks promote especially in eutectic areas with low plasticity and therefore low value of fracture toughness (fig. 5f).

The ratio $R_{e0,2}/R_m$ declared by the manufacturer is 0.68, while for the material obtained is 0.75 for the centrifugal and 0.72 for the vacuum-pressure method. The value of the elongation obtained is

2–3%. These results are comparable with those published in [8, 13] and testify for unsatisfactory ductility. There are some experiments taken to increase the strength and ductility by heat treatment [8, 12], except that the problem is the selection of the treatment conditions for alloys with a high carbon content (~ 1% in tested material).

Assessment of the intensity of casting defects made by image analysis (fig. 7a, b) indicates the presence of about 1.3% of pores in the element cross-section, whereas their largest concentration usually occurs in the central part. There is also a large amount of radial cracks, which in the case of fatigue loads will significantly shorten the service life by facilitating the propagation of fatigue cracks. It should be noted that the evaluation has been carried out in the cross section, while in the longitudinal section the longitudinal defects occur (fig. 7 c), significantly reduce the flexural strength and fatigue life.

Table 1. Results of tensile tests for specimens made by both casting methods

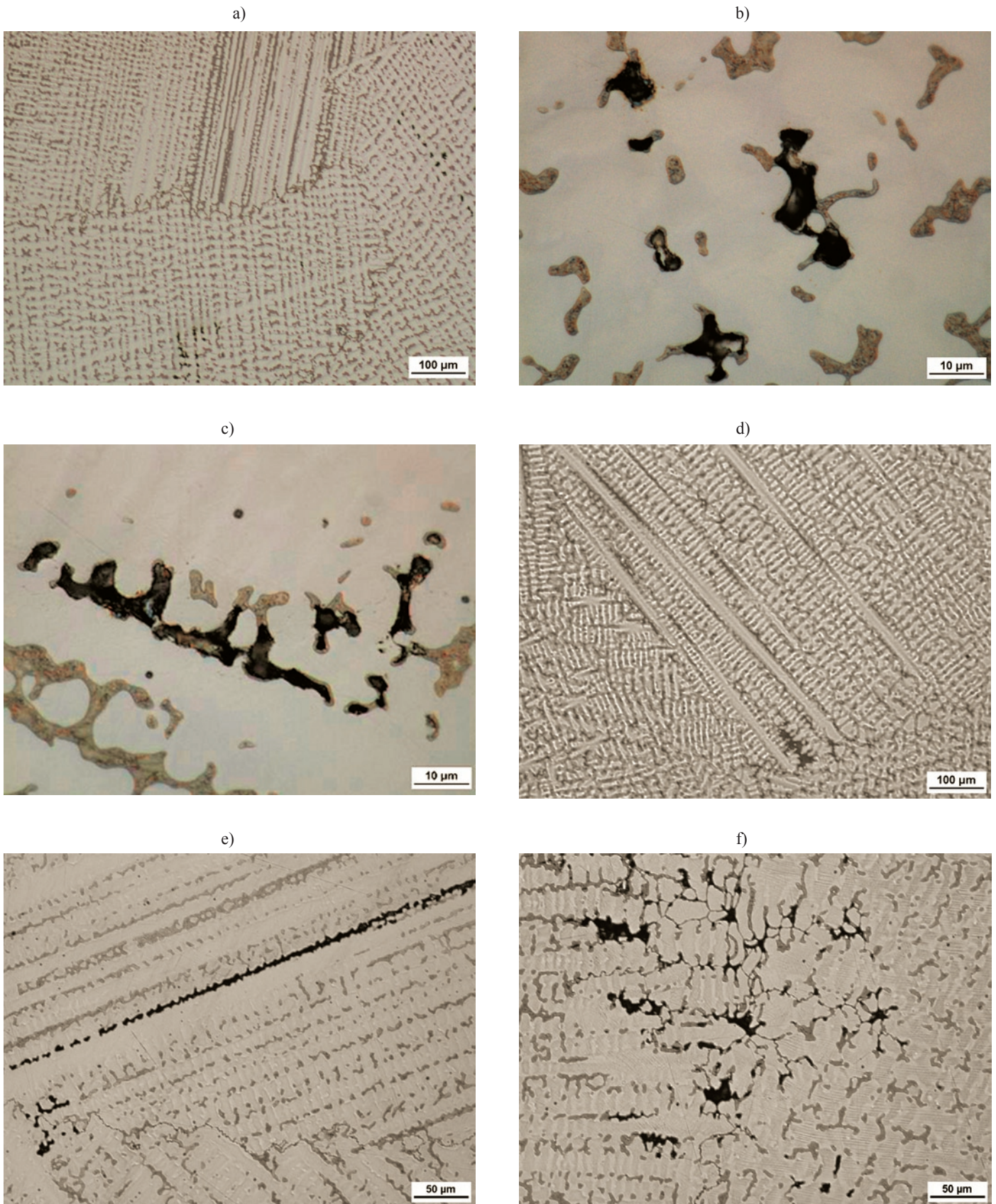|	Metoda odśrodkowa/ Centrifugal casting method[MPa]	Współczynnik zmienności /coefficient of variation [%]	Metoda próżniowo-ciśnieniowa/ Vacuum –pressure method [MPa]	Współczynnik zmienności/ coefficient of variation [%]
R_m	781	2,6	838	3,9
$R_{e0,2}$	585	2,5	601	1,1

a)

b)

c)

d)

e)

f)

Fig. 5. A microstructure of castings a), b), c) – a structure of a Wironit extra-hard cast alloy after vacuum pressure casting, single microcracks – b), c); d), e), f) – a structure of a Wironit extra-hard cast alloy after centrifugal casting: microcrack along the dendrite axis – e), shrinkages in the dendritic arms and micro-craks propagating between shrinkage areas – f)
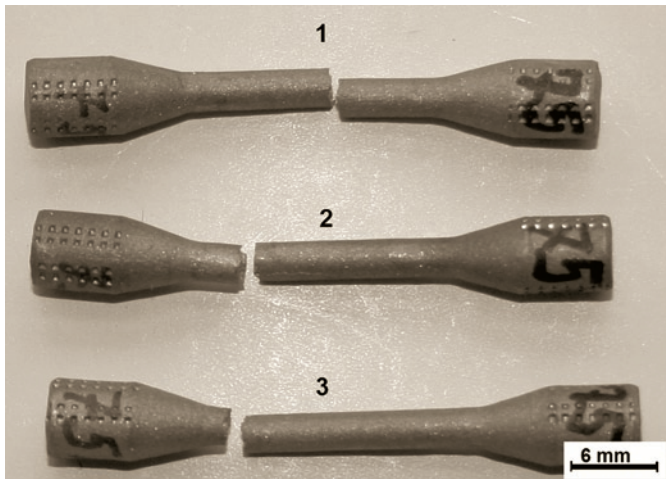
Fig. 6. Samples after a static tensile test: 1 – a fracture on the measuring length; 2, 3 – fractures out of measuring length

4. Summary

Presented studies have shown that the castings made in accordance to the procedure valid in prosthodontics laboratories are characterized by a significant amount of casting defects in the form of pores and shrinkage porosity. Microstructural studies showed the presence of a typical dendritic structure with presence of primary precipitates. Fractures are brittle and obtained mechanical properties provide low ductility. This type of structure in conjunction with casting defects is the cause of the cracking during exploitation of dentures.

Risk reduction of the occurrence of defects in casting structures and increasing of mechanical properties requires to refine the guidelines of casting technology and parameters of possible heat treatment, while maintaining an acceptable level of production costs.

In addition, in order to prevent complications that developed after damage of the dentures (damage of the teeth or choking), it is advisable to monitor the status of the denture by a visual evaluation at the time recommended by dentists (every 6 months). During such visits the doctor should assess the status of the prosthesis by sensible observation under a dentist microscope (available in a growing number of surgeries) or with the use of other optical instruments. Metal elements should be primarily subjected to assessment (for prevalence of scratch or microcracks – as the beginning of a fatigue fracture). The other neuralgic area are the edges of the dentures – also for the presence of the microcracks and any damage leading within a short period of time to fatigue failure and the loss of functionality of the prosthesis.
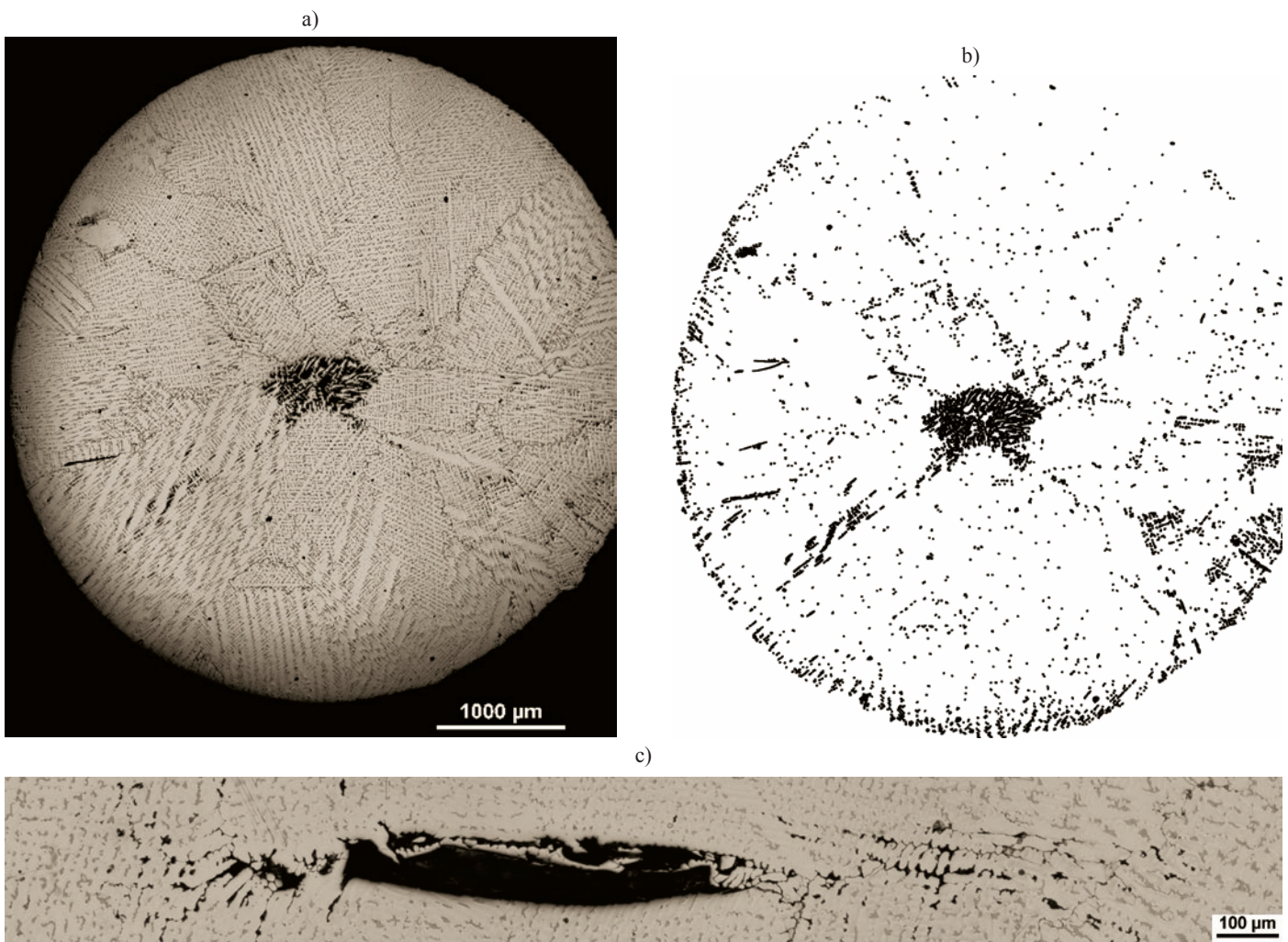

Fig. 7. a) A microstructure of selected element from Fig. 6, b) objects mask (shrinkages), c) longitudinal failures in a longitudinal section of a selected element

References

1. Anusavice KJ. Phillips' Science of Dental Materials. Philadelphia 2006; 11th ed. W.B. Saunders: 621–654.
2. Barclay CW, Walmsley AD. Fixed and Removable Prosthodontics. Churchill Livingstone, London 2001; 2nd ed.
3. Beer K, Walczak M. Structure and mechanical properties of modified CoCrMo alloys for use in dental prosthetics. Engineering of Biomaterials. 2011; 106–108: 110–115.
4. Giacchi JV, Morando CN, Fornaro O, Palacio HA. Microstructural characterization of as-cast biocompatible Co–Cr–Mo alloys, Materials Characterization. Vol. 2011; 62: 53–61.
5. Giacomelli, F.C., Giacomelli, C., Spinelli, A.: Behavior of Co–Cr–Mo biomaterial in simulated body fluid solutions studied by electrochemical and surface analysis techniques. J. Braz. Chem. Soc. 2004; 15 (4): 541–547.
6. Grądzka-Dahlke M, Dąbrowski JR, Dąbrowski B. Modification of mechanical properties of sintered implant materials on the base of Co–Cr–Mo alloy. Journal of Materials Processing Technology. 2008; 204: 199–205.
7. Henriques B, Soares D. Silva FS. Microstructure, hardness, corrosion resistance and porcelain shear bond strength comparison between cast and hot pressed CoCrMo alloy for metal-ceramic dental restorations. Journal of the mechanical behavior of biomedical materials. 2012; 83–92.
8. Herrera M, Espinoza A, Méndez J, Castro M, López J, Rendón J. Effect of C content on the mechanical properties of solution treated as-cast ASTM F75 alloys. J Mater Sci Mater Med 2005; 16:607–11.
9. Matković T, Matković P, Malina J. Effects of Ni and Mo on the microstructure and some other properties of Co-Cr dental alloys. Journal of Alloys and Compounds. 2004; 366: 293–297.
10. McCabe, JF, Walls AWG. Applied Dental Materials. 2008; 9th ed. Blackweell Publishing: 71.
11. Metikoš-Hukovi´c, M, Babi´c, R. Passivation and corrosion behaviors of cobalt and cobalt chromium–molybdenum. Corrosion. Science. 2007; 49: 3570–3579.
12. Mineta AS, Namba S, Yoneda T, Ueda, Narushima T. Precipitates in As-Cast and Heat-Treated ASTM F75 Co-Cr-Mo-C Alloys Containing Si and/or Mn. Metallurgical and Materials Transactions A. 2011; 42A: 1941–1949.
13. Montero OC, Talavera M, Lopez H. Effect of alloy preheating on the mechanical properties of as-cast CoCrMoC alloys. Metallurgical and Materials Transactions A 1999; 30: 611–620.
14. O'Sullivan ST, McGreal GT, Reardon CM. Hehir DJ, Kirwan WO, Brady MP. Selective endoscopy in management of ingested foreign bodies of the upper gastrointestinal tract is it safe? Int. J. Clin. Pract. 1997; 5: 289–292.
15. Roberts HW, Berzins, DW, Moore BK, Charlton DG. Metal–ceramic alloys in dentistry: a review. Jourrnal of Prosthodontics. 2009; 18: 188–194.
16. Velasco Suarez M, Nisa Gutierrez E, Asteinza Daganzo M, Ramírez Armengol JA. Incidence of foreign bodies in endoscopic emergencies. Rev. Esp. Enferm. Dig. 1992; 2: 91–94.
17. Velitchkov NG, Grigorov GI, Losanoff JE, Kjossev KT. Ingested foreign bodies of the gastrointestinal tract retrospective analysis of 542 cases. World J. Surg. 1996; 8: 1001–1005.
18. Walczak M, Beer K, Surowska B, Borowicz J. The issue of using remelted CoCrMo alloys in dental prosthetics. Archives of Civil and Mechanical Engineering. 2012; 12: 171–177.
19. Weiland ST, Schurr MJ. Conservative management of ingested foreign bodies. J. Gastrointest. Surg. 2002; 3: 496–500.
20. www.bego.com/ – Website of Bego Company; 13 December 2012

Karolina BEER, M.Sc. (Eng.)
Krzysztof PAŁKA, Ph.D. (Eng.)
Prof. Barbara SUROWSKA, Ph.D., D.Sc. (Eng.)
Mariusz WALCZAK, Ph.D. (Eng.)

Department of Materials Engineering
Faculty of Mechanical Engineering; Lublin University of Technology
ul. Nadbystrzycka 36; 20-618 Lublin
e-mails: k.beer@pollub.pl, k.palka@pollub.pl, b.surowska@pollub.pl,
m.walczak@pollub.pl

Tomasz ŁUSIAK

THE EXPERIMENTAL AND NUMERICAL ANALYSIS OF HELICOPTER PERFORMANCE IN URBAN AREAS AND IN SAR OPERATIONS

ANALIZA EKSPERYMENTALNA ORAZ NUMERYCZNA EKSPLOATACJI ŚMIGŁOWCÓW W AGLOMERACJACH MIEJSKICH ORAZ W AKCJACH RATOWNICZYCH*

The paper discusses the methods of experimental and numerical analysis of helicopter performance in urban areas and search and rescue operations. The phenomenon of aerodynamic interference between the helicopter and the object located in its immediate vicinity was examined. The main focus was on the impact of interference on helicopter loading, airflow around the helicopter and helicopter properties in these specific cases. The paper provides a set of research results using the FLUENT software on the dynamic response to the disturbed simulation model of the helicopter rotor including the deformation of helicopter blades as well as the results of laboratory research on physical helicopter models.

Keywords: *numerical modeling, helicopter, aerodynamic interference, maintenance in town.*

Praca przedstawia sposoby analizy eksperymentalnej oraz numerycznej użytkowania śmigłowca w aglomeracjach miejskich oraz akcjach ratowniczych. Rozpatrzono zjawisko interferencji aerodynamicznej pomiędzy śmigłowcem a obiektem znajdującym się w jego bezpośredniej bliskości. Analizie poddano wpływ zjawiska interferencji na obciążenia, opływ i własności śmigłowca w szczególnych przypadkach jego użytkowania. Przedstawiono wyniki obliczeń wykorzystujących program FLUENT, odpowiedzi dynamicznych na zaburzenia symulacyjnego modelu wirnika śmigłowca uwzględniającego deformacje łopat oraz rezultaty laboratoryjnych badań eksperymentalnych na modelach fizycznych śmigłowca.

Słowa kluczowe: *modelowanie numeryczne, śmigłowiec, interferencja aerodynamiczna, użytkowanie w mieście.*

1. Introduction

Typically, helicopters are capable of major aircraft maneuvers like take-off, landing, vertical ascending and descending with no cruising speed. Hence, helicopters are often used for special tasks and operations such as high-altitude rescue, military operations, mountain rescue, and other air operations in urban areas with tall buildings. Such incidents occur during high-altitude rescue around multi-storey buildings, at heliports as well as during mountain and medical rescue (Tatrzańskie Ochotnicze Pogotowie Ratunkowe (TOPR) - Tatra Volunteer Search and Rescue, Lotnicze Pogotowie Ratunkowe (LPR) - Air Emergency Medical Services). Similar incidents can happen when crane operating, military operations in cities and helicopter operations by media workers and the police to control cities. The use of helicopters in urban areas results in aerodynamic interference of the helicopter - object airflow [6, 7, 8]. Consequently, the pilot needs to be attentive if this phenomenon occurs during flight, particularly if there is turbulence due to wind flow around buildings and convection due to a temperature discrepancy between buildings and the ground, e.g. local areas of fire [10, 11]. Interference at a lee side of a building during special operations is regarded as one of the most dangerous helicopter - object interference incidents.

These incidents are intensively studied in the global leading helicopter centers, which is supported by a rapidly improved computing capacity, special software to visualise complex helicopter flow disturbance fields and improved computational methods. This theoretical examination is verified by wind-tunnel and flight experimental studies. As this subject develops fast, the latest accomplishments can be found only in conference proceedings, mostly of the American Helicopter Society Annual Forum and Technology Display (e.g. [1, 2, 3]) or the European Rotorcraft Forum. Although books and papers published in principal journals provide basic methodological knowledge, they are significantly behind the rapidly developing applications mentioned in the above conference proceedings.

2. Numerical analysing urban-area helicopter operation study cases

Numerical calculations refer to the assumed pressure distribution in the rotor. The airflow including objects in its close proximity was calculated with the FLUENT software [4]. The determined velocity field of airflow across the rotor plane enabled the characteristics of the basic parameters of load (developed at the Institute of Aviation, the OBCWN software was modified to analyse aerodynamic interference). This new airflow across the rotor blade enabled rotor load parameters and a new rotor surface pressure distribution. This new pressure distribution was introduced to correct and re-calculate airflow around a helicopter using the FLUENT. Iteration was carried out until the values obtained were convergent. To accelerate the convergence, a velocity field of the arithmetic average of the field from the previous and current iterations was entered into the next iteration. Such an approach was necessary for a highly flexible blade due to its significant sensitivity to the disorder and its response as a function of twisting the blade. Consequently, a satisfactory convergence of the calculations was already achieved in the second calculation step.

Figure 1 shows a helicopter model developed on the real geometry of helicopter W3-A SOKÓŁ. This geometry employs triangular and quadrilateral cells, and the size of the divisions was specified at the edges of the surface or adopted a constant length of element edges.
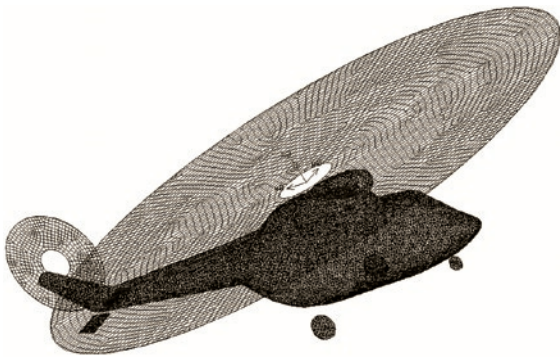

Fig. 1. *Helicopter calculating grid (non-structural – triangular cells in the fuselage (edge is 0.05m), quadrilateral cells in the master and tail rotors (edge is 0.2m))*

Figure 2 shows the distribution of measurement points generated by the FLUENT input file. File Journal is a list of commands to be entered manually using a graphical environment. The input file speeds and automates the creation of measurement points.

Vertical velocity values at the measurement points were collected in a table applied later as a source of information about the rotor induced speed in special software to calculate strength.
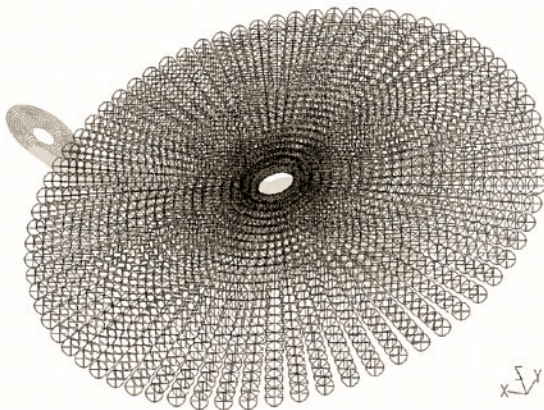

Fig. 2. *Schematic of the arrangement of measurement points on the rotor*

In addition, the calculations are based on the following assumptions: unsteady airflow calculations; helicopter free movement was simulated and modeled using a static mesh; calculations were done for compressible and viscous fluids; and a k-ε turbulence model was applied [5, 9]. The parameter distributions for the rotor model were defined by means of the velocity profiles developed (Fig. 3).

The strength calculation resulted in the table to provide the changes in rotor pressure distribution. This distribution can be used to define a real initial condition for a rotor pitch pressure model. It was entered by means of the profile file compatible with the previously measurement point distribution.

2.1. Numerical calculation results

One of the methods of numerical analysis of aerodynamic interference between the helicopter and the object located in its immediate vicinity was examined. The impact of interference on helicopter aerodynamic load, flow and properties in specific use was studied. The results of FLUENT calculations, dynamic response to the simulated disturbed rotor model including the deformation of helicopter rotor blades and the results of laboratory experimental tests on aircraft physical models are provided in this paper. Figure 4 shows this method of analysing the phenomenon, depicting the method of analysis of aerodynamic interference if helicopters are used in urban areas or for rescue. This method was applied to analyse the use of the helicopter in hover for the cases in Figure 5 –7.

Several characteristics and values were determined for the cases depicted in Figure 5 – 7. The most reliable parameters to prove aerodynamic interference are the values of power needed to manoeuvre and torque coefficient as in Table 2.1.

The values in Table. 2.1 confirm the growing demand for power to be delivered to the rotor to hover in the vicinity of the well object relative to other cases.

Table 2.1. *Thrust and power in low hover*

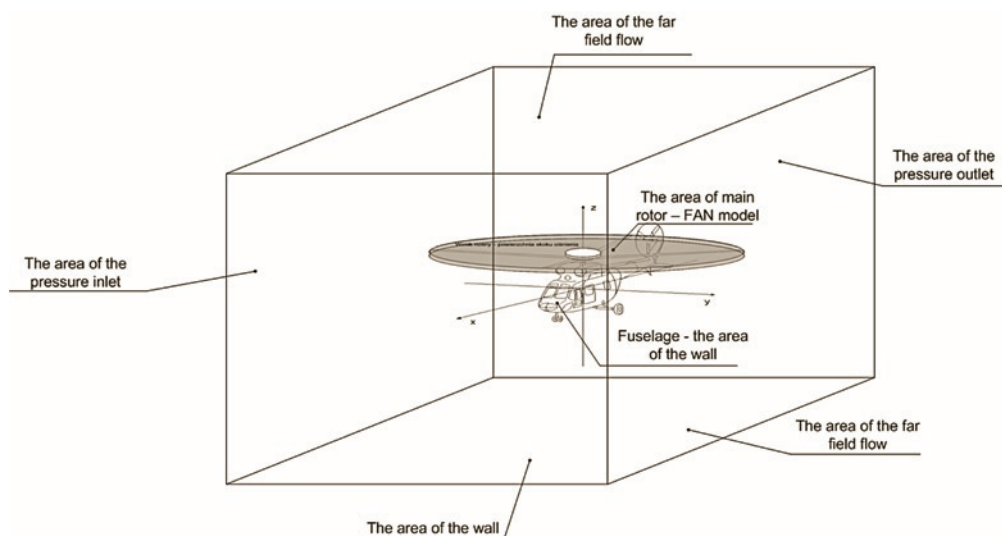| Case	Thrust - N	Power - kW	Cz	Cmz
Fig. A	61000	913.26	0.1632	0.01163
Fig. B	61000	810.48	0.1632	0.0103
Fig. C	61000	619.51	0.1632	0.0079

Fig. 3. *Geometric assumptions for the calculation model and structure of the airflow area*
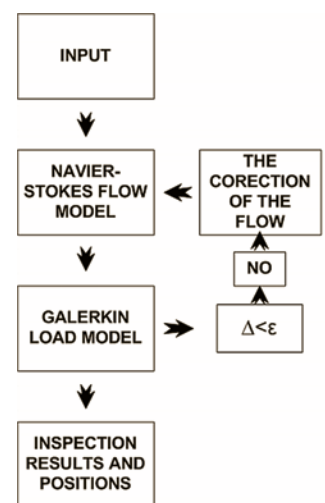

Fig. 4. *Diagram with one of the methods used to deal with aerodynamic interference*
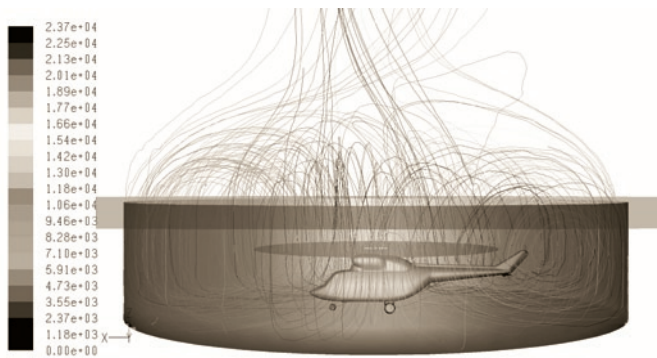
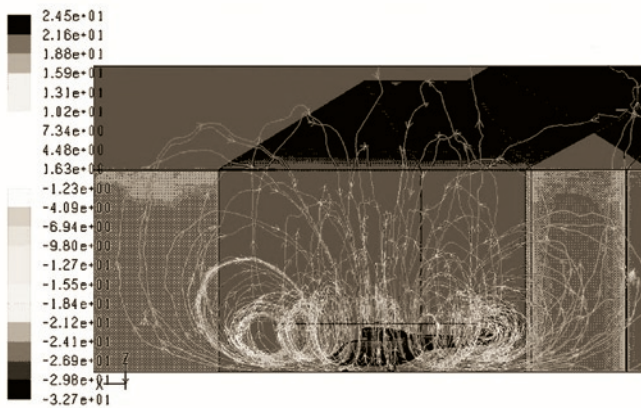Fig. 5. Streamline distribution in hover in the well object

Fig. 6.   Streamline distribution in hover in object "Royal Castle in Warsaw"
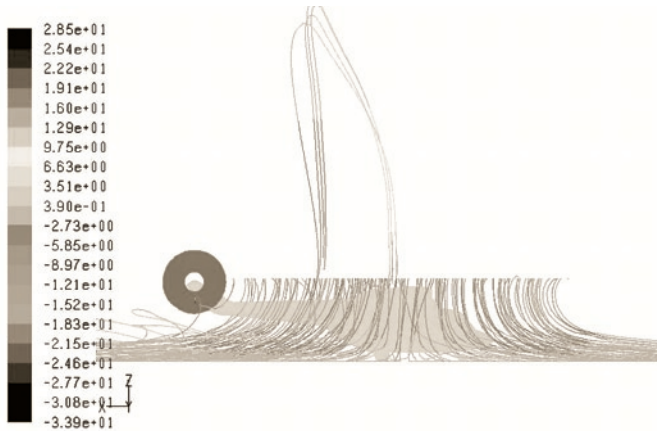

Fig. 7. Streamline distribution in hover with no nearby objects

Rotor-hull interference including the impact of the near ground was examined (Fig. 8). A Navier and Stokes model was applied to calculate airflow for three cases of hover by helicopter W3 - SOKÓŁ (Fig. 9): 1 – hover with the landing gear (wheels) very close to the ground, 2 – hover at the height of the landing gear 16 m above the ground, and 3 – hover at 32 m above the ground.
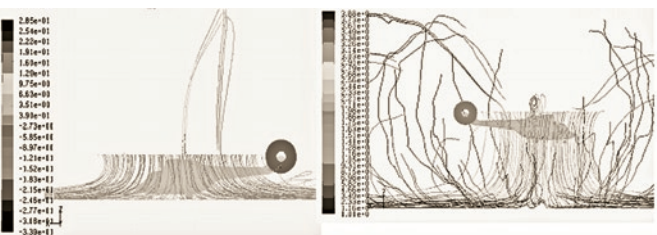

Fig. 8.   Streamlines: a – hover, the landing gear in contact with the surface, b – hover, the landing gear at 16m

For the calculation of the charges for the analysis of interference phenomena and blade uses OBCWN program calculates the load on the rotor of the helicopter carrier with the ability to podczytywania any field disturbance in the speed box, speed disturbed fuselage in the vicinity of the substrate. The results of the analyses are illustrated in Figure 1. 9.

On the basis of the analysis, it was found the impact of proximity to Earth on the parameters characterizing accident carrier rotor helicopter. A significant impact was noted the presence of ground motion
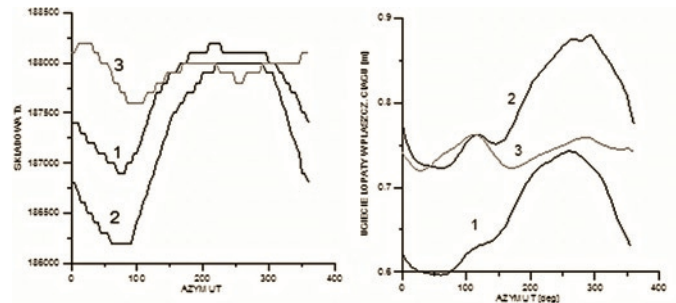

Fig. 9.   The impact of the hull and on the ground: a-horizontal component of the Tx, b-swing shovel

and dynamics of loads asymmetry caller blades even in this State, which is zawis. In perfect for insulated, rotor zawisie notes to significant changes to the parameters of its work.

3. Experimental analysis of helicopters' exploitation cases in urban agglomerations

In order perform a verification of some of the results of computer simulation of interference phenomena taking place during the helicopter's operation in the urban area experimental studies corresponding to the cases analyzed numerically (Fig. 10) were carried out.

Fig. 10. The structure of the behind-rotor stream during experimental tests on the real helicopter W3-A FALCON

During a low hovering flight maneuver of the helicopter performed close to the ground at insufficient excess of the engine power an acceleration of the craft is possible. This may be realized by the use of kinetic energy of the carrying-rotors' inert system, in order to overcome the area, where the drive's required power is greater, than the disposable one. The result is a decrease of the carrying-rotor's speed. The limit condition of the permissible ratio of the rotor's kinetic energy utilization is non-crossing of the speed limit due to a possibility of the rotor blades' streams detachment. The possibility of reducing the minimal excess of the starting power by using the above

mentioned take-off technique strongly increases the helicopter's usability. Namely, an operational payload increases, as well as the starting ceiling at a given load. Fig. 11 shows a schematic diagram of the distribution of forces acting on the helicopter during the maneuver of the low hovering flight.

Fig. 11. Schematic diagram of the distribution of forces acting on the helicopter during the low hovering flight

Fig. 12 shows a comparative analysis of the Effective Translation Lift (ETL) phenomenon (instantaneous power demand growth necessary during the spin-on-the-fly low to the ground) obtained by a numerical analysis and compared with the results obtained from the experimental tests carried out on the real object W3-FALCON [11].

Interference analysis of rotor-induced flow with a horizontal influx of the stream and the method used for the determination of the temporary power demand (ETL) phenomenon influence on the helicopter's load allows to specify the effective loads, as well as the required power during the spin-up maneuver. This analysis may be useful in a preparation of the special take-off techniques of helicopters at their limit operational use.

4. Conclusions

The conclusions coming out from the study of the phenomenon of interference can be useful in the process of operational use of helicopters among buildings on heliports, particularly with regard to the assessment of dangerous zones due to the presence of an intense aerodynamic interference. This also applies to the use of marine helicopters based on the helidecks (ships' boards or drilling platforms'
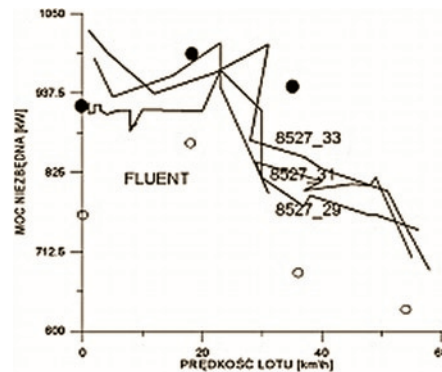

Fig. 12. The necessary power change along with the airspeed increase. Solid lines: the subsequent flight tests with a sample number; the indication of the results of the calculations of the FLUENT software: "o" is a helicopter without a draft, "•"- a helicopter with draft (adding power to accelerate and the "air bag" escape along with the tilt and the speed of flight increase)

aerodromes). The usefulness of such knowledge also applies to the designers of the air strips located on the roofs of tall buildings. Investigations were carried out due to the occurrence of operational problems encountered by the users such as the State Fire Department (SFD) and the Polish Air Ambulance Service (PAAS) during the relief operations carried out by these services in towns and due to the fact of building the elevated helipads for sanitary helicopters.

On the basis of the performed numerical and experimental studies of the aerodynamic interference of the helicopter's flow around a conclusion comes out, that the pilot and other users should be warned against the situations, when the vicinity of an obstruction causes danger and that the minimal separation areas should be specified, for which the interference phenomenon between the helicopter and the other object may trouble the operational task.

References

1. Dietz M, Kneisch T, Roth G, D'Alascio A, Schimke D. EC145 T2: Comprehensive and Challenging Industrial CFD Applications. Proceedings of the 68th AHS Annual Forum. Texas, May 2012.
2. Haycock B, Grant P. Off-Axis Dynamics and Simulator Fidelity, Proceedings of the 68th AHS Annual Forum, Fort Worth, Texas, May 2012.
3. He Ch, Zhao J. High Fidelity Simulation of Tiltrotor Aerodynamic Interference. Proceedings of the 68th AHS Annual Forum, Texas, May 2012.
4. Introductory Fluent Notes. Introduction to CFD Analysis. Introductory FLUENT Training, ANSYS.INC, 2006.
5. Katz J, Plotkin A. Low-speed aerodynamics. From Wing Theory to Panel Method. International Edition, 1991.
6. Łusiak T, Dziubiński A, Szumański K. Interference between helicopter and its surroundings, experimental and numerical analysis. TASK QURTAERLY 2008; 13(4): 379–392.
7. Łusiak T. Szczególne przypadki interferencji aerodynamicznej opływu śmigłowca. PrzeglądMechaniczny; Maj 2007; 86-88.
8. Łusiak T, Dziubiński A, Specific case of interference between a helicopter and surrounding: hover flight over a well-shaped object. Transactions of the Institute of Aviation 2007; 191: 43–50.
9. Piechna J, Szumowski A. Numerical Simulation of the Vortex Airfoil Interaction in Transonic Flow, Second Seminar on RDPAE 1996: 29–34.
10. Szabelski K, Łucjanek W, Jancelewicz B. Wstęp do konstrukcji śmigłowców. Warszawa: Wydawnictwo Komunikacji i Łączności, 2002.
11. Wyd. Wew. ILot Nr GR/0032/BP/2009, Projekt badawczo-rozwojowy Nr R 00 033 02 pt.: Określenie granicznych warunków użytkowania śmigłowców w systemie operacji z wysokich budynków.

Tomasz ŁUSIAK, Ph.D. (Eng.)
Department of Thermodynamics, Fluid Mechanics and Aviation Propulsion Systems
Mechanical Engineering Faculty
Lublin University of Technology
ul. Nadbystrzycka 36, 20-618 Lublin, Poland
e-mail: t.lusiak@pollub.pl

Konrad KOWALIK
Barbara SYKUT
Halina MARCZAK
Marek OPIELAK

A METHOD OF EVALUATING ENERGY CONSUMPTION OF THE CUTTING PROCESS BASED ON THE EXAMPLE OF HARD CHEESE

METODA BADANIA ENERGOCHŁONNOŚCI PROCESU CIĘCIA NA PRZYKŁADZIE SERA ŻÓŁTEGO*

The article demonstrates a method of measuring energy requirements of a cutting process as researched at the Department of Process Engineering, Safety and Ecotechnology. The specially constructed workstation and examples of results obtained are presented. The cutting process has been conducted using stainless steel and low-friction coated blades with each blade's entry conditions variables, such as speed and the angle of entry, determined. In order to compare cutting resistance caused by friction between the blades' surface and the cut substance, wire cutting has also been performed.

Keywords: cutting, slicing, energy consumption, blade angle, speed, coating.

W artykule przedstawiono metodę badania energochłonności procesu cięcia opracowaną w Zakładzie Inżynierii Procesowej, Bezpieczeństwa i Ekologii. Zaprezentowano skonstruowane stanowisko badawcze oraz przykładowe wyniki badań wykonane z wykorzystaniem tego stanowiska. Proces cięcia prowadzono nożami ze stali narzędziowej oraz pokrytymi powłokami charakteryzującymi się małym współczynnikiem tarcia, przyjmując w planie badań dla każdego noża zmienne wejściowe: kąt ostrza oraz prędkość cięcia. Aby porównać opory cięcia wynikające z tarcia materiału o powierzchnię noża przeprowadzono także cięcie materiału drutem.

Słowa kluczowe: cięcie, energochłonność, kąt ostrza, prędkość, powłoka.

1. Introduction

One of many types of processes of industrial technology are comminution processes. They are associated with high energy consumption. One of the most frequently employed is cutting to specific size and shape. Desired shapes are dictated by available technogy, usability, and, for produce, organoleptic effect.

The main factor that affects the cutting process and its energy consumption is the firmness of the material which is related to its composition, internal structure, and, in agriculture or food processing, particular produce type, variety, sample origins, place or conditions of production [6, 7, 8, 9]. In case of raw materials for food production, conditions and type of thermal processing (boiling, blanching, drying, microwaving) [13, 14] are also of significant importance.

There are also other factors influencing efficiency and energy consumption of the cutting process; they are related to the construction and use of a particular device, including the shape and kinematic-dynamic parameters of the cutting element. Until the present time, many researchers working on the cutting process have focused on improving the design of the cutting device, analysis of the blade parameters and their role in the process [2, 3, 5, 12].

Energy consumption of the cutting process is higly correlated with friction between the cutting tool and the cut substance. In slicing or cutting to size, friction depends on the physical properties and the type of material used to manufacture the blade and specific characteristics of the surface coming into contact with the substance being worked upon [1].

Some food items (e.g. hard cheese) are characterised by a high friction factor. Lowering of this undesirable friction during cutting can be achieved by, e.g., raising the blades temperature or reducing the surface of the cutting blade coming into contact with the produce being cut (e.g. wire cutting) [4, 10, 11].

A review of literature related to energy consumption of the cutting process showed that most studies have been done with the use of high durability machinery and speed maintenance in quasi-static conditions. Measuring systems at testing stations described in scientific literature, usually enable measuring of applied force in only one direction, parallel to the direction of the main motion, which, in some conditions, does not allow for a full analysis of the full range of forces that are significant for the whole process [3, 4, 5, 10, 11, 13, 14].

The above limitations prompted us to create our own method and a workstation for reaserching energy consumption of the cutting process.

2. The Goal

The purpose of our research was to use the new method in evaluation of the effect that particular tools have on energy consumption in the cutting process.

3. Reaserch Methodology

3.1. The Workstation

"Cutting Resistance Reaserch Workstation" has been designed and constructed in the Department of Process Engineering, Safety and Ecology at the Mechanical Engineering Faculty of the Lublin Univer-

sity of Technology. A patent application has been filed and the design is protected under applicable intellectual property and industrial design laws of the Republic of Poland.

One of the distinguishing qualities of this design is the capacity to register, at the same time, forces acting in two perpendicular directions: parallel and perpendicular to the direction of the main force. A schematic of the workstation's layout is presented in Fig. 1.
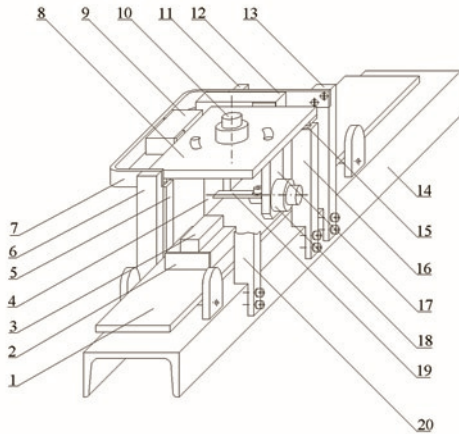

Fig. 1. Layout schematic: 1 – steel beam, 2 – grip, 3 – cut sample, 4, 5, 6 – posts, 7 – outside band, 8 – measuring plate, 9 – induction sensor, 10 – knife position control dial, 11 – post, 12 – induction sensor, 13 – post, 14 – base, 15 – ball bearings, 16 – post, 17 – mount, 18 – knife position control dial, 19 – knife, 20 – post

Workstation's layout presented in drawing 1 shows the horizontal base (14), on which steel beam 1 moves lengthwise. Grip 2 for the cut sample is positioned on the beam. The beam is powered by hydrolic pressure. Mount 17 is attached below the rectangular measuring plate (8) and it holds the knife (19) with the knife position control dial (18). Plate 8 with the knife position control dial 10 moves on ball bearings (15), which are on top end of vertical posts 4, 5, 16, and 20. Induction sensors 9 and 10 that measure forces acting in two mutually perpendicular directions, are fastened to the outside band (7), which is mounted on posts 6, 11 and 13. Information from the sensors, via electronic measuring devices and the data card is passed on to a computer with a 'Testing' application installed. This application has been created to kontrol the input from the installed data card and enables reception of signals, their processing, visualisation and storage.

The workstation makes it possible to change the cutting knife which enables evaluation of any influence of blade geometry (blade angle, thickness, etc.). It is also possible to adjust the position of the knife, i.e. entry angle and the angle of the cutting edge. Sample grip 2 is replaceable and can be chosen according to any requirements related to the properties od the sample to be cut (shape, size or method of cutting).

Another important feature of the workstation is the possibility of performing the process at higher speeds than the quasi-static that can be achieved while employing a high durability machine, Intron, most commonly used by reaserchers in this field). At the present time the range is 50–450 mm·s⁻¹. The workstation is equipped with a photo-optical system that allows for controlling of the actual speed whille cutting the sample.

On the basis of data collected from the measuring system, and specifically the registered tracking of the cutting force, the value for slicing work may be arrived at from the following equation:

$$L = \int_S F \cdot ds = \sum_i F_i \cdot \Delta s \text{ , (J)} \tag{1}$$

where:

$\sum_i F_i$ – the sum of forces registered while cutting the sample (N),

Δs – distance that the sample travels betweet subsequent registered values of of the force in time (m).

Unitary energy consumption of the cutting process defined as work needed in order to slice through a unit of surface area of the sample is calculated from the following:

$$e_j = \frac{L}{A} \quad , \quad \left(J \cdot m^{-2} \right) \tag{2}$$

where:

L – slicing work (J),
A – surface area of the sample that has been cut (m²).

3.2. Tools and Materials

During the energy consumption research, as the material subjected to the cutting process we have used hard cheese 'Podlaski' from OSM Wloszczowa (the producer). This produce is characterised by uniform structure and fat content of 45% in dry matter. Slices of 10 mm were cut off the top surface of cuboid samples of the cheese (Fig. 2).
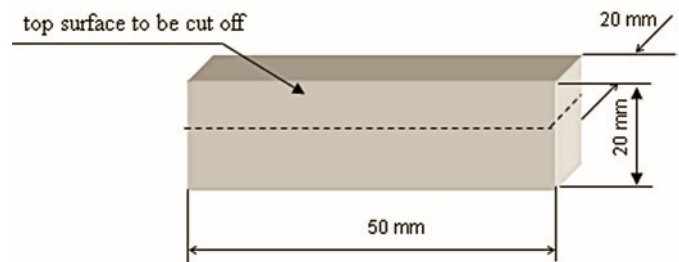

Fig. 2. Cheese samples' dimensions

Flat knives, 1.5 mm thick, 27 mm in length and 70 mm wide have been used. In order to obtain a plane graph based on 'Statistica' package we had to use a set of knifes with blade angles varying from 5° to 45°. The cut was a regular slice. The angle between the cutting edge and the direction of the cut 90°. The clearance angle was 0°.

In order to lower friction and, as a result, the energy consumption, the cutting proces was performed employing knives coated with TiN (Titanium-Nitrogen) and AS48 (trade name of fluoropolymer coating produced by 'PFP Polska'). Basic testing was done with steel knives intended for cold cutting (NC6). The knives used are shown in Fig. 3.

Additionally, we have performed test cutting with chrome-molybdenum steel wire with 0.3 mm diameter. This choice has been made based on initial research and literature.

All the cutting has been done in the same reasearch plane with entry values (independent variables): β – knife blade angle, V – cutting speed, and exit values (dependent variables): directly determined: F – cutting force, indirectly determined: e_j – unitary energy consumption of the cutting process. The value of energy consumption of the cutting, constituting a variable dependent on the model of research, has been

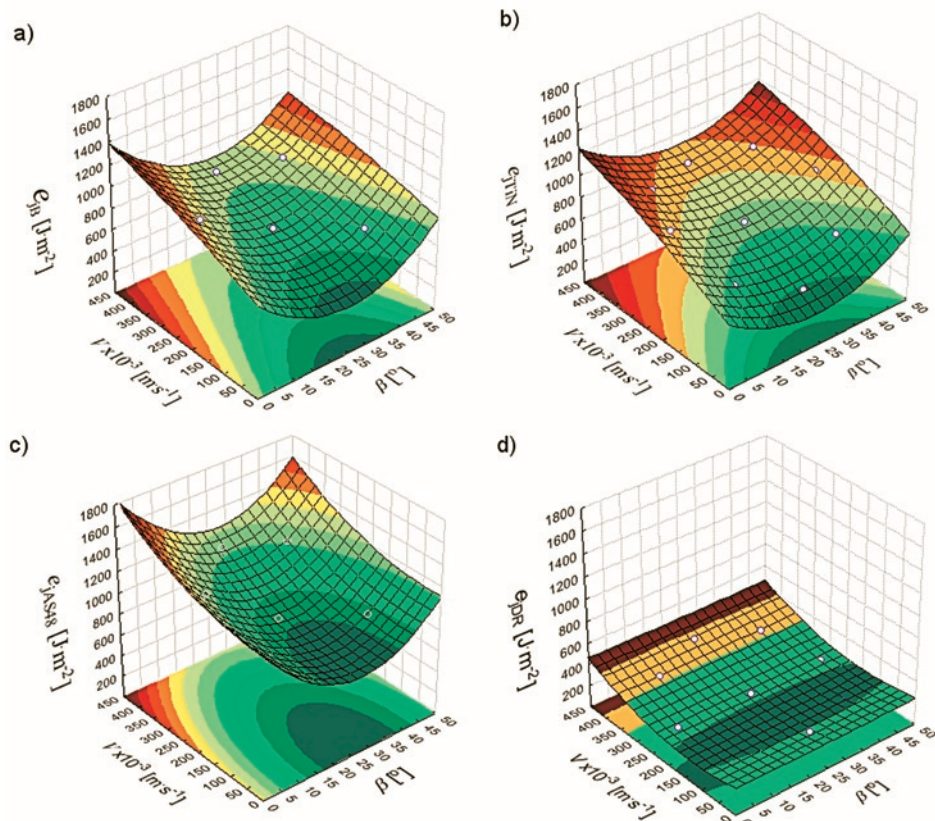*Fig. 3. Test knives: a) steel NC6, b) TiN coated, c) AS48 coated*

Fig. 4. Graphs presenting result planes for all cutting tools: a) steel NC6 knife, b) TiN coated knife, c) AS48 coated knife, d) wire

related to the unit of surface area of the cut substance. Thus, we have arrived at the unitary energy consumption of the cutting process.

A computerised image analysis workstation was employed in order to measure the surface area of the cut samples. Values of differences of energy efficiency of the cutting process while using steel NC6 as compered to energy efficiency of the cutting process while using other cutting tools has been calculated as follows:

$$R_{(X)} = \frac{\left(e_{jB} - e_{j(X)}\right)}{e_{jB}} \cdot 100, \quad (\%) \tag{3}$$

where:

Table 1. General format of the eperimental matrix

No.	Entry values X_i			
	Coded matrix		Physical form	
	X_1	X_2	β [°]	$V \times 10^{-3}$ [m·s^{-1}]
1.	$-\alpha$	0	5.0	225.0
2.	1	1	39.1	348.7
3.	$+\alpha$	0	45.0	225.0
4.	-1	1	10.9	348.7
5.	0	0	25.0	225.0
6.	-1	-1	10.9	101.3
7.	0	$+\alpha$	25.0	400.0
8.	0	0	25.0	225.0
9.	1	-1	39.1	101.3
10.	0	$-\alpha$	25.0	50.0

e_{jB} – unitary energy consumption of the cutting process with a steel NC6 knife (J·m^{-2}),
$e_{j(X)}$ – unitary energy consumption of the cutting process with other cutting tools (J·m^{-2}).

Relevance of the calculated differences was tested with the Student t-test for independent testing.

4. Test results and analysis

For plane graphs of the experimental research we used the module *Planowanie Doświadczeń* of *Statistica 9.0 PL* software package. Central-compositional plane for a standard rotary-uniform plane with two independent variables was accepted. The general format of the eperimental matrix adopted for the research plane in a normalised (coded) and physical form is shown in table 1.

The presented values of cutting speed V also constituted the independent variable for the single-factor regression analysis while cutting with wire.

The mathematical model of the cutting process has a basic formula shown in the following equation (4):

$$Y = b_0 + b_1x_1 + b_2x_2 + b_{12}x_1x_2 + b_{11}x_1^2 + b_{22}x_2^2 \tag{4}$$

Values of unitary energy consumption of the cutting process and differences resulting from cutting with various cutting tools are shown in table 2. Cases for which the calculated differences are statistically relevant, assuming the relevance of $\alpha=0.05$, are highlighted in gray.

Best results understood as lowered energy consumption are highest for the wire cutting technique. Differences in energy consumption vary from 54.1% to 80.3%. Best results were achieved while cutting with the speed of 0.225 m·s^{-1}, and worst for 0.050 m·s^{-1}.

Slicing cheese with a TiN coated knife lowered the unitary energy consumption in all points of the test up to the value of 21.1%. Differ-

Table 2. Values of unitary energy consumption of the cutting process and differences resulting from cutting with various cutting tools

β [°]	$V \times 10^{-3}$ [m·s⁻¹]	e_{jB} [J·m⁻²]	e_{jTiN} [J·m⁻²]	R_{TiN} [%]	e_{jAS48} [J·m⁻²]	R_{AS48} [%]	e_{jDR} [J·m⁻²]	R_{DR} [%]
10.9	101.3	664.4	543.3	18.2	923.2	-38.9	183.5	72.4
25.0	50.0	485.3	390.5	19.5	684.5	-41.0	222.6	54.1
25.0	400.0	868.6	848.6	2.3	1164.1	-34.0	355.1	59.1
10.9	348.7	911.5	897.6	1.5	1156.6	-26.9	331.4	63.6
5.0	225.0	1064.1	878.2	17.5	1341.0	-26.0	209.3	80.3
39.1	348.7	904.9	894.8	1.1	1125.7	-24.4	331.4	63.4
45.0	225.0	867.4	838.4	3.3	987.5	-13.8	209.3	75.9
25.0	225.0	688.4	660.9	3.9	833.5	-21.1	209.3	69.6
39.1	101.3	724.6	571.8	21.1	908.0	-25.3	183.5	74.7
25.0	225.0	688.4	660.9	3.9	833.5	-21.1	209.3	69.6

ences approaching this value were reached in four points accross the plane of the research. The biggest difference values appeared for the lowest values of cutting speeds.

Cutting with the knife coated with AS48, caused an increase in unitary energy consumption in comparison to the steel NC6 knife. The lowest variation of unitary energy consumption of the cutting process was observed at the speed of 0.225 m·s⁻¹. Result planes for all cutting tools are shown in Fig. 4.

All result planes, except the wire cutting (d) conducted for just one variable V, share many similarities. Regression equation describing the wire cutting of cheese shows a polynomial of the second degree (8). For the tested values of the independent variable V, the lowest value of the energy consumption process appeared at the cutting speed of 0.1013 m·s⁻¹.

Established regression equations describing relationships among the variables are:

• for the process performed with steel NC6 knives:
$e_{jB} = 846.35769 - 33.26005 \cdot \beta + 0.66846 \cdot \beta^2 + 1.53258 \cdot V - 0.000699 \cdot V^2 - 0.00955 \cdot \beta V$; $R^2 = 0.93485$ (5)

• for the process performed with TiN coated knives :
$e_{jTiN} = 583.33605 - 23.87759 \cdot \beta + 0.49226 \cdot \beta^2 + 1918.20684 \cdot V - 1039.86427 \cdot V^2 - 4.46894 \cdot \beta V$; $R^2 = 0.99632$ (6)

• for the process performed with AS48 coated knives:
$e_{jAS48} = 1326.18205 - 44.67264 \cdot \beta + 0.80701 \cdot \beta^2 - 20.323399 \cdot V + 2705.00281 \cdot V^2 - 2.24283 \cdot \beta V$; $R^2 = 0.9073$ (7)

• for the process performed with wire:
$e_{jDR} = 237.2352 - 715.031 \cdot V + 2673.851 \cdot V^2$; $R^2 = 0.9594$ (8)

5. Conclusions

An analysis of the results allowed us to arrive at the following conclusions:

1. Experimental research confirmed suitability of the proposed research method for analyses addressing energy consumption of the cutting process.
2. Experimental research confirmed the existence of statistically significant differences in energy consumption of the cutting process while using a steel NC6 knife and knives coated with TiN or AS48. In the assumed research plane, in case of cutting with TiN, the differences in energy consumption approached statistically relevant values reaching 21.1%. These were points corresponding to the lowest cutting speeds of the assumed plane of research. Energy consumption differences observed while cutting with AS48 coated knife appear to be statistically relevant in all points of the researched plane. However, this is the result of the increased energy consumption of the process.
3. Experimental research indicated that the wire cutting unitary energy consumption of the process significantly differs from the unitary energy consumption of the steel NC6 cutting process , with the results ranging from 54.1% to 80.3%.
4. With the exception of the wire, the characteristics of changes in the unitary energy consumption were similar. It increased with the speed applied. It was minimal for blade angle of 25°.
5. Mathematical models of relationships between the energy consumption and entry values for the presented cutting techniques could provide a tool for technicians and designers in efforts of controlling and directing the cutting process with the highest energy efficiency.

References

1. Dowgiałło A. Doświadczalna weryfikacji teorii mikroostrzy. Postępy Techniki Przetwórstwa Spożywczego 2002; 2: 15–17.
2. Flizikowski J, Bieliński K, Bieliński M. Podwyższanie energetycznej efektywności wielotarczowego rozdrabniania nasion zbóż na paszę. Wyd. ATR – OPO, Bydgoszcz 1994.
3. Goh SM, Charalambides MN, Williams JG. On the mechanics of wire cutting of cheese. Engineering Fracture Mechanics 2005; 72: 931–946.
4. Kamyab I, Chakrabarti S, Williams JG. Cutting cheese with wire. Journal of Materials Science 1998; 33: 2763–2770.
5. Nadulski R, Wawryniuk P. Wpływ wybranych parametrów konstrukcyjnych zespołu tnącego na proces cięcia warzyw. Inżynieria Rolnicza 2003; 8: 297–305.
6. Opielak M. Rozdrabnianie materiałów w przemyśle rolno-spożywczym. Badanie wpływu konstrukcji rozdrabniacza i cech materiału rozdrabnianego na jakość i energochłonność procesu. Wyd. Politechniki Lubelskiej, Lublin 1996.
7. Opielak M. Analiza teorii procesu rozdrabniania materiałów w przemyśle rolno-spożywczym. Folia Societatis Scientiarum Lublinensis. Technika 1999; 8: 95–106.

8. Opielak M, Komsta H. Kierunki doskonalenia konstrukcji urządzeń rozdrabniających w przemyśle spożywczym. Zeszyty Naukowe Politechniki Opolskiej 2000; 61: 167–173.
9. Popko H, Miszczuk M. Badania oporów krajania niektórych produktów spożywczych. Zeszyty Problemowe Postępów Nauk Rolniczych 1989; z. 354: 147–151.
10. Schneider Y, Zahn S, Rohm H. Power requirements of the high-frequency generator in ultrasonic cutting of foods. Journal of Food Engineering 2008; 86: 61–67.
11. Schneider Y, Zahn S, Schindler C, Rohm H. Ultrasonic excitation affect friction interactions between food materials and cutting tools. Ultrasonic 2009; 49: 588–593.
12. Sykut B, Kowalik K, Opielak M. Badanie wpływu kątów ostrza i przystawienia na opory krojenia produktów spożywczych. Inżynieria Rolnicza 2005; 9: 339–344.
13. Szarycz M, Fidos M, Jałoszyński K. Wpływ zakresu ciśnień podczas suszenia mikrofalowego pod obniżonym ciśnieniem selera korzeniowego na kinetykę procesu i pracę cięcia rehydrowanego materiału. Inżynieria Rolnicza 2006; 4: 239–246.
14. Ślaska-Grzywna B. Wpływ parametrów obróbki cieplnej selera na siłę cięcia. Inżynieria Rolnicza 2008; 6: 175–180.

Konrad KOWALIK, Ph.D. (Eng.)
Barbara SYKUT, Ph.D. (Eng.)
Halina MARCZAK, Ph.D. (Eng.)
Prof. Marek OPIELAK, Ph.D., D.Sc. (Eng.)

Department of Process Engineering, Safety and Ecology
Institute of Transport, Combustion Engines and Ecology
Mechanical Engineering Faculty
Lublin University of Technology
ul. Nadbystrzycka 36, 20-618 Lublin, Poland
e-mails: k.kowalik@pollub.pl; b.sykut@pollub.pl; h.marczak@pollub.pl, m.opielak@pollub.pl

Elżbieta JACNIACKA
Leszek SEMOTIUK

EXPERIMENTAL METHODS FOR DETERMINING UNCERTAINTY OF MEASUREMENT USING INSPECTION PROBES

DOŚWIADCZALNE METODY WYZNACZANIA NIEPEWNOŚCI POMIARU SONDAMI PRZEDMIOTOWYMI*

The paper presents the results of determining uncertainty of measurement using an inspection probe on numerically controlled vertical milling machines. To do the measurements, methods developed for coordinate measuring machines were employed. For the measurement system consisting of a vertical machining center FV-580A and OMP60 touch probe, the uncertainty of measurement was determined for the coordinates of the point, one-dimensional length measurement, two-dimensional length measurement, as well as for length measurement using multiple measurement strategies.

Keywords: *uncertainty of measurement, CNC machines, inspection probe.*

W pracy przedstawiono wyniki wyznaczania niepewności pomiaru sondą przedmiotową na frezarkach pionowych sterowanych numerycznie. Do pomiarów zaadaptowano metody opracowane dla współrzędnościowych maszyn pomiarowych. Dla systemu pomiarowego składającego się z centrum obróbkowego FV580A i sondy OMP 60 wyznaczono niepewność pomiaru: współrzędnych punktu, jednowymiarowego pomiaru długości, dwuwymiarowego pomiaru długości oraz pomiaru długości z zastosowaniem przedmiotu niekalibrowanego.

Słowa kluczowe: *niepewność pomiaru, obrabiarki CNC, sonda przedmiotowa.*

1. Introduction

Inspection probes have become a standard feature of CNC machine tools. These probes are mainly used to determine workpiece position in the mill area and for inter operational dimensional control. Given the present developments in computer software and special equipment for machine tools, technological capabilities of on-machine measurement systems are greatly enhanced. Owing to the integration of measurement systems with CNC machine tool controls, special software interfaces such as PC-DMIS NC GAGE or STEP-NC could be created. These systems allow for performing measurement cycles directly on the machine tool, without using postprocessors. They also allow for creating reports on the conducted measurements. The development in modern software (OMV) allows for controlling dimensional conformity of a workpiece with the CAD model. Reverse engineering can also be applied.

Irrespective of its purpose, the use of a machine tool equipped with an inspection probe requires that measurement inaccuracy of such system be defined. Using the inspection probe to locate the zero point when machining in several positions can lead to the accumulation of measurement errors, which – in turn – can lead to the unconformity of workpiece shape and dimensions.

2. Inaccuracy of measurement by inspection probes

Determining uncertainty of measurement using an inspection probe is a complex problem. Manufacturers of inspection probes usually provide unidirectional repeatability (2σ) as the parameter that characterizes measurement inaccuracy. Yet, it is only one of many components of uncertainty budget. Other components characterizing the probe pertain to its calibration, direction of the stylus tip access to the workpiece being measured [2], or repeatability of fix [9].

The accuracy of measurements made by inspection probes depends on the machine-holder-workpiece-tool (MHWT) arrangement. For this reason, both geometric and kinematic accuracy of the machine tool, the accuracy of standards as well as of positioning have a considerable effect on measurement accuracy [2, 13, 14]. To date, no uniform methods for determining measurement uncertainty of a measurement system by an inspection probe have been developed. In the works [13] and [14], measurement inaccuracy is evaluated based on the difference between the measurement result of a hole diameter obtained using a probe and a coordinate measuring machine. The observed differences are considerable, as the values vary even by 1 mm. Based on the results of measuring geometric accuracy of a machine tool by a laser interferometer and of measuring a certified gauge ball, the authors of the work [2] created a map of errors with pre-travel variation depending on the access direction. The authors of [5] take advantage of the difference between the probe-measured dimensions before and after the first and second pass of the machine tool. The obtained measurement results and evaluation of inaccuracy of the measurement system equipped with an inspection probe presented in [2, 5, 13, 14] were employed to correct the tool path, which – according to the authors—led to the expected improvement in workpiece quality. The presented methods for determining inaccuracy cannot, however, be applied to evaluate inaccuracy of dimensional control effected in-between the operations and after the machining process. To this end, the method described in [11] can be employed; it is based on measuring the material standard of size in accordance with the procedures used to verify coordinate measuring machines.

Apart from instrumental errors generated by measurement systems, the workpiece being measured can also become a source of

measurement errors [1]. Systematic uncertainty resulting from the temperature of the workpiece being measured is of vital importance in the case of on-machine measurement systems. Considerable amounts of heat generated during the machining process (even up to 20% [6]) are accumulated inside the workpiece, thus causing an increase in its temperature. The temperature distribution over the workpiece volume is uneven, which results in uneven strains [6]. The problem of thermal strains generated in the course of machining a thin-walled profile has also been analyzed in [3]. The work analyzes the time change in temperature and thermal strain distributions. In both cases, the distributions were uneven, and the regions of maximum strains only slightly corresponded with the regions in which the maximum temperature was observed. After the machining process, a further increase in strain was observed. It is vital if one takes the use of inspection probes into consideration. Unfortunately, the experiment was stopped 5 seconds after the end of the machining process. The time needed to substitute the tool with the inspection probe as well as the duration of a measurement cycle itself are usually much longer. Therefore, another crucial problem of measurement uncertainty is to investigate changes in workpiece dimensions after the machining process, in the course of workpiece cooling.

3. Methodology and measurement results

The measurement system consisted of a machining center FV-580A with the Fanuc 0iMC control, equipped with a direct measurement system, and of the Renishaw OMP 60 touch trigger probe. The maximum travel of the table and machine tool spindle are as follows: for the X axis – 580 mm, for the Y axis – 420 mm, and for the Z axis – 520 mm. The machine is available in the Department of Production Engineering and it is used by both the Department staff and students to conduct scientific research. The probe technical specifications are given in Table 1.

Table. 1. Technical specifications of OMP 60.

Sense directions	±X, ±Y, ±Z
Signal transimssion	optical-infrared 360°
Transmission range	6m
Unidirectional repeatability (2 σ using standard stylus)	± 1μm
Stylus trigger force XY minimum XY maximum Z	0.75 N 1.4 N 5.3 N
Stylus overtravel XY Z	±18° 11mm

Inspection probes are based on the coordinate measurement technique. To date, no standards for determining the uncertainty of measurement for inspection probes have been established. In the tests, the methods developed for coordinate measuring machines were employed. For the measurement system consisting of a machining center FV-580 A and OMP 60 touch trigger probe, the uncertainty of measurement was determined for:
  • the coordinates of the point,
  • a one-dimensional length measurement
  • a two-dimensional length measurement
  • a length measurement using multiple measurement strategies.
In order to determine the measurement uncertainty of the coordinates of the point and one- and two-dimensional length measurements, computational algorithms used in the calibration of instruments and measurement systems described in [4] were employed. The

measurement uncertainty of length using an uncalibrated workpiece was determined by means of the instructions given in [8].

3.1. Measurement uncertainty of the coordinates of the point

The repeatability of measuring the coordinates of the point is affected by the repeatability of position and stability of pre-travel length. The measurements of the coordinates of the point were made for the point located on the measurement plane of the gauge block of class 1. The block was placed in a specially designed handle, thanks to which the block could be placed in such way that its measurement planes were not parallel to any of the base planes of the machine. Fig. 1 shows the designed handle.
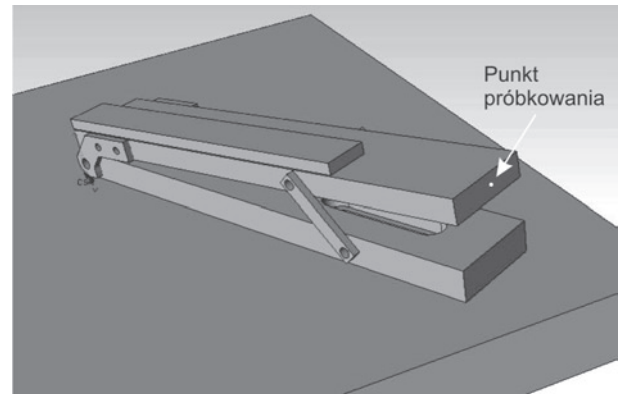

Fig. 1. Designed model of the handle used to measure the coordinates of the point

The coordinates of the vector components normal to the measurement plane were [−0.8924; −0.4462; −0.0667]. The measuring of the coordinates was repeated 10 times, each time changing the travel path. The probe traveled with the velocity v_f of 1000 mm/min, while the measuring motion velocity v_f was of 50 mm/min.

The standard uncertainty of measuring the coordinates consists of the uncertainty resulting from the dispersion of the measurement values u_A evaluated by the Type A method and the uncertainty which results from the resolution of the measurement system u_R. The standard uncertainty u_a is taken as the standard deviation of the arithmetic mean [4], calculated in accordance with the formula (1):

$$u_a = \sqrt{\frac{\sum_{i=1}^{n}(x_i - \overline{x})^2}{n(n-1)}} \tag{1}$$

where u_a is the standard uncertainty, $\overline{x}$ is the arithmetic mean, n is the number of measurements, x_i is the x coordinate obtained in the i-measurement.

The measurement system resolution r was of 0.001, which resulted from the linear encoders the machine tool was equipped with. The effect of the resolution was estimated using the Type B method, adopting the rectangular probability distribution:

$$u = \sqrt{u_a^2 + u_R^2} = \sqrt{u_a^2 + \frac{r^2}{3}} \tag{2}$$

where: u is the combined standard uncertainty, u_a is the standard uncertainty, u_R is the resolution uncertainty, r is the variation of indications.

Table. 2. Measurement results of the coordinates of the point.

Travel path	100 mm			200 mm			300 mm		
Coordinate	X	Y	Z	X	Y	Z	X	Y	Z
Standard uncertainty u_a [mm]	0.0003	0.0001	0.0000	0.0003	0.0003	0.0000	0.0011	0.0004	0.0001
Combined standard uncertainty u [mm]	0.0007	0.0006	0.0006	0.0007	0.0007	0.0006	0.0012	0.0007	0.0006
Expanded uncertainty U [mm]	0.0014	0.0012	0.0012	0.0014	0.0014	0.0012	0.0024	0.0014	0.0012

In order to evaluate the properties of instruments and measurement systems, the expanded uncertainty was employed, calculated by the formula:

$$U = k \cdot u \tag{3}$$

where U is the expanded uncertainty, k is the coverage factor, u is the combined standard uncertainty.

The coverage factor k is selected depending on the assumed trust level. In technical measurements, the trust level is set to 0.95, while the coverage factor k is set to 2 [4], on the assumption that the uncertainty budget components are subject to the normal distribution. In the case of measuring the uncertainty of the coordinates of the point using the inspection probe, at least one of the components does not meet this condition. Based on the analyses presented in [7], when evaluating the Type B uncertainty it can be assumed that k is equal to 2 also for the uniform distribution. Table 2 presents the measurement and calculation results.

It can be observed that the travel path affects the value of uncertainty, yet this effect is insignificant. The length of the travel path was measured along the direction determined by the vector normal to the plane, therefore the probe motion along the particular axes has different values, which results in different values of the uncertainty u_a.

3.2. Uncertainty of one-dimensional length measurement

Even though the coordinate measuring technique is based on, first, measuring the coordinates of the points and then, with the application of measurement algorithms, relevant values are determined, it is not possible to determine the uncertainty of measurement of length based on the measurement uncertainty of the coordinates. Determining the one-dimensional measurement inaccuracy by means of an inspection probe for particular axes was conducted using the material standard of size, i.e. gauge blocks of class 1. A detailed description of the conducted research is given in [11]. The equation of the measurement has the following form:

$$L = \overline{L} + P_{Ex} + P_t + P_r \tag{4}$$

where L is the length of the gauge block, $\overline{L}$ is the arithmetic mean, P_{Ex} is the correction resulting from the systematic indication error, P_t is correction of the temperature difference between the gauge block and measurement system model, P_r is the correction of changing the gauge block length that results from the unparallelity of the gauge block position relative to the machine axis.

The systematic indication error is calculated from the dependence (5), while the correction P_{Ex} is calculated using the dependence (6)

$$E_x = \overline{L} - L_N \tag{5}$$

where E_x is the systematic indication error, L_N is the nominal length of the gauge block.

$$P_{Ex} = -E_x \tag{6}$$

It was assumed that the corrections $P_t = 0$ and $P_r = 0$ [11]. The combined standard uncertainty was determined using the following dependence:

$$u = \sqrt{u_a^2 + u_L^2 + u_R^2} = \sqrt{u_a^2 + \frac{te^2}{6} + \frac{r^2}{3}} \tag{7}$$

where u is the combined standard uncertainty, u_a is the standard uncertainty resulting from dispersion, u_L is the uncertainty of the gauge block length, u_R is the resolution uncertainty, te is the limit deviation of the gauge block length, r is the variation of indications.

The nominal length was taken as the real length of the gauge blocks, with a dimensional tolerance limit defined as the upper and lower limits of the length variation range [16]. The limit deviations

Table.3. Measurement results of gauge block lengths.

	X Axis				Y Axis				Z Axis		
Gauge block dimensions,[mm]	100	150	200	300	100	150	200	300	50	100	150
Mean, mm	100.002	150.004	200.003	300.010	100.007	150.009	200.001	300.001	50.006	100.010	150.017
Standard uncertainty u_a [mm]	0.0005	0.0005	0.0005	0.0005	0.0004	0.0003	0.0003	0.0003	0.0001	0.0003	0.0001
Combined standard uncertainty u, [mm]	0.0006	0.0006	0.0007	0.0008	0.0005	0.0005	0.0006	0.0007	0.0004	0.0005	0.0005
Expanded uncertainty U, [mm]	0.0012	0.0012	0.0014	0.0016	0.0010	0.0010	0.0012	0.0014	0.0008	0.0010	0.0010
Systematic indication error, [mm]	0.002	0.005	0.003	0.010	0.007	0.009	0.001	0.001	0.006	0.010	0.017
Correction P_{Ex}, [mm]	−0.002	−0.005	−0.003	−0.010	−0.007	−0.009	−0.001	−0.001	−0.006	−0.010	−0.017

of the length *te* had the following values: gauge block $L = 50$ mm – $te = \pm0.4$ μm, $L = 100$ mm – $te = \pm0.6$ μm, $L = 150$ mm – $te = \pm0.8$ μm, $L = 200$ mm – $te = \pm1$ μm, $L = 300$ mm – $te = \pm1.4$ μm and $L = 400$ mm – $te = \pm1.8$ μm [16]. The triangular probability distribution was assumed, with the center in the nominal dimension of the gauge block. The measurement system resolution was 0.001 mm. The variability of indications *r* was estimated to be of ±0.0005 mm, assuming the triangular probability distribution. The combined standard uncertainty was calculated from the dependence (7), while the expanded uncertainty was calculated using the dependence (3), on the assumption that the coverage factor *k* had a value of 2. Table 3 presents the measurement results of the gauge block lengths as well as inaccuracy calculation results.

Analyzing the results presented in Table 3, it can be observed that in all cases the systematic indication error has considerably greater values than the measurement inaccuracy. This is caused by the stylus head motion parallelity to the linear encoders and the rectilinearity of this motion.

3.3. Uncertainty of two-dimensional length measurement

As shown in numerous publications on the coordinate measurement technique, e.g. in [12], determining the uncertainty of one-dimensional length measurement cannot be used to evaluate the accuracy of measurements which are not parallel to the machine tool axis or to the measurement of diameters. The two-dimensional uncertainty of length measurement was determined based on the measurements of the gauge ring and gauge blocks of class 1 positioned at an angle of 28° to the X axis of the machine tool. A detailed description of this is given in [1]. The equation for measuring the gauge blocks takes the following form:

$$L = \overline{L} + P_{Ex} + P_t + P_r \qquad (8)$$

where *L* is the gauge block length, P_{Ex} is the correction resulting from the systematic indication error, P_t is the correction of the temperature difference between the gauge block and the gauge measurement system, P_r is the correction of the gauge block length resulting from the unparallelity of the gauge block position relative to the indicated measurement direction.

The temperature correction can be omitted given the long time needed for leveling the temperatures of the gauge blocks and machine tool units. The correction of the gauge length resulting from the position relative to the measurement direction P_r had a value of 0, while its uncertainty was estimated according to the scheme given in [10]. The correction P_{EX} was calculated according to the dependences (5) and (6). The assumed standard uncertainty was calculated according to the dependence (9):

$$u = \sqrt{u_a^2 + u_L^2 + u_R^2 + u_{cos\alpha}^2} \qquad (9)$$

where *u* is the combined standard uncertainty, u_a is the standard uncertainty, u_L is the uncertainty of the gauge length, u_R is the resolution uncertainty, and $u_{cos\alpha}$ is the uncertainty of the gauge position.

The gauge length uncertainty and resolution uncertainty were calculated in the same way as when calculating the one-dimensional uncertainty. Table 4 presents the results of determining the two-dimensional uncertainty of length measurement, using the gauge blocks, whereas in Table 5 the results of determining it using the gauge ring

Table. 4. Two-dimensional measurement uncertainty of the gauge block length [10]

Gauge block length [mm]	50	100	150	200	300
Mean [mm]	50.0091	100.0014	150.0116	200.0236	299.9990
Standard uncertainty u_a [mm]	0.0004	0.0004	0.0003	0.0005	0.0004
Gauge length uncertainty u_L [mm]	0.0002	0.0002	0.0003	0.0004	0.0006
System resolution uncertainty u_R [mm]	0.0006	0.0006	0.0006	0.0006	0.0006
Cosine error uncertainty u_{cos} [mm]	0.0002	0.0004	0.0006	0.0008	0.0013
Combined uncertainty u [mm]	0.0007	0.0007	0.0006	0.0008	0.0009
Expanded uncertainty U [mm]	0.0014	0.0014	0.0012	0.0016	0.0018
Correction P_{EX} [mm]	−0.0091	−0.0014	−0.0116	−0.0236	0.0010

Table. 5. Two-dimensional measurement uncertainty of the ring diameter [10]

Mean[mm]	49.9480
Standard uncertainty u_a[mm]	0.0010
Uncertainty of gauge length u_L [mm]	0.0002
Syatem resolution uncertainty u_R [mm]	0.0006
Combined uncertainty u [mm]	0.001
Expanded uncertainty U[mm]	0.002
Correction P_{EX} [mm]	+0.0552

with $50^{+0.0005}$ diameter. To measure the ring, there was no need to take the positioning accuracy into account.

In the case of parts produced using the machine tool, the uncertainty component resulting from the positioning accuracy cannot be taken into consideration, as the positioning conformity between the measured planes and the assumed model depends on the production accuracy. The repeatability of the investigated measurement system for both cases was satisfactory, while the systematic indication error had high values.

3.4. Uncertainty of length measurement using multiple measurement strategies

The standards for determining the uncertainty of measurement using the coordinate measuring machine based on the measurement of an uncalibrated workpiece are still being developed. Some instructions can be found in ISO/CD TS 15530-2 Geometrical Product Specification (GPS). Coordinate measuring machines (CMM): Technique for determining the uncertainty of measurement. Part 2: Use multiple measurement strategies [8]. According to this project, any part from the batch is measured at different positions, with different measuring strategies for every position. Such measurement is then used to determine the following parameters of uncertainty: u_{rep} which denotes the uncertainty of the obtained measurement repeatability connected with the measuring of the same element at different orientations, as well as u_{geo} which denotes the uncertainty component connected with the product geometric accuracy. Likewise, the measuring of the gauge length is conducted. The gauges should be measured in the same measuring volume in which the product was measured. The measuring should be made three times, in three different directions, each time with a different arrangement of the measuring points. The standard uncertainty is calculated in accordance with the dependence (10):

$$u = \sqrt{s_{wz}^2 + s_p^2} \qquad (10)$$

where: *u* is the uncertainty of measurement, s_p is the standard deviation of the workpiece , s_w is the standard deviation of the model.

In order to determine the uncertainty of measurement using the method described above, the workpiece shown in Fig. 2 was designed.

The workpiece was produced on a vertical machining center FV580A equipped with the numerical control Fanuc 0iMC. The programme controlling the work of the vertical machining center was generated from the NX6 system. To this end, a 3D model was designed and machining scheme was developed, whose particular stages are shown in Fig. 3. In the machining process, a carbide end-mill (two blades) with 16 mm diameter was used. The machining parameters of rough milling were as follows: the milling cutter speed n was of 4500 rpm, the feed v_f was of 1200 mm/min; in finish milling the parameters were: n = 6000 rpm and v_f = 800 mm/min, respectively. In the course of milling, the workpiece was cooled using an oil emulsion.
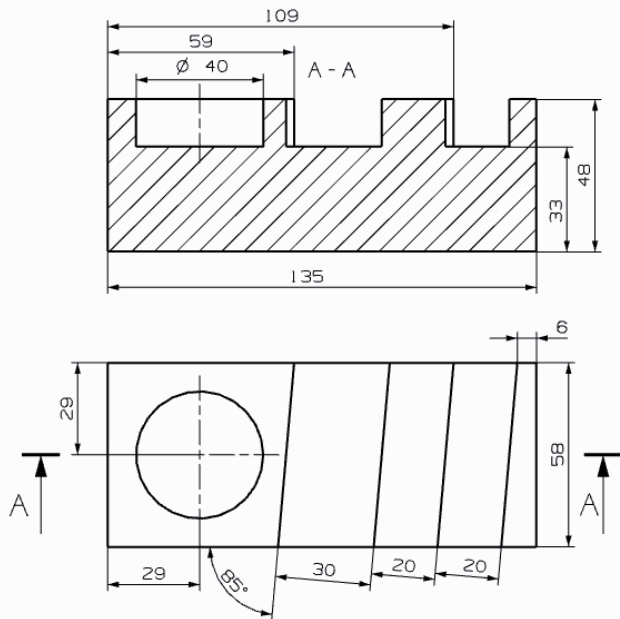
Fig. 2. Dimensions of the uncalibrated workpiece
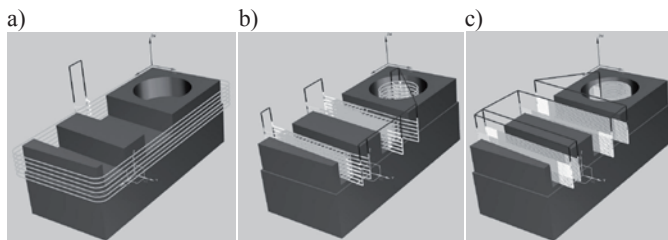
Fig. 3. Tool paths in consecutive stages of milling: a) outer surface roll forming, b) rough milling of ribs and circular pocket, c) roll forming of ribs and circular pocket

The measuring of the workpiece was conducted in two stages in order to better visualize and observe differences between the dimensions of its particular elements as well as to eliminate expansion errors. The first stage was conducted immediately following the end of the milling process when the workpiece temperature was still high – this stage is later referred to as "hot measurement." The second stage of the tests was conducted 24 hours later, when the temperature of the workpiece and moving knots of the machine tool was leveled to the ambient temperature of 20°C.

The hot measurement consisted of three measuring series, in each series the following workpiece elements were inspected (Fig. 4):
  • Hole diameter (nominal dimension – 40 mm),
  • Length (nominal dimension – 135 mm),
  • Rib A (nominal dimension – 58 mm),
  • Rib B (nominal dimension – 58 mm),

  • Pocket 1 (nominal dimension – 30 mm),
  • Pocket 2 (nominal dimension – 20 mm).
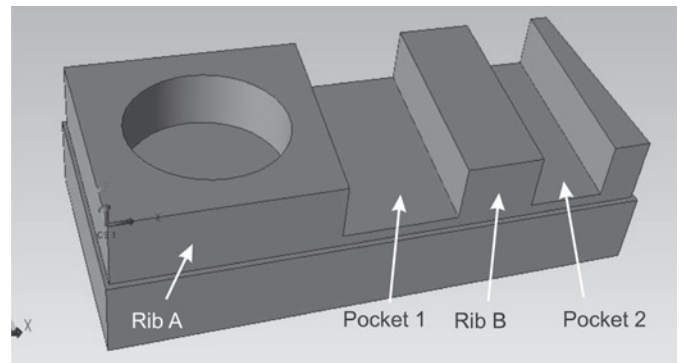
Fig. 4. Geometric features of the measured workpiece

In order to enhance the measurement process, Productivity+ was used on the machine. To measure the characteristic features of the workpiece (hole, pocket, rib), a relevant measuring cycle was used. The change in the measurement strategy consisted in using three and four sampling points when measuring the hole (Fig. 5) and in using the measurements on three different levels, determined starting from the taken zero point (the upper, left, front corner of the workpiece). The employment of these variables allowed for considering the effect of shape deviations of the element being examined (e.g. ovality), as well as considering the effect of the tool and its possible strains. The pockets and ribs were measured using a varying number of the sampling points (3, 5 and 7) on the level distanced by 5 mm from the upper plane of the workpiece (Fig. 6).
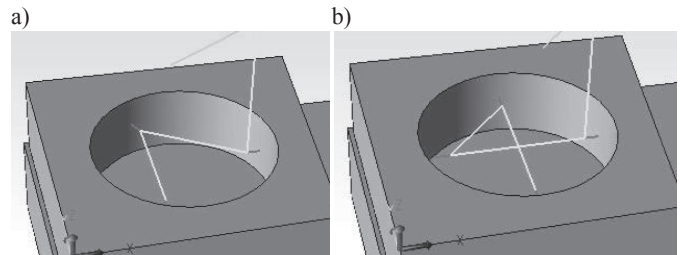

Fig. 5. Strategy for measuring the hole: a) measurement with 3 sampling points, b) measurement with 4 sampling points
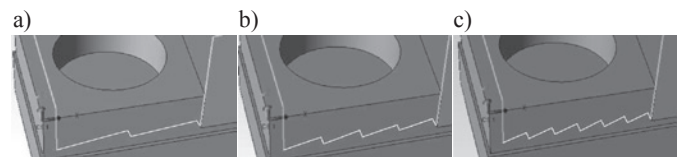

Fig. 6. Strategy for measuring the ribs and pockets: a) measurement with 3 sampling points, b) measurement with 5 sampling points, c) measurement with 7 sampling points

Such selection of points is in a way a compromise, as the optimum solution to achieve measurement accuracy would have been to select as many sampling points as possible (due to the fact that with an increase in the number of points, the uncertainty of profile evaluation decreases). Yet, an excessive increase in the number of sampling points can have a negative effect on the uncertainty of measurement, because every sampling point will be burdened with the measurement system error, which affects the coordinate measurement result. Such solution is especially vital in the case of measurements performed on machine tools and – to a lesser degree – in the case of measurements performed under laboratory conditions. Besides affecting the measurement accu-

Table 6. Measurement results of the uncalibrated workpiece

Start time	after 1min						after 24 h					
Dimension	Hole	Length	Rib A	Rib B	Pocket 1	Pocket 2	Hole	Length	Rib A	Rib B	Pocket 1	Pocket 2
Mean, [mm]	39.908	135.035	58.030	58.023	29.952	19.952	39.909	135.034	58.034	58.030	29.944	19.946
Standard deviation of dimension s_p [mm]	0.0016	0.0035	0.0007	0.0027	0.0009	0.0031	0.0027	0.0005	0.0025	0.0012	0.0009	0.0022
Standard deviation of gauge s_{wz}, [mm]	0.0004	0.0015	0.0009	0.0009	0.0009	0.0009	0.0004	0.0015	0.0009	0.0009	0.0009	0.0009
Standard uncertainty u, [mm]	0.0017	0.0039	0.0012	0.0029	0.0013	0.0032	0.0028	0.0016	0.0026	0.0015	0.0013	0.0024
Expanded uncertainty U, [mm]	0.0034	0.0078	0.0024	0.0058	0.0026	0.0064	0.0056	0.0032	0.0056	0.0030	0.0026	0.0048

racy of the workpiece shape, the number of measuring points has also a considerable effect on the duration of a measuring cycle.

Productivity+ registered the measurement results in a declared memory cell of the Fanuc system. The results were then transferred to a spreadsheet in which the necessary calculations were made. The following gauge lengths were used: for the dimensions of 58 mm, 30 mm and 20 mm a 50mm length gauge block of class 1 was used, for a dimension of 135 mm a 150 mm length gauge clock of class 1 was used, for the 40 mm diameter hole a 50 mm diameter gauge ring was used. Table 5 presents the results of the measurements and calculations of measurement uncertainty.

For the comparison reasons, the sample workpiece was measured using the coordinate measuring machine whose measurement uncertainty u_1 given by the manufacturer is of $\pm(2.5 + L/250)$ μm, where L was the length measured in mm. The following results were obtained:
• Hole diameter – 39.911 mm,
• Length -135.042 mm,
• Rib A – 58.017 mm,
• Rib B – 58.019 mm,
• Pocket 1- 29.951mm,
• Pocket 2 – 19.945 mm.

4. Result analysis and conclusions

The measurement results described in the present paper are unequivocal. The results of the uncertainty measurement of the coordinates of the point given in Table 2 demonstrate that in most cases the standard uncertainty u_a is lesser than the one-dimensional repeatability given by the manufacturer. It is only in the case of the uncertainty of measurement of the X coordinate that it slightly exceeds this value for the 300 mm travel path. Therefore, the main reason for the scatter of results is caused by the resolution of the measurement system. It is worth noticing that the results of measurement of the Z coordinate are stable. This is due to the probe design. This can also be observed analyzing the results of determining the one-dimensional uncertainty of measurement of length that are given in Table 3. In the case of the gauge blocks parallel to the Z axis, the standard uncertainty u_a has lower values than in other cases. Analyzing the results presented in Table 3, it can be observed that the standard uncertainty u_a of the on-machine measurement system using the OMP60 is much lower than the systematic indication error. The high values of the systematic indication error are caused by lack of parallelity of the head motion to the linear encoders, while the considerable differences in the values of this error results from the misalignment of this motion. This is due to the geometric accuracy of the machine tool and the condition of its power units.

Analyzing the results presented in Table 4, it can be observed that the standard uncertainty of Type A (which results from the repeatability of measurements) has low values and does not exceed 0.5 μm in the whole investigated measurement range. The combined standard uncertainty depends on the length of the gauge block being measured. This results from two components – the uncertainty of the gauge

length u_L and the uncertainty resulting from the precision of setting $u_{cos\alpha}$. In the case of the workpieces produced on the machine tool, the uncertainty component resulting from the accuracy of positioning can be omitted, because the compatibility between the position of the planes being measured and the assumed model depends on the precision of production. The repeatability of the investigated measurement system is satisfactory, while the systematic error has high values. Comparing the results given in Table 4 with the results of determining the unidirectional uncertainty given in Table 3, it can be claimed that in the case of 50, 100, 150 and 300 mm length gauge blocks, such correction values result from the geometric accuracy of the machine tool, while the high value of the systematic error of the 200mm length gauge block results from is probably caused by its relatively inaccurate positioning.

Given in Table 5, the measurement results of the gauge ring demonstrate that the standard uncertainty of Type A is almost by two times higher than in the case of the 20mm length gauge block (the worst case). Also, the corrections for the gauge ring have considerably higher values than the corrections for the gauge blocks. This is due to a different way of ball radius compensation when measuring the planes and circles.

Comparing the measurement results of the uncalibrated workpiece presented in Table 6, it can be observed that the dimensions of the sample workpiece measured immediately after the end of the machining process and after a 24-hour time lapse can be considered identical (except for the dimensions of pocket 1 and pocket 2). The measuring cycle lasted for about 30 minutes. The workpiece underwent cooling during this period of time. Pockets 1 and 2 were measured at the beginning of the measuring cycle, i.e. when the effect of the thermal expansion caused by the milling process was the most significant. These factors led to the differences in the results of the measurements taken immediately after the process and after the 24-hour time lapse. The difference in the dimensions caused by the occurrence of thermal strains was also observed in the values of the standard deviations of the workpiece. Comparing the standard deviation of 'length' (nominal dimension of 135) whose value was of 0.0035 after the machining process and of 0.0005 mm after the 24-hour time lapse, it can be claimed that the temperature decrease in the course of the measuring cycle led to the change in the dimensions and, consequently, to the dispersion of their measured values. When measuring the hole, a reverse situation could be observed: a higher scatter of results of the diameter measurement was obtained after 24 hours. According to the measurement of the hole using the coordinate machine, the cylindricity deviation was of 0.006 mm – conicity (diameter decreases together with depth). The measurements of the hole using the probe were made at three depths, starting from the highest one. It partially compensated the diameter decrease caused by the temperature decrease. The on-machine measurement system using the OMP 60 and the coordinate measuring machine had different control and measurement software. In effect, different measuring strategies had to be employed, which – combined with the geometric deviations of the workpiece (deviations

of the plane parallelity and flatness, cylindrical deviations) can cause differences in measurement results that exceed the acceptable differences resulting from metrological properties of measurement systems.

The present paper described various methods for determining the uncertainty of measurement of the on-machine measurement system using the OMP 60 probe. The discussed methods differ in terms of their labor-consumption. The most labor-consuming methods are based on the measurement of the material standard of size. Additionally, they require interpolating corrections for the systematic error of the dimensions different from the ones used for the gauge blocks or gauge rings. The advantage of these methods is that the calibration once made can then be used when measuring other workpieces. The method with the uncalibrated workpiece is less labor-consuming, but the determined uncertainty of measurement has higher values than the uncertainty of calibration. A clear disadvantage of this method is the fact that it can only be applied to a specific workpiece.

Based on the measurement results and their analysis, the following observations were made:

- selecting the method for determining the uncertainty of measurement should depend on its purpose;
- if the purpose of the measurement is to locate the zero point, the uncertainty of measurement of the coordinates of the point should be determined;
- if the purpose of the measurement is to perform an inter operational control, after-machining control or reverse engineering, then the method based on the uncalibrated workpiece can be employed proved that the machining technology allows for minimizing thermal strains;
- if the machining process generates considerable amounts of heat, the following need to be determined: unidirectional uncertainty of measurement for the dimensions parallel to the axis, bidirectional uncertainty of measurement using gauge blocks for the dimensions in the XY plane, for holes – bidirectional uncertainty of measurement using a gauge ring.

References

1. Arendarski J. Niepewność pomiarów. Oficyna Wydawnicza Politechniki Warszawskiej, Warszawa 2006.
2. Cho MW, Kim H, Seo I, Hong YC, Cheng HH. Integrated machining error compensation method using OMM data and modified PNN algorithm. International Journal of Machine Tools and Manufacture 2006; 46: 1417–1427.
3. Deneka B, Schmidt C, Krüger M. Experimental investigation and modeling of thermal and mechanical influence on shape deviation in machining structural parts. International Journal of Machine Tools and Manufacture 2010; 50: 1015–1021.
4. Dokument EA-4/02. Wyrażanie niepewności przy wzorcowaniu. GUM. Warszawa 1999.
5. Guissa R, Mayer JRR. Predictive compliance based model for compensation in multi-pass milling by on-machine probing. CIRP Annals – Manufacturing Technology 2011; 60(1): 391–394.
6. Hang Y, Hoshi T. Optimizaton of fixture design consideration of thermal deformation in face milling. Journal of Manufacturing System in face milling 2000; 19.
7. Horálek V. Analysis of basic probability distributions, their properties and use in determining type B evaluation of measurement uncertainties. Measurement 2012; 46: 16–23.
8. ISO/CD TS 15530-2 Geometrical Product Specification (GPS). Coordinate measuring machines (CMM): Technique for determining the uncertainty of measurement. Part 2: Use multiple measurement strategies.
9. Jacniacka E, Semotiuk L. Powtarzalność mocowania jako składnik budżetu niepewności pomiaru sondą przedmiotową na obrabiarkach CNC. Mechanik 2012; 5–6: 456–459.
10. Jacniacka E, Semotiuk L, Babkiewicz M. Wyznaczenie dwuwymiarowej niepewności pomiaru wewnątrzobrabiarkowego systemu pomiarowego z zastosowaniem sondy OMP60. Pomiary, Automatyka, Robotyka 2012; 10: 68–73.
11. Jacniacka E, Semotiuk L, Pieśko P. Niepewność pomiaru wewnątrzobrabiarkowego systemu pomiarowego z zastosowaniem sondy OMP 60. Przegląd Mechaniczny 2010; 69(6): 36–42.
12. Jakubiec W. Analityczne wyznaczanie niepewności pomiaru we współrzędnościowej technice pomiarowej. Akademia Techniczno-Humanistyczna w Bielsku-Białej. Bielsko-Biała 2008.
13. Kwon Y, Jeonng MK, Omitaomu OA. Adaptive support vector regresion analysis of closed-loop inspection accuracy. International Journal of Machine Tools and Manufacture 2006; 46(6): 603–610.
14. Kwon Y, Tseng T-Z, Ertekin Y. Characterization of closed-loop measurement accuracy in precision CNC milling. Robotics and Computer-Integrated Manufacturing 2006; 22: 288–296.
15. Pakiet oprogramowania Inspection Plus. Podręcznik programowania. Renishaw 2003.
16. PN EN ISO 3650:2000. Specyfikacje geometrii wyrobów (GPS) – Wzorce długości – Płytki wzorcowe.

Elżbieta JACNIACKA, Ph.D. (Eng.)
Leszek SEMOTIUK, Ph.D. (Eng.)

Department of Production Engineering
Mechanical Engineering Faculty
Lublin University of Technology
ul. Nadbystrzycka 36, 20-618 Lublin, Poland
e-mails: e.jacniacka@pollub.pl, l.semotiuk@pollub.pl

Mirosław FERDYNUS

AN ENERGY ABSORBER IN THE FORM OF A THIN-WALLED COLUMN WITH SQUARE CROSS-SECTION AND DIMPLES

ABSORBER ENERGII W POSTACI CIENKOŚCIENNEGO SŁUPA O PRZEKROJU KWADRATOWYM Z WGŁĘBIENIAMI*

The object of the research was a thin-walled energy absorber made of aluminium in the form of a column having square cross-section and a series of dimples in the corners. As the possibilities of practical applications of the absorber appear to be considerable, the paper presents prospects of building a palletization head. An influence of the global initial deflections on sub-critical form of the equilibrium path was examined. This was an attempt to assess the structure's susceptibility to deviations of the column's axis from the ideal one. In the article a way of the column's model construction was described in detail. The model takes into account the corner dimples, the initial deflections and the perturbations caused by geometrical imperfections. Advantages of the new solution were presented in comparison with a column having smooth walls.

Keywords: energy absorber, damage, palletization head.

Obiektem badań jest cienkościenny absorber energii w postaci słupa o przekroju kwadratowym z szeregiem wgłębień w narożach wykonany z aluminium. Możliwości zastosowań praktycznych wydają się duże, przedstawiono perspektywę dotyczącą budowy głowicy do paletyzacji. Bada się wpływ globalnych ugięć wstępnych na podkrytyczną postać ścieżki równowagi, jako próbę oceny wrażliwości tej konstrukcji na odchylenia od osi idealnej słupa. W pracy przedstawiono szczegółowo sposób budowy modelu słupa z wgłębieniami oraz ugięciem wstępnym i zaburzeniami imperfekcjami geometrycznymi. Zalety nowego rozwiązania przedstawiono w porównaniu ze słupem o gładkich ścianach.

Słowa kluczowe: absorber energii, zniszczenie, głowica do paletyzacji.

1. Introduction

During the operation of the machinery sometimes a collision and damage takes place in result of a human mistake or a machine's failure. In 2011 in one of the sugar factories a robot with its' working head hit a pallet full of sacks, as result of the operator's mistake. Damage appeared not only in the head, but also a serious breakdown of the robot occurred (one of the robot's arms was broken and another one fractured). The damaged robot with its working head is shown in Fig. 1. Such a serious breakdown during a sugar campaign is a serious problem, as the production line cannot have long-lasting shutdown. A repair of the working head is not simple, but it is cheap enough and relatively quick. The robot's breakdown is incomparably more expensive, it needs highly skilled crew and usually long delivery time of spare parts. From that practical point of view, i.e. issues of a concrete plant, the reliability of production line, understood as a probability of the above described collision and a minimization of its negative effects is certainly an important matter. The minimization of negative effects means costs of repairs and the time spent for complete reconditioning of the production line.

The paper treats of minimization of negative effects of such events by introducing in the working head's structure special zones able to absorb large energy and impact. Particularly dangerous are these impact events, in which the compliance of the working head's operating elements cannot be exploited and in result the impact is transferred in its major part to the head's arm and farther to the robot's wrist. In many palletization heads the frame is bipartite with both parts joined by compliant elements. However, such structural solution not always can absorb the destructive energy and – on the other hand often renders it difficult to gain sufficient stiffness of the frame.

The current paper is a study of some engineering conception and precedes the planned laboratory experiment, as well as practical application. It is concentrated on some case of a thin-walled column with dimples, which could later serve as an energy absorber in working heads of robotized production lines, but also in other applications, where the thin-walled structure is expected to absorb large energy. Introduction of the dimples had in target to make the column more compliant, ordering of the structure's destruction process, such that the element underwent the concertina folding and thus saved the damage sensitive parts of the equipment from destruction. This would
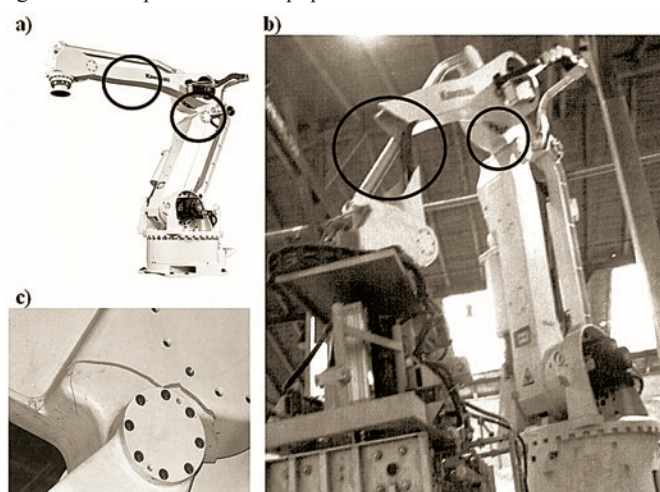

Fig.1.   *The industrial palletizing robot's break-down which occurred in one of the sugar factories*

naturally reduce the total cost of repairs and the time of shutdown after the break-down.

In the paper an influence of the global initial deflections (the initial curvature of the column's axis) on subcritical form of the equilibrium path was examined. The meaning of these analyses consists in an assessment of the structure's sensitivity to a deviation of its axis from its ideal shape. A possibility of performing by the absorber its function even when it underwent meaningful deviation was also tested. Reliable results were gained for very large deformation. A comparison was performed of the behaviour of the columns with dimples and those with smooth walls in the aspect of their ability to absorb the impact energy.

The subject of the limit load-carrying ability of isotropic columns with square cross-section has been well recognized so far. However, there is a considerable lack of papers on practical applications of the above described phenomena. Many articles depict experimental tests of such structures, for example [8,9,16,17]. Abramowicz [1,2] dealt with steel columns, among others, in the aspect of their application as energy absorbers. In the works [18,19] Teter considered a phenomenon of interactive buckling of analogous structures within a static and a dynamic regime. The works of Langseth and Hopperstad [10, 11] concentrated on the columns made of aluminium. Meng and Wierzbicki [13, 20, 21] analysed failure mechanisms of closed cross-section columns. However, no articles concerning columns with corners shaped as described above (with dimples) were found in the open literature. Even though in [12, 14] the authors studied the behaviour of tubular columns with dimples, these flaws were treated as damage and each column had only one dimple at a time. This allows to presume, that the presented study of a thin-walled structure can be considered as unique.

2. Object of research. A model of column with dimples

The object of the analysis was a model of the hollow column with a square cross-section □68x1 made of aluminium alloy EN AW6060-T6 (R_e=175 MPa, R_m=250 MPa, ν=0.33). This material exhibits linear hardening during plastic flow (E=70000MPa, E_t=937,5MPa). The column's height was assumed to be six times greater than its average cross-section dimension l=6x67=402 mm. The analysis of buckling modes of a smooth column (without dimples) yielded a location of nodal line for the first mode. This allowed to place the corner dimples properly. The process of modelling of the column with dimples was realized with the Catia v. 5 software package in the Generative Shape Design module. The model of the column with a magnified corner dimple is presented in Fig. 2.

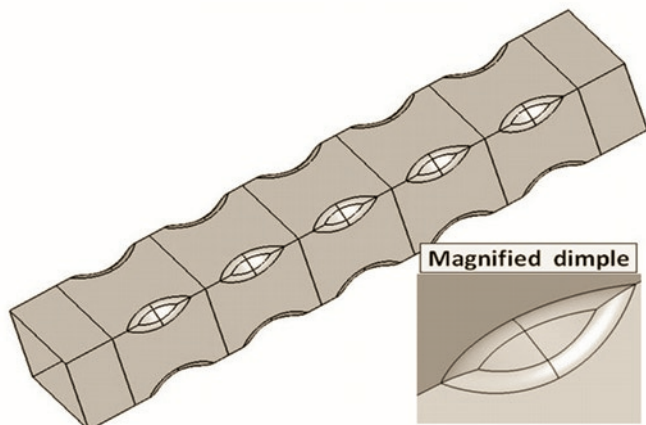The dimple's geometry was characterized by the main radius R=30 mm, whereas its surface passed into the column's wall with another radius r=6 mm. The depth of the dimple was 6.7 mm, what equalled 10 % of its width. As it is shown in Fig. 2, quads of dimples were made at five levels every 67 mm. A surface model elaborated in the Catia v. 5 software was fully parameterized. Thus, the location and the geometry of the dimples could be modified very easily.

The model of the column was subsequently imported to the ABAQUS software environment in order to perform the Finite Element Analysis (FEA) [3]. The analysis was performed in three stages:

1. An analysis of the buckling eigenmodes of the column with dimples, calculations of the critical force,
2. An elaboration of the column's models with some global initial deflection (initial curvature of the axis); the models differed among each other with an amplitude of the initial deflection (from 0 to 5 mm every 0.5 mm);
3. Performing a static nonlinear analysis with many variants of compressed column with dimples.

The way of modelling of the phenomena taking place in the compressed columns did not differ from some procedures presented in [4, 6]. Similar multi-stage way of modelling was shown in [5, 7, 15].

In all stages the same boundary conditions, as well as loading conditions were applied. Due to the fact, that in the planned experiments the real columns will be loaded through the existing grips with articulated support and that the current paper is a pre-experimental study, a special care is taken about a conformity of the real and the numerical boundary conditions. In the FEA model two reference points RP1 and RP2 were established and by the "Coupling" type constraints the column's boundaries were fixed to them in stiff. The reference points were located at h=65 mm from the column's boundaries, what referred to a distance between an articulated joint sphere's centre and the grip's bearing surface. In the RP1 point the structure was devoid of the three translational degrees of freedom and the rotational degree of freedom around the Z axis. In the RP2 point, in which a concentrated load was applied, the boundary conditions were changed only by enabling translations along the Z axis, in comparison with the RP1.

In Fig 3 the ABAQUS model of the column with the applied boundary and loading conditions is presented.
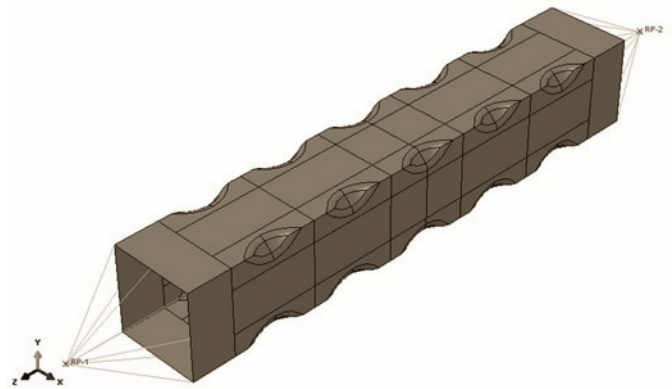

Fig. 3. The ABAQUS model of the column with applied boundary conditions

At the first stage of the analysis special attention was paid to obtain an optimal FEA mesh, i.e. dense enough in significant areas and generally regular. It was very important to evade any influence of the mesh quality on simulation results, as at subsequent stages still the same mesh was used. In Fig. 4 the model of the column with the FEA mesh was presented. It is well visible, that the areas, where the mesh is regular, made of the S4R 4-noded shell elements with reduced integration prevail in the model. However, in the vicinity of the dimples the S3 3-noded elements appear, even though the 4-noded elements still dominate there.

Before performing the analysis it was necessary to add in the input file a routine enabling introduction of the profile's shape deformation
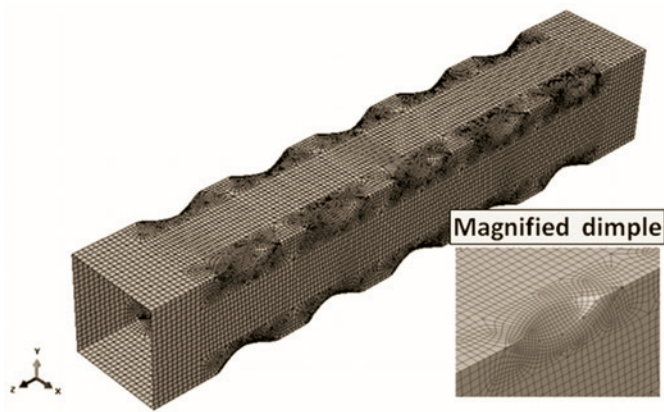

Fig. 2. A model of the column elaborated in the Generative Shape Design module of the Catia v. 5 software

Fig. 4. *The ABAQUS model of the column after the FEA mesh generation*

by calling a file with a "fil" extension. The final effect of the first stage was finding the critical force, as well as the buckling modes. These data in the form of file were exploited in a subsequent stage of modelling. In Fig. 5 the first and the second buckling mode together with the respective critical force values are displayed.
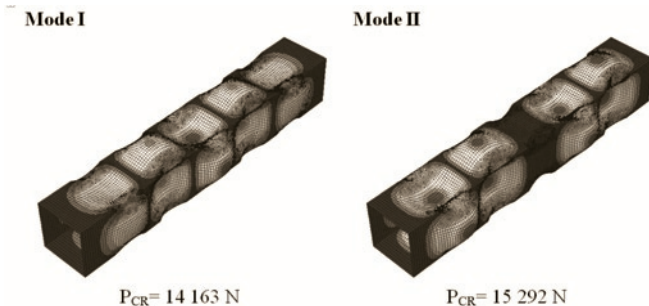

Fig. 5. *The first and the second buckling mode of the profile and the respective values of critical forces*

The second stage of building the model had in target getting the column's shape allowing for two kinds of perturbations: small initial deflection of the whole profile and geometrical imperfections imitating the first buckling mode. The global initial deflection (corresponding to the primordial curvature of the symmetry axis) of the column was obtained by the displacement method. Namely, the displacement along the x axis of the central cross-section of the column was declared. Fig. 6 shows the column's model with the assumed displacement. A set of models with the initial deflection being a multiple of 0.5 mm within the range of 0 to 5 mm was elaborated.
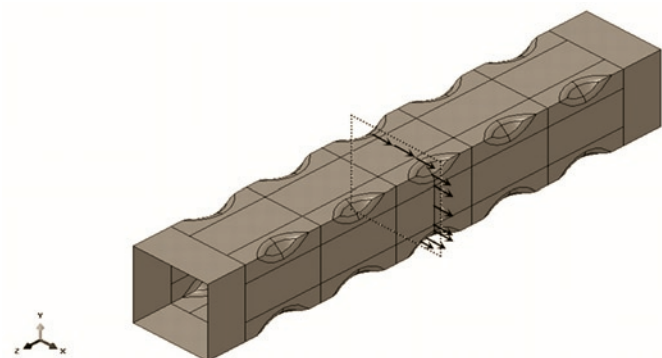
Fig. 6. *The column's model with the declared displacement of the central cross-section*

The way of getting perturbations of the column's shape with geometrical imperfections was based (as mentioned above) on adding in the ABAQUS job input file the routine downloading the geometry definition from the appropriate "*.fil" file. In the routine a consecutive mode number, as well as the imperfection's magnitude in millimetres had to be determined. The result of the second stage was the shape of the column distorted by the global deflection and the imperfection. After running the analysis the deformed column was brought into a particular stress state. For the purpose of obtaining a stress-free form of the structure it was necessary to import the model into the ABAQUS environment once again. The model had to be read as a "Part" from an appropriate "*.odb" database file.

At the third stage the model had no geometry, but the deformed FEA mesh. In order to conduct any computations on such a column the whole process of the model preparation had to be started from the beginning, excluding only the FEA mesh generation. The obtained distorted model of the column with the applied boundary conditions and the load is shown in Fig. 7.

Fig. 7. *The ABAQUS model of the column with distorted FEA mesh, applied load and boundary conditions*

In result of the first and the second stage of modelling a set of 10 models of the columns varying in the amplitude of initial deflection was obtained. The models were designated by the symbols from A00 to A50, where the number stands for the amplitude of initial deflection multiplied by 10.

The column was loaded with a force P= 25 kN and subjected to the analysis, taking into account geometrical and material nonlinearities. The FEA model allowed for contact phenomena, both at internal and external surfaces. The specificity of the nonlinear analysis extorted, that the column was loaded incrementally and in the first step the load equalled 0.05P. In order to gain the nonlinear equilibrium path in as wide range as possible, a stabilization was introduced in the iterative method by declaring damping of energy at the level of 0.02% (an appropriate damping factor was specified).

3. Results

The analysis of the deformation process of column's models differing among each other with the amplitude of initial deflection lead to interesting conclusions. In case of the columns with the initial deflection amplitude from 0 to 2 mm the absorber's damage process started from the middle cross-section and propagated subsequently to the upper levels, in order to move in the final stage to the lower zone. It can be seen in Fig. 8, where the modes of deformation of the columns at the beginning and in the end of the process are shown. In the columns characterized by the initial deflection amplitude from 2.5 to 5 mm the absorber's damage process started in a cross-section above the middle one and the subsequent destruction ran similarly. It is shown in Fig. 9, where the modes of the columns' deformation at the beginning and in the end of the process are shown. It is visible, that at relatively large deviations from the ideal column's axis the simulation of the nonlinear structure's crushing process did not reach its end (even though the software package made ca. 1000 of iterations).

As numerical simulation of the crushing is a strongly nonlinear process, both in the material properties' and in the geometrical sense, with contact phenomena taken into account, the obtained results should be considered as a success, because they show the course of the absorber's destruction within a wide range of its functioning. An ideal would be gaining the effect of the column's concertina folding, what means absorbing maximal possible amount of energy. In practical applications the amount of absorbed energy depends, however, on some external factors and it might turn out, that the columns would never be exposed to such a high loads.
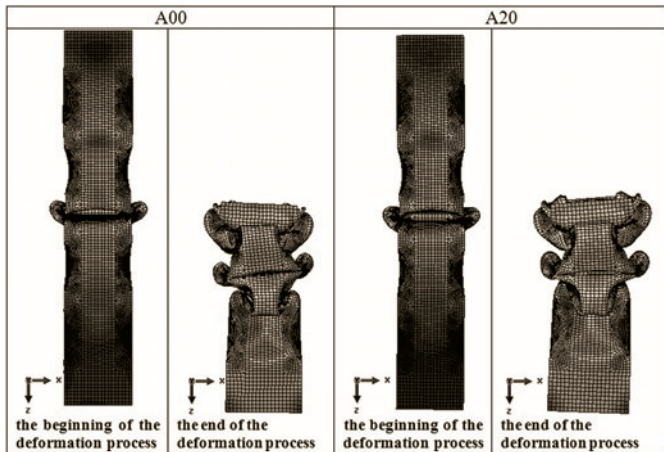
Fig. 8. Modes of deformation of the columns No. A00 and A2
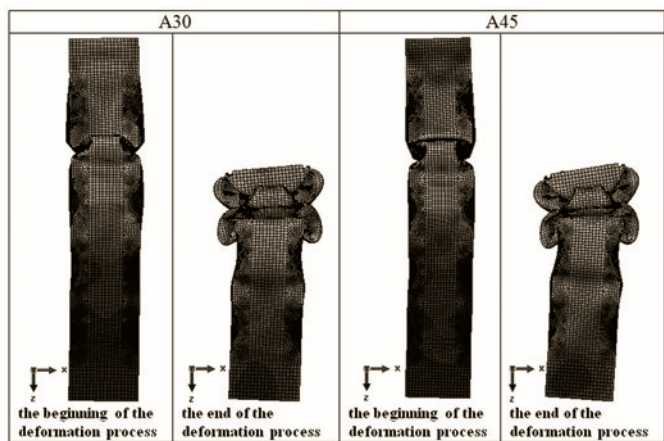
Fig. 9. Modes of deformation of the columns No. A30 and A45

Fig. 10 presents a relation between the load RF3 (the reaction force along the Z axis) and the column's shortening U3. The plot shows the absorber's crushing process associated with the energy absorption. The specific peaks of the curves depict the crushing of subsequent levels of the columns. Similar curves can be found in many works treating of experimental results, among others [7, 8, 15, 16]. When the load increased together with the column's shortening then the stress increased, as well. A decrease in the reaction force value RF3 together with the increase in the column's shortening was associated with the plastic flow of the subsequent levels.

The numerical simulation succeeded to reach large deformations. The columns shortened by 185mm to 230 mm, depending on the column's type, what was, taking into account its initial length equal 402 mm, from 46% to 57%. One can see, that the operating mode of the structure at the stage of its crushing is similar, apart from the column's model. In spite of this resemblance, at the shortening U3 equal approximately 70 mm, the following groups of models: A00 A20 and A25 A50 started to diversify. In the second group (having the amplitude of initial deflection equal to 2.5 5 mm), a specific pla-
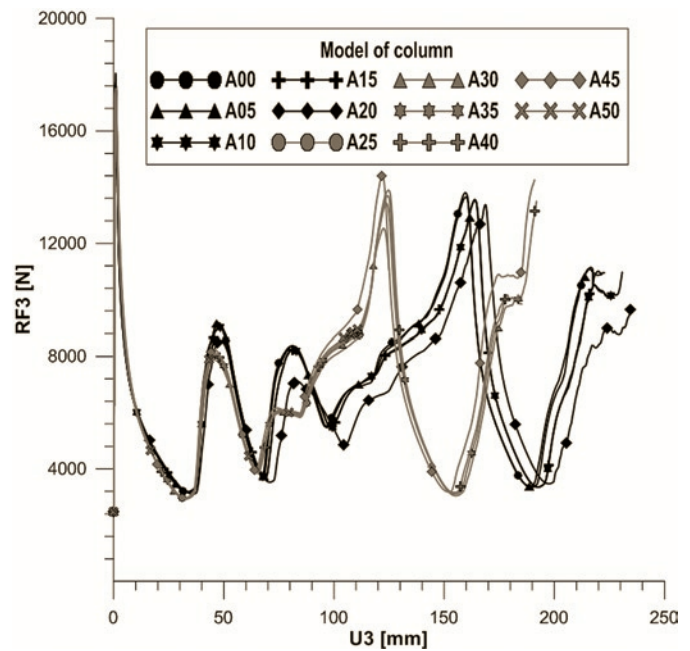
Fig. 10. The reaction force RF3 vs. the column's shortening U3 for the models of the columns differing with the amplitude of initial deflection

teau appeared; it was associated with the structure's shortening within the range of 70.7 to 91.6 mm. A penetrating observation of this fact indicates, that the respective fragment of the characteristic curve is related to the local deformation of the column in the vicinity of its support, as shown in Fig. 11. The occurrence of such perturbations in so strongly nonlinear process, does not change the overall character of the plots, in which the subsequent peaks depict the deformation of consecutive levels.
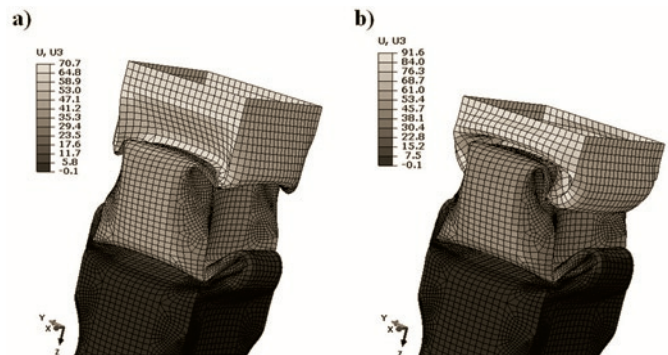

Fig. 11. Operation of the structure in the plateau phase

4. Comparison of the new solution with the classical column

Advantages of the new solution become visible, when one compares the behaviour of the columns with dimples and those with smooth walls. The models were elaborated and numerically analysed for the whole family of columns without dimples. The models had identical boundary conditions and differed besides their shape only with the load, which equalled P=28 kN. However this had no practical meaning due to the fact, that the load was applied stepwise. The way of models' designation was analogous as for those with dimples, i.e. G00 G50.

The course of the deformation process of the smooth columns at the initial deflection's amplitude not exceeding 1.5 mm was very close to that of the dimpled columns, what can be seen in Fig. 12.
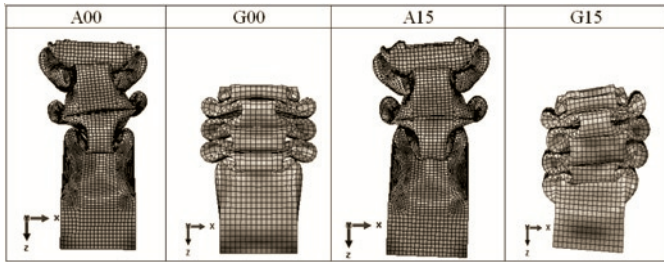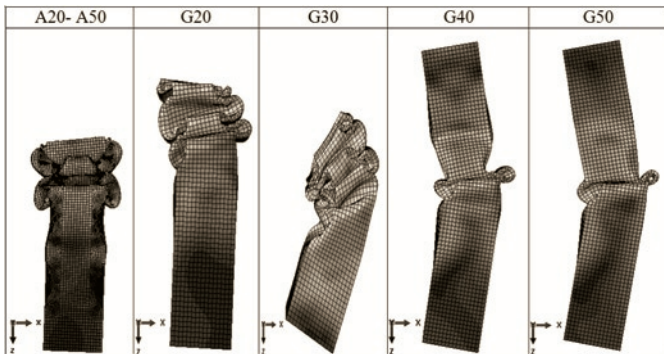
Fig. 12. *Modes of deformation of the columns with dimples in comparison to the columns with smooth walls at the amplitude of initial deflection equal 0 – 15 mm*

However, with the increase of the initial deflection amplitude a considerable difference in the course of the structure's deformation process occurred. It is superbly visible in Fig. 13, where the mode of the dimpled absorber's structure deformation practically does not depend on the initial deflection's amplitude. The columns with smooth walls "did not want to" make the concertina folding together with the increase of the initial deflection's amplitude, but they rather broke, what very adversely influenced the amount of absorbed energy and in consequence the reliability and the functionality of this type of structure operating as a specific protector.

Fig. 13. *Modes of deformation of the columns with dimples in comparison with the columns with smooth walls at the amplitude of initial deflection equal 20 – 50 mm.*

Fig. 14 presents a plot of operation of the column with dimples and the one with smooth walls for the models of structures with ideally straight axes. In the magnification box one can see, that the model with dimples started to operate, i.e. to absorb the energy under the
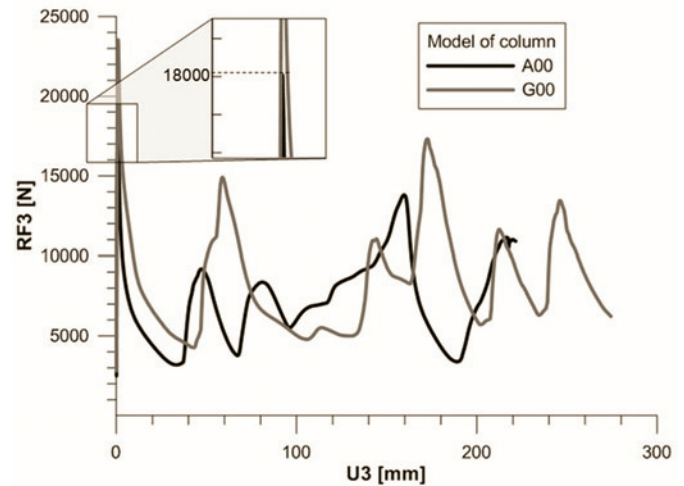
Fig. 14. *Reaction RF3 vs. shortening U3 for the models of columns with dimples and with smooth walls (straight axis).*

load ca. 23% lower than the smooth column. In case of an impact loading the former structure would react earlier, thus protecting the machinery against damage.

5. Conclusions

The structural solution presented in the paper is currently at the stage of numerical analyses. It exhibits a big potential to be applied as an absorber. In comparison with classical solution it shows an exceptional resistance to any perturbations in the form of some initial curvature, which can yield from manufacturing errors or from the fact, that the structure experienced deviation as a result of collision etc. In the areas of the dimples the plasticization appeared at the earliest and the structure in some sense compensated deviations from its original shape. Subsequent numerical research is needed in order to assess an influence of the dimples' lay-out and their geometry on the structure's behaviour. The research would have in target finding optimal solutions in respect of the structure's ability to absorb the energy. The main goal would be gaining high degree of deformation at an adequate load, such that the absorber had appropriate characteristics. The next stage would be experimental verification of the numerical model and an implementation of the elaborated solutions in a specific industrial machinery.

References

1. Abramowicz W. Thin-walled structures as impact energy absorbers. Thin Walled Structures 2003; 41: 91–109.
2. Abramowicz W, Jones N. Dynamic Axial Crushing of Square Tubes. International Journal of Impact Engineering 1984; 2: 179–208.
3. Abaqus HTML Documentation.
4. Arbocz J. Post-buckling behaviour of structures. Numerical techniques for more complicated structures. Lecture Notes In Physics, 228, 1985
5. Bieniaś J, Dębski H, Surowska B, Sadowski T. Analysis of microstructure damage in carbon/epoxy composites using FEM, Computational Materials Science 2012; 64: 168–172.
6. Doyle FJ. Nolinear analisys of thin- walled structures. New York: Springer-Verlag, 2001.
7. Dębski H, Koszałka G, Ferdynus M. Application of FEM in the analysis of the structure of a trailer supporting frame with variable operation parameters. Eksploatacja i Niezawodnosc – Maintenance and Reliability 2012; 14 (2): 107–113.
8. Hambly ET, Calladine CR. Buckling Experiments on damaged Cylindrical Shells. International Journal of Solids and Structures 1996; 33 (24): 3539–3548.
9. Hamouda AMS, Saied RO, Shuaeib FM. Energy absorption of square tubular structures. Journal of Achievements in Materials and Manufacturing Engineering 2007; 24: 36–42.
10. Langseth M, Hopperstad OS, Hanssen AG. Crash Behaviour of Thin-Walled Aluminium Members. Thin Walled Structures 1998; 32:127–150.
11. Langseth M, Hopperstad OS. Static and Dynamic Axial Crushing of Square Thin-Walled Aluminium Extrusions. International Journal of Impact Engineering 1996; 18 :949–968.
12. Lancaster ER, Palmer SC. Model Testing of Mechanically Damaged Pipes Containing Dents and Gouges. ASME Pressure Vessels & Piping Conference New York 1992; 235:143–148.

13. Meng Q, Al Hassani STS, Soden PD. Axial crushing od square tubes. International Journal of Mechanical Science 1983; 25: 747–773

14. Ronalds BF, Dowling PJ. Buckling of Inpact and Damaged Offshore Shell Structures in: Advanced Marine Structures, C.S. Smith and J.D. Clarke. Eds. Elsevier Applied Science, London 1987: 201–218.

15. Rudawska A, Dębski H. Ocena wytrzymałości połączeń klejowych ze stopu aluminium z wykorzystaniem analizy numerycznej MES. Eksploatacja i Niezawodnosc- Maintenance and Reliability 2011; 1 (49): 4–10.

16. Singer J, Arbocz J, Weller T, Buckling Experiments. Experimental methods in buckling of thin-walled structure. Basic concepts, columns, beams, and plates, Volume 1, John Wiley & Sons Inc. New York 1998.

17. Singer J, Arbocz J, Weller T, Buckling Experiments. Experimental methods in buckling of thin-walled structure. Shells built-up structures, composites and additional topics. Volume 2. New York: John Wiley & Sons Inc, 2002.

18. Teter A, Kolakowski Z. Interactive buckling and load carrying capacity of thin-walled beam-columns with intermediate stiffeners. Thin Walled Structures 2004; 42(2):211–254.

19. Teter A. Static and dynamic interactive buckling of isotropic thin-walled closed columns with variable thickness. Thin Walled Structures 2007; 45(10-11):936–940.

20. Wierzbicki T, Huang J. Initiation of plastic folding mechanism incrushed box columns. Thin Walled Structures 1991;13: 115–143.

21. Wierzbicki T, Abramowicz W. On the Crushing Mechanics of Thin-Walled Structures. ASME Journal of Applied Mechanics 1983; 50: 727–734.

Mirosław FERDYNUS, Ph.D. (Eng.)
Department of Machine Design
Mechanical Engineering Faculty
Lublin University of Technology
ul. Nadbystrzycka 36, 20-618 Lublin, Poland
e-mail: m.ferdynus@pollub.pl

Przemysław FILIPEK

ESTIMATING AIR-FUEL MIXTURE COMPOSITION IN THE FUEL INJECTION CONTROL PROCESS IN AN SI ENGINE USING IONIZATION SIGNAL IN THE COMBUSTION CHAMBER

SZACOWANIE SKŁADU MIESZANKI W PROCESIE STEROWANIA WTRYSKIEM BENZYNY W SILNIKU ZI Z WYKORZYSTANIEM SYGNAŁU JONIZACJI W KOMORZE SPALANIA*

The paper offers a comparison between signals produced by a lambda sensor and ionization sensor to estimate air-fuel mixture composition in the fuel injection control process in an SI engine. The method of measurement is described and characteristics of the ionization signal in the conducted experimental tests are given. The paper also presents a numerical model of the internal combustion engine that was designed and then used in the simulations to examine the usefulness of ionization signal for estimating air fuel mixture composition. The conducted tests demonstrated the advantage of the controller using the ionization measurement in the combustion chamber over the controller using signals produced by a classic lambda sensor.

Keywords: internal combustion engine, composition of air-fuel mixture, ionization current, fuel injection, spark plug .

W artykule zawarto porównanie sygnałów z sondy lambda oraz czujnika jonizacji do szacowania składu mieszanki w procesie sterowania wtryskiem benzyny w silniku o zapłonie iskrowym. Opisano sposób pomiaru i charakterystykę sygnału jonizacji w przeprowadzonych badaniach doświadczalnych. Przedstawiono stworzony model matematyczny silnika spalinowego, którego użyto do przeprowadzenia badań symulacyjnych, testujących użyteczność sygnału jonizacji do szacowania składu mieszanki paliwowo-powietrznej. Wykazano przewagę regulatora wykorzystującego pomiar jonizacji w komorze spalania w porównaniu z regulatorem korzystającym z sygnału klasycznej sondy lambda.

Słowa kluczowe: silnik spalinowy, skład mieszanki, prąd jonizacji, wtrysk benzyny, świeca zapłonowa.

1. Introduction

There are three control functions which play a vital role in the operation of an internal combustion spark ignition engine: fuel injection control, ignition control and throttle control. Out of the three control functions, the fuel injection control affects the performance of the engine most. Any change in injection parameters affects not only fuel consumption and vehicle power; above all, it determines exhaust gas composition. Fuel injection control requires predicting air fuel mixture composition in the cylinder after the charge exchange [23].

It is very difficult to measure the mixture composition in the cylinder. The most widely used method is to measure it in an indirect manner, using in-cylinder signals which occur in the combustion process. On the other hand, the methods based on cylinder pressure measurement or optical emission from the combustion chamber are impractical to be employed in engine operation [23].

Modern vehicles are equipped with a sensor of air-fuel mixture composition in the exhaust gas, mounted in the exhaust system. The sensor facilitates estimating mixture composition based on oxygen concentration in the exhaust gas. The mixture composition sensor signal is characterized by a long time delay relative to the fuel injection signal. The delay can have values of even dozens of consecutive fuel injections. In the case of an incorrect value of a fuel injection dose, the correction will occur with a considerable time shift. The state with incorrect values of oxygen concentration in the exhaust gas has a clearly negative effect on engine operation, as it decreases combustion efficiency and catalysis of toxic exhaust gas components

(decreased life of an exhaust gas catalytic reactor) as well as leads to the worsening of vehicle ecological properties [3].

In order to minimize the error which occurs when adjusting air-fuel mixture composition, the excess air factor should be much earlier evaluated in a thorough way. An alternative method for estimating mixture composition, with a much shorter time delay is to measure gas ionization in the cylinder of an internal combustion engine. The measurement is done using the cylinder spark plug electrodes as a sensor [20, 24, 25].

The method based on measuring gas ionization current in the engine cylinder has been repeatedly employed to detect knocking [2, 16, 18] and misfiring [17], to determine temperature [13], to estimate cylinder pressure [15, 19, 21] or, finally, to estimate air-fuel mixture composition, proving a strong dependence of ionization signal on mixture composition [1, 22]. Modern methods of analysis for measuring signals SI engines are also based on artificial neural network models [4], which are broadly used in many fields of science [11, 12].

A significant disadvantage of the indirect measurement of mixture composition based on ionization in the cylinder is a considerable dispersion of such signal and local character of the sensor position, i.e. the spark plug located in the combustion chamber. Based on ionization signal in the cylinder, ignition can be controlled [6], yet the available literature offers little information on the suitability of this signal for fuel injection control. The aim of the present paper is to demonstrate the suitability of using ionization signal for fuel injection control owing to a much faster way of measuring mixture composition in the cylinder and better dynamics of the signal produced by the air-

fuel mixture composition sensor and its high correlation in the range λ between 0.9 and 1.1.

2. Fuel injection control

Fuel injection control is generally based on oxygen measurement in the exhaust gas by means of a lambda sensor. The sensor of combustible mixture in the exhaust gas has a serious disadvantage of time delay between a change in the mixture composition after injection and the sensor reaction to it, and the value of the time delay depends on whether the mixture changes from rich to lean (or the other way round) and on the sensor temperature [3].

Figure 1 illustrates the fuel injection control registered by the author for a production, four-cylinder car engine. In the experiments, an electronic controller allowing for injection time control was used. Figure 1 shows a reaction of the adjusting correction k_s to the changing, enforced by the author, characteristic of the injection model, expressed as the correction coefficient k. Figure 1a illustrates time intervals for the mixture that is too rich or too lean, occurring right after the disturbance of the injection model characteristic. The control delay is predominantly due to inertia of the air fuel mixture composition sensor. A similar process is shown in Figure 1b, where the rapid and quick change of the model coefficient k by 15 % led the system to adjust to the correct value only after nine seconds, which shows a long rich mixture time burn of the engine.

a)   b)
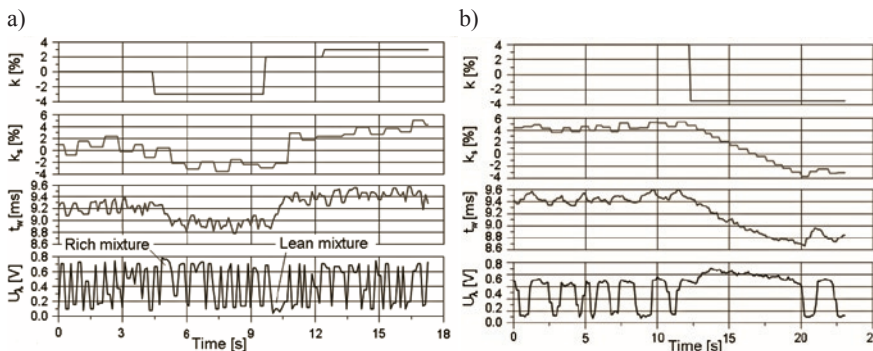
Fig. 1. Fuel injection control in a production, four-cylinder car engine during irregularly forced changes to controller injection model expressed as coefficient k (the author's own research)

3. Ionization signal in the combustion chamber of an internal combustion SI engine

Combustion in an SI engine is initiated by a spark breakdown on spark plug electrodes. The flame propagates along the spark plug and toward the combustion chamber walls, burning the air fuel mixture. Chemical reactions and a temperature increase inside the flame front led to the ionization of charged particles over the whole cylinder volume. The amount of the ionized charged particles is small, yet it can be measured. Following the voltage loss on the spark plug electrodes – i.e. the ionization sensor – a current is induced from free electric
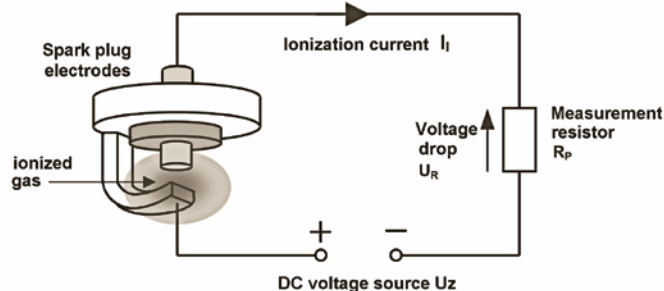
Fig. 2. Method for measuring ionization current between spark plug electrodes

Fig. 3. Measuring system used to measure ionization current in four cylinders

charges contained in the ions. This kind of current is referred to as ionization current.

3.1. Method of measurement

Figure 2 illustrates a circuit for measuring the ionization current. The system is powered by an external DC voltage U_z of 200 V [10]. The current I_I, which flows in the circuit, depends on the conductivity of a gas mixture between the spark plug electrodes in the combustion chamber, i.e. on the value of the ionized gases. The measurement is done on a measurement resistor, R_p, on which the voltage drop U_R (according to the Ohm's law) is proportional to the ionization current.

Figure 3 shows the author-designed measuring system that allows for measuring the ionization current simultaneously in four cylinders of the internal combustion engine.

3.2. Characteristic of the ionization signal in the experimental tests

The experimental tests were performed on a C20LE Holden gasoline engine with a multi-point fuel injection into the inlet manifold, adapted toLPG supply. The C20LE Holden is a four-stroke, four-cylinder, liquid cooled engine, with two valves per each cylinder moved by a single camshaft mounted in the head, equipped with a hydraulic valve adjustment. The engine has a direct ignition system DIS and is equipped with a mechanically controlled exhaust gas recirculation (EGR) valve.

In the experimental tests, a DTS–700 control system for an internal combustion SI engine, co-designed and constructed by the author at the Faculty of Mechanical Engineering at Lublin University of Technology. The apparatus is equipped with four communication interfaces RS232/422/485 and with CAN 2.0B that allow for supervisory computer control of the engine.

The experiments involved measuring the signal of the ionization current in the cylinder, at different values of the excess air coefficient, for set values of the air fuel mixture composition. In the experiments, the following were measured: the pressure signal for the fourth cylinder, the ionization current signal, and two signals describing the
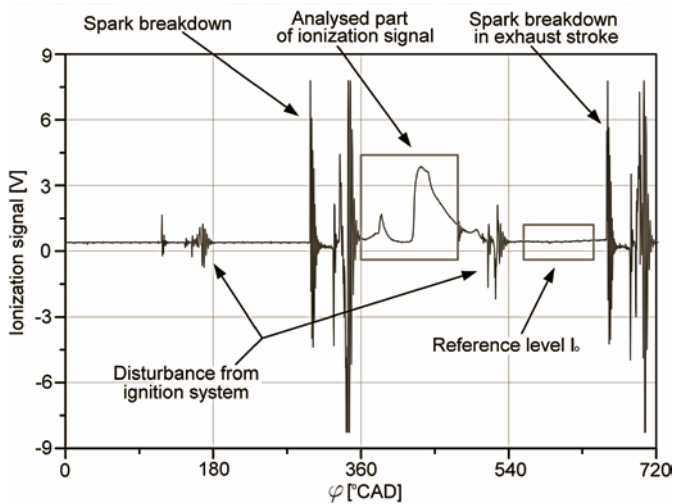
Fig. 4. Ionization signal measured in the fourth cylinder

mixture composition – one generated by the wideband lambda sensor and the other generated by the narrowband lambda sensor. Simultaneously, the TDC indicator signal was being measured.

The cylinder pressure was measured for two reasons:
- to detect potential cases of incorrect combustion (knocking, misfiring),
- to compare dispersions of the pressure signal and ionization signal in the consecutive engine cycles.

Figure 4 shows one of the registered ionization signal waveforms in the fourth cylinder. The following can be distinguished: spark breakdowns, ionization current signal, reference level as well as disturbances from the ignition system.

In order to obtain the required mixture composition, a wideband lambda sensor was used. The assumed mixture composition value was obtained by controlling the fuel injection time. The throttle position can analogically be altered, yet this process is much slower.

The ionization signal has three phases (Fig. 5) [5, 7, 14]:
a) the ignition phase which lasts until discharge of a coil,
b) the flame-front phase which covers the period of flame kernel formation until the flame front leaves the area of the spark plug – chemi-ionization is dominant in this phase,
c) the post-flame phase which covers the remaining time of combustion inside the cylinder – thermal-ionization is dominant in this phase.
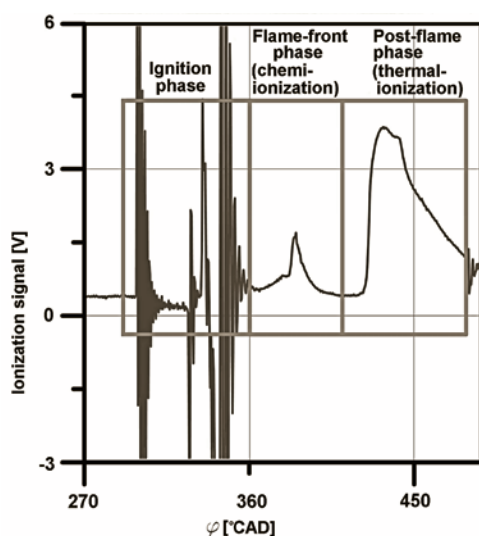
Fig. 5. Fragment of ionization signal characteristic with marked phases

When analyzing the ionization signal, the ignition phase is omitted due to the considerable effect of phenomena generated by the ignition system.

Based on the analysis of the available literature [5, 6, 7, 13, 14, 19, 20, 21] and test results obtained by the author in [8, 9, 10], it was decided that in further analysis a verifiable parameter, I_2, would be used to describe ionization in the engine cylinder. This constitutes the mean value of the thermal ionization signal.

A model of the parameter I_2 was developed as a second degree polynomial (Fig. 6):

$$I_2 = -12,37 \cdot \lambda^2 + 20,29 \cdot \lambda - 7,09 \qquad (1)$$

The correlation coefficient had a value of 0.995, while the quantile of correlation significance t was of 38.78, with only a 2.8 % share of the random component. Next, the rests were analyzed, which proved the normal distribution of the standard error δI_2, at a test probability of 0.227. The stationarity test allowed for obtaining a quantile of the t-Student test t which had a value of 0.146, i.e. much smaller than the limit value ($t_{\alpha=0.05} = 1.782$). Also, the value of the t-Student test quantile obtained in the symmetry test of the random component was smaller than the limit value ($t = 0.146$), which confirmed the correctness of the model. The correctness of the model was only undermined by the randomness test of the random component, which resulted from a small number of data on which the model identification was based. With the other test results taken into consideration, the developed model can be considered as correct.
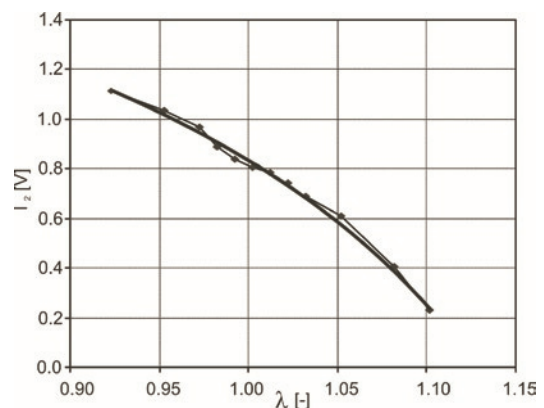

Fig. 6. Characteristics of parameter I_2 in function of λ

3.3. Comparison between the reactions of the oxygen sensor signal to lean burn and enrichment of air-fuel mixture composition

In order to compare the oxygen sensor reaction to lean burn and enrichment of the air-fuel mixture composition, some tests were conducted that involved determining time delay between fuel injection and feedback signals. The obtained results were then used to compare the delays in operation of the lambda sensor and ionization sensor.

The tests were performed at 1000 rpm rotational speed and 40 kPa mean pressure in the inlet system. The engine was in a steady thermal state. The temperatures of both the cooling agent and lubricating oil were maintained at the nominal level. At this stage, the tests consisted in decreasing or increasing the excess air coefficient by changing the injector opening time in an irregular manner.

Figure 7.a illustrates the excess air coefficient set by the fuel injection and the reaction of the classic oxygen sensor to the lean burn. Analogical data are presented in Figure 7.b. The difference between them lies in changing the mixture composition, from lean to rich. The determined time delay of the oxygen sensor signal was specified as
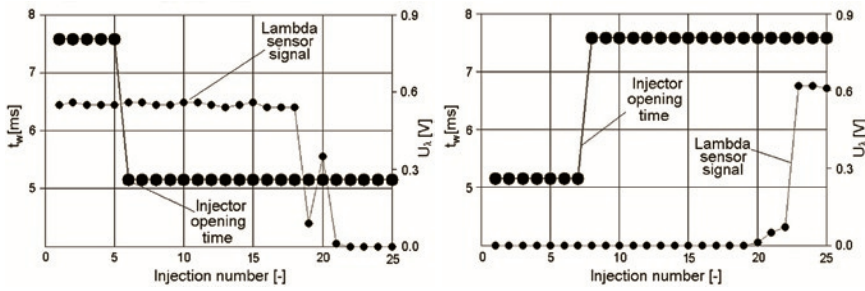
Fig. 7. Fuel injection timing and reaction of classic oxygen sensor to a) lean burning; b) enriching of air-fuel mixture composition

16 consecutive engine strokes (i.e. 16 consecutive fuel injections in a four-stroke, four-cylinder engine).

3.4. Estimating the mixture composition based on signals produced by the oxygen and ionization sensors

Having determined the time delay of the signal from the oxygen sensor relative to changes in the fuel injection time, a PI controller was designed, with the coefficient of mixture composition A_λ set to 0.1. The developed control algorithm was put into the DTS–700 electronic controller.

Figure 8 illustrates the timing for the excess air factor in the course of fuel injection control by the PI controller algorithm based on the lambda sensor signal. Two signals are compared: one estimated on the basis of the fuel injection and the other based on ionization and lambda sensor measurements.
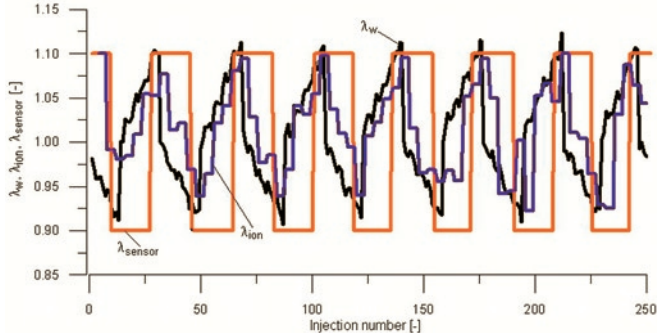
Fig. 8. Timing of excess air factor λ estimated on the basis of fuel injection λ_w, ionization signal λ_{ion} and lambda sensor signal λ_{sensor}

The value of the excess air factor generated during the fuel injection was calculated from the dependence:

$$\lambda_w = \frac{\overline{t_w}}{t_w} \qquad (2)$$

where t_w denotes a consecutive value of fuel injection time, while $\overline{t_w}$ denotes the mean value calculated on the basis of all values registered in the experiment (assuming control error symmetry).

The value of excess air coefficient estimated on the basis of the registered ionization signal I_2 was calculated in accordance with a converse model of the dependence (1).

$$\lambda = -0,11 \cdot I_2^2 - 0,05 \cdot I_2 + 1,12 \qquad (3)$$

With regard to the lambda sensor signal, it was assumed that the voltage values of the oxygen sensor greater than 0.4 V would de-

note a rich mixture ($\lambda_{sensor} = 0.9$), while the values smaller than or equal to 0.4 V would denote a lean mixture ($\lambda_{sensor} = 1.1$). It should be stressed that the estimation of λ_{ion} was done four times more rarely compared to the signals λ_{sensor} and λ_w, which resulted from measuring the ionization current in only one cylinder of this four-cylinder engine.

The timings given in Figure 8 show that substituting the lambda sensor signal with an on-off control system by the ionization signal with an one-to-one characteristic and a slight nonlinearity and considerably wide range allows for a more accurate estimation of excess air factor values.

It should be stressed that the positive verification of using ionization signal to predict mixture composition will be even more positive after considering (measuring) ionization in all the engine cylinders.

4. Simulations of fuel injection control based on signals produced by the oxygen sensor and ionization sensor

In the simulations, the designed numerical model of a gasoline engine equipped with a control system as well as the results of the simulations conducted with this engine model were used.

The fundamental role of the model was to calculate control as injector opening time based on the injection time under steady conditions and the adjusting correction calculated in the PI controller. The data for calculating the injection time under steady conditions pertained to the assumed cylinder filling, ambient conditions and the adopted value of injector output. The PI controller coefficients were calculated based on the adopted deviation for the mixture composition and time delay of measuring the feedback signal. In the model, ionization signal also based on the signal noise model is simulated.

In the simulations, 10000-cycle fuel injections were calculated, for two types of estimating air-fuel mixture composition and for several variants of the PI controller coefficients.

4.1. Numerical model of the engine with the control system

When designing the model, the following assumptions were made:
– the simulations would involve operation of a four-cylinder engine with 2000 cm^3 displacement;
– the cylinder would have 50% filling;
– the injector would be characterized by linear injection.

Given the number of calculations performed, only the final formulae have been presented [10].

The fuel mass injected into the engine:

$$m_{pal} = t_w(i) \cdot w_B \cdot \frac{1}{1 + \dfrac{k(i)}{100}} \qquad (4)$$

where:
m_{pal} – is the fuel mass,
t_w – is the injection time,
w_B – is the injector output constant set to 3.0 [mg/ms],
$k(i)$ – is the coefficient of variation of the injection model [%].

The real excess air factor:

$$\lambda_w(i) = \frac{m_{pow}}{L_t \cdot m_{pal}(i)} \qquad (5)$$

where:

λ_w – is the calculated lambda value,
m_{pow} – is the air mass,
L_t – is the theoretical demand for combustion air set to 14.7 [kg air/ kg fuel].

The control coefficient $k_s(i)$:

$$k_s(i) = \frac{\Delta t_w(i) \cdot 100}{t_w^M} \qquad (6)$$

where:

$k_s(i)$ – denotes the injection control coefficient,
t_w^M – denotes the basic injection time.

4.2. Simulation results

The simulations were performed for two measurement (estimation) variants of the excess air factor and the following eight values of the parameter A_λ: {0.005; 0.010; 0.015; 0.018; 0.020; 0.025; 0.030; 0.040}. In this way, a synthesis of the PI controller for both variants of mixture composition measurement was conducted.

The timings of the set variation coefficient of injection k, the controller response k_s, the fuel injection time t_w and the air-fuel mixture composition λ directly after the injection are shown in Figures 9 and 10.
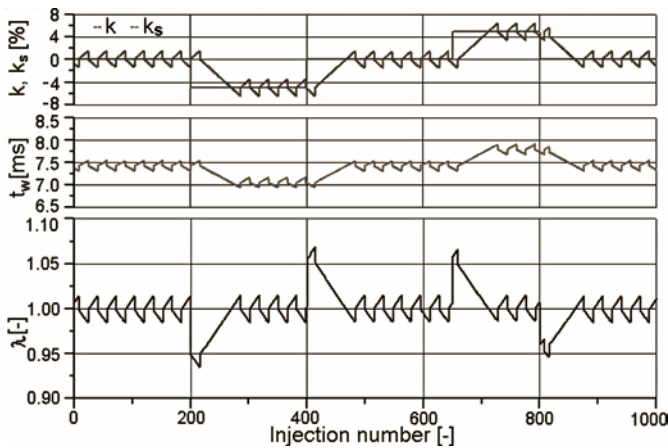
Fig. 9. Injection control with mixture composition measured by oxygen sensor at $A_\lambda = 0.015$
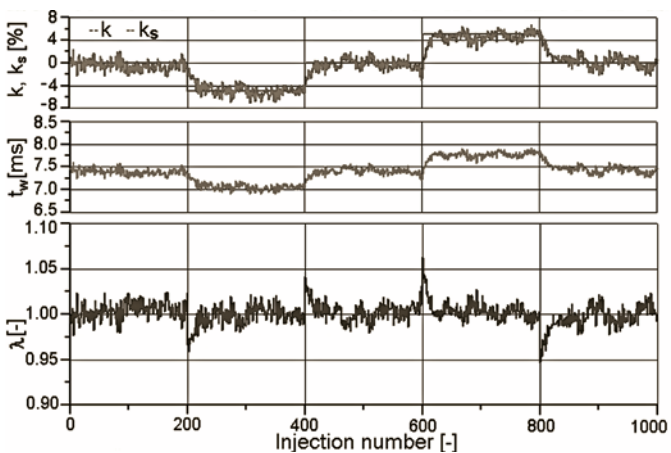
Fig. 10. Injection control with mixture composition measured by ionization sensor at $A_\lambda = 0.015$

4.3. Result analysis

For both variants, three stabilization coefficients of mixture composition were calculated. The following definitions of stabilization coefficients were taken:

1) $\delta_{\lambda 1}$ denotes the coefficient of control error energy $\varepsilon(i)$:

$$\varepsilon(i) = \lambda_w(i) - 1 \qquad (7)$$

$$\delta_{\lambda 1} = 1000 \cdot \sum_{i=1}^{10000} \varepsilon^2(i) \qquad (8)$$

2) $\delta_{\lambda 2}$ denotes the coefficient of maximum control error:

$$\delta_{\lambda 2} = \int_{i=i_1}^{i=i_2} |\varepsilon(i)|, \quad \underset{i \in \{i_1, i_2\}}{\wedge} \quad sign[\varepsilon(i)] = sign[\varepsilon(i-1)] \qquad (9)$$
$$i_{\max} \in \{i_1, i_2\}$$

where i_{max} is the maximum error coefficient $\varepsilon(i)$.

3) $\delta_{\lambda 3}$ denotes the mean error coefficient, defined as:

$$\delta_{\lambda 3} = \frac{\delta}{j_{\max}} \qquad (10)$$

where:

$$\delta = \sum_{j=1}^{j_{\max}} \sum_{i=i_1(j)}^{i=i_2(j)} |\varepsilon(i)|$$
$$\underset{i \in \{i_1(j), i_2(j)\}}{\wedge} \quad sign[\varepsilon(i)] = sign[\varepsilon(i-1)] \qquad (11)$$

Figure 11 offers a comparison of the dependence of the stabilization coefficients $\delta_{\lambda 1}$, $\delta_{\lambda 2}$ and $\delta_{\lambda 3}$ on the coefficient A_λ. In each presented case, the advantage of the controller using the ionization signal to estimate the mixture composition can be observed.

The optimum values of the PI controllers are located in the vicinity of A_λ equal to 2%, which is consistent with the observations made for real gasoline engines.

The performed simulations demonstrated the advantage of the controller using the measurement of ionization in the cylinder over the controller using the signal from the classic lambda sensor.

5. Conclusions

1. The conducted experimental tests have confirmed the suitability of using an ionization transducer in the combustion chamber to estimate values of mixture composition in the fuel injection control system.
2. A considerable dependence of the I_2 parameter characterizing the ionization signal on the λ coefficient (of the air-fuel mixture composition) was proved. The linear correlation in the range λ between 0.9 and 1.1 exceeded 0.99.
3. It was observed that the time distance between the ionization signal and fuel injection was equal to three power strokes of a four-cylinder, four-stroke engine with injection to the inlet manifold.
4. It was observed that the time distance between the signal from the oxygen sensor and fuel injection was equal up to dozens of power strokes of the four-cylinder, four-stroke engine with injection to the inlet manifold.
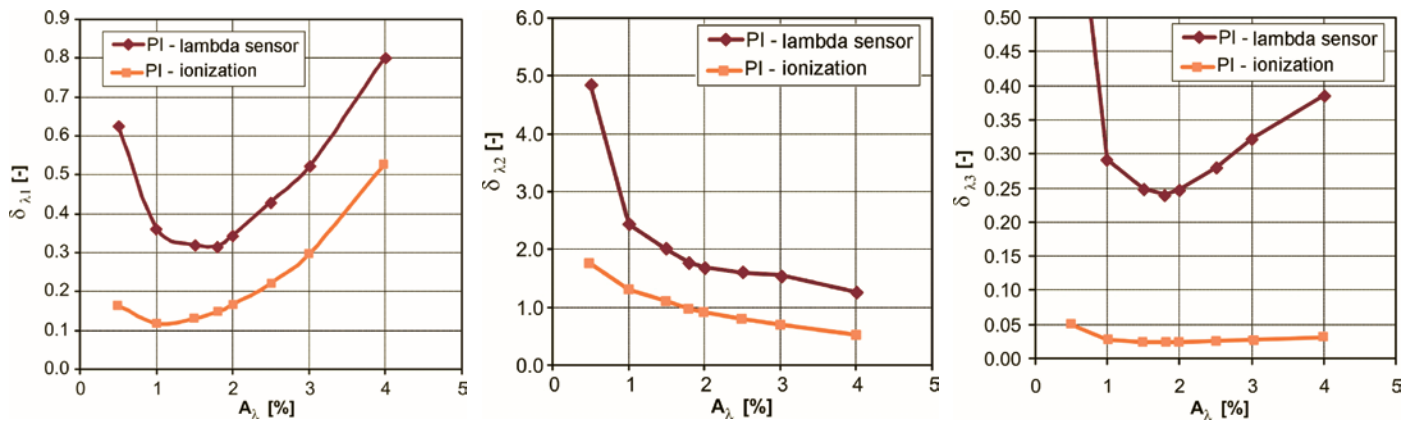
Fig. 11. Dependence of stabilization coefficients $\delta_{\lambda1}$, $\delta_{\lambda2}$, $\delta_{\lambda3}$ on coefficient A_λ for both control variants

5. By adding to the car engine control algorithm a spark plug ioniza-tion signal, an individual control of the mixture composition coef-ficient in each cylinder will be possible.

References

1. Abhijit A, George G, Naber J. Correlation of Air Fuel Ratio with Ionization Signal Metrics in a Multicylinder Spark Ignited Engine. SAE SP 2009; 2248: 45–62.
2. Abhijit A, Naber J. Ionization Signal Response during Combustion Knock and Comparison to Cylinder Pressure for SI Engines, SAE SP 2009; 2159: 25–40.
3. Ambrozik A, Kruczyński S, Łączyński J, Tomaszewski D. Badania sygnałów z sond lambda w trójfunkcyjnym reaktorze katalitycznym na potrzeby OBD II. Journal of KONES 2002; 12(3): 5–9.
4. Czarnigowski J. A neural network model-based observer for idle speed control of ignition in SI engine. Engineering Applications of Artificial Intelligence 2010; 23: 1–7.
5. Eriksson L, Nielsen L, Glavenius M. Closed Loop Ignition Control by Ionization Current Interpretation. SAE Technical Paper 1997; doi:10.4271/970854.
6. Eriksson L, Nielsen L. Ionization current interpretation for ignition control in internal combustion engines. Control Eng Pract 1997; 5 (8): 1107–1113.
7. Eriksson L, Nielsen L, Nytomt J. Ignition control by ionization current interpretation. SAE Technical Paper 1996; doi:10.4271/960045.
8. Filipek P. Badania jonizacji pomiędzy elektrodami świecy zapłonowej silnika ZI w aspekcie obserwacji procesu spalania. Raport końcowy z projektu badawczego KBN nr PB-8T 12D 022-20. Politechnika Lubelska 2001.
9. Filipek P. Badania poziomu jonizacji w komorze spalania silnika spalinowego o zapłonie iskrowym. Folia Societatis Lublinensis 2002; 11: 66–73.
10. Filipek P. Sterowanie wtryskiem benzyny w silniku o zapłonie iskrowym z wykorzystaniem sygnału jonizacji w komorze spalania. Rozprawa doktorska Politechnika Lubelska 2006.
11. Gajewski J, Jedliński Ł, Jonak, J. Classification of wear level of mining tools with the use of fuzzy neural network. Tunnelling and Underground Space Technology 2013; 35: 30–36.
12. Gajewski J, Jonak J. Towards the identification of worn picks on cutterdrums based on torque and power signals using Artificial Neural Networks. Tunnelling and Underground Space Technology 2011; 26: 22–28.
13. Gao Z, Wu X, Man Ch, Meng X, Huang Z. The relationship between ion current and temperature at the electrode gap. Applied Thermal Engineering 2012; 33(34): 15–23.
14. Gao Z, Wu X, Gao H, Liu B, Wang J, Meng X, Huang Z. Investigation on characteristics of ionization current in a spark-ignition engine fueled with natural gas–hydrogen blends with BSS de-noising method. International Journal of Hydrogen Energy 2010; 35(23): 12918–12929.
15. Hellring M, Holmberg U. A comparison of ion-current-based algorithms for peak pressure position control. SAE Technical Paper 2001; doi:10.4271/2001-01-1920.
16. Hung D, Zhu G, Danne N, McKoskey J. Knock Detection for a Large Displacement Air-Cooled V-Twin Motorcycle Engine Using In-Cylinder Ionization Signals. SAE Technical Paper 2008; doi:10.4271/2008-32-0028.
17. Lundstrom D, Schagerberg S. Misfire detection for prechamber SI engines using ion-sensing and rotational speed measurements. SAE Technical Paper 2001; doi:10.4271/2001-01-0993.
18. Minelli G, Moro D, Solieri L, Cavina N, Corti E. Knock indexes normalization methodologies. SAE Technical Paper 2006; doi:10.4271/2006-01-2998.
19. Rivara N, Dickinson P B, Shenton A T. A neural network implementation of peak pressure position control by ionization current feedback. J Dyn Syst Meas Control 2009; 131(5): 051003.
20. Saitzkoff A, Reinmann R, Berglind T, Glavmo M. An ionization equilibrium analysis of the spark plug as an ionization sensor. SAE Technical Paper 1996; doi:10.4271/960337.
21. Saitzkoff A, Reinmann R, Mauss F, Glavmo M. In-cylinder pressure measurements using the spark plug as an ionization sensor. SAE Technical Paper 1997; doi:10.4271/970857.

22. Schneider D, Lai M. Real-time air/fuel ratio control in a small SI engine using the ionic current signal. SAE Technical Paper 1999; doi:10.4271/1999-01-3323.
23. Wendeker M. Sterowanie wtryskiem w silniku samochodowym. Lubelskie Towarzystwo Naukowe, 1999.
24. Wu X. M, Gao Z, Jiang D M, Huang Z H. Experimental investigation of the effect of electrodes on the ionization current during combustion. Energy Fuels 2008; 22(5): 2941–2947.
25. Yoshiyama S, Tomita E, Hamamoto Y. Fundamental study on combustion diagnostics using a spark plug as ion probe. SAE Technical Paper 2001; doi:10.4271/2000-01-2828.

Nomenclature

A_λ	–	assumed amplitude of variation of excess air factor,
I_{jon}	–	ionization current,
I_0	–	reference current for ionization signal,
I_2	–	thermal ionization signal value,
I_I	–	ionization current in measuring circuit,
$k(i)$	–	coefficient of variation of injection model [%],
$k_s(i)$	–	injection control coefficient [%],
L_t	–	theoretical combustion air demand,
m_{pal}	–	fuel mass,
m_{pow}	–	air mass,
$^\circ CAD$	–	crankshaft angle degrees,
R_p	–	resistance of measurement resistor,
t_w^M	–	basic injection time,
t_w	–	injection time [ms],
U_R	–	voltage drop on measurement resistor,
U_z	–	DC voltage in ionization current measuring circuit [V],
U_{jon}	–	voltage of measuring ion density in combustion chamber,
U_λ	–	lambda signal voltage [V],
w_B	–	injector output constant,
ΔI_2	–	thermal-ionization signal deviation,
Δt_w	–	injection time correction,
δ_λ	–	quality control coefficient,
λ	–	oxygen content in exhaust gases,
λ_{jon}	–	calculated value of lambda based on ionization,
λ_{sonda}	–	lambda sensor signal,
λ_w	–	calculated value of lambda.

Przemysław FILIPEK, Ph.D. (Eng.)
Department of Machine Design
Faculty of Mechanical Engineering
Lublin University of Technology
ul. Nadbystrzycka 38, 20-618 Lublin, Poland
e-mail: p.filipek@pollub.pl

Piotr JAKLIŃSKI

ANALYSIS OF THE DUAL CONTROL SYSTEM OPERATION DURING FAILURE CONDITIONS

ANALIZA DZIAŁANIA DUBLOWANEGO SYSTEMU STEROWANIA W STANACH AWARYJNYCH*

The paper presents an analysis of the ASz-62IR-16E aircraft engine dual control system during failure conditions. The studies which are part of the certification tests in accordance with CS-E are described. The engine was equipped with a prototype electronic fuel injection control system. The experiments were conducted on the ASz-62IR-series piston aircraft engine test stand located in WSK "PZL-Kalisz" S.A. Robustness of the electronic control system has been studied for a single sensor failures and the effects of these failures have been evaluated. The tests included simulated failures of engine speed, manifold air pressure and engine temperature sensors. The results of these tests were described and presented on the time-domain charts. The paper concludes with an analysis and a summary.

***Keywords**: aircraft engine, certification process, bench testing, CS-E.*

W artykule przedstawiono analizę działania dublowanego systemu sterowania silnika lotniczego ASz-62IR-16E w stanach awaryjnych. Opisano badania stanowiące fragment próby dowodowej zgodnej z normą CS-E. Silnik wyposażony był w prototypowy, elektroniczny układ sterowania wtryskiem paliwa. Próby wykonano na stoisku hamownianym silników lotniczych tłokowych ASz-62IR w WSK „PZL-Kalisz" S.A. Badano odporność układu na pojedyncze awarie czujników oraz oceniano skutki tych awarii. Wykonano próby, w których symulowano awarie czujników prędkości obrotowej, ciśnienia powietrza w kolektorze dolotowym i temperatury silnika. Wyniki tych prób opisano i przedstawiono na wykresach przebiegów czasowych oraz przeprowadzono ich analizę. Artykuł zakończono podsumowaniem.

***Słowa kluczowe**: silnik lotniczy, certyfikacja, badania stanowiskowe, CS-E.*

1. Introduction

Safety is the most important requirement imposed on aircraft engines. The engines have to comply with standards which are focused primarily on reliability and robustness to failure conditions. These requirements are contained in the *"Certification Specifications for Engines"* (CS-E) issued by the European Aviation Safety Agency (EASA). For aircraft engine control systems, the standard emphasizes the system's robustness to single failure conditions. The systems are to be designed in such a way as to minimize the possibility of a failure and to mitigate its consequences [1, 7, 13].

One of the commonly applied practices to fulfill those requirements is to use a dual system. These systems are able to operate in parallel or supersede each other. However, the design process of such systems is very complex and demands a series of functional tests to be carried out. There are many different methods and techniques for system safety assessment and life prediction [6, 8, 11, 12, 14]. In this particular case, the correct system operation is definitively proved through a functional test involving failure induction [9, 10].

The targeted project no 04305/C.ZR6-6/2008 „Multi-fuel supply system for ASz-62IR engine", sponsored by the Ministry of Science and Higher Education, completed successfully in 2011. As a result of its realization, the electronically controlled fuel supply and injection system for the ASz-62IR engine was created. The version equipped with the electronic fuel injection system was labeled ASz-62IR-16E and has been undergoing a type certification process since 2010. The requirements of both certification and production preparation processes imposed a substantial series of reliability and durability tests to be carried out, in order to unequivocally demonstrate invulnerability to malfunctions of individual components of the engine equipped with the electronic gasoline injection system.

The ASz-62IR-16E aircraft engine is a 9-cylinder, single-row, air-cooled, radial piston engine with a displacement of 29.87 dm3. The engine underwent numerous constructional and technological modifications since the beginning of its production in 1961. The engine has two valves and two spark plugs per cylinder. It is fuelled by the 100 LL aviation gasoline. The ignition system is composed of two independent ignition subsystems, one per set of spark plugs. The technical specification of the engine are presented in table 1.

The developed electronic fuel injection system is based on the known automotive conception of a multipoint indirect fuel injection, but the control of engine operation is performed in an open loop. The fuel from the central tank is taken by the mechanical fuel pump, filtered and supplied under the correct pressure to the fuel manifold. The fuel is then led to the individual injectors mounted in the inlet pipes of the corresponding cylinders. The fuel pressure is regulated by the pressure regulator, which directs excess fuel back to the tank [4, 5].

For safety reasons, the fuel injection system is a dual system. It is composed of two control subsystems with two independent sets of sensors and one set of actuators - the fuel injectors. The fundamental objective of the design was to ensure that a single failure, be it a failure of a sensor or other system component, cannot adversely affect, or the effect will be negligible, the engine operation. Such assurance is consistent with the requirements contained in the *"Certification Specifications for Engines"* (CS-E) issued by the European Aviation

Table 1.   Technical specification of the ASz-62IR engine

Name	Value
Engine diameter	1380 mm
Length	1130 mm
Dry weight of an engine	567 kg (±2%)
Cylinder diameter	155,5 mm
Piston stroke	174,5 mm
Total displacement	29,911 dm^3
Compression ratio	6,4±0,1
Maximum power at 2200 RPM, Pk=1050 mmHg	1000 KM (735 kW)
Rated power at 2100 RPM, Pk=900 mmHg	820 KM (603 kW)
Rated power at an altitude of 1500 m	840 KM (618 kW)
Power at 2030 RPM, Pk=830 mmHg	738 KM (543 kW)
Power at 1930 RPM, Pk=745 mmHg	615 KM (452 kW)
Power at 1770 RPM, Pk=665 mmHg	492 KM (362 kW)
Average fuel consumption	ca. 200 dm^3/h
Maximum fuel consumption	ca. 330 dm^3/h
Weight to power ratio	0,57 kg/KM (0,42 kg/kW)
Power to displacement ratio	33,43 KM/dm^3 (24,58 kW/dm^3)

Safety Agency. The requirements imposed on the engine control system are described in CS-E 50 [1].

The supplemental type certification process for the ASz-62IR-16E engine involves theoretical analyses and certification tests developed in cooperation with and approved in advance by the certification authority (EASA), including tests carried out during both normal operation of the system and during failure conditions. This meets the requirements set forth in the above-mentioned standards.

2. The objective and scope of research

The purpose of the research was to analyze the operation of the dual control system during failures of selected sensors. These studies were conducted in order to ensure compliance with selected provisions of the CS-E 50 "Engine Control System" [1] with particular emphasis on:

Point (b):

"*(b) Control Transitions. It must be demonstrated that, when a Fault or Failure results in a change from one Control Mode to an-*

other, or from one channel to another, or from the Primary System to the Back-up System, the change occurs so that:

(1) The Engine does not exceed any of its operating limitations,

(2) The Engine does not surge, stall, flame-out or experience unacceptable thrust or power changes or oscillations, or other unacceptable characteristics (...)"

Point (c):

(c) Engine Control System Failures. The Engine Control System must be designed and constructed so that:

(1) The rate for Loss of Thrust (or Power) Control (LOTC/LOPC) events, consistent with the safety objective associated with the intended aircraft application, can be achieved,

(2) In the Full-up Configuration, the system is essentially single Fault tolerant for electrical and electronic Failures with respect to LOTC/LOPC events.

(3) Single Failures of Engine Control System components do not result in a Hazardous Engine Effect,

(4) Foreseeable Failures or malfunctions leading to local events in the intended aircraft installation, such as fire, overheat, or Failures leading to damage to Engine Control System components, must not result in a Hazardous Engine Effect due to Engine Control System Failures or malfunctions."

The scope of the research included certification tests described in the test program, including demonstration of the system robustness to single failures *"failure conditions tests - failure of a single sensor"* and the assessment of the impact of individual failures. The sensors involved in the tests are presented in table 2.

3. Test bench and research methodology

The study was conducted on the ASz-62IR-16E engine test stand located in a WSK „PZL-Kalisz" S.A. facility. The test bench is equipped with measurement devices allowing the tests to be compliant with the provisions imposed by the CS-E. Additionally, as it is practiced by other authors [2, 3, 9], the test bench was equipped with proprietary measurement systems:

1. The diagnostics system allowing to collect and store information about the current operation state of the engine control system 10 times per second;
2. The device allowing to induce failures of individual components during the engine operation – the signal breaker (Fig. 1).

Table 2.   Sensors of the control system for the ASz-62IR-16E aircraft engine

| Name	Symbol	Type	Manufacturer
Manifold air pressure sensor	MAP	ATM.1ST - 0,22 – 2 pcs	STS Sensor Technik Sirnach AG
Fuel pressure sensor	FP	ATM.1ST - 0,8 – 2 pcs	STS Sensor Technik Sirnach AG
Air temperature sensor	MAT	TP - 371 K-4-22-1000-M2x1.5-SPEC – 2 pcs TP-952-2-2T-SPEC 2x45+120°C/4-20mA (measuring transducer) – 2 pcs	CZAKI Thermo-Product
Fuel temperature sensor	FT	TP - 371 K-4-22-1000-M2x1.5-SPEC – 2 pcs	CZAKI Thermo-Product
Engine temperature sensor	ET	TP - 373 K-1.0-118-SPEC - 2 pcs TP-952-SPEC 2x45+300°C/4-20mA (measuring transducer) – 2 pcs	CZAKI Thermo-Product
Rotational speed sensor	RPM	1GT101DC – 2 pcs	Honeywell International, Inc.
Throttle position sensor	TPS	9851 (clockwise) – 1 pc 9852 (counterclockwise) – 1 pc	BEI Sensors
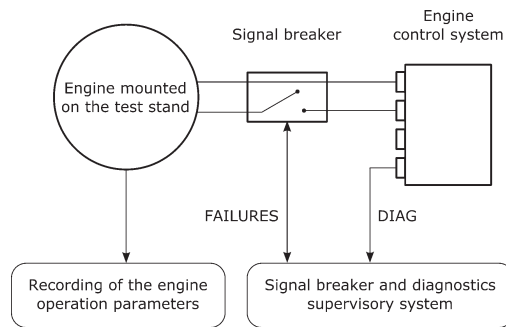
Fig. 1. Overview of the test system

The signal breaker is a device inserted between the engine and the controller. It is designed to physically disconnect electrical circuits connecting the controller to the sensors and injectors.

During the tests, relays embedded in the circuits between the engine harness and the controller were appropriately driven using a computer program. The relays were connected in such a way that the corresponding circuit was connected during the inactive state of the relay. By that means, failures of individual sensors and injectors were simulated.

The signal breaker and diagnostics system were operated with the supervisory system in a form of a PC with special software that allows to induce failures (the FAILURES program) and to record the data sent by the controller (the DIAG program). This allowed to conduct the tests and store the results:

DIAG – the program that allows to register the engine operation by recording measured values, coefficients of the control algorithm and the resulting injection times generated by the controller;

FAILURES - the program that allows to break electrical circuits connecting each sensor and injector to the controller through a physical change of a relay state in the signal breaker.

Table 3.   Quantities recorded during the tests

Symbol	Name
t_o	Ambient temperature, ºC
B	Ambient pressure, mmHg
ΔB	Absolute humidity, mmHg
t_{pg}	Temperature of inlet air, ºC
P_{01}	Oil pressure in the oil pump, kG/cm²
P_{02}	Oil pressure in the back lid, kG/cm²
P_{03}	Oil pressure in the reducer, kG/cm²
P_p	Fuel pressure, kG/cm²
t_1	Temperature of the oil entering the engine, ºC
t_2	Temperature of the oil exiting the engine, ºC
t_{head}	Cylinder head temperature, ºC
W	Oil flow rate, kg/min
Q	Oil cooling power, kcal/min
n	Crankshaft rotational speed, 1/min
P_k	Manifold air pressure, mmHg
N_{eo}	Power, HP
C_e	Specific fuel consumption, g/KMh
t_{inj}	Fuel injection time, ms
k_{ch}	Cylinder head cooling coefficient, %
t_{fuel}	Fuel temperature, ºC
t_{air}	Manifold air temperature, ºC
a_{TPS}	Throttle position angle, º

A second, independent recording of the engine operation was performed using the test bench measurement system. The registered values are presented in table 3.

The second, independent measurement recording is required for certification tests compliant with the CS-E.

All tests included a comparison of the engine operation without failure and during a single failure of a chosen sensor at 75% of the nominal engine power defined by the rotational speed n=1910 RPM and manifold air pressure Pk=745±15 mmHg (99.325±2 kPa). During the tests, the engine's operation parameters were continuously recorded. During failure conditions, the injection times, fuel consumption, cylinder head temperatures and output power were measured and evaluated by comparing with the values obtained during normal engine operation. Failure of every sensor was simulated.

In accordance with the control algorithm objectives, a malfunction of a single sensor triggers an automatic detection of an associated failure condition and, as a matter of course, the measurement process is switched from the dual sensor mode to the single sensor mode utilizing only one, operational sensor. This transition may cause a short-lived variation of the time, but not greater than 3% during steady states and 7% during transient states. Variation of output power, fuel consumption and cylinder head temperatures are not expected to exceed 5%.

4. Certification tests

4.1. Failure of the rotational speed sensor

The figure below shows the time plot graph of the injection time and rotational speed measured by both control subsystems during simulated failure of RPM sensor #1 (Fig. 2) and RPM sensor #2 (Fig. 3). Disconnection of the RPM sensor #1 occurred at t=78 s. Disconnection of sensor #2 occurred at t=40 s.
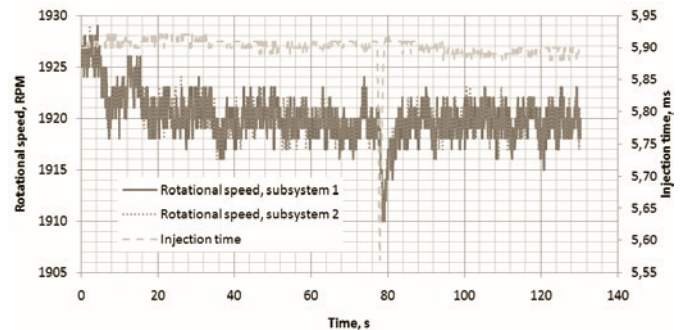

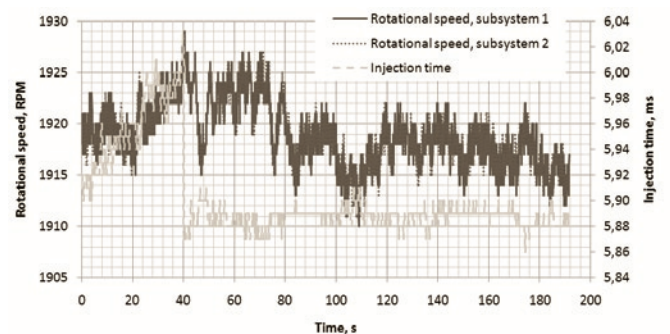Fig. 2.   Injection time and rotational speed during simulated failure of RPM sensor #1

Fig. 3.   Injection time and rotational speed during simulated failure of RPM sensor #2

The figures below present the results of the measurements of the engine operating parameters during both normal operation and failure conditions of the RPM sensor #1 (Fig. 4) and sensor #2 (Fig. 5).
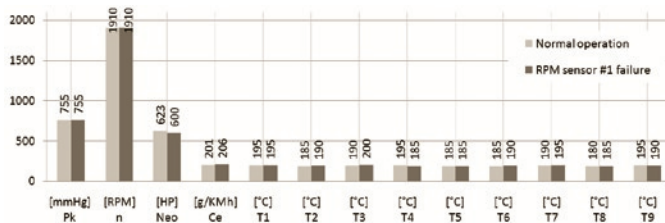

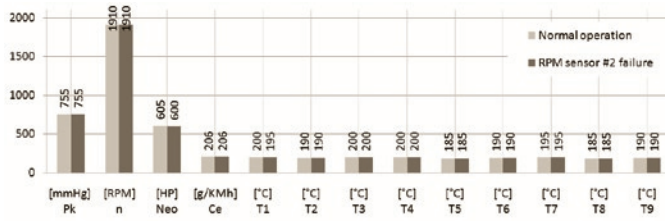*Fig. 4.   Measured values of selected engine operation parameters during simulated failure of RPM sensor #1*

Fig. 5.   Measured values of selected engine operation parameters during simulated failure of RPM sensor #2

Both rotational speed sensors included in the control system are triggered by the same tooth of a pulse wheel. Each sensor is connected in parallel to both control subsystems. Due to manufacturing and assembly tolerances, the signals from both sensors are slightly shifted in time. The control algorithm takes into account the earlier signal. Only signals from rotational speed sensors are processed in this manner.

Analysis of the control system operation during failure of RPM sensor #1 shows that failure of the sensor results in a momentary decrease of the rotational speed by 10 RPM and decrease of the injection time by 0.3 ms (which accounts for 5% reduction of the injection time). This state lasts for 2 seconds and after that the system returns to its normal operation. This is confirmed by the results of measurements of the operation parameters of the engine. The failure contributes to a 3.5% reduction of the output power and 2.5% reduction of the specific fuel consumption. The cylinder head temperatures stayed at the same level with variation not exceeding more than 5°C, which in fact is a typical variation for this engine on the test stand.

Analysis of the control system operation during failure of RPM sensor #2 reveals that failure of the sensor results in a momentary decrease of the rotational speed by 5 RPM and increase of the injection time by 0.1 ms (which accounts for 2% increase of the injection time). This state lasted for about 2 seconds. The injection time stabilized immediately after the failure, which is confirmed by the measurements of the engine's operation parameters. The failure contributes to a negligible loss of power (0.8%) without altering the specific fuel consumption. The cylinder head temperatures stayed at the same level with variation not exceeding more than 5°C, which in fact is a typical variation for this engine on the test stand.

4.2. Failure of the manifold air pressure sensor

The control system includes two manifold air pressure sensors, both measuring the same pressure. Each control subsystem is connected to one of the sensors. The values measured by each sensor is exchanged by the subsystem by a means of digital communication link. The control algorithm uses an arithmetic mean based on both values, provided that both values are considered correct by an assessment procedure. When one of the measured values is considered incorrect (e.g. outside a specified range), only the valid one is used. This solu-

tion is common for algorithms processing the values obtained from the temperature, pressure and throttle position sensors.

Fig. 6 presents the time plot graphs of the rotational speed and the injection time, whereas fig. 7 shows the signals from both manifold air pressure sensors and the resulting pressure value used for fuel injection time calculation during simulated failure of the MAP sensor #1. The failure condition begins at t=62s and lasts until t=162s.
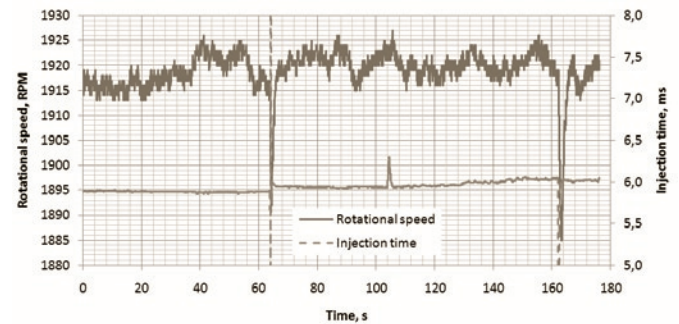

Fig. 6.   Injection time and rotational speed during simulated failure of MAP sensor #1
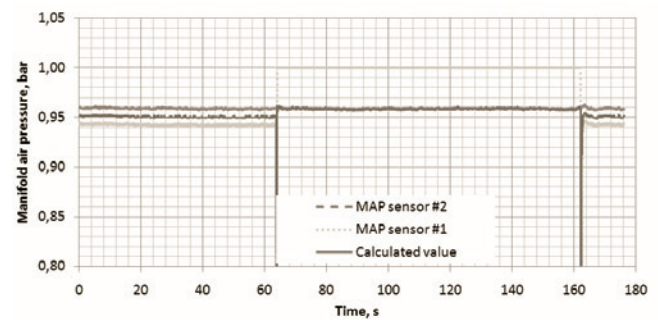

Fig. 7.   Measured and calculated values during simulated failure of MAP sensor #1

The results of the measured engine operation parameters during normal operation and the failure state of the MAP sensor #1 are presented in fig. 8.
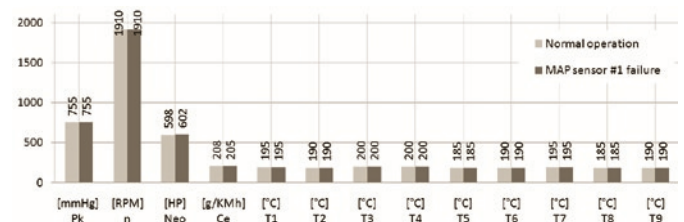

Fig. 8.   Measured values of selected engine operation parameters during simulated failure of MAP sensor #1

Fig. 9 presents the time plot graphs of the rotational speed and the injection time, whereas fig. 10 shows the signals from both manifold air pressure sensors and the resulting pressure value used for fuel injection time calculation during simulated failure of the MAP sensor #2. The failure condition begins at t=62 s and lasts until t=158 s.

The results of the measured engine operation parameters during normal operation and the failure state of the MAP sensor #2 are presented in fig. 11.

Failure of the MAP sensor #1 causes the control system to set its corresponding manifold air pressure value with a default value of 1 bar. This value is not used further in fuel injection time calculation. The transition causes a momentary calculation error resulting from averaging of the measured signals. Such a rapid change of the manifold air
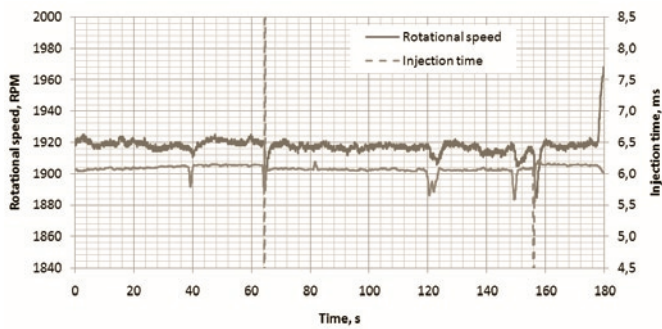
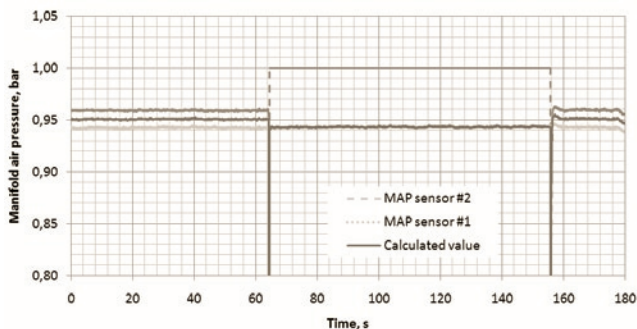*Fig. 9. Injection time and rotational speed during simulated failure of MAP sensor #2*

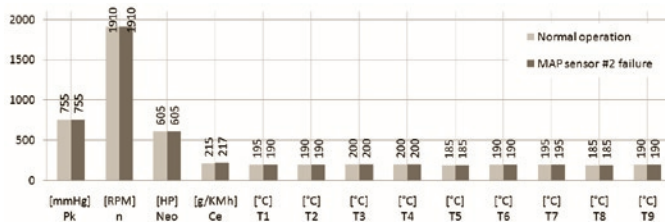*Fig. 10. Measured and calculated values during simulated failure of MAP sensor #2*

Fig. 11. Measured values of selected engine operation parameters during simulated failure of MAP sensor #2

pressure value influences the fuel film compensation algorithm, which contributes to momentary increase of the injection time to 12 ms, following a decrease to 0 ms in the next cycle. Such behavior is consistent with the design of the control algorithm. This results in a short-lived decrease of the rotational speed by 20 RPM for about 1 second.

During the failure condition, the injection time is increased by 0.1 ms (1.5%). The rotational speed is maintained at a constant level, equal to the engine speed during normal operation.

The recovery from failure condition results in a return of the control algorithm from a single sensor mode back to the dual sensor mode, resulting in an insignificant decrease of the pressure value used in calculations. The transition causes a second execution of the fuel film compensation algorithm, resulting in a one cycle injection cut-off. This is consistent with the design of the control algorithm.

The failure condition of the MAP sensor #1 results in a small increase of the engine output power by 0.5% and decrease of the specific fuel consumption by 1.4%. The temperatures of the cylinder heads remained unchanged.

The failure condition of the MAP sensor #2 results in similar behavior. The state transition causes a momentary error in fuel injection time calculation. Such a rapid change of the measured manifold air pressure manifests itself with a dynamic adjustment of the injection time, resulting in a momentary increase of the injection time to 12 ms, following a decrease to 0 ms in the next cycle. Such behavior

complies with the design of the control algorithm. It results with a decrease of the rotational speed by 15 RPM for 1 second.

During the failure condition the injection time is reduced by 0.1 ms (1.5%). The rotational speed is maintained on a constant level, equal to the speed during normal operation of the engine.

The recovery from failure condition results in a return of the control algorithm from a single sensor mode back to the dual sensor mode, resulting in an insignificant decrease of the value used in calculations. The transitions triggers execution of the fuel film compensation algorithm, resulting in a one cycle injection cut-off. This is consistent with the design of the control algorithm.

The failure of the MAP sensor #2 had no measureable impact on the output power. The cylinder head temperatures and specific fuel consumption also remained unchanged.

4.3. Failure of the engine temperature sensor

The control system includes two engine temperature sensors. The ET sensor #1 measures the temperature of cylinder head #2 and the ET sensor #2 measures the temperature of cylinder head #7. The signals from the sensors are processed by external signal measuring transducers and then fed to the corresponding control subsystems. Measured values are different. The control algorithm uses the greater of the two values, provided that both values are considered correct by an assessment procedure.

Fig. 12 presents the time plot graphs of the rotational speed and the injection time, whereas fig. 13 shows the signals from both engine temperature sensors and the resulting temperature value used for fuel injection time calculation during simulated failure of the ET sensor #1. The failure condition begins at t=50 s and lasts until t=152 s.
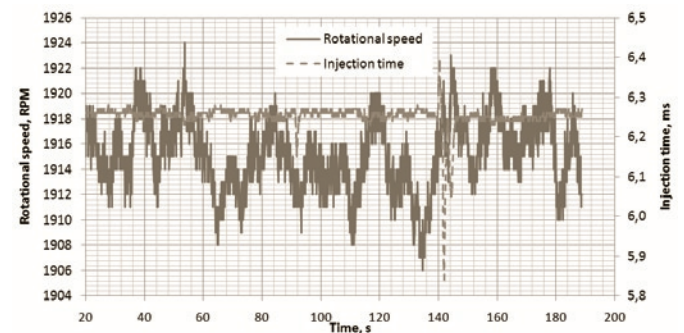

Fig. 12. Injection time and rotational speed during simulated failure of ET sensor #1
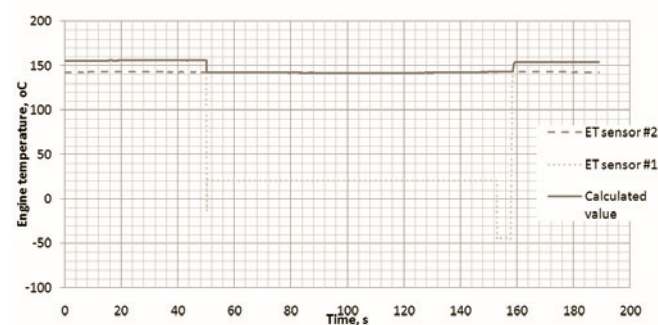

Fig. 13. Measured and calculated values during simulated failure of ET sensor #1

The results of the measured engine operation parameters during normal operation and the failure state of the ET sensor #1 are presented in fig. 14.
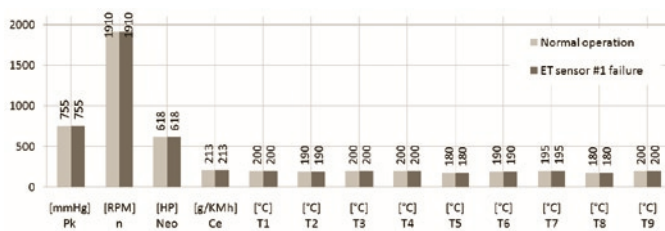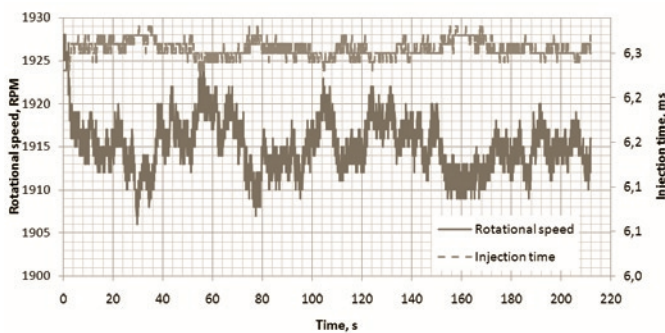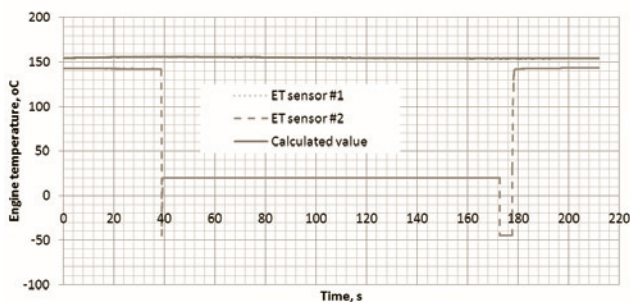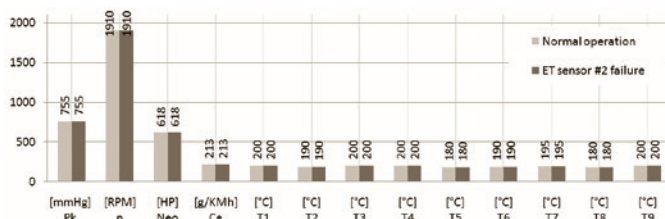
Fig. 14. *Measured values of selected engine operation parameters during simulated failure of ET sensor #1*

Fig. 15 presents the time plot graphs of the rotational speed and the injection time, whereas fig. 16 shows the signals from both engine temperature sensors and the resulting temperature value used for fuel injection time calculation during simulated failure of the ET sensor #2. The failure condition begins at t=39 s and lasts until t=172 s.

Fig. 15. *Injection time and rotational speed during simulated failure of ET sensor #2*

Fig. 16. *Measured and calculated values during simulated failure of ET sensor #2*

Fig. 17. *Measured values of selected engine operation parameters during simulated failure of ET sensor #2*

The results of the measured engine operation parameters during normal operation and the failure state of the ET sensor #2 are presented in fig. 17.

Failure of the cylinder head temperature sensor may result in a change of the calculated engine temperature, which is determined by the higher value from both sensors. Due to the nature of the transducer operation, the drop of the measured value is not instantaneous, but takes about 0.5s. Consequently, the response of the control system to the failure condition is delayed until the signal reaches a value outside valid operational range. As the engine temperature value is used by the engine cooling algorithm, the injection time is altered only when the engine temperature is above a certain threshold. This was not the case in the given test, therefore there was no alteration of the injection time.

During the failure condition the engine operates properly and the injection time is consistent with the injection time during fully functional system operation.

During recovery from the failure condition, the sensor and its signal transducer is powered back on, but the transducer is fully operational only after a 7 second delay, which contributes to a significant error in engine temperature's calculation. However, it does not affect the injection time.

The failure condition had no effect on the engine performance. There were no changes in engine power or fuel consumption. The actual cylinder head temperatures also were unchanged.

Since the value measured by the ET sensor #2 was lesser then the ET sensor #1, the calculated engine temperature remained unaffected during ET sensor #2 failure condition, which resulted in no change of the engine performance.

5. Conclusions

Although the described sensors were of various types and each sensor type was utilized in a different manner by the control algorithm, no single failure of any sensor had a negative impact on the engine's operation.

The tests showed that no single sensor malfunction results in loss of engine's performance. The engine and the control system operated properly without going beyond the accepted limits. In most cases, there was no change in engine operation parameters greater than 5% and there was no power output variation beyond acceptable limit.

The tests demonstrated that the requirements contained in CS-E b (1) and (2) were satisfied. During failure conditions there was no engine usability reduction, which satisfies the objectives of CS-E 50 b (1), and there was no engine stall, unwanted oscillations or other unacceptable phenomena, which satisfies CS-E 50 b (2).

The tests proved that the designed control system is completely immune to single sensor failures. In all examined cases, a single sensor failure did not result in a loss of power control, which is required by CS-E 50 c (2).

Simultaneously, the Unsafe Engine Condition did not occur and there was no indication such a possibility could arise, which satisfies the requirements imposed by CS-E 50 c (3), (4).

It can be concluded that the design and control algorithm is insusceptible to a single sensor failure.

References

1. Europejska Agencja Bezpieczeństwa Lotniczego, Specyfikacje Certyfikacyjne dla Silników CS-E, Aneks do Decyzji Dyrektora Wykonawczego 2010/015/R, Zmiana 3, 23 grudnia 2010.
2. Gęca M, Wendeker M, Czarnigowski J, Jakliński P, Nazarewicz A, Pietrykowski K, Barański G. Stanowisko laboratoryjne do badania samolotowego układu wtryskowego. P07-C149, PTNSS Kongres 2007.
3. Gronostajski Z, Hawryluk M, Kaszuba M, Sadowski P, Walczak S, Jabłoński D. Systemy kontrolno-pomiarowe w przemysłowych procesach kucia matrycowego. Eksploatacja i Niezawodnosc – Maintenance and Reliability 2011; 3 (51): 62–69.

4. Jakliński P, Wendeker M, Czarnigowski J, Duk M, Zyska T, Klimkiewicz J. The Indicated Pressure Analyses of Aircraft Radial Piston Engine Fuelled by 100LL and ES95 Gasoline. PTNSS-2009-SC-065, Combustion Engines, Silniki Spalinowe, Special Series 2009-SC2: 162–170.

5. Jakliński P, Wendeker M, Czarnigowski J, Duk M, Zyska T, Klimkiewicz J. The Comparison of the Operating Parameters in an Aircraft Radial Piston Engine Fuelled by 100LL and ES95 Gasoline. PTNSS-2009-SS1-C064, Combustion Engines, Silniki Spalinowe 1/2009: 52–59.

6. Kowalczyk M, Czmochowski J, Rusiński E. Budowa modelu diagnozowania stanów awaryjnych organów roboczych koparki wieloczerpakowej. Eksploatacja i Niezawodnosc – Maintenance and Reliability 2009; 2 (42): 17–24.

7. Lewitowicz J, Kustroń K, Podstawy eksploatacji statków powietrznych cz.1. Warszawa: Wydawnictwo ITWL, 2001.

8. Li Y, Huang H, Liu Y, Xiao N, Li H. Nowa metoda analizy drzewa uszkodzeń; rozmyta analiza dynamicznego drzewa uszkodzeń. Eksploatacja i Niezawodnosc – Maintenance and Reliability 2012; 14 (3); 208–214.

9. Lingaitis LP, Mjamlin S, Baranovsky D, Jastremskas V. Badania eksperymentalne operacyjnej niezawodności eksploatacyjnej silników diesel dla spalinowozów. Eksploatacja i Niezawodnosc – Maintenance and Reliability 2012; 14 (1): 6–11.

10. Olearczuk E, Sikorski M, Tomaszek H. Eksploatacja samolotów (elementy teorii). Warszawa: Wydawnictwo MON, 1978.

11. Pang Y, Huang H, Xiao N, Liu Y, Li Y. Posybilistyczna analiza niezawodnościowa systemu naprawialnego z pominiętym lub opóźnionym efektem uszkodzenia. Eksploatacja i Niezawodnosc – Maintenance and Reliability 2012; 14 (3): 195–202.

12. Wang Z, Huang H, Du X. Projektowanie niezawodnościowe z wykorzystaniem kilku strategii utrzymania. Eksploatacja i Niezawodnosc – Maintenance and Reliability 2009; 4 (44): 37–44.

13. Yu T, Cui W, Song B, Wang S. Ocena wzrostu niezawodności w bezzałogowym statku latającym podczas kolejnych faz badania w locie. Eksploatacja i Niezawodnosc – Maintenance and Reliability 2010; 2 (46): 43–47.

14. Zhou Y, Ma L, Mathew J, Sun Y, Wolff R. Prognozowanie trwałości środków technicznych z wykorzystaniem wielu wskaźników degradacji i zdarzeń awaryjnych w ujęciu modelu ciągłej przestrzeni stanów. Eksploatacja i Niezawodnosc – Maintenance and Reliability 2009; 4 (44): 72–81.

Piotr JAKLIŃSKI, Ph.D. (Eng.)
Department of Thermodynamics, Fluid Mechanics and Aviation Propulsion Systems
Lublin University of Technology
Mechanical Faculty
ul. Nadbystrzycka 38D, 20-618 Lublin, Poland
e-mail: p.jakliński@pollub.pl

Piotr TARKOWSKI
Jarosław PYTKA
Piotr BUDZYŃSKI
Łukasz KAZNOWSKI

A TEST METHOD FOR EVALUATION AND CLASSIFICATION OF UNSURFACED AIRFIELDS

METODA OCENY I KLASYFIKACJI GRUNTOWYCH NAWIERZCHNI LOTNISKOWYCH*

The study presents a project of a method for testing, evaluation and classification of unsurfaced airfields, with respect to wheel-soil interactions analysis. Basic theoretical considerations have been included in this study, together with a review of existing methods as well as instrumentation, which will be applied in the presented method. It is supposed the method to be advantageous for a better utilization of grassy, unsurfaced airfields in Poland and other EU countries, mainly through improving the safety level of airfield operations.

Keywords*: airfield operations, general aviation aircrafts, unsurfaced airfiels, airstrips, test methods.*

W pracy przedstawiono projekt metody oceny gruntowych nawierzchni lotniskowych w aspekcie warunków współpracy kół podwozia samolotu z nawierzchnią. Zawarto podstawy teoretyczne, dostępne metody pomiarowe możliwe do zastosowania w projektowanej metodzie a także opisano projektowane rozwiązania. Przewiduje się, że przygotowywana do wdrożenia metoda może przynieść znaczne korzyści w zakresie lepszego wykorzystania licznych lotnisk trawiastych w Polsce, także w aspekcie bezpieczeństwa operacji lotniczych.

Słowa kluczowe*: naziemne operacje lotnicze, lotnictwo ogólne, samoloty, lotniska gruntowe i darniowe, metody badań.*

1. Introduction

Aircraft ground performance on grassy airfields is weakened and depends upon a number of factors that we are unable to control. Safe take-offs and landings on an airfield require that the pilot know how the actual conditions may affect take-off or landing distance. Deformability of a soft surface affects rolling friction and traction of aircraft wheels. Moreover, there is a significant and poorly predicted effect of meteorological conditions upon the latter. Thus, the safety of aircraft operations on unsurfaced airfields requires the knowledge of their actual conditions with regard to a given aircraft.

For testing and classification of paved airfields, the ICAO has adopted two methods: the LCN (**L**oad **C**lassification **N**umber) method, which is currently out of use and an ACN-PCN system [4], introduced between 1980 and 1983. This system uses two values: ACN – aircraft classification number and PCN, pavement classification number. The value of ACN is dependent upon airplane mass, center of gravity location, wheel base, and tire inflation pressure. Various experimental methods can be used to determine PCN. Moreover, airfield test methods include friction testers, i.e. ASFT (**A**irport **S**urface **F**riction **T**ester) or SARSYS Friction Tester [1, 10, 17] as well as the use of specially designed, instrumented vehicles (for example the *CRREL Insrumented Vehicle* [18]). In these methods, braking friction is determined and the methods are widely used in northern hemisphere and cold regions, where runways are often covered by ice or snow. The presented methods are mainly applied for rigid surfaces, not for soft grassy airfields. They utilize models of wheel-surface in-

teractions based on Boussinesque or Westergaard theories [9], which may perform not exactly in cases of moist surface and for a variety of soils. Consequently these methods do not ensure the required level of accuracy with their predictions. From the above mentioned, an introduction of a new method, especially designed for soft, unsurfaced airfields is reasonable.

An increase of air transport is one of the priorities in new EU countries, like Poland. The utilization of unsurfaced airfields for general aviation operations may include such activities as crop dusting, fire fighting, personal transport on demand (the so called "air taxi"), medical or rescue flights, sport aviation, etc. There are lots of small and medium, unsurfaced airfields in the EU countries and they are important elements of ATM (**A**ir **T**raffic **M**anagement), mainly for general aviation. Expected effects of utilization of the presented methods could be very advantageous since the GA community forms a strong complementation for the "big" air transport industry.

2. An idea of the proposed method

Authors' idea was to propose an integrated method which would enable to evaluate the surface of an airfield, giving a precise information for pilots or airfield operators about the actual surface conditions. The purpose of the method is determination of important parameters, describing wheel-soil interactions and influencing the resulting aircraft ground performance:
- takeoff distance;
- ground roll distance;

– passenger comfort.

The important parameters are rolling and braking friction as well as surface roughness. The users of the method will be operators of airports and pilots of general aviation aircrafts. Knowing the actual values of the parameters, it would be possible to determine ground performance of a given airplane. The method consists of the following elements:

- braking friction measurement, performed with the use of a wheel tester;
- rolling friction measurement, very important for soft surface airfields, not included in other known methods;
- surface roughness measurement with the use of LIDAR method (**L**ight **D**etection **a**nd **R**anging);
- a mobile application, which will be an end-user toll of the method, enabling the calculation of ground performance of a given aircraft, knowing the measured parameters of the surface.

This paper covers the background of the method together with details of instrumentation used in the method.

3. Theoretical background of the method

3.1. Rolling friction of a wheel

Rolling friction of an aircraft wheel on an unsurfaced airfield affects ground performance of a given aircraft significantly. Stinton [15], gives values of rolling friction coefficient for a grassy airfield: 0,05 and 0,08, for short and long grass, respectively as well as 0,13 for long wet grass. The effect of high rolling friction on grassy surfaces is a significant increase of takeoff distance, typically by 10 to 25% when compared to paved runways. It is of great importance in the case of numerous private and casual airstrips, which are short or sometimes surrounded by trees or other obstacles. Filippone [8] gives simplified formulas to calculate takeoff ground roll l_r and landing roll l_d as functions of rolling friction, f_{RF} and braking friction, μ:

$$l_r = \frac{mV^2}{2\frac{\eta P}{V} - \frac{1}{4}\rho A C_D V^2 - f_{RF}mg} \qquad (1)$$

$$l_d = \frac{1}{2g\left(\mu + f_{RF}\right)}\ln\left(\frac{1}{2}\rho A\left(C_D - f_{RF}C_L\right)V^2 + mg\left(\mu + f_{RF}\right)\right) \quad (2)$$

where: m – aircraft mass, V – touchdown speed, η – propeller efficiency, P – engine rating power, A – wing area, C_D – aerodynamic drag coefficient, C_L – lift coefficient, ρ – air density, g – Earth's gravity.

Rolling friction on paved runway is easy to determine. Frequently used methods include pull test or coast down procedure. On soft, deformable surfaces at lower speed, rolling friction of aircraft wheels can be measured with the use of pull test method or an indirect method, in which a rut depth is measured and this parameter is used for further calculations of rolling drag.

Some problems arise by higher speed, 10 m/s and more. Dynamics of soil deformation result in additional phenomena, such as the so called „spray effect" besides the wheel, with soil granules ejected outside with a relative high kinetic energy. Traditional methods of rolling friction measurements fail in such situations and only special instrumentation enables to fix the methodological problems. It is a method with the use of an instrumented vehicle, equipped with the so called "fifth wheel" or a trailer, enabling the determination of rolling friction at high speed. Also, a multi-channel rotating wheel dynamometer, installed in a test vehicle could be a good solution here.

Measuring the wheel forces and moments with the use of a rotating dynamometer was introduced and practically applied for testing

wheel performance on a grassy airfield by the present authors in the cited work [13]. In this method, wheel forces and moments measured during a test ride can be recalculated into rolling friction coefficient. The following measures have to be known or determined during a test run:

- M_y – driving or braking moment on a test wheel;
- F_v – vertical load on a test wheel;
- r_d – dynamical radius of the tyre.

Rolling friction coefficient can be calculated from the equation below:

$$f_{RF} = \frac{M_y}{r_d} \times \frac{1}{F_v} \qquad (3)$$

Preliminary tests with the use of an instrumented vehicle with a rotating wheel dynamometer were conducted on a grassy airfield, what is shown in figure 1. Riding at 3 m/s forward speed, braking moment on the measuring wheel has been measured together with vertical load on this wheel. The rotating dynamometer was installed in the right front wheel and it was in rolling mode (not driven) during the test. Measured data has been averaged for a chosen range, where the values of measured forces tend not to oscillate. A sample set of data for the rolling friction force, F_{RF}, calculated from measured braking moment, M_y is shown in figure 2. It is to point out that the method enabled to determine of rolling friction for a given tyre, which, in the case of the tests performed in the cited work, wasn't any typical aircraft tyre. Therefore, an additional wheel trailer has been designed and a typical aircraft tyre is a part of this measuring device.

Fig. 1. A rotating wheel dynamometer installed on a test vehicle, during a test ride on a grassy surface. Braking moment MY¬ of a wheel is being measured
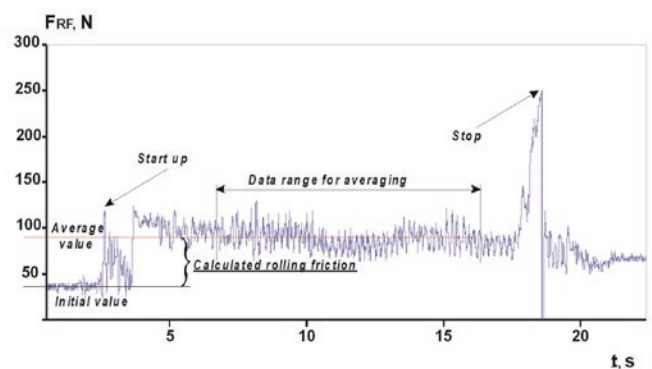

Fig. 2. Sample data of rolling friction force, calculated from measured braking moment, MY¬ of a wheel on a grassy surface with pre-calculation analysis

The effect of speed on rolling friction is significant. Mitschke [12] has shown the components of the rolling friction of a passenger car on a bitumen surface as follows:

$$f_{RF} = k_{R0} + k_{R1}\frac{V}{100} + k_{R4}\left(\frac{V}{100}\right)^4 \qquad (4)$$

with: k_{R0}, k_{R1}, k_{R4} – factors for the sub-ranges of forward velocity: 0 – 30 km/h, 30 – 120 km/h and above 120 km/h respectively, determined experimentally.

The relationships between rolling friction coefficient and aircraft ground speed (see references[13] and [14]), shown in figure 3, proofs that taking speed into account is of highest importance also for soft, deformable surfaces like grassy airfields. The use of wheel trailer, pulled by a test vehicle will enable to determine wheel rolling friction for a wide range of forward speed, with no necessity of rather difficult and expensive flight tests. Also, identification of rolling friction components, showed in the equation (4), can be performed.
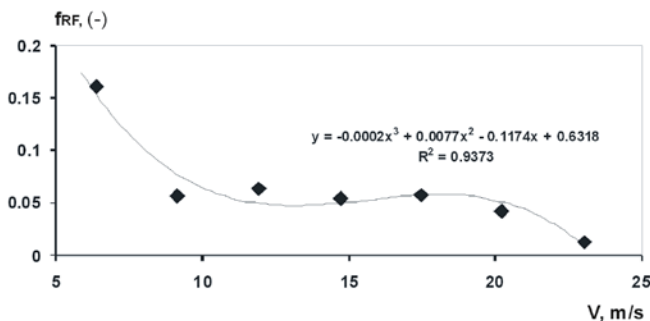
Fig. 3. Effect of forward speed upon rolling friction coefficient, fRF for an aircraft tyre on a grassy surface, determined in a flight test

3.2. Braking friction of a wheel

Let's consider a wheel rolling over a surface. Two general modes of operation are possible:
- free rolling, without any driving moment;
- driving or braking, which is caused by an external moment applied to the wheel.

In a contact area there exists a horizontal component of surface reaction to wheel loads. This force has a longitudinal direction and its value may be expressed by a well known Amontons law of friction:

$$X = F_v \mu \qquad (5)$$

with: F_v – vertical load on the wheel and μ – correlation factor, known as a braking friction coefficient or simply traction.

Braking friction coefficient is of a fundamental importance for safe landings, especially when an airplane is of huge mass and at high landing speeds. In such cases, extensive ose of braking during rollout is mandatory. But even a very powerful brakes don't help if a sufficient braking friction hasn't employed. For a grassy, unsurfaced airfield, braking friction is important because of two facts. Firstly, grass, especially when wet, doesn't ensure high braking friction. Secondly, surface unhomogenity and roughness act as additional factors decreasing braking efficiency. Finally, wheel-surface friction is strongly affected by weather, yet more on natural, soft fields [1, 3].

Measuring of braking friction of aircraft wheels rolling over a paved runway is performed by means of a friction tester, which is typically a fifth wheel attached to a service vehicle that allows to gather friction data at a range of speed. This measuring wheel can be loaded

vertically to reconstruct real conditions of a given aircraft undercarriage. During a test run, the wheel is braked until full stop and the resulting friction force is measured with a load cell. Measured data are then used to calculate friction coefficient, which are published in a form of NOTAM (*Notice to Airmen*).

The use of rotating wheel dynamometers, described in [15] is naturally advantageous, since this device enables to measure all variables needed to determine friction coefficient and it can be installed on a wheel. A basic measure required to determine wheel braking friction is braking moment on a wheel, M_Y. The relationship between longitudinal force, X, acting on a contact surface and the M_Y can be expressed by the equation below:

$$\vec{M}_Y = \vec{r} \times \vec{X} \qquad (6)$$

where $\vec{r}$ is the radius of the longitudinal force (wheel dynamical radius).

Finally, braking friction can be determined with the following equation:

$$\mu = \frac{M_y}{r\, F_z} \qquad (7)$$

Neglecting the effect of tyre vertical deflection due to wheel load will not affect the accuracy of the method when tyre stiffness is much higher than surface. This is not true for low pressure, baloon tyres. In this case, tyre dynamics should be taken into account. Another simplification is that we neglect tyre longitudinal deflection as a result of wheel-surface traction. We simply determine braking friction as a function of kinematical wheel slip.

3.3. Surface unevenness and roughness

The surface of paved runways is usually well maintained, so the unevenness or roughness do not affect wheel performance. Typically, statistical methods are used to describe tarmac or bitumen pavement profile, as is often used in highway construction and maintenance. The surface profile is described as a two-dimensional, homogenous and isotropic, stochastic process [5]. A synthetic measure of hard surface roughness is performed by means of power spectrum density function and typical values of unevenness belong to the range between 0,001 – 0,04 m. The surface of grassy, natural airfield is characterized by its roughness, which depends on the type of soil, its activity with time, the presence of small animals and plants. Typical natural surface unevenness is about 0,01 – 0,2 m and similar analytical methods can be used to describe its profile. For the presented method for evaluation and classification of unsurfaced airfields, it was important to develop a simple, durable and precise enough technique for measuring roughness.

Among a number of methods possible, a non-contact remote measurements with the use of LIDAR may provide a good solution. LIDAR is an optoelectronic device that uses nanosecond impulse mode of a laser. Very short but of high energy laser impulses are being sent toward a measuring surface and after they are backscattered and come to a selective detector integrated with the laser. An analyzer determines spectra of laser impulses and this analysis forms a background for obtaining the so called point clouds. Assuming, LIDAR would be used as a very precise and fast range meter, which determines the time of laser impulse travel, to and from the surface. A certain disadvantage of this method is its sensitivity to aerosols and contamination in the atmosphere. This can be fixed or minimized when scanning would be performed from a low passing airplane.

4. Applied methods

4.1. Single wheel tester

We have designed and developed a single wheel tester, towed behind a SUV. The main frame of the tester is joined with the base vehicle and the movable frame with the test wheel is connected by means of two rotating joints. This allows to apply various loads on the test wheel as well as compensation of vertical movements when rolling over rough surfaces. The test wheel is from a PZL 104 Wilga multipurpose aircraft and is used with the complete suspension. The entire construction of the tester allows to reconstruct loads and kinematics of the main undercarriage of the aircraft. A schematic of the tester is shown in figure 4.
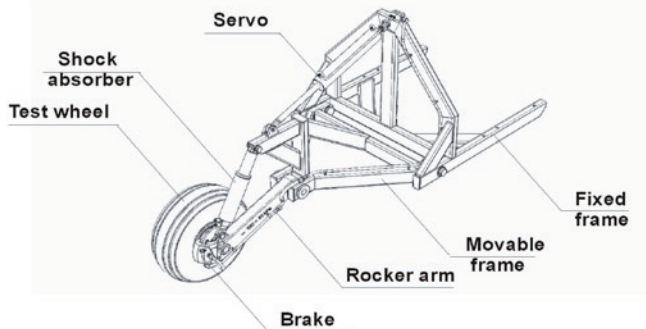
Fig. 4. A schematic of the wheel tester developed in the study

The range of applied vertical load on the test wheel is limited by the mass of the base vehicle, but when needed, the load can be extended by installation the tester on a heavier vehicle. The range of forward speed is between 0 – 60 km/h, although this can be limited for tests performed on very rough surfaces. A typical test run may include the following measuring procedures:
– free rolling – determination of rolling friction coefficient;
– braking – determination of braking friction coefficient.

The wheel tester is equipped with instrumentation, which enables the following measurements:
– measuring the vertical load and the braking moment on the wheel;
– measuring the rotation speed of the test wheel to determine wheel slip during braking action.
Description of the instrumentation follows.

4.2. A multielement rotating wheel dynamometer

The test wheel installed on the tester, is a measuring wheel, integrated with a multi-element rotating dynamometer. This device enables to perform dynamic measurements of forces and moments acting on the test wheel during test runs. The device has been built based on strain gage technology. There are two elastic elements, one is used to determine braking moment M_Y, the other one for the remaining components, F_Z, F_Y, F_Z and M_Z, M_X. The test wheel is shown in figure 5. The entire dynamometer is installed in the wheel hub together with electronics, which forms the measuring signals and allows to send them wirelessly to a portable computer for downloading and analysis.

4.3. Wireless telemetry system

This system has been built based on a portable device with Android operating system. It can be a tablet computer or even a cellular phone. A special software has been developed to communicate with the rotating dynamometer. A primary function of the software is to control the measurements performed with the use of the tester. The
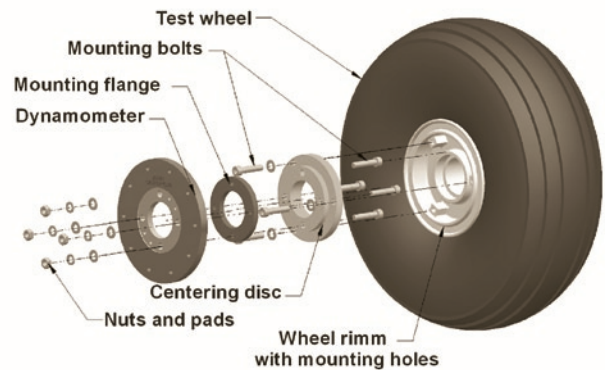

Fig. 5. The test wheel with the rotating wheel dynamometer, based on a PZL 104 Wilga undercarriage wheel

user can also transmit the measuring data wirelessly after a test run is finished. Finally, the program gives a possibility to calculate the required coefficients as well as to visualize their values or time courses if needed.

The telemetry system consists of a 16-bit, 8-channel analog-to-digital converter, performing the successive approximation (SAR – **S**uccessive **A**pproximation **R**egister), with a highest data sampling rate of 115 ksps (*kilo samples per second*). Another subsystem in the architecture of the telemetry is a data acquisition system, based on a 32-bit controller. Finally, the measured data can be transmitted by a Bluetooth Class 2.0 module which ensures communication range of more than 600 m. The purpose of the microcontroller is managing of data acquisition, preliminary data analysis and filtering the digital data. An important advantage of the presented telemetry system is the use of a mobile device driven by the Android system. There is a possibility to add more applications, which could help in performing the measurements or in data analysis.

4.4. Determining the profile of grassy surface with the use of LIDAR

Scanning and creating of numerical charts of terrain can be performed with the use of laser technology. A practical range of laser devices used in highway construction and maintenance is about 1m. The laser is installed on an external rim and works vertically to the surface. The idea of the present authors was to examine the possibility of the use of LIDAR to scan the surface of an airfield from a flying aircraft. A schematic of the LIDAR is presented in figure 6. The laser impulse is optically formatted and sent toward the object (surface). Backscattered signal is registered by a photodetector, then analyzed. Although the subject of signal analysis in LIDAR systems is well described and mature, there are some interesting aspects, such a for example developing new algorithms to obtain required information from the so called point clouds [4].

Surface roughness of an airfield can be described with the use of quadratic mean or root mean square. If we consider the high of the elementary uneveness as a function of the linear dimension, *x* (in case of surface analysis, two dimensional function will be used) to be a measure of roughness, the root mean square of the roughness can be expresses as below:

$$z_{RMS} = \sqrt{\frac{1}{x} \int_{x_0}^{x_0+x_i} z^2(x)dx} \qquad (8)$$

The so called point clouds, obtained from the LIDAR scanning enable to determine the over mentioned parameters, based on known algorithms. The idea of scanning with the use of airborne equipment
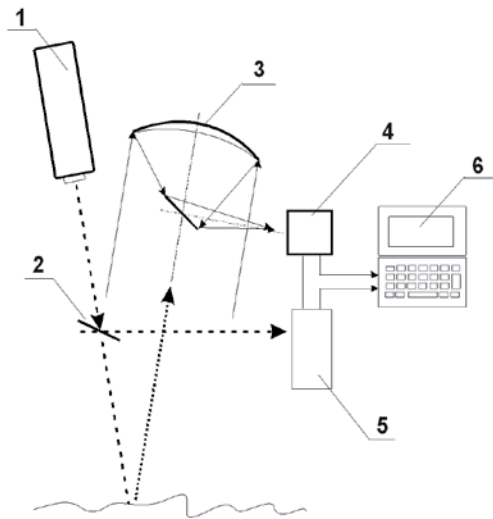
Fig. 6. A schematic of LIDAR. 1 –laser, 2 – beam splitter, 3 – telescope, 4 – photomultiplier, 5 – impulse counter, 6 – data analyzer

has the advantage over the use of vehicular scanners, that there is no need to compensate of vertical movements of the vehicle. On the other side, airborne scanners have to be characterized by much higher parameters (laser impulse power and its frequency) what is caused by higher ground speed of an airplane.

4.5. Estimation of measurements precision and the accuracy of the proposed method

The rotating wheel dynamometer is a measuring device with the class of 1, so at the full scale of the braking moment channel, the error of measurement of the rolling or braking friction is ± 0,0033

in laboratory conditions. Taking into account the effect of test conditions, the uncertainty of the measurement in realm is of the order of 0,0075. If we use equations to determine takeoff or landing roll, cited in this work, then the accuracy of the entire method may reach about 25 m and 30 m, respectively. A more precise determination of the accuracy requires the analysis of covariance of the measured and estimated values of braking moment and is expected to be as low as about 10m [2].

5. Conclusions

In the paper a description of a new method to evaluate and for classification of unsurfaced airfield is presented. The method respects parameters affecting wheel-surface interactions, especially the deformability of soft grounds and its effects on aircraft ground performance, such as takeoff roll and landing distance. Based on theoretical analysis from the literature, the following parameters have been chosen as important: rolling and braking friction coefficients, surface roughness. Instrumentation proposed to be applied in the method has also been presented in the paper. The solutions include a single wheel tester and the LIDAR for air scanning of the surface roughness. Estimated error of the method is about 10m of the takeoff or landing distance for a typical GA airplane on a grassy surface.

Prospective users of the method could be operators of the airfields and the pilots flying from them. The application of the method may have positive effects on the regional air transport through increasing of the use of unsurfaced airfields for different air operations

References

1. Antvik G. History of friction measurements at airports. Airport International / www. Airport-int.com.
2. Arendarski J. Niepewność pomiarów. Oficyna Wydawnicza Politechniki Warszawskiej, Warszawa 2006.
3. Bergstrom A, Astrom H, Magnusson R. Friction Measurement on Cycleways Using a Portable Friction Tester. J. Cold Reg. Engrg., 2003; 17: 37–57.
4. Czarnecki K. Klasyfikacja nośności nawierzchni lotniskowych metodą ACN-PCN. Technika Lotnicza i Astronautyczna, 1987: 1: 23–28.
5. Detweiler Z.R., Ferris J.B. Interpolation methods for high-fidelity three-dimensional terrain surfaces. J.of Terramechanics, 2008; 47: 219–226.
6. Durst PJ, Mason GL, McKinley B, Baylot A. Predicting RMS surface roughness using fractal dimensionand PSD parameters. J. of Terramechanics, 2011; 48: 105–111.
7. van Es GWH. Method for predicting the rolling resistance of aircraft tires in dry snow. Journal of Aircraft, 1999: 36: 1089–1096.
8. Filippone A. Flight Performance of Fixed and Rotary Wing Aircraft. AIAA Education Series, 2006.
9. Jakliński L. Modele oddziaływania koła pneumatycznego na glebę. Prace naukowe Politechniki Warszawskiej, Seria: Mechanika, 1999; Z.175.
10. Johnson C. Airport Runway Friction Tester. Airport International / www. Airport-int.com.
11. Lozia Z. Symulatory jazdy samochodem. WKiŁ Warszawa, 2008.
12. Mitschke M, Wallentowitz H. Dynamik des Kraftfahrzeuges. Springer Verlag, Heidelberg, 2004.
13. Pytka J. Model i identyfikacja układu koło ogumione – podłoże odkształcalne. Raport końcowy z realizacji Projektu badawczego 4T12C 06028 finansowanego ze środków MNII w latach 2005–2007. Lublin, 2007.
14. Pytka J. Identification of Rolling Resistance Coefficients for Aircraft Tires on Unsurfaced Airfields. AIAA Paper No. 2007–7853.
15. Stinton D. Flying Qualities and Flight Testing of the Aeroplane. Blackwell Science, 1996.
16. Raymer D. Aircraft Design. A Conceptual Approach. AIAA Publishing, 1991.
17. SARSYS Trailer Friction Tester, Scandinavian Airport and Road Systems AB, Trelleborg, Sweden.
18. Shoop S.A. , Richmond P.W., Eaton R.A. Estimating rolling friction of loose till for aircraft takeoff on dirt runways. Proc. 13th Conference of the ISTVS, Munich, Germany, 1999.

Prof. Piotr TARKOWSKI, Ph.D., D.Sc. (Eng.)
Jarosław PYTKA, Ph.D. (Eng.)
Piotr BUDZYŃSKI, Ph.D., D.Sc. (Eng.), Assoc. Prof.
Department of Automotive Vehicles
Department of Mechanical Engineering
Lublin University of Technology
ul. Nadbystrzycka, 20-816 Lublin, Poland
e-mails: p.tarkowski@pollub.pl, j.pytka@pollub.pl, p.budzynski@pollub.pl

Łukasz KAZNOWSKI, M.Sc. (Eng.)
c/o Mechanical Engineering Faculty
Lublin University of Technology
ul. Nadbystrzycka, 20-816 Lublin, Poland
E-mail: l.kaznowski@wp.pl

Janusz TOMCZAK
Zbigniew PATER
Tomasz BULZAK

EFFECT OF TECHNOLOGICAL PARAMETERS ON THE ROTARY COMPRESSION PROCESS

WPŁYW PARAMETRÓW TECHNOLOGICZNYCH NA PRZEBIEG PROCESU OBCISKANIA OBROTOWEGO*

The paper presents results of a numerical analysis of the rotary compression process for producing extreme steps of a multi-step hollow shaft. The numerical simulations of the process were conducted by the finite element method (FEM), using Simufact Forming version 11.0. Applications of hollow parts in industry are discussed and benefits of their use are presented. With numerical modeling, the effect of basic rotary compression parameters (deformation ratio δ, wall thickness g_o, billet initial diameter D, advance speed v and rotary speed n of the tools) on shape of the produced parts are determined. Also, force parameters of the process, tool thrust force and torques are determined. The presented numerical analysis results confirm the possibility of producing multi-step hollow shafts using tube sections as billet material by metal machining methods.

Keywords: *rotary compression, multi-step hollow shafts, FEM.*

W artykule przedstawiono wyniki analizy numerycznej procesu obciskania obrotowego skrajnych stopni odkuwki wielostopniowego wałka drążonego. Symulacje numeryczne procesu przeprowadzono metodą elementów skończonych (MES), przy zastsowaniu komercyjnego pakietu oprogramowania Simufact Forming w wersji 11.0. Omówiono obszar wykorzystania elementów drążonych w przemyśle i przybliżono korzyści płynące z ich stosowania. Poprzez modelowanie numeryczne określono wpływ podstawowych parametrów obciskania obrotowego (stopnia gniotu δ, grubości ścianki go, początkowej średnicy wsadu D, prędkości postępowej v i obrotowej n narzędzi) na kształt otrzymanych wyrobów. Wyznaczono parametry siłowe procesu siły nacisku narzędzi i momenty obrotowe. Opisane rezultaty badań numerycznych potwierdzają możliwość wytwarzania odkuwek wielostopniowych wałków drążonych ze wsadu w postaci odcinków rury metodami obróbki plastycznej.

Słowa kluczowe: *obciskanie obrotowe, drążone wałki wielostopniowe, MES.*

1. Introduction

Rotary compression is a modern process for forming metals and their alloys. Nowadays it is mainly used to produce local reduction in cross section of hollow parts (pressed semi-finished products, tubes, bushings, and many more). The process has a number of advantages owing to the tool motion [5, 8]. For this reason, research studies have been undertaken to investigate technological applications of the rotary compression process. Also, it has been proposed that the process be used to produce more complex machine parts such as multi-step shafts and hollow axles.

These days a growing demand for hollow parts can be observed in the global industry; given a general trend to lower production and machine maintenance costs, such parts are more and more often used instead of their solid counterparts [4, 11]. One of the ways to lower production costs is to use tubular parts in place of commonly used solid elements, as in this way material and labor consumption can be decreased. Strength properties of hollow elements of machine parts are similar to those of solid ones (under bending and torque shaft loads), while their weight is considerably lower compared to their solid counterparts. In effect, machines that are equipped with hollow parts have a lower total weight and, in consequence, consume less energy and are more eco-friendly (lower fuel consumption and lower gas emissions). For these reasons, hollow parts are more and more often used

in both automotive and aircraft industry, as the decreased weight of vehicles and aircraft helps enhance their performance (power, speed, load capacity, maneuverability etc.) and, at the same time, lower their maintenance costs [1, 10, 12].

When investigating rotary processes for forming metals and their alloys, an innovative method for rotary compression was developed at Lublin University of Technology. This method can be used to produce axisymmetric hollow shafts and axles [6, 7]. The proposed method allows for forming parts from sections of commercial tubes or bushings as billet material, using tools with a simple geometric design.

A series of numerical simulations of rotary compression were performed in order to determine the process stability in terms of such disturbances as uncontrolled slipping (loss of rotary motion capability by a workpiece being formed) and collapse of a tube as well as to determine relations between individual process parameters.

2. Description of the rotary compression process

Rotary compression consists in forming a billet material by means of three cylindrical rollers which rotate in the same direction and, simultaneously, move radially towards the axis of the element being formed. The billet material (a tube or bushing section) is placed between the rollers and then rotated by the tools around its own axis during compression. Due to the tool action, the billet external diameter

---

changes and, at the same time, the billet wall thickness increases. The increase in the billet wall thickness of formed parts can be considered positive owing to strength reasons. Parts formed by this method have an axisymmetric shape. Compared to the presently employed methods for producing hollow parts, rotary compression has a number of advantages such as enhanced strength properties of a part, higher production efficiency, lower implementation and production costs, as well as relatively simple process mechanization and automation.

An example of forming a multi-step shaft (with two extreme neckings) by the rotary compression method is shown in Figure 1.
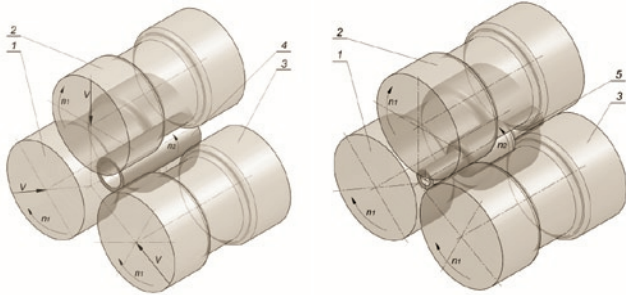
Fig. 1. Design of the rotary compression process for producing axisymmetric hollow part in which three tools perform rotary motion, moving simultaneously towards billet axis: 1, 2, 3 – forming rollers, 4 – billet (tube section), 5 – part; a) process start, b) process end

One characteristic of the rotary compression process is a gradual reduction in the billet diameter (Fig. 2) by the rotating tools, which can be defined by the deformation ratio:

$$\delta = D/d, \qquad (1)$$

where D is the external diameter of the billet before the process, d is the external diameter of a journal after the compression process.

Owing to the billet diameter reduction, the material flows radially, in effect of which the wall thickness increases by Δg compared to the initial value of the tube (billet):

$$\Delta g = g - g_o, \qquad (2)$$

where g is the thickness of the formed part, g_o is the thickness of the billet wall.

In the course of forming, the metal also moves along the billet axis, which results in an increase in the part length by Δl compared to the initial billet length:

$$\Delta l = l - l_o, \qquad (3)$$

where l is the part length, l_o is the billet length.

Obviously, the increase in the wall thickness and length of the part depends on the compression parameters used. The most important ones are: value of the deformation ratio δ, the ratio of initial wall thickness g_o to initial billet diameter g_o/D and the ratio of advance speed v of the tools towards the billet axis to their rotary speed n.

3. Numerical analysis of rotary compression for producing an extreme step of the axisymmetric hollow part

In order to determine the effect of the selected rotary compression process parameters (δ, g_o/D and v/n) on the wall thickness increase Δg and workpiece length Δl, a series of numerical simulations of forming a hollow part with extreme journals were performed. A geometric model of one of the analyzed rotary compression processes, with
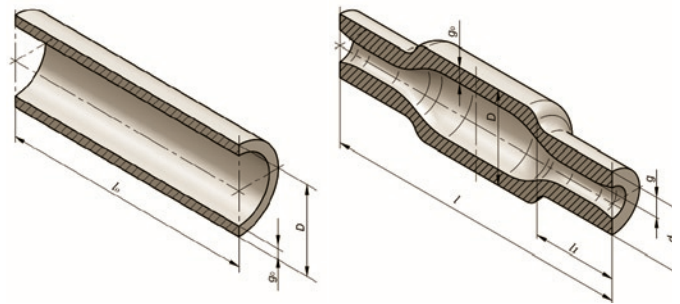

Fig. 2. Shape and dimensions of the billet used in rotary compression – a) and of the formed part with two extreme journals – b)

forming symmetry applied to reduce the computation time, is shown in Figure 3. The simulations were conducted by the finite element method (FEM), using Simufact Forming version 11.0, a metal forming simulation program that has been used by the authors many times to analyze rotary processes for forming metals and alloys, and the results have been positively verified in the experimental tests [2, 9, 3].
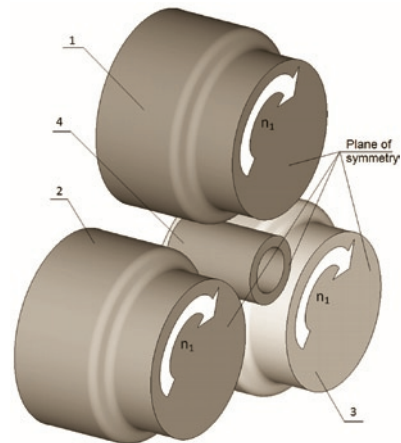

Fig. 3. Geometric model of the rotary compression process for producing extreme steps of a hollow shaft (its description provided in the paper)

The model consists of three identical multi-step rollers – 1, 2, 3 and a billet – 4. The tools (rollers) rotate at a constant speed n_1 of 60 rpm in the same direction and move towards the billet axis at constant speeds v. The billet material was a tube with 42.4 mm external diameter, length $l_o = 120$ mm and wall thickness g_o. The tube was modeled using 8-node hexahedral first order elements. The value of initial tube wall thickness g_o depended on the tube dimensions available on the market, and it was 3 mm, 5 mm, 7 mm, 9 mm and 11 mm, respectively. Also, it was assumed that the tube was made from constructional carbon steel (C45). This material is commonly used to produce all kinds of gears, shafts, axles, toothed shafts, connecting rods, and other average loaded machine elements. The material model of steel C45 was taken from the material database of Simufact Forming, and examples of flow curves are shown in Figure 4. Other parameters used in the computations included: initial billet temperature −1150°C, rigid tool model with a constant temperature of 150°C, friction factor on metal-tool contact surface $m = 1$, material-tool heat exchange coefficient – 10 kW/m²K and material-environment heat exchange coefficient – 0.2 kW/m²K.

The numerical simulations were based on the assumption that the tools (forming rollers) would rotate at a constant speed in all process variants. The only parameter that would vary in the process would be the speed at which the rollers move towards the billet axis. Other parameters that were being changed in the process included: the deformation ratio δ (in the range from 1.2 to 2.1) and the billet wall thick-
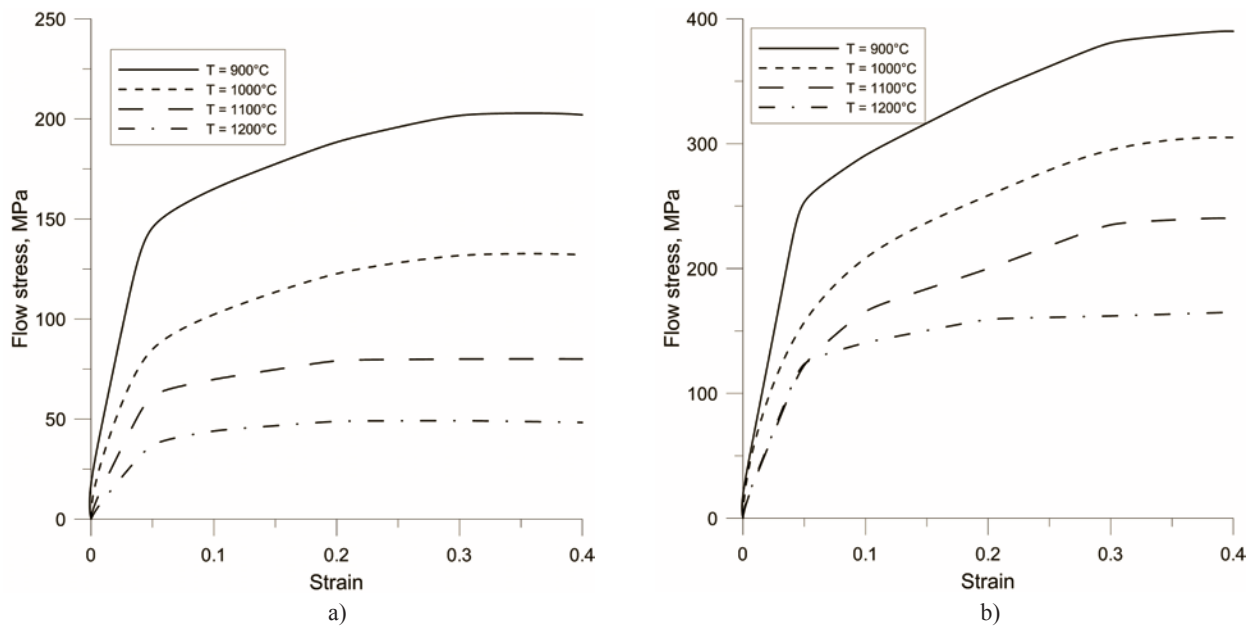
Fig. 4. Flow curves of steel C45 at strain rates of: a) $0.1\ s^{-1}$, b) $100\ s^{-1}$

Table. 1.   Technological parameters used in FEM simulations of rotary compression to produce extreme steps

Rotary speed of tools	n [rpm]	60						
Linear speed of tools [mm/s]	v [mm/s]	0.5	1	2	4	6	8	10
Advance speed-to-rotary speed ratio	v/n [mm/r]	0.46	0.92	1.84	3.69	5.54	7.38	9.23
Billet external diameter	D [mm]	42.4						
Wall thickness	g_o [mm]	3	5	7		9		11
Wall thickness-to-billet diameter ratio	g_o/D	0.07	0.12	0.16		0.21		0.26
Deformation ratio	δ	1.2		1.5		1.8		2.1

ness. The main parameters applied in rotary compression to produce extreme steps of a hollow shaft are listed in Table 1.

As a result of the performed computations, material flow kinematics in the rotary compression process for producing hollow parts could be analyzed. Figure 5 illustrates changes in the product shape depending on progress of the process for one of the analyzed compression cases. It can be observed that the material begins to move towards the workpiece axis due to the reduction in the billet external diameter, which leads to an increase in the wall thickness. Also, it can be observed that the material moves along the workpiece axis, particularly at the surface regions, which results in an increase in the workpiece length compared to the initial billet length and leads to the occurrence of concave (funnel-like) frontal surfaces. In the final stage of compression, the advance motion of the tools is stopped, and they only perform the rotary motion. In effect, the workpiece shape undergoes sizing and the surface irregularities that occurred in the initial process stages are removed.

Figure 5 illustrates the distributions of effective strain both on the surface and in the cross section of the workpiece being formed. In the region of the tool action, the material is deformed inside-out, which makes it flow towards the billet axis, and the strains are not homogenous in the cross section of the steps being compressed. At the surface, the material is subjected to higher deformation relative to the central regions (located in the vicinity of the internal wall).
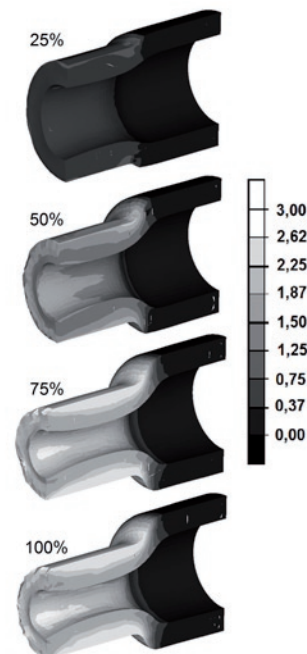
Fig. 5.   Numerically determined hollow shaft shape changes with effective strain

This is characteristic of rotary metal machining processes, as it results from the process kinematics as there are considerable differences in the circumferential speeds of the workpiece being formed (due to the variable tool radius). As a result, slipping between the material being formed and tools occurs and considerable circumferential strains are generated (by the action of friction forces).

In the numerical simulations, the effect of the basic forming process parameters (δ, g_o/D and v/n) on the wall thickness increase Δg and workpiece length Δl was determined. Based on the performed simulations, the following could be observed:

- an increase in the deformation ratio δ in the range between 1.2 and 2.1 leads to an increase in both the wall thickness Δg and workpiece length Δl (Fig. 6),
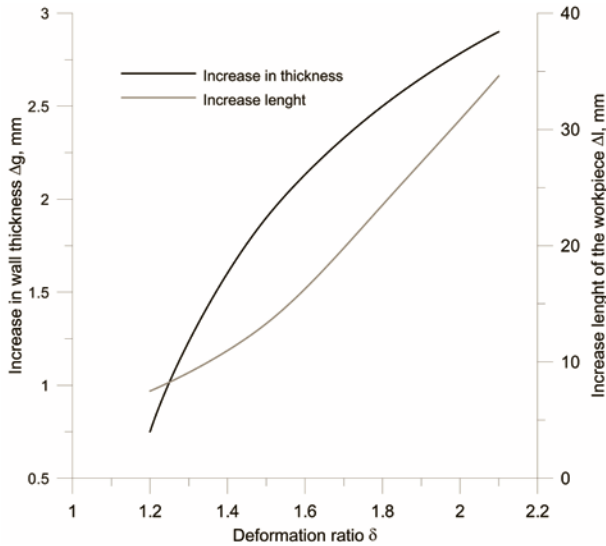
Fig. 6. Effect of deformation ratio δ on increase in wall thickness and length of the workpiece, determined at: $g_o = 5$ mm, $v = 6$ mm/s

- an increase in the tool advance speed v relative to their rotary speed n results in an intensive increase in the wall thickness Δg and a decrease in the workpiece length Δl (Fig. 7),
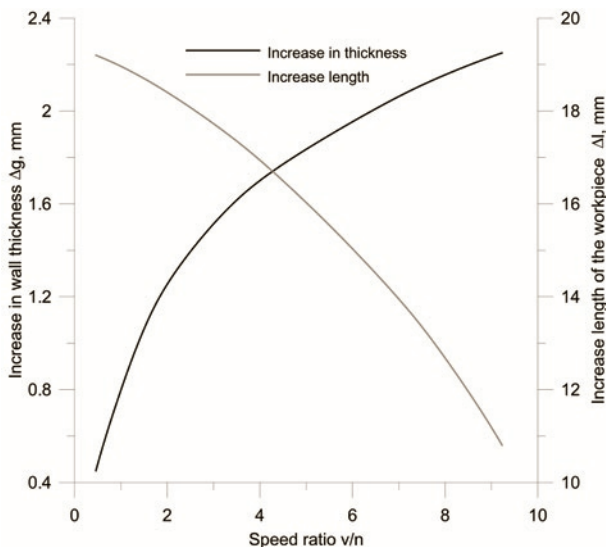
Fig. 7. Effect of the tool radial motion relative to their rotary speed on changes in the wall thickness and workpiece length, determined at: $\delta = 1.5$, $g_o = 7$ mm

- an increase in the ratio of initial wall thickness g_o to billet diameter D (g_o/D) leads both to a decrease in the wall thickness Δg and to an increase in the workpiece length Δl (Fig. 8).
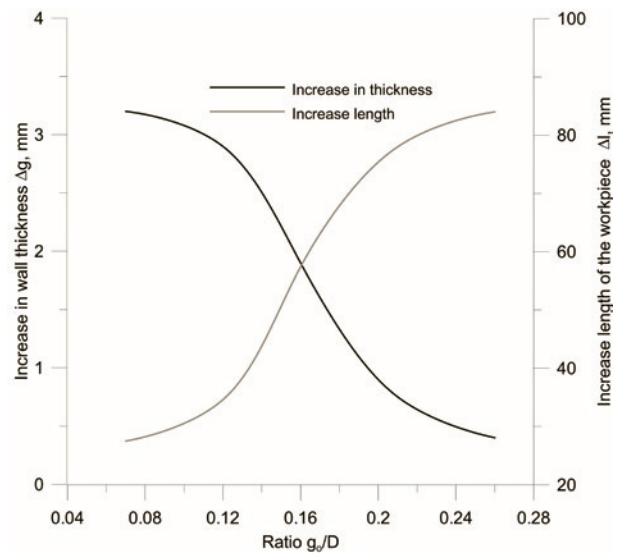
Fig. 8. Effect of the initial wall thickness relative to billet diameter on changes in the wall thickness and workpiece length, determined at: $\delta = 2.1$, $v = 8$ mm/s

The variations of forces and torques were also analyzed in the conducted numerical simulations. If maximum values of these parameters are estimated accurately, both the technology and design of tools and forging unit can be developed in a suitable manner. Additionally, the information about the force variations helps control the process in terms of predicting phenomena that could disrupt its stability. Examples of the force parameters (tool thrust force and torque) determined by the FEM simulations of rotary compression are shown in Figures 9 and 10.
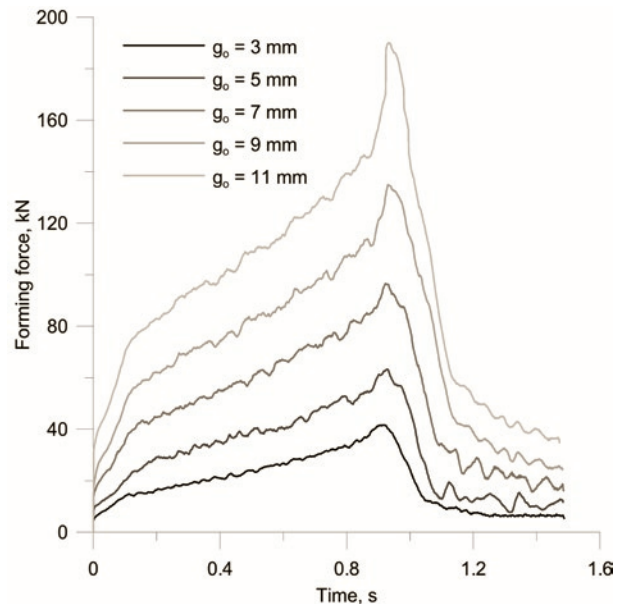

Fig. 9. Numerically determined tool thrust forces in rotary compression at: $\delta = 1.5$, $v = 6$ mm/s

The distributions have a similar shape, yet with an increase in the billet wall thickness, the values of the tool thrust force and torque increase, too. The compression process can be divided into two basic stages. In the first stage, the radially moving tools reduce the billet
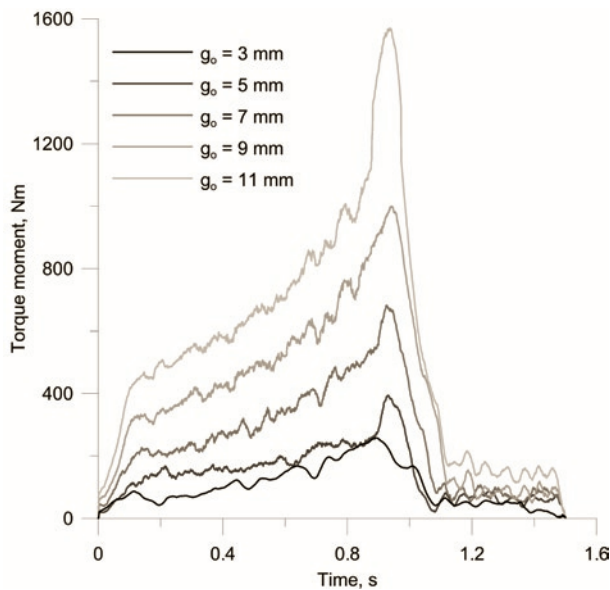
Fig. 10 Numerically determined torques on one tool in rotary compression at: δ = 1.5, v = 6 mm/s

external diameter, which is accompanied by a gradual increase in the force parameters. At the end of the first stage of compression, a sudden increase in the forces and torques can be observed, which results from the contact of the central (undeformed) step with the tools. In the second stage, during sizing (the advance motion of the tools is stopped), the surface irregularities generated in the first stage of the compression process are removed. In effect, a sudden decrease in the force parameters can be observed.

4. Conclusions

The conducted analysis of the rotary compression process confirmed the possibility of using this method to form hollow stepped shafts and axles. The multi-variant numerical analysis of rotary compression was performed using the finite element method (FEM) in spatial state of strain. The simulations positively verified most of the adopted technological and design-related assumptions; also, material flow kinematics was determined and, above all, the effect of the selected compression process parameters (δ, g_o/D and V/n) on shape of the produced parts was determined. It was proved that the tool motion speed has the most considerable effect on increasing the workpiece wall thickness Δg. As the tool speed v increases, a higher increase in the wall thickness can be observed, whereas at lower speeds, the material flows more intensively in the axial direction, which results in an increased workpiece length. The initial wall thickness of the billet used is also of vital importance for the material flow kinematics. The increased wall thickness g_o leads to an increase in radial deformation resistance, which causes a decrease in the workpiece wall thickness and, simultaneously, a sudden increase in its length. The intensity of the thickness and length increase depends not only on the deformation ratio, but it is also affected by the other two parameters (g_o/D and v/n).

Summing up, it can be stated that the developed method can be used to form axisymmetric hollow elements using tubular semi-finished products as the billet material. In effect, the labor and material consumption costs can be significantly lowered, while the strength properties of the formed parts are enhanced. Moreover, the production and machine maintenance costs can be lowered, too. The results are promising, yet in order to fully understand the rotary compression process and phenomena that disturb its stability, a comprehensive theoretical and analytical analysis needs to be conducted.

References

1. Ashby M, Jones D. Materiały inżynierskie. Tom I – Właściwości i zastosowanie. Wydawnictwo Naukowo-Techniczne. Warszawa 1995.
2. Bartnicki J, Pater Z. Walcowanie poprzeczno-klinowe wyrobów drążonych. Wydawnictwo Politechniki Lubelskiej. Lublin 2005.
3. Li X, Wang M, Du F. The coupling thermal-mechanical and microstructural model for the FEM simulation of cross wedge rolling. Journal of Materials Processing Technology 2006; 172: 202–207.
4. Neugebauer R, Kolbe M, Glass R. New warm forming processes to produce hollow shafts. Journal of Materials Processing Technology 2001; 119: 277–282.
5. Pater Z. Walcowanie poprzeczno-klinowe. Wydawnictwo Politechniki Lubelskiej. Lublin 2009.
6. Pater Z, Tomczak J. Method for plastic forming of toothed shafts. Zgłoszenie Patentowe Europejskie nr EP 11461501.
7. Pater Z, Tomczak J. Rotary Compression of Hollow Parts by Cross Rolling. Zgłoszenie Patentowe Europejskie nr EP 11461502.
8. Pater Z. Nowa technologia kształtowania metali: Walcowanie klinowo-rolkowe. Rudy i Metale Nieżelazne 2003; 10–11: 483–485.
9. Tomczak J, Pater Z, Gontarz A. Termomechaniczna analiza kształtowania plastycznego wałka ze stopu tytany Ti6Al4V. Mechanik 2012; 3: 205–211.
10. Tomczak J, Pater Z. Analysis of metal forming process of a hollowed gear shaft. Metalurgija 2012; 51: 497–500.
11. Urankar S, Lovell M, Morrow C, Kawada K. Establishment of failure conditions for the cross-wedge rolling of hollow shafts. Journal of Materials Processing Technology 2006; 177: 545–549.
12. Wong CC, Lin J, Dean TA. Effects of roller path and geometry on the flow forming of solid cylindrical components. Journal of Materials Processing Technology 2005; 167: 344–353.

Janusz TOMCZAK, Ph.D. (Eng.)
Prof. Zbigniew PATER, Ph.D., D.Sc. (Eng.)
Tomasz BULZAK, M.Sc. (Eng.)
Department of Computer Modelling andMetal Forming Technologies
Faculty of Mechanical Engineering
Lublin University of Technology
ul. Nadbystrzycka 36, 20-618 Lublin, Poland
e-mail: j.tomczak@pollub.pl

Jarosław BIENIAŚ
Patryk JAKUBCZAK
Krzysztof MAJERSKI
Monika OSTAPIUK
Barbara SUROWSKA

METHODS OF ULTRASONIC TESTING, AS AN EFFECTIVE WAY OF ESTIMATING DURABILITY AND DIAGNOSING OPERATIONAL CAPABILITY OF COMPOSITE LAMINATES USED IN AEROSPACE INDUSTRY

METODY BADAŃ ULTRADŹWIĘKOWYCH, JAKO EFEKTYWNY SPOSÓB SZACOWANIA TRWAŁOŚCI ORAZ DIAGNOZOWANIA ZDOLNOŚCI EKSPLOATA-CYJNYCH LAMINATÓW KOMPOZYTOWYCH STOSOWANYCH W LOTNICTWIE*

The paper presents selected issues in the field of exploitation research and the prediction capabilities of durability of composite laminates by ultrasonic methods used in the aerospace industry. Some research methods allow to set the quality parameters and operating in real aircraft structures. The study determined the relationship between the amplitude decrease of the ultrasonic wave and the level of porosity for hand lay-up manufactured glass / epoxy laminate using the method Through-Transmission of representative in C (TT C-Scan). In addition, showing the ability of amplitude attenuation imaging methods to detect and determine the extent of damage of high quality laminate and metal fiber composite after at low-dynamic velocity. It was specified real area an internal damage in FML laminates subjected to dynamic impact on low-energy, for which there was no visible damage in the outer layers. The study also determined the relationship between energy and the impact of dynamic surface area in testing laminates.

Keywords: *composites , impact resistance, porosity, ultrasonic testing.*

W pracy przedstawiono wybrane zagadnienia z zakresu badań zdolności eksploatacyjnych oraz prognozowania trwałości metodami ultradźwiękowymi laminatów kompozytowych stosowanych w przemyśle lotniczym. Wybrane metody badawcze umożliwiają określenie parametrów jakościowych jak i eksploatacyjnych rzeczywistych struktur lotniczych. W pracy określono zależność pomiędzy wartością spadku amplitudy fali ultradźwiękowej a poziomem porowatościdla wytworzonego metodą laminowania ręcznegolaminatu szklano/epoksydowego przy użyciu metody Through-Transmissionw zobrazowaniu w trybie C (TT C-Scan). Dodatkowo pokazano zdolność metody obrazowania tłumienia amplitudowego do wykrywania i określania wielkości uszkodzeń wysokojakościowych laminatów kompozytowych i metalowo włóknistych po uderzeniach dynamicznych o niskich prędkościach. Określono rzeczywiste pola powierzchni uszkodzeń wewnętrznych laminatów FML poddanych uderzeniom dynamicznym o niskich energiach, dla których nie odnotowano widocznych uszkodzeń w warstwach zewnętrznych. W pracy wyznaczono również zależność pomiędzy energią uderzenia dynamicznego a polem powierzchni uszkodzenia badanych laminatów.

Słowa kluczowe: *kompozyty, odporność na udar, porowatość, badania ultradźwiękowe.*

1. Introduction

The modern aircraft structures belong to those main fields of technology where the performance and reliability characteristics are of primary importance. This is due to ensuring an adequate level of stability and safety of aircrafts. Materials engineering developing innovative technologies and advanced materials plays particularly important role in this area.

Composites are a leading and prospective group of construction materials used in the aerospace industry. Among them, the biggest development trend is attributed to fibre reinforced polymer matrix composites and to hybrid materials. This is due to the modification of the physical and mechanical characteristics influenced by the introduction of the reinforcement to the matrix, considering the tendency to reduce the density of a finished composite product. The composites

are characterized by high strength-to-density ratios, unattainable for other groups of materials [6, 22, 32, 35].

Currently, a group of modern hybrid composites encompasses the fibre metal laminates consisting of alternately stacked layers of metal and fibre-reinforced polymer composite. These laminates are characterized by high fatigue strength, high strength properties, corrosion resistance and to dynamic impact (impact) [1, 4, 14 ,33 ,36 ,38].

Composite materials are used to manufacture critical components of aircraft structures referred to as the primary structures (primary structure) and other responsible structures (secondary structure) as: skin elements, fuselages, spars, blades, landing gears, stabilizers, flaps and many others. Initially, the use of composites in aircraft structures has only reached a few percent (aircrafts and military structures), currently is equal to about 20–30%. The flagship product is the Boeing 787 "Dreamliner" made with more than 50% composite materials [7, 33, 13].

Performance and reliability features of composite aircraft structures may be attributed to their individual elements ensuring their ability to perform specific tasks in determined period of time and operational conditions. Therefore, the principal requirements to be met by composites can include inter alia.: to obtain a material with high mechanical properties and low density. Reliability aspects should be taken into account in composite elements design, fabrication and operation phase of [22, 6, 37].

The assessment of quality of received composite and structures is of extreme importance at the manufacturing stage. The presence of defects such as pores and delaminations can have a significant impact on the reduction of composite properties and consequently deteriorate its functional characteristics [6, 19, 21, 37, 39].

One of the essential problems occurring in course of operation of composite structures is their resistance to dynamic impact (impact). There is a high risk of developing this type of phenomena denoted in the operation of aircraft. This is associated with e.g. operations performed by ground handling services, solid bodies thrown from under the wheels of an airplane or moved by the wind. Dynamic impact can cause visible damages in composite structure, which can be detected during routine inspections as well as the invisible internal ones, particularly dangerous residual strength [11, 20, 26, 27].

The principal non-destructive methods i.e. mainly ultrasonic flaw detection, thermography, eddy current method and X-ray computed tomography are the principal methods in the scope of quality control and evaluation of composite structures [22].

The paper presents a characterization of the structure of selected composite materials by means of a non-destructive method - ultrasonic flaw detection, in order to identify and characterize structural discontinuities associated with the manufacturing process and the possibility of using ultrasonic method to diagnose internal failures in fibre metal laminates caused by dynamic low-velocity impact.

2. Structural characteristics

The detection of discontinuities in the form of porosity and delaminations is an essential factor in the scope of quality inspection of manufactured composite structures. The minimization of porosity level is possible thanks to the use of advanced manufacturing methods e.g. autoclave process. Nevertheless, some of less responsible elements of airspace structures are still produced in manufacturing processes generating unavoidable porosity [6, 10]. The occurrence of porosity leads to the disturbance in the structural uniformity and to the changes in mechanical characteristics of fibre polymer laminates. The ultrasonic inspection is used as one of the non-destructive methods used for quality testing of composite materials structures. This technique is based on the use of physical phenomena associated with ultrasonic waves propagation in materials.

The object of study was a laminate made of fibre glass fabric (fibre type E) and epoxy resin. The laminate was made by hand lay-up method and tested in the form of a plate using the Through-Transmission (TT C-scan) method by means of an ultrasonic detector. The plate was scanned at the frequency of 1 MHz. The areas of constant drop of ultrasonic wave amplitude have been determined on the basis of the map generated. The level of porosity was determined by means of microscopic image analysis using Nikon MA200 optical microscope.

Figure 1 shows TT C-Scan map for tested composite panel. The areas with diversified colours are visible, which correspond to specific levels of ultrasonic waves absorption. It has been observed that the level of amplitude reduction is related to the intensity of occurrence of the structural discontinuity. Red colour represents a decrease in amplitude greater than 20 dB. The level of porosity marked in this area was equal to about 15%.

The level of porosity in composite structures significantly affects the operational capability and durability of composite aircraft com-
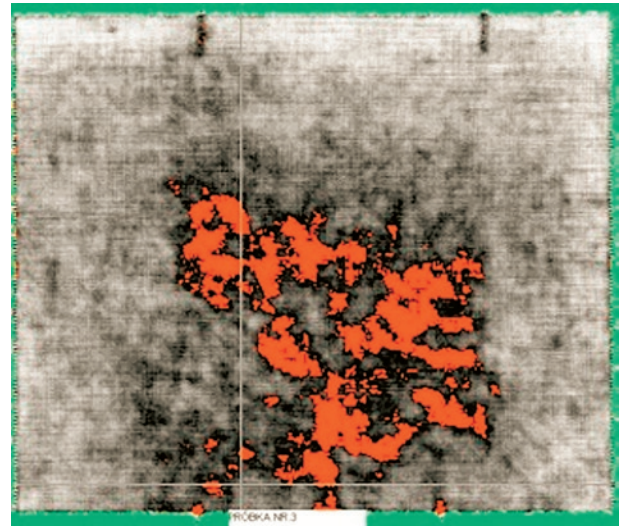

Fig. 1. C-scan imaging of glass epoxy plate

ponents. The percentage of porosity, as well as their distribution and shapes have a significant impact on their fatigue life and delamination tendency [15]. The relationship between the level of porosity and crack propagation process in a laminate structure has been also denoted [9]. An intensified impact of the occurrence of voids in the material, has been characterized by Chambers et al [9]. They distinguished four main levels of porosity depending on the size of voids occurring in the material. In the opinion of Purslow [25], the laminates containing more than 5% (v/v) of porosity are characterized by poor quality and should not be used in the aerospace industry.

A cross-section of the microstructure of an epoxy-glass laminate is shown in Figure 2. The value of determined porosity was equal to approximately 3%. The porosities visible in the microstructure as the dark areas with diversified shapes and dimensions are situated mainly in interlayer spaces. Porosity of larger size tend to form agglomerates. Fine porosities similar to the spherical shape are characterized by more dispersed distribution within laminate volume. In the paper [5] it was found that pores dispersion decreases in case of higher level of porosity. Staffan [31] identified two types of porosity i.e. cylindrical voids between the fibres and the spherical voids located between the bundles of fibres. Bowles and Frimpong [5] have achieved identical results determining the porosity characteristics for high quality laminates with a low pores content.
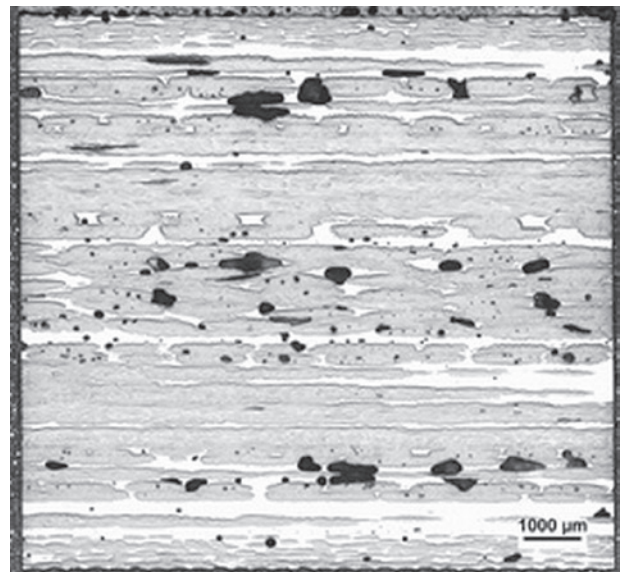

Fig. 2. The microstructure of the glass fiber reinforced polymer composite

Figure 3 shows the attenuation level of porosity vs. proportion of epoxy-glass laminate. The value of attenuation is associated with the porosity proportion in the composite structure and this relationship is approximately linear. The results are consistent with the results of studies obtained in the study [19], where Liu and co-authors noted that there is an approximately linear relationship between the level of discontinuity and elastic wave absorption coefficient for carbon-epoxy laminates. A lower content of porosity in structure has been found for lower attenuation values.
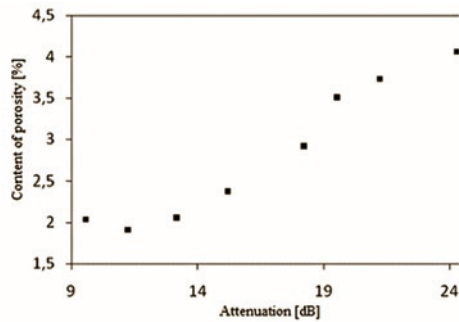
Fig. 3. The relationship between the percentage of porosity and the level of attenuation in epoxy-glass laminate

On the basis of obtained results, selected research method has been classified as a method useful for the detection of structural disconti-nuities in both carbon and glass epoxy laminates. Individual levels of attenuation reflect the contents of the porosity in a relatively accurate manner, which implies the possibility to determine the threshold lim-its assigning the attenuation value to the specific maximum porosity level.

3. Evaluation of operational capabilities after a dynamic impact

Under operating conditions, the fibre polymer composites and fi-bre metal laminates are exposed to unpredictable loads, first of all high or low speed single impact of concentrated force. As a result of high speed dynamic loads, a catastrophic structure failure takes place and usually said structure is eliminated from further operation or qual-ified for immediate repair [2, 30, 34, 36]. In case low speed dynamic impact of concentrated energy, internal structural failures are possible (delaminations, matrix cracking), particularly in case of energy not exceeding 5 J [17]. The phenomenon of inner failures propagation in composite structures makes it necessary to monitor their condi-tions by means of non-destructive methods, because the damaged composite material is unable to withstand the whole scope of loads assumed as early as in design phase [16, 29, 34]. In order to evaluate the possibility to diagnose the condition of composite laminates after single low speed impact by means of ultrasonic echo method, this type of loads has been simulated fully controlling the speed, energy and geometry of hitting body. The ultrasonic echo method is the most popular non-destructive testing method used in aircraft industry for flying objects in their operation phase due to limited, often one sided access to an element under test.The controlled dynamic impact test was carried out on the dynamic machine called drop-weight tester us-ing a hemispherical indenter. The test was performed in accordance with ASTM D7136 standard [3] in energy range of 1,5 ÷ 25 J. The tests were carried out for carbon fibre reinforced polymer composite materials (CFRP) certified for the airspace applications in critical and high – loaded elements as well as for innovatory fibre metal laminates (FML) consisting of carbon fibre reinforced polymer composite mate-rials (CFRP), alternately arranged layers in rectangular layout (0/90) and 2024-T3 (Al/CFRP) aluminium alloy. The materials for tests have

been produced in autoclave process in the Materials Engineering De-partment in Lublin University of Technology.

The aim of the study was to analyze the influence of impact en-ergy on character and range of failure in composite materials in the aspect of their further operation and possibility to apply the ultrasonic echo method for qualitative and quantitative description of their con-dition after single impact. OmniScan ultrasonic flaw detector with multi-transducer head (64 active elements) has been used for non-destructive analysis. Figure 4 illustrates the value of low speed impact energy vs. maximum force transmitted by the material and caused by the impact.
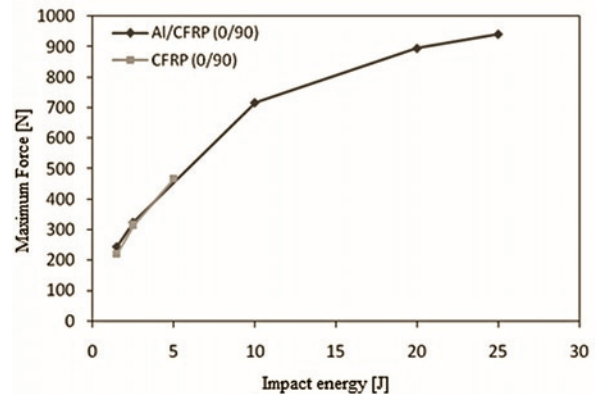

Fig. 4. The relationship between strength and maximum impact energy in a dynamic test

On the basis of obtained data (Fig. 4) it can be concluded that the force exerted on the material increased with increasing impact energy [28, 33, 34]. At low impact energies, CFRP laminates are character-ized by force transmission capacity resulting from the dynamic load similar to Al/CFRP laminates. The impact energy of 10 J causes the complete perforation of CFRP laminate, as shown in Figure 5.
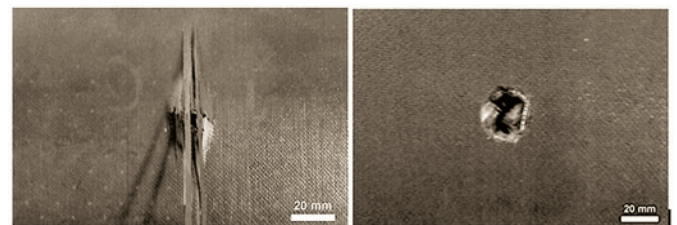

Fig. 5. CFRP laminate damage zone after being hit with the energy of 10J - bottom side (left), side impact (right)

Total disruption of the material eliminates it from further exploi-tation. However, fibre-metal laminates, subjected to further impact energy levels were gradually degraded, as shown in Figure 6.
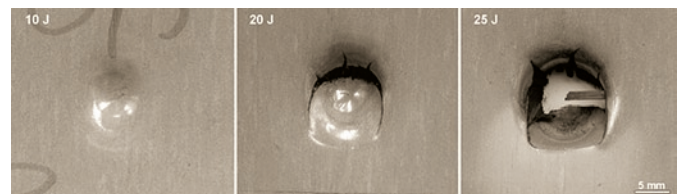

Fig. 6. Macroscopic figure of the extent of degradation fiber metal laminates after low velocity impact (impact side)

Finally, their complete perforation has been caused by impact en-ergy of 25 J by means of an indenter. The phenomenon of structure destruction degree growth vs. energy increase has been described in

studies [23, 34]. The cracks of bottom aluminium layer propagate perpendicularly to the orientation of bottom composite layer. The correlations between the orientation of composite fibres and the direction of metal layer cracking have been also described by Liaw B.M. et al. [18] who analyzed the direction of bottom aluminium layer cracking propagation in epoxy-glass aluminium-composite laminates. Liaw B.M. denoted that cracking direction in aluminium coincides with the orientation of bottom composite layer.

Any influence of metal sheet rolling direction on the direction of aluminium layers cracking propagation in laminates has been not found in the tests, this fact has been also denoted by Caprino G. et al. [8]. On the basis of macroscopic analysis, it can be found that Al/CFRP laminates are characterized by higher resistance to dynamic loads than conventional fibre reinforced polymer composites. In case of metal fibre laminates used for aircraft skin elements it possible to increase durability and functioning possibility under more demanding operational conditions, this fact is also confirmed i.a. by Vlot A. [34].

However, the low energy dynamic loads are of greater importance for operational reliability and safety because the materials are still subjected to the full spectrum of loads and additionally to fatigue without causing any visible changes of the surface. Nevertheless, quantitative and qualitative identification of potential internal structural discontinuities after low energy impact is possible by means of ultrasonic non-destructive methods [26]. Fig 7 illustrates selected amplitude representations (Type B and C) presented in gray scale for composite and
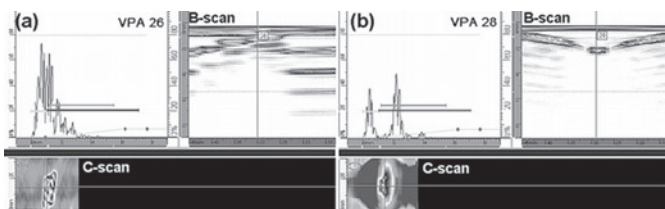
metal-fibre laminates being tested after low energy impact.

The application of multi-transducer techniques in ultrasonic non-destructive tests makes it possible to precisely perform quantitative identification of the area influenced by an impact with specified energy. It is important in the operational aspect, because it is more easy to carry out potential repairs of damaged structures fragments. In case of conventional polymer fibre composites, an amplitude representation makes it possible to determine the type of occurred failures e.g. delaminations (amplitude change), determined by fibres orientation. Furthermore, C representation indicates to multilevel character of delaminations occurred after the impact, as represented by diversified colours of individual failure zones at various depths. Similar conclusions have been presented by Pearson M.R. et al. in their studies [24]. By means of B representation it is possible to determine the depth of individual delaminations and to determine their axial-lateral dimension. Furthermore, the image analysis makes it also possible to determine the surface area of identified discontinuities. In case of Al/CFRP laminates, it is difficult to precisely identify potential discontinuities due to numerous signal noises represented by multiple secondary reflections generated as a result of acoustic impedance change on metal-composite interface. Permanent plastic strain occurring after impact generates an additional amplitude reduction and amplifies recorded noises. C image representing the failures in a view parallel to laminate surface is the response to the lack of an explicit image of discontinuities in FML laminates. Impossibility to separate the image of plastic strain from potential delaminations and cracks is of importance in repair process and consequently in further operation. On the basis of performed non-destructive tests using ultrasonic echo method it has

been found that there was no propagation of structural discontinuities out of zone of permanent plastic strain caused by indenter. Similar problems in the scope of identification of structural discontinuities in metal-fibre laminates have been denoted and described by Dragan K. at al. [12].

The macroscopic analysis of damage zones was performed in order to verify the ultrasonic echo method. Selected images of CFRP and Al/CFRP laminate microstructure are illustrated in Figure 8.
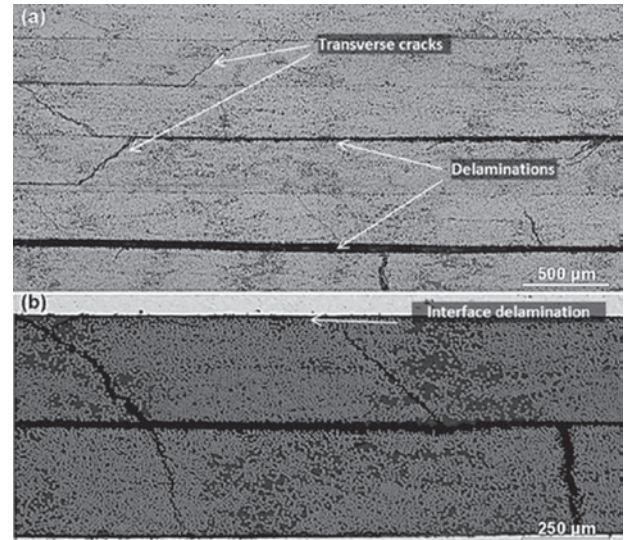

Fig. 8. CFRP laminate cross-section (a) and Al / CFRP (b) the impact of energy – 5 J

The microstructural analysis confirms that the dynamic impact with low-speed and low energy cause internal degradation of the polymer-carbon composites and fibre metal carbon laminates. CFRP composites are characterized by a more complex nature of the breakdown of the structure. Delaminations occurring under the influence of dynamic impact and transverse cracks connecting said delaminations are prevailing in tested materials. Additionally, longitudinal matrix cracks are formed on metal-composite interface, which results from the hybrid nature of components and adhesive bond between them. Delaminations between the composite layers are limited. Similar observations are described among others H. Nakatani et.al [23]. As a result of performed tests, the authors have denoted the relationship between the total area of cracks and delaminations and impact energy in CFRP composite and Al/CFRP laminates. The relationship between damaged surface area and impact energy is shown in Figure 9.
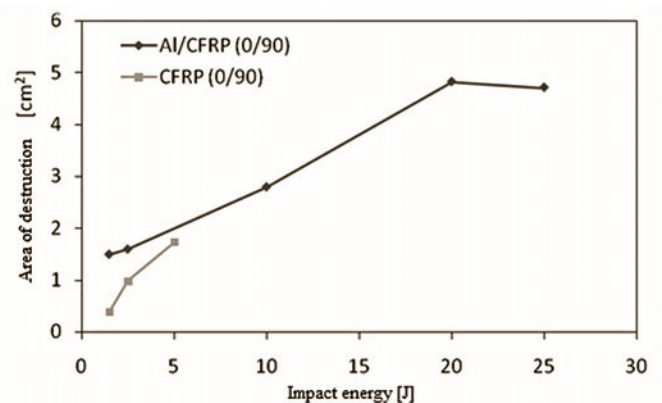

Fig. 9. The area of damage after impact in composite laminates at a low speed, depending on the impact energy.

It was observed that the growth of the destruction surface area vs. impact energy is almost linear. The damage area in CFRP composites detected by means of ultrasonic echo method is lower than in Al/CFRP laminates, which is a direct result of permanent deformation of laminates as a result of contact with the indenter. However, the energy of 10 J causes their complete perforation. Fibre-metal laminates are resistant to significantly higher energies of dynamic loads and are subject to proportional failure expansion. Polymer-fibre laminates have an evident limit of low speed impact loads capacity regardless of less negative influence of said loads in low energy range. Due to operational reasons, the use of fibre-metal laminates seems to be justified for those components exposed to dynamic loads, for which high strength and fatigue properties are also required.

4. Conclusions

1. Fibre-metal laminates are the materials with a higher potential in the scope of reliability and operation in comparison to conventional fibre-reinforced polymer composite materials.
2. The level of porosity in composite structures has an important impact on their service life and operational capabilities.

Demonstrated relationship between the decrease in amplitude of ultrasonic wave passing through the laminate and porosity percentage indicates the potential of ultrasonic methods in the testing of structural condition of fibre reinforced polymer composites.

3. During aircrafts operation, the skin materials are exposed to the unpredictable phenomena of dynamic impact with specified speed and energy. Fibre metal laminates carry the loads induced by supplied energy in the scope of energies many times higher in comparison to conventional composite materials. Failure mode of composite laminates as a result of low speed dynamic loads is complex. Delaminations and extensive polymer matrix cracks prevail. Sufficiently low impact energy causes internal failures in composite structures without possibility to assess its condition by means of macroscopic methods.
4. Ultrasonic echo method with multi-transducer technique allows qualitative and quantitative identification of negative effects of low speed and low energy dynamic loads in composite materials.

References

1. Alderliesten RC, Homan JJ. Fatigue and damage tolerance issues of Glare in aircraft structures. International Journal of Fatigue 2006; 28: 1116–1123.
2. Ardakani M A, Khatibi A A, Ghazavi S A. A study on the manufacturing of Glass-Fiber-Reinforced Aluminum Laminates and the effect of interfacial adhesive bonding on the impact behavior. Proceedings of the XI International Congress and Exposition 2008; Florida, USA.
3. ASTM D7136. Standard test method for Measuring the Damage Resistance of a Fiber-Reinforced-Polymer matrix Composites to a Drop-Weight Impact event. Book of Standards 2006; 3 (15).
4. Bieniaś J. Fibre metal laminates – some aspects of manufacturing process, structure and selected properties. Kompozyty 2011; 11: 39–43.
5. Bowles KJ, Frimpong S. Void effects on the interlaminar shear of unidirectional graphite reinforced composites. Journal of Composite Materials 1992; 26: 1487–1509.
6. Campbell FC. Manufacturing Technology for Aerospace Structural Materials. Elsevier, 2006.
7. Cantor B, Assender H, Grant P. Aerospace Materials. Bristol: IOP Publishing Ltd, 2001.
8. Caprino G, Spatarob G, Del Luongo S. Low-velocity impact behaviour of fibreglass–aluminium laminates. Composites 2004; 35: 605–616.
9. Chambers AR, Earl JS, Squires CA, Suhot MA. The effect of voids on the flexural fatigue performance of unidirectional carbon fibre composites developed for wind turbine applications. International Journal of Fatigue 2006; 28: 1390–1395.
10. Ciliberto A, Cavaccini G, Salvetti O, Chimenti M, Azzarelli L, Bison PG, Marinetti S, Freda A, Grinzato E. Porosity detection in composite aeronautical structures. InfraredPhysics and Technology 2002; 43: 139–143.
11. Davies GA, Zhang X. Impact damage prediction in carbon composite structures. International Journal of Impact Engineering 1995; 16 (1): 149–170.
12. Dragan K, Bieniaś J, Leski A. Inspection methods for quality control of fibre metal laminates (FML) in the aerospace components. XVI Seminarium Kompozyty Teoria i praktyka 2012; Poraj, Poland.
13. Freeman WT. The Use of Composites in Aircraft Primary Structure. Composites Engineering 1993; 3: 767–775.
14. Hodgkinson JM. Mechanical testing of advanced fibre composites. Woodhead Publishing Ltd, 2000.
15. Joeng H, Hsu DK. Experimental analysis of porosityinduced ultrasonic attenuation and velocity change in carbon composites. Ultrasonics 1995; 33(3): 200–202.
16. Laliberte JF, Poon C, Straznicky PV, Fahr A. Post-impact fatigue damage growth in fiber-metal laminates. International Journal of Fatigue 2002; 24: 249–256.
17. Lawcock GD, Ye L, Mai YW, Sun CT. Effects of fibre/matrix adhesion on carbon-fibre-reinforced metal laminates-II. Impact behavior. Composites Science and Technology 1997; 57: 1621–1628.
18. Liaw BM, Liu YX, Villars EA. Impact Damage Mechanisms in Fiber Metal Laminates, Proceedings of the SEM Annual Conference on Experimental and Applied Mechanics 2001; Portland, USA.
19. Liu L, Zhang B. Effects of cure cycles on void content and mechanical properties of composite laminates. Composite Structures 2006; 73: 303–309.
20. Lopes CS, Remmers JC, Gürdal Z. Influence of porosity on the interlaminar shear strength of fibre-metal laminates. Key Engineering Materials 2008; 383: 33–52.
21. Leali M, Costa S, Almeida M, Rezende M. The influence of porosity on the interlaminar shear strength of carbon/epoxy and carbon/bismaleimide fabric laminates. Composites Science and Technology 2001; 61: 2101–2108.
22. Miracle DP, Donaldson SL. ASM Handbook Vol. 21 Composites. ASM International, 2001.

23. Nakatani H, Kosaka T, Osaka K, Sawada Y. Damage characterization of titanium/GFRP hybrid laminates subjected to low-velocity impact. Composites2011; 42: 772–781.

24. Pearson MR, Eaton MJ, Featherston CA, Holford KM, Pullin R. Impact Damage Detection and Assessment in Composite Panels using Macro Fibre Composites Transducers. Journal of Physics. Conference Series, 2012; 305.

25. Purslow D. The optical assessment of the void content in composite materials, Composites 1984; 15(3): 207-210.

26. Reid A, Zhou G. Impact behavior of fibre-reinforced composite materials and structures. USA: CRC Press, 2000.

27. Richardson MO, Wisheart MJ. Review of low-velocity impact properties of composite materials. Composites 1996; 27: 1123–1131.

28. Sayer M, Bektas NB, Sayman O. An experimental investigation on the impact behavior of hybrid composite plates. Composite Structures 2010; 92: 1256–1262.

29. Short GJ, Guild FJ, Pavier MJ. Post-impact compressive strength of curved GFRP laminates. Composites 2002; 33: 1487–1495.

30. Sohn MS, Hua XZ, Kimb JK, Walker L. Impact damage characterization of carbon fbre/epoxy composites with multi-layer reinforcement. Composites 2000; 31: 681–691.

31. Staffan T. Void formation and transport in manufacturing of polymer composites. Doctoral thesis. Luleå University of Technology, www.epubl.luth.se/avslutade/0348-8373/184

32. Swanson SR. Introduction to Design and Analysis with Advanced Composite Materials. Prentice-Hall, 1997.

33. Vlot A, Gunnink JW. Fibre Metal Laminates: an introduction. Kluwer Academic Publishers, Dordrecht, The Netherlands 2001.

34. Vlot A. Impact loading on fibre metal laminates. International Journal of Impact Engineering 1996; 18(3): 291–307.

35. Vlot A, Krull M. Impact Damage Resistance of Various Fiber Metal Laminates. Journaldephysique 1997; 7(3): 1045–1050.

36. Vogelesang LB, Vlot A. Development of fibre metal laminates for advanced aerospace structures. Journal of Materials Processing Technology 2000; 103: 1–5.

37. Woerden HJ, SinkeJ, Hooijmeijer PA. Maintenance of glare structures and glare as riveted or bonded repair material. Applied Composite Materials 2003; 10: 307–329.

38. Wu G, Yang JM. The mechanical behaviour of glare laminates for aircraft structures. JOM 2005; 57:72–79.

39. Zhu H et al. Influence of Voids on the Tensile Performance of Carbon/epoxy Fabric Laminates. Journal of Materials Science & Technology 2011; 27(1): 69–73.

Jarosław BIENIAŚ, Ph.D. (Eng.)
Patryk JAKUBCZAK, M.Sc. (Eng.)
Krzysztof MAJERSKI, M.Sc. (Eng.)
Monika OSTAPIUK, M.Sc. (Eng.)
Prof. Barbara SUROWSKA, Ph.D., D.Sc. (Eng.)
Department of Materials Engineering
Faculty of Mechanical Engineering
Lublin University of Technology
ul. Nadbystrzycka 36, 20-618 Lublin, Poland
e-mail: j.bienias@pollub.pl

Jarosław PYTKA
Piotr TARKOWSKI
Włodzimierz KUPICZ

A RESEARCH OF VEHICLE STABILITY ON DEFORMABLE SURFACES

BADANIE STABILNOŚCI RUCHU SAMOCHODU NA PODŁOŻACH ODKSZTAŁCALNYCH*

The paper includes results form a research of ride stability of a SUV (Sport Utility Vehicle), driven over deformable surfaces. An analytical method, in which stability of a mathematical model of vehicle's lateral dynamics is tested. The mathematical model has been reconstructed by means of a system identification method. We have used steering wheel angle as an input signal and lateral acceleration, side slip angle and yaw velocity as output signals to create the model. The data required to perform system identification have been gathered in a full size experiment, with the use of an instrumented vehicle. Final results in a form of poles and zeros diagrams have been included in the paper together with a discussion.

***Keywords**: vehicle ride stability, lateral dynamics, offroad vehicles, deformable surfaces, system identification.*

W artykule zawarto wyniki badań stabilności ruchu samochodu osobowo-terenowego na podłożu odkształcalnym. Zastosowano analityczną metodę badania stabilności, w której badana jest stabilność matematycznego modelu danego obiektu. W rozpatrywanym przypadku, model matematyczny odtworzono na podstawie analizy sygnałów wejściowych (kąt obrotu kierownicy) oraz wyjściowych (przyspieszenie boczne i kąt bocznego znoszenia środka ciężkości, prędkość kątowa odchylania od kierunku ruchu, moment na kole kierownicy), z zastosowaniem metody identyfikacji systemów.

***Słowa kluczowe**: stabilność ruchu, dynamika ruchu samochodu, podłoża odkształcalne, metoda identyfikacji systemów.*

1. Introduction

Vehicle stability can be tested by means of a variety of methods. One of them is that we assume stability analysis will be performed based on experimental data. Trajectory of the vehicle ride has to be determined and the stability can be performed by analyzing this trajectory and observing if the trajectory is within a stability margin. However, this method is of low accuracy and time consuming. Subjective valuation may lead to erroneous conclusions. One of the possible methods to evaluate ride stability of a vehicle is testing of its mathematical model. In this method, eigenvalues or roots of the so called characteristic equation of the model are evaluated. For a given system to be stable, or to have positive stability requires all the roots have negative real components.

A purpose of the present study was to apply the system identification and stability analysis method to evaluate ride stability of a SUV, driven over deformable surfaces.

2. Modeling of lateral dynamics of a SUV by system identification

System identification (SI) is a process in which a model and its parameters are reconstructed based on experimental data. There is a wide range of methods used for SI, from simple approximation to complex statistical analysis (Ljung, 1999). The method is widely used in modeling of aircraft dynamics and control (Klein and Morelli, 2006). Also, modeling studies in vehicle dynamics have been performed by means of the SI method (James, 2002). Reconstruction of mathematical models by means of the SI method may provide with

sufficient data to perform stability analysis. It is needed, however, the experimental data used for identification procedures are fully informative for a given system. Based on the data models of linear and nonlinear systems can be reconstructed. When the identified model is linear, it is possible to analyze stability of a modeled system by means of eigenvalues evaluation. The procedure, called the zeros and poles test, gives an accurate verdict.

Instrumentation and measurements

Analysis if ride stability of a vehicle can be performed based on lateral dynamics analysis and therefore, the following measures are of high performance [1, 4, 5, 7]:
  – lateral acceleration of the centre of gravity;
  – yaw rate of the vehicle's gravity center;
  – sideslip angle of the vehicle.

In our approach, the over-mentioned are output signals and the input will be steering wheel angle.

One of the requirements for the SI experiment is that the data obtained are accurate and informative. That can be fulfilled by designing the so called open-loop experiment. In other words, output signals have to be not dependent of the system response. It is not possible, when a person (driver) applies steering wheel angle as an input signal. One possible solution to apply here is to use a steering robot. We used ABDynamics steering robot, which consisted of five major subsystems:
  – a motor unit mounted on the steering wheel
  – a mounting fixture with torque transducers
  – a control unit
  – a power supply

– a computer with control software.

The steering robot can perform various steering scenarios to re-produce standard vehicle dynamic tests according to the ISO 7401, 3888, et cetera. One can also compose custom maneuvers by setting up important test parameters such as steering wheel angle rate 0 – 1800 deg/sec, frequency 0 – 10 Hz, steering wheel angle amplitude up to the limit of a vehicle, and duration of the maneuver. Installation of the robot in the research vehicle was simple with no special modifications (Figure 1). Before the test runs, the robot underwent typical procedures for aligning and setting the neutral point.

Measuring the input and output signals was performed with the following instrumentation:
- lateral acceleration, side slip angle and yaw rate have been measured by means of a DGPS (**D**igital **G**lobal **P**ositioning **S**ystem);
- steering wheel moment and angle have been measured with the use of a instrumented steering wheel, which was one of the components of the steering robot.

The DGPS receiver coupled with an inertial platform has been used to measure kinematics parameter of vehicle motion. This system features 20-mm position accuracy at 10-ms acquisition time. It consists of an on-board subsystem (a receiver, power supply, and antenna) and a field-portable base station with external antenna. Coupling the DGPS with the robot allows to fully monitor vehicle motion and to define test runs by x-y coordinates of waypoints.
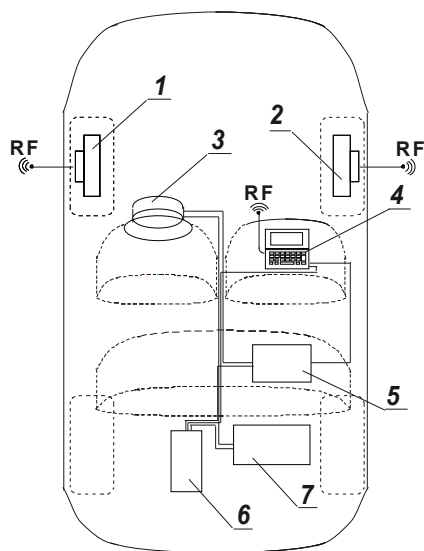
Fig. 1. *A schematic of the instrumentation installed into the test vehicle and a cockpit view of the steering robot arrangement. 1, 2 – rotating wheel dynamometers, 3 – steering robot, 4 – interface computer, 5 – master computer, 6 – DGPS onboard unit, 7 – power supply*

Procedures

The tests were performed on three different surfaces: sandy and loess soils and a wet snow surface. We chose loess and sandy soils as test surfaces because they represent different mechanical proper-

ties: cohesion for loess and internal friction for sand. The two soil materials are major components of many soil types. We conducted experiments on two different sites where the soil surfaces exist naturally: Sulejówek, near Warsaw, Central Poland for sandy soil and Paulinów, near Lublin, Southeast Poland for loess soil. The surfaces were rototilled after each pass of the test vehicle. Experiments on wet snow surface were carried out in February 2010 in Sulejówek. Snow depth was approximately 50cm, its density 500 – 700 kg/m^3, and temperature −0.3°C. We used only sine wave input for the snow surface experiments.

In the tests we have applied two different excitation methods: a step input excitation for dynamics test and a periodical excitation for steady state tests.

Ramp change (or trapezoidal) excitation mode is a typical dynamic method, in which we can determine dynamical response of the vehicle to continuously changing input. This ramp change input provides a substitute for step input (which is technically impossible to perform). Vehicle response has to be measured continuously and at a high sampling rate, since the observed parameters (yaw rate, lateral acceleration, sideslip angle, and the position of the center of gravity [CG]) changes dynamically, especially at the moment of and after the steering input.

Sine wave excitation is a typical steady state procedure. The vehicle is steered by harmonic excitation of the steering wheel at a given frequency and amplitude. We used 0.5, 1.0, and 2.5 Hz frequencies and ± 90 deg amplitudes. Vehicle response (yaw rate, lateral acceleration, and sideslip angle) is observed when it reaches stability (after a couple of steering periods). This requires that the test be performed on a sufficiently long test track.

Both excitation variants are presented in Figure 3.The three values of steering angle rate for ramp change excitation were 100, 500, and 1500 deg/s, while the amplitude was 180 degrees. The frequencies of sine wave excitation were 0.5, 1.0, and 2.5 Hz, with an amplitude of 90 degrees. The steering ratio of the vehicle used for the test was 1 to 9. A graphical presentation of the excitation modes is given in figure 2.
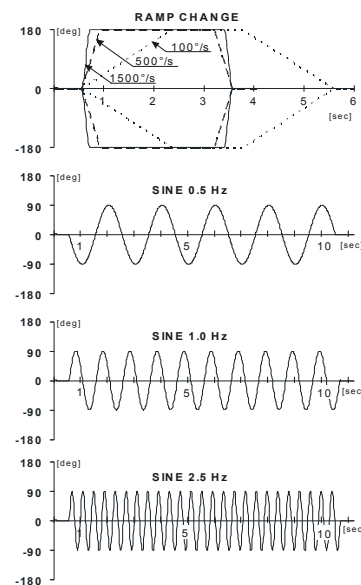

Fig. 2. Steering wheel excitation modes

The vehicle was driven in 4×4 mode (mechanically coupled drive chain, all four wheels driven) with a reduction gear on. The velocity of the test rides was approximately 10 km/h – almost the highest possible speed on those surfaces at low slip conditions. At least five replications were performed for each test variant.

3. The method of evaluation of the vehicle ride stability

One method of stability testing is the so called zeros and poles test. Stability of a given system is positive (the system is stable) if eigenvalues of the following equation:

$$\ddot{x}(t) + 2\xi\omega_n\dot{x}(t) - \omega_n^2 x(t) = bu(t) \qquad (1)$$

are placed within the (−1;1) range. With roots, which have their real part is higher then 1 and imaginary part is zero, a system is unstable and we can say about non periodic instability. If an imaginary part is different from zero, the instability is of an oscillating type. Possible cases are shown in figure 3. If the roots have only real components (there aren't complex roots), we can speak of an asymptotical stability of the tested system (Figure 3a). If there are such roots (complex roots), the response of the system is of oscillating character (b). Those oscillations would disappear faster for roots placed apart of the imaginary axis. If one of the toots is placed exactly on the imaginary axis, the system has marginal stability and the oscillations will not disappear. For positive roots, right to the imaginary axis, the system is not stable (c and d).
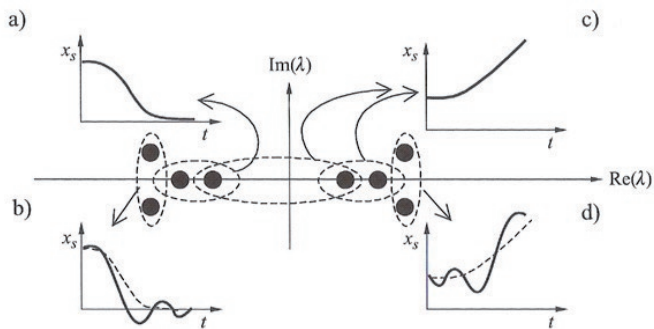
Fig. 3. Possible locations of eigenvalues of the characteristic equation of the model and their effects on stability (see text)

The software used to perform zeros and poles testing allowed to analyze the roots as well as poles, which are points where the model function has an asymptote.

4. Results and analysis

Figures 4 thru 18 contains results of performed zeros and poles tests for the models of lateral dynamics of the vehicle, based on experimental data obtained in the experiments performed on two different surfaces. Results for both periodical as well as ramp change steering input are included.

Based on the results presented in figs. 4 thru 6 we can say the stability evaluation based on lateral acceleration data is positive for loess and wet snow surfaces, at 1 Hz excitation. For the remaining variations we obtained negative evaluation of vehicle stability. The highest instability, quantified by means of real component value, was observed on sandy soil surface. This can be related to high deformability of this surface, what leads to deep ruts and consequently tripping the roadwheels of the vehicle. This may be the cause of the so called *tripped roll-over*, a very frequent scenario of accidents in cases of leaving the road [8].

The three following figures, 7 – 9 show the results for the second important lateral dynamics measure, the side slip angle.

Evaluation of vehicle stability based on side slip angle data shows a diverse trend. Here, positive stability occurs on sandy soil surface only. There are some but not numerous exceptions, moreover these roots are very close to stability margins. Physically, it can be explained as follows: the wheels grip the surface as the ruts are deep and no significant yaw motion is possible. A quite different trend was observed on loess soil surface. The wheels don't sink deep into the soil so they do a lot of side slipping and consequently yawing motion of the vehicle is much more visible. A similar situation occurred on wet snow. That was rather unexpected, since deep ruts in snow could eventually help to keep the track, but a high decrease in wheel-surface friction on wet snow played a more important role.

Figures 10 thru 12 show root locus plots for the third measure that is important for lateral dynamics of a vehicle, the yaw rate.

Analyzing these graphs, we have concluded the motion of the test vehicle to be least stable. For the yaw rate, there has been observed the highest value of real part of a root. It was 20,38, noticed on sandy loess surface. Moreover, instability occurred on all the three surfaces, loess, sandy and wet snow. On loess surface a case of periodical instability was observed. The only stable motion occurred on sandy soil surface for 1,0 Hz sine wave excitation.

Another step in our study was an analysis of vehicle motion for trapezoidal steering excitation. The method of stability analyzing was similar to that for sine wave excitation. Autoregressive models have been reconstructed from measured data of steering angle as an input parameter and for the three lateral dynamics measures, as output signals. Figures 13 thr 18 contains root locus plots for the two soil surfaces (no data for wet snow surface has been collected). Stability evaluation based on lateral acceleration is shown in figs 13 and 14.

The figures consist of two graphs, one of them represents turning to the left, another to the right. We observed instability for the two surfaces, generally for higher values of steering wheel angular velocity (500 and 1500 deg/s). In case of sandy soil surface, instability occurred at the lowest velocity (100 deg/s), while for the remaining higher velocities vehicle motion was stable. On the loess surface there was observed the highest instability (Re = 18,22 for 500 deg/s) while on the sandy soil surface a periodic instability was observed at 500 deg/s.

Stability evaluation of the vehicle motion based side slip angle data and yaw rate was similar to that obtained with sine wave excitation tests. Figures 15 and 16 show results for the evaluation based on side slip angle data. There was noticed instability for test runs on loess soil surface for all the three steering wheel angular velocities. Moreover, a periodic instability occurred at 100 deg/s. Results for the two directions of turning (to the right and to the left) are similar. On sandy soil surface, vehicle motion was stable only for the lowest steering wheel angular velocity. For the remaining cases, at 500 and 1500 deg/s there was noticed instability. At 1500 deg/s by turning to the left and at 500 deg/s and turning to the right there were observed severe oscillations.

The third important measure used for evaluation of vehicle motion stability by trapezoidal excitation of the steering wheel was yaw rate. Root locus plots obtained based on yaw rate analysis is shown in figures 17 i 18. By turning to the right on loess soil surface, vehicle motion was stable at 100 deg/s, for the remaining excitations we observed instability. By turning to the left, the highest instability was noticed at 500 deg/s (Re = 17,76). For both, turning to the right and to the left, oscillating instability occurred at 500 deg/s. Zeros and poles tests based on data gathered during test rides over sandy soil surfaces showed instability for all cases of angular velocity of the steering wheel. On the other side, there was no oscillating instability in those tests.
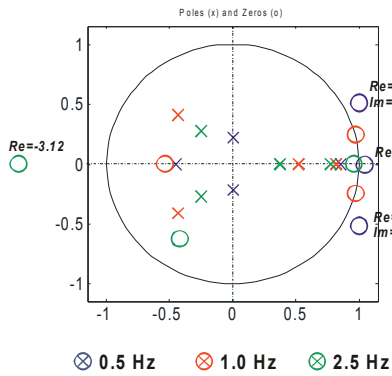
Fig. 4. Root locus plot for sine wave excitation, lateral acceleration. Tests on less soil surface
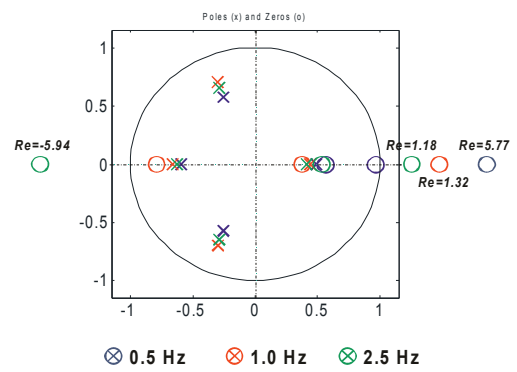

Fig. 5. Root locus plot for sine wave excitation, lateral acceleration. Tests on sandy soil surface
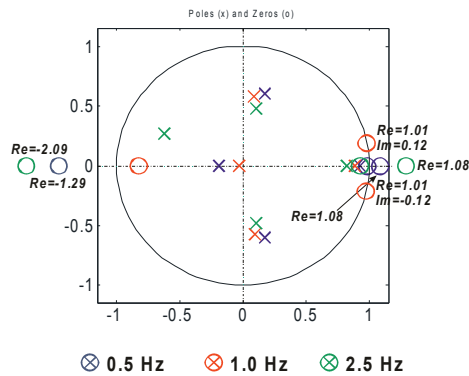

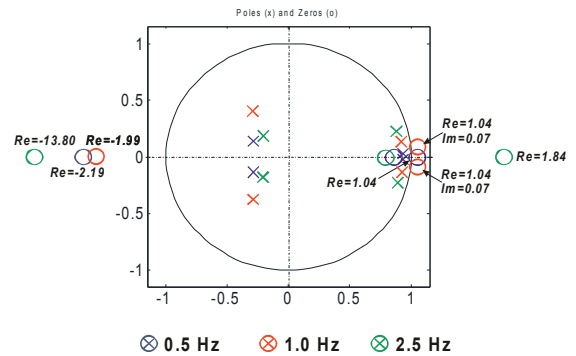Fig. 6. Root locus plot for sine wave excitation, lateral acceleration. Tests on wet snow surface

Fig. 7. Root locus plot for sine wave excitation, side slip angle. Tests on less soil surface
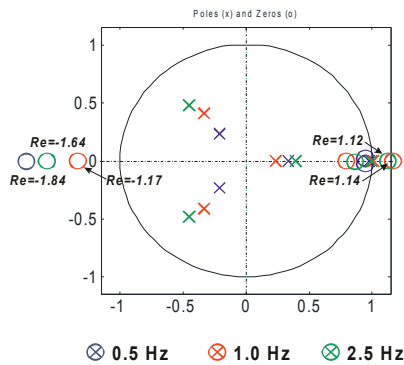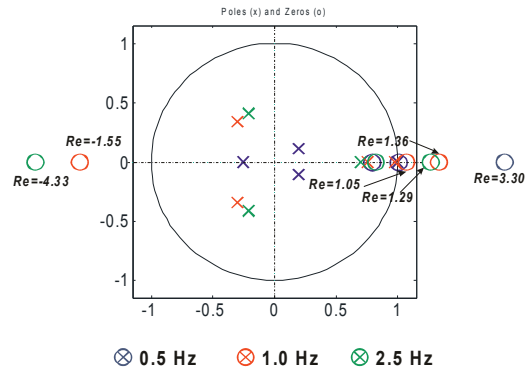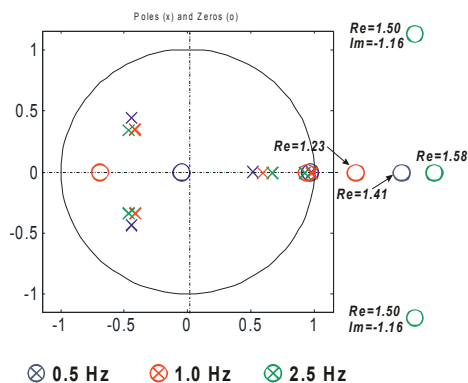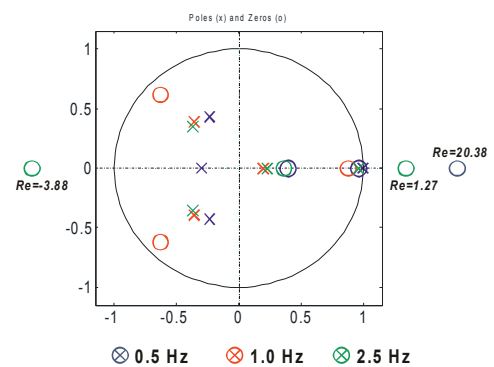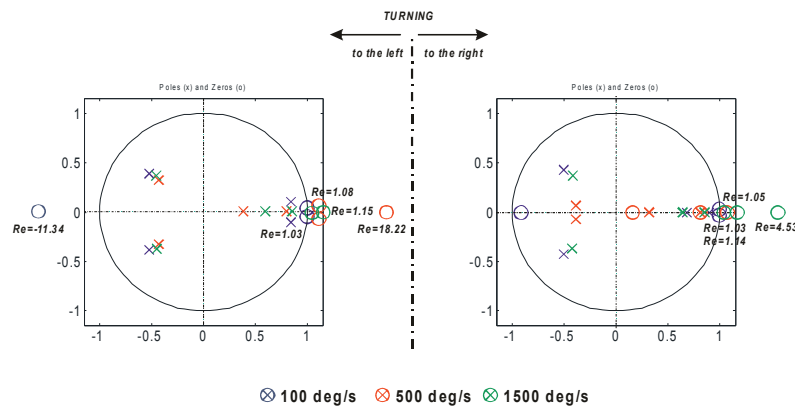

Fig. 8. Root locus plot for sine wave excitation, side slip angle. Tests on sandy soil surface

Fig. 9. Root locus plot for sine wave excitation, side slip angle. Tests on wet snow surface

Fig. 10. Root locus plot for sine wave excitation, yaw rate. Tests on less soil surface

Fig. 11. Root locus plot for sine wave excitation, yaw rate. Tests on sandy soil surface
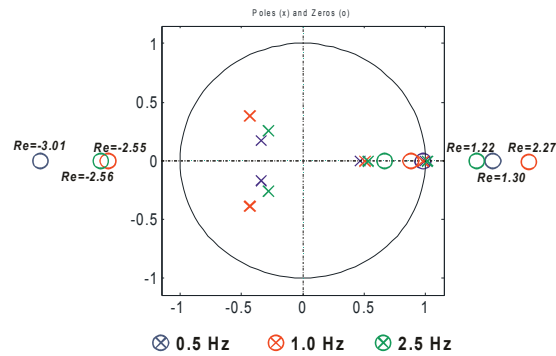
Fig. 12. *Root locus plot for sine wave excitation, yaw rate. Tests on wet snow surface*

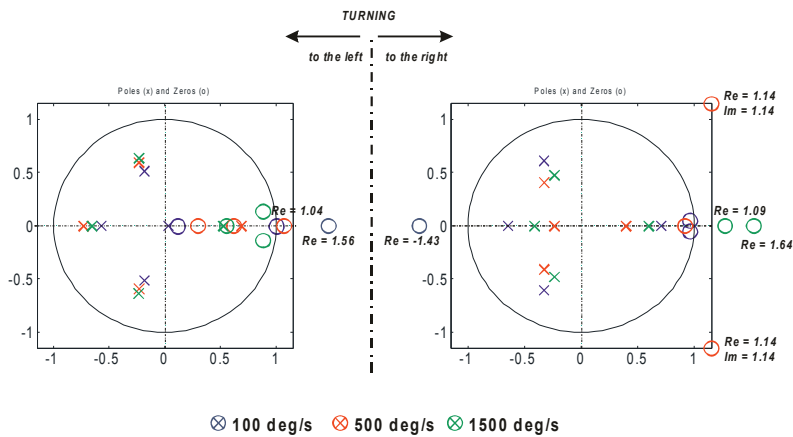Fig. 13. *Root locus plot for trapezoidal excitation, lateral acceleration. Tests on less soil surface*

Fig. 14. *Root locus plot for trapezoidal excitation, lateral acceleration. Tests on sandy soil surface*
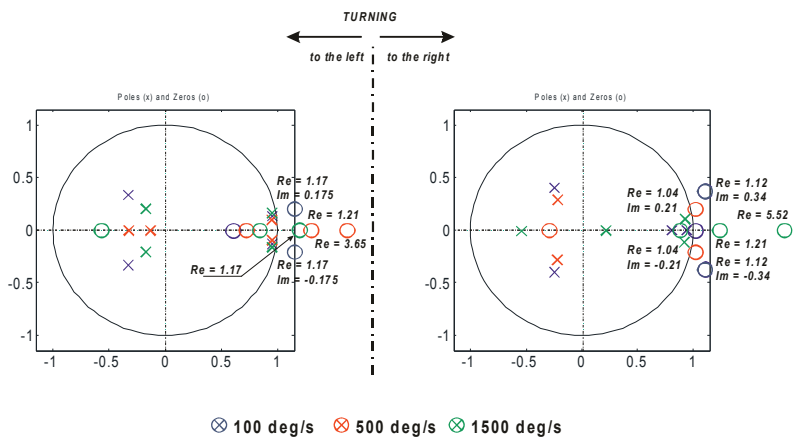

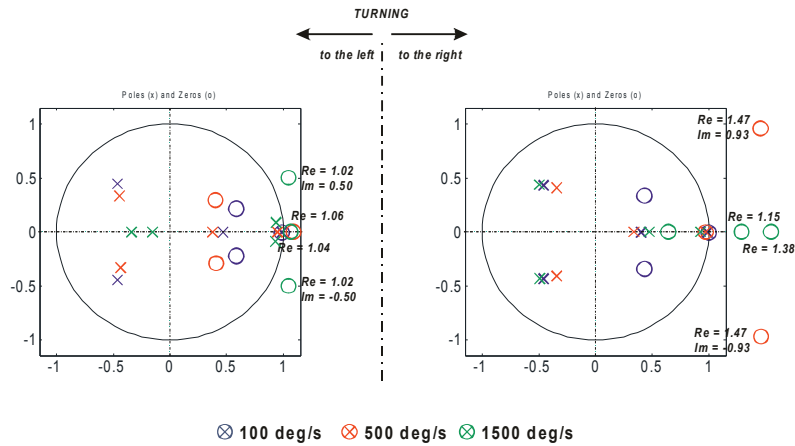Fig. 15. *Root locus plot for trapezoidal excitation, side slip angle. Tests on less soil surface*

Fig. 16. *Root locus plot for trapezoidal excitation, side slip angle. Tests on sandy soil surface*
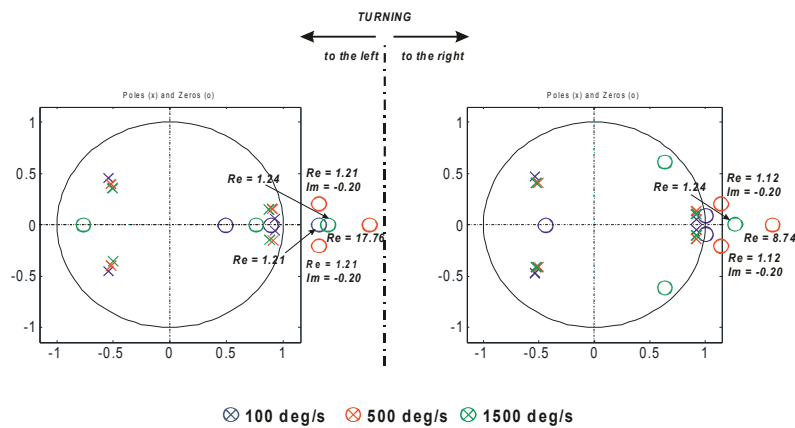

Fig. 17. *Root locus plot for trapezoidal excitation, yaw rate. Tests on less soil surface*
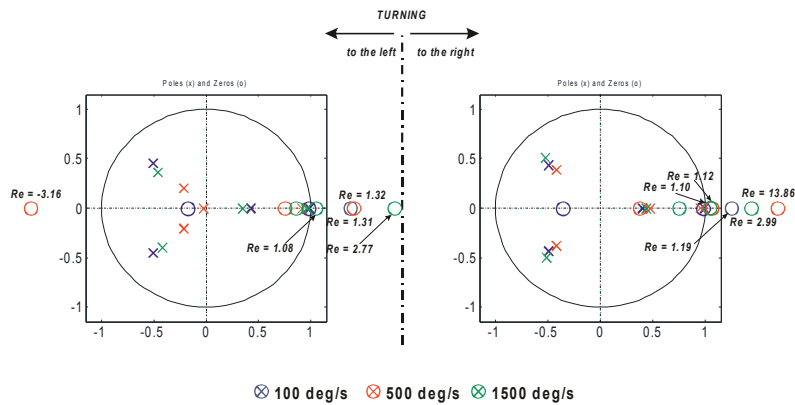

Fig. 18. *Root locus plot for trapezoidal excitation, yaw rate. Tests on sandy soil surface*

5. Conclusions

We have analyzed vehicle motion stability based on experimental data obtained in a real size, field experiments. The method of analysis consisted of reconstructing the autoregressive models of lateral dynamics of the vehicle and of performing the zeros and poles tests for these models. We have designed an open loop experiment with the use of a steering robot and two different excitation methods have been applied: sine wave (periodical) and trapezoidal. All the tests and analysis have been performed for the vehicle driven over three different deformable surfaces, loess and sandy soils and a wet snow. The result of the stability evaluation have been presented in a form of root locus plots and they have been discussed. A general conclusion is that the presented method is of a practical applicability, but needs some enhancements, firstly filtering of measured signals could help in obtaining more homogenous data, what is required in analytical studies of stability.

References

1. Gillespie TD. Fundamentals of Vehicle Dynamics. SAE Warrendale, USA, 1992.
2. Ljung L. System identification: theory for the user, 2nd edition. Prentice Hall, Englewood Cliff, USA, 1998.
3. Lozia Z. An analysis of vehicle behaviour during lane-change manoeuvre on an uneven road surface, Vehicle System Dynamics, 1992; 20: 417–431.
4. Milliken WF. Race car vehicle dynamics. SAE Warrendale, USA, 2003.
5. Mischke M, Wallentowitz J. Dynamik der Kraftfahrzeuge. Springer Verlag, 2004.
6. Pytka J. Steering Effects Upon Lateral Dynamics of a SUV On Deformable Surfaces. SAE Technical Paper Series, 2011; Paper No. 2011-01-2159.
7. Zomotor A. Fahrverhalten. Vogel Verlag, Wurzburg, 1988.
8. http://www.nhtsa.gov/

Jarosław PYTKA, Ph.D. (Eng.)
Prof. TARKOWSKI, Ph.D., D.Sc. (Eng.)
Department of Automotive Vehicles
Mechanical Engineering Faculty
Lublin University of Technology
ul. Nadbystrzycka, 20-816 Lublin, Poland
e-mails: j.pytka@pollub.pl, p.tarkowski@pollub.pl

Włodzimierz KUPICZ, Ph.D. (Eng.)
Military Institute of Armour and Automotive Technology
ul. Okuniewska 1, 05-070 Sulejówek, Poland
e-mail: wlodekkupicz@wp.pl